# Single Cell Motility and Apoptosis Dynamics on Micropatterns

**Peter Johan Friedrich Röttgermann**


München 2016

# Single Cell Motility and Apoptosis Dynamics on Micropatterns

**Peter Johan Friedrich Röttgermann**

Dissertation
an der Fakultät für Physik
an der Ludwig-Maximilians-Universität
München

eingereicht von
Peter Johan Friedrich Röttgermann
aus München

München, 11.04.2016

Erstgutachter: Prof. Dr. Joachim O. Rädler
Zweitgutachter: Prof. Dr. Dieter Braun
Tag der mündlichen Prüfung: 15.06.2016

# Contents

**Zusammenfassung** vii

**Summary** ix

**1 Introduction** 1

Micropatterning for Single Cell Studies . . . 2
Quantitative Cell Migration . . . 2
Time Series & Signal Pathways of Apoptosis . . . 3
Nanoparticles: From Risk Assessment to Therapeutic Use . . . 4
Overview of this Work . . . 5

**2 A Versatile Method to Generate Multiple Types of Micropatterns** 7

Micro-Scale Plasma-Initiated Protein Patterning . . . 7
Controlling Substrate and Protein Surface Concentration . . . 8
Multicomponent Patterning . . . 10

**3 Cellular Self-Organization on Micro-Structured Surfaces** 13

Cellular Self-Organization on Microstructured Surfaces . . . 13
Quantification via Order Parameters . . . 14
Model for Mean-Time to Settle . . . 15
Optimal Lattice Geometry . . . 17

**4 Cell Motility on PEG Block Copolymers Correlates to Fibronectin Surface Adsorption** 19

Surface Passivation . . . 19
Cell Morphology and Motility . . . 20
Neutron Reflectivity on Polymer Layers . . . 21
Interpretation of PEG-Protein Interface . . . 22
Interpretation Cell Behavior on Polymer Layers . . . 23

**5 Stochastic Transitions and Relative Affinity of Single Cells on Two-Adhesion Site Micropatterns** **25**
Phenomenon of Cell Hopping . . . 25
Dependence of Cell Migration on Geometry . . . 26
Relation between Cell Transition and Lamellipodium Protrusion . . . 28
Affinities for Different Proteins and Nano-Patterned Sites . . . 29

**6 Time-Resolved Study of Nanoparticle-Induced Toxicity** **31**
Parallel Assessment of Cell Death Time Courses . . . 31
Time-Dependent Dose Response Function . . . 32
Two Parameter Correlation of Cell Death . . . 34

**7 Multiparameter and Kinetic Correlation Analysis of Apoptosis Events** **37**
Marker Specific Phenomenological Time Courses . . . 38
Distribution of Apoptotic Event Times . . . 41
Two-Color Pair Correlation of Successive Events . . . 41
NP-Dose Dependence of ROS . . . 44
High Content Analysis of Lysosomal Break . . . 45
Noise in Heterogeneous Timing of Apoptosis Signal Events . . . 46

**8 Conclusion and Outlook** **47**
Extension from Single to Oligo-Cell Analysis . . . 48
Towards High-Throughput Screening and Analysis . . . 49

**List of Abbreviations** **51**

**List of Figures** **53**

**Bibliography** **55**

**Associated Publications** **69**
Publication 1: Cellular Self-Organization on Microstructured Surfaces . . . 71
Publication 2: Cell Motility and FN Adsorption on PEG Block Copolymers . . . 87
Publication 3: PEG - Studies from Tethered Lipid Bilayers to Protein-Cell Interactions . . . 99
Publication 4: Versatile Method to Generate Multiple Types of Micropatterns . . . 103
Publication 5: Time-Resolved Study of Nanoparticle Induced Apoptosis . . . 117
Publication 6: Biocompatible DNA-Gold Nanorods for Ultrafast DNA Detection . . . 133
Publication 7: Stochastic Transitions and Relative Affinity of Single Cells . . . 207
Publication 8: Kinetic Correlation Studies of Apoptosis Events . . . 217

**Danksagung** **235**

# Zusammenfassung

Zeitaufgelöste Microarrayanalysen ermöglichen die Quantifizierung heterogener Einzelzelldynamiken und die Aufschlüsselung biologischer Signalwege. Dies kann für die Medikamentenentwicklung insbesondere bei der personalisierten Medizin von großem Nutzen sein. In dieser Arbeit wird eine neue Microarraymethode und deren Charakterisierung sowie Anwendung für Toxizitätsstudien vorgestellt.

Im ersten Teil wird eine neu entwickelte Mikrostrukturierungstechnik eingeführt, die plasmainduzierte Strukturierung und Copolymerpassivierung kombiniert. Dadurch wurden einfach und schnell homogene Strukturen auf verschiedenen Oberflächen erzeugt und die Oberflächenkonzentration unterschiedlicher Proteine variiert. Als Erweiterung der Technik wurden in Kombination mit *Micro-Contact Printing* verschiedene Proteine gleichzeitig aufgebracht.

Basierend auf dieser Mikrostrukturierung wird eine Methode für Einzelzellarrays vorgestellt, bei der die Besetzung über zelluläre Selbstorganisation erfolgt. Aufgrund unterschiedlicher Affinität migrieren Zellen ungerichtet auf den passivierten Flächen des Arrays und besetzen nach und nach dessen Proteinfelder. Dadurch muss nach der Zellaussaat nicht mehr gewaschen werden. Das Phänomen der Selbstorganisation wurde für mehrere Zelllinien gezeigt, und die optimale Gittergeometrie abhängig von der Zellmotilität bestimmt. Der Ordnungsprozess wurde mit einem Reaktions-Diffusions-Modell charakterisiert.

Partielle Zelladhäsion auf passivierten Flächen auf den Microarrays wurde beobachtet. Dieses Phänomen wurde mittels Neutronenreflektometrie und Fluoreszenzmikroskopie untersucht. Dabei wurde die Proteinadsorption an Block-Copolymeren mit hydrophilem oder hydrophobem Rückgrat und unterschiedlichen Polyethylenglykol (PEG)-Kettenlängen verglichen. Ein hydrophobes Rückgrat wird durch die PEG-Ketten so abgeschirmt, dass weder Proteine adsorbieren noch Zellen adhärieren können. Im Gegensatz dazu wurde beim hydrophilen Rückgrat Proteinadsorption und Zelladhäsion beobachtet. Zudem wurde das Migrationsverhalten auf passivierten Flächen im Vergleich zu reinen Proteinoberflächen untersucht: Es wurden zwar höhere Geschwindigkeiten aber geringere Persistenzzeiten gemessen.

Mittels der oben beschriebenen Mikrostrukturierung wurden künstliche Zweizustandssysteme hergestellt. Indem zwei Adhäsionsinseln durch dünne Verbindungsstege verbunden werden, können Zellen diskrete Platzwechsel vornehmen. Zunächst wurde der Stegabstand variiert. Mit zunehmendem Abstand fallen die Transferraten, die durch die Lamellipodienausbildung bedingt werden, exponentiell. Zudem wurden relative Affinitäten zwischen verschiedenartigen Adhäsionsflächen durch die Bestimmung der Besetzungszeiten und der Transferraten quantifiziert.

Die beschriebenen Einzelzellarrays wurden für zeitaufgelösten Toxizitätsstudien amino - funktionalisierter Polystyrol-Nanopartikel genutzt. Aus den Fluoreszenzsignalen zweier Apoptosemarker wurden der Anteil toter Zellen als Funktion der Zeit ermittelt. Es wurde eine Zeitabhängigkeit der Dosis-Wirkungs-Beziehung gezeigt. Um dies zu berücksichtigen wird statt der mittleren effektiven Wirkkonzentration $\mathrm{EC}_{50}$ ein neuer zeitabhängiger Parameter eingeführt: die toxische Halbwertszeit $\tau_{50}$. Im letzten Kapitel wird das Konzept der zeitlichen Korrelation erweitert. Es werden sechs Marker analysiert, die apoptototische Veränderungen der Lysosomen, Mitochondrien und Plasmamembran, den oxidativen Burst und die Caspaseaktivität anzeigen. Das Anschlagen dieser Marker wurde aus den Fluoreszenzsignalen bestimmt. Durch paarweise Messung wurde die Zeitdifferenz zwischen den Markern ermittelt, um einen kinetischen Fingerabdruck der Apoptosesignalkaskade zu erstellen. Erste Messungen bestätigten die Hypothese, dass die Polystyrol-Nanopartikel den lysosomalen Signalweg induzieren.

Die Ergebnisse zeigen, dass Einzelzell-Antwortfunktionen Einblick in dynamische Verläufe intrazellulärer regulatorischer Netzwerke geben. Durch Ensemblemessungen ist dies nicht möglich. Die hier vorgestellten zeitaufgelösten Toxizitätsanalysen können daher neue Erkenntnisse für die Wirkstoffsuche liefern.

# Summary

Time-resolved microarray analysis allows to quantify heterogeneous single-cell dynamics and to elucidate biological signaling pathways. This bears significant potential for drug development and helps to pave the way for personalized medicine. In this thesis, an innovative microarray method and its detailed characterization are presented together with a first application for toxicity studies.

In the first part, a novel microstructuring method is introduced which combines plasma-induced patterning with copolymer passivation. This approach enables straightforward fabrication of homogenous patterns on various surfaces. In addition, surface concentration of various proteins can easily be adjusted. The technique was further extended with micro-contact printing to achieve multicomponent patterns consisting of different proteins.

Based on this micropatterning technique, a single-cell array approach is presented, in which filling is achieved by cellular self-organization: Cells randomly migrate on passivated areas and gradually occupy the protein coated adhesion sites. Therefore, no rinsing step is needed after cell seeding and thus, all input cells can be analyzed. The self-ordering phenomenon was shown for various cell lines and the optimal lattice geometry was determined for different cell motilities. The self-organization process was characterized using a reaction-diffusion model.

Partial cell adhesion is observed on passivated areas. This phenomenon was investigated by neutron reflectometry and fluorescence microscopy. Protein adsorption to block-copolymers was compared between hydrophobic and hydrophilic backbones and with polyethylene glycol (PEG) chains of various lengths. It was found that hydrophobic backbones are shielded by the PEG chains, so that protein adsorption and hence cell adhesion are not possible. In contrast, charged backbones exhibit protein adsorption and partial cell adhesion. In addition, cell migration on passivated areas was compared to pure protein surfaces: Higher cell speed but smaller persistent lengths were measured.

The characterized micropatterning approach was also used to generate artificial two state systems. On a pattern with two adhesion sites, interconnected by a narrow bridge, single cells can perform discrete transitions. First experiments showed that an increasing bridge length leads to an exponential decrease of transfer rates and is related to the growth of lamellipodia. With this setup relative affinities of two different adhesion sites were measured by quantifying occupation times and transition rates.

As a first application, the single-cell arrays were used for time-resolved toxicity studies of amino - functionalized polystyrene nanoparticles. The ratio of dead cells was determined as a function of time by analyzing fluorescence signals of two apoptosis markers. We show that the dose-response behavior is time-dependent. To consider this time dependence, we introduce a new parameter instead of the half maximal effective concentration $\mathrm{EC}_{50}$: the toxic half-life period $\tau_{50}$.

In the last part, the concept of time correlation was augmented: Six markers were analyzed which indicate apoptotic changes in lysosomes, mitochondria, and plasma membrane, oxidative burst, and caspase activity. The onset/breakdown time points of these markers were determined and time differences were evaluated by pairwise marker measurements. This leads to a kinetic fingerprint of the signaling cascade in apoptosis. First results confirm that amino-modified polystyrene particles induce cell death via the lysosomal pathway.

In summary, single cell response functions provide information on dynamic courses of intracellular regulatory networks. This would not be possible with commonly used ensemble measurements. Thus, the described time resolved toxicity analysis can provide unprecedented insights for automated drug discovery.

# Chapter 1

## Introduction

Personalized medicine is going to revolutionize patient care. The individual response of a patient is hereby linked to disease behavior or responses to drugs. In particular, advances in nanotechnology and biomarker discovery have raised new opportunities for improved predictive medicine, disease detection and diagnostic testing.[1, 2] This *in-vitro* profiling requires methods to define characteristic cellular properties, a so-called cellular "fingerprint". Such fingerprints are used for example on compound screening for anti-cancer drugs.[3, 4]

However, standard immuno-staining techniques, for example enzyme linked immunosorbent assays (ELISA) western blots, or real-time polymerase chain reactions require destructive preparation of cells into a homogenous solution and therefore provide only information on the average cellular response. Using this averaged response of the bulk population leads to false conclusions, as the average signal masks the heterogeneous response of single cells (see Fig. 1.1 a). Predictions become particularly imprecise, if an entire population does not behave uniformly and/or is divided into sub-populations.[5–7] These cell-to-cell variations are caused by differences at genetic, gene expression or protein level, and due to stochastic variations.[8] These drawbacks of bulk analysis are overcome by single cell tests such as flow cytometry.[9, 10] Nevertheless, flow cytometry only observes a static system at a single time point.

In contrast, a continuous observation of the cell track reveals the full dynamic, as visualized in Fig. 1.1b. Automated continuous screening of cell chips has already been developed. These chips allow to determine cell properties such as shape and motility or intra-/inter-cellular signaling and hence can give diagnostically relevant information.[11, 12] In spite of their high potential, such methods have not yet found their way into diagnostics and pharmaceutical development. With regard to these applications, this work presents technical innovations and optimizations of time-resolved single cell analysis. Before these innovations are described in detail (chapter 2-7), chapter 1 gives an overview of the underlying principles and background.

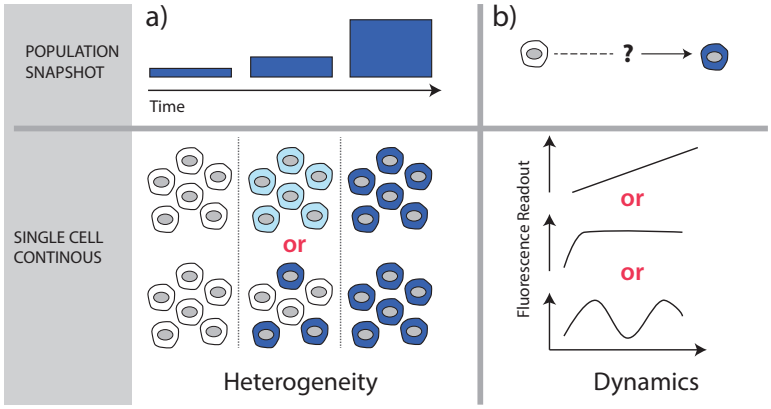


**Figure 1.1:** Necessity of continuous single-cell analysis a) Population heterogeneity: bulk analysis masks the heterogeneity of a cell population. Only single-cell approaches reveal possible population heterogeneity (e.g., heterogeneous molecule expression, variable cellular behavior). b) Dynamics: only continuous observation of single cells reveals the dynamics of cellular properties changing over time. Adapted from [13] with permission of Elsevier.

## Micropatterning for Single Cell Studies

For time-resolved measurements, assays are advantageous where cells are bound to a surface. Tracking cells over time at low concentrations in a cell culture dish without any trapping can be tedious due to time-consuming and often insufficient tracking success.[14] Micropatterned platforms solve these problems as cells stay on a position over time. Micro-fabrication techniques have evolved into a broadly used technique in cell biology.[15, 16] This can also be seen in the large variety of newly introduced patterning techniques.[16, 17] On the one hand, microstructures offer defined geometries for all cells. The response of single cells to the underlying geometry and the restriction of degrees of freedom (e.g. from 3D to 1D migration) allows for quantitative characterization of cell migration behavior. On the other hand, the single cell response can be read-out over time with low noise and high accuracy as all cells occupy an equal area. Fig. 1.2 shows a possible setup of a 2D micropattern for single cells. By automated image analysis for each cell, fluorescence time-traces can be extracted.

## Quantitative Cell Migration

Micropatterns can facilitate the study of cell motion. Cell migration plays an important role in processes such as wound healing or embryogenesis, but also in tumorigenesis. Some of the ”hallmarks of cancer” [20] correspond to ’classical’ *in-vitro* phenotypes: sustained proliferation, resistance to cell death, evasion of growth suppressors, and invasion.[21] In order to identify invasive migration of cancerous cells, it is necessary to find characteristics parameters. Cancer migration can be described by three types of motion, which is sketched in Fig. 1.3.[19, 22] Between 10 and 40% of carcinomas undergo an epithelial to mesenchymal transition. It is characterized by elongated cell morphology with established cell-polarity and by degradation of ECM upon proteolysis. Cell speed is with 0.1 -1 $\mu$m/min relatively low. This kind of motility can be studied well on rigid 2D

surfaces. The amoeboid motility is characterized by a much weaker cell-ECM attachment and by a much faster cell movement (up to 4 $\mu$m/min). The analysis of this motility is optimally studied in 3D environments. Collective motility in contrast to single cell movement maintain adherens junctions.[19] For instance, clusters or sheets of tumor cells can infiltrate lobular breast carcinoma and soma-ovarian carcinomas.[23, 24]

Quantitative analysis of these different migration behaviors can be conducted on micropatterns where the movement is restricted due to the lower degrees of freedom (1D or 2D) and due to geometric limitations of the patterns. There exist many studies on cell sheet migration tracking individual cells [25–28] as well as studies of single cells setups with various geometry designs, starting from narrow lanes, circle structure or ratchet formed patterns.[29–32] By characterizing migrative "fingerprints" such as cell speed, persistence in motion and rest times cancer cells could be identified.

Thereby, theoretical descriptions allow the reconstruction of experimental data as well as the prediction of cellular behavior. The mode of migration, for example, can be described by a bimodal correlated random walk.[33] Shape and traction forces of stationary cells on any micropattern can be reproduced, using a cellular Potts model.[33] Simulations, taking these constraints into account, show the spontaneous emergence of periodic cellular migration for crawling cells on stripe patterns.[34] In addition, energetic terms accounting for the adhesion energies of the micropattern and the cell elasticity are determining factors.[35]

## Time Series & Signal Pathways of Apoptosis

For personalized medicine, it is essential to understand the highly complex and sophisticated signal cascades in cell death. This information on cell death signaling can produce new strategies to exploit apoptosis for therapeutic benefit.[37] The different forms of cell death were initially classified by morphological changes: The programmed form of cell death (PCD), apoptosis, goes along with cell shrinkage, membrane blebbing, chromatin condensation, and DNA fragmentation; the

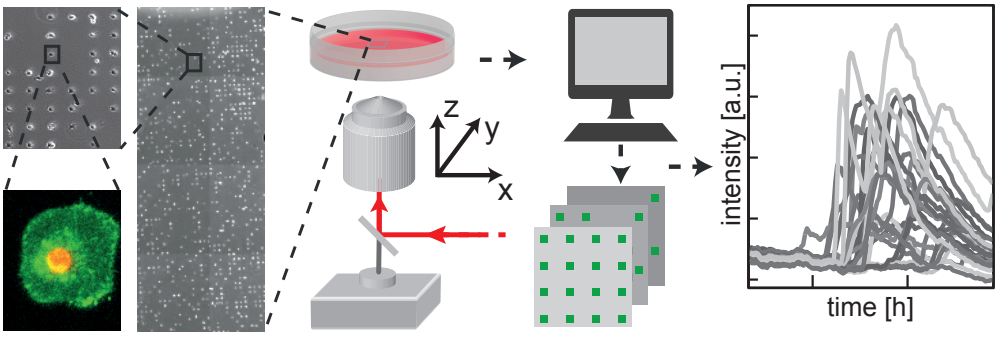


**Figure 1.2:** Overview of the process of single cell time-lapse analysis. Single cells are trapped onto a microarray. Via a fully automated microscope, fluorescence signals can be recorded at different wavelengths. The ease of automated image processing on the cell lattice enables high-throughput analysis of the kinetics of single-cell fluorescence. Adapted from [18] with permission of Multidisciplinary Digital Publishing Institute.

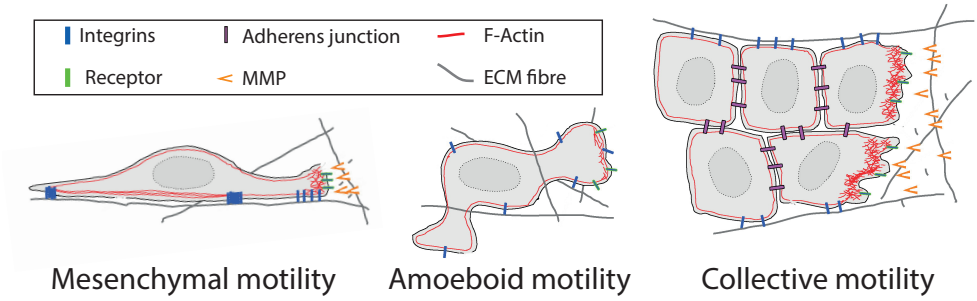


**Figure 1.3:** Schematic overview of cancer cell motion: i) Mesenchymal motility is characterized by elongated morphology, and it is dependent on matrix metallo proteases (MMP), ii) amoeboid motility is characterized by an amorphous cell shape and rapid changes in direction, iii) collective motility is characterized by collections of cells invading with retained cell-cell-contacts. Adapted from [19] with permission of Elsevier.

uncontrolled form, necrosis, goes along with cell swelling, membrane rupture, and uncontrolled release of the cytosolic content into the environment. The morphological phenotype of PCD underlies molecular signaling which can be divided into two main pathways, the extrinsic and intrinsic pathway (see Fig. 1.4). The extrinsic pathway is triggered via death ligands, such as TRAIL, FAS-L, FAT2, or TWEAK, which bind to corresponding cell membrane receptors. Upon binding of the death ligands, death domains change their conformation and turn pro-caspase8 into the active caspase8 form, which further activates the execution pathway with caspase3. The intrinsic pathway is triggered by different stimuli, such as radiation, UV, DNA damage, and hence activating the mitochondria permeabilization. The mitochondria contains pro- and anti-apoptotic factors (Bax Bad, Bcl-2) which either get increased or inhibited, causing a decrease of mitochondrial membrane potential and release of cytochrome C. Cytochrome C activates the caspase9, which induce the execution pathway. In literature, many new forms of cell death have been introduced regarding the high complexity of the pathways, e.g. mixed forms with crosstalk between apoptosis and necrosis, the so-called necroptosis.[38]

## Nanoparticles: From Risk Assessment to Therapeutic Use

Nanoparticles have found widespread use in consumer products, as e.g. in food, sunscreens, toothpastes and skin care. That is because NPs have exceptionally physico-chemical properties with high surface area, tunable chemical composition, electronic properties and surface structure. These properties are benefitial for many applications, yet the interaction of these nano-sized materials with cells is not fully understood and has raised concerns about potential toxicity and environmental issues.[39, 40] For example, the large surface area to volume ratio could lead to an alteration in biological activity compared to parent bulk materials. In particular, metal oxide particles are known candidates to induce oxygen radicals and oxidative stress.[41] But also the size of particles could induce adverse effects, for example small gold NPs induce high toxicity on embryonic stem cells.[42]

Nevertheless, many studies showed that a broad class of particles are non-toxic or in combination

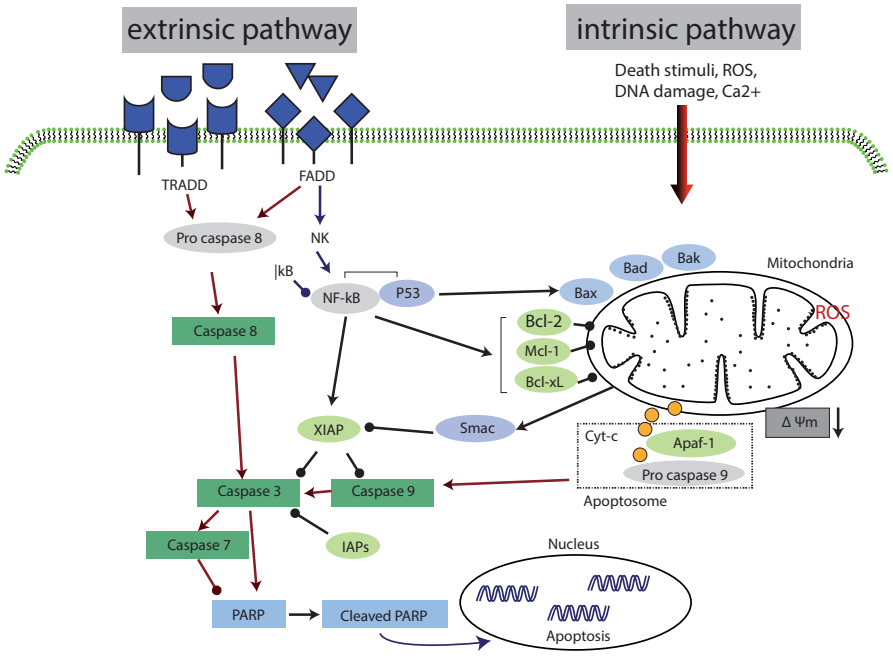


**Figure 1.4:** Schematic overview of apoptosis which can be divided into two main pathways: The extrinsic apoptosis is triggered via ligand binding (TRAIL, FAS, FAT2) to cell receptors, the intrinsic pathway is triggered by different stimuli (UV, radicals) and is characterized by the stimulation of the mitochondria. The execution pathway by activation of caspase3 is the same for both main pathways. Adapted from [36] with permission of Dove Press.

with polymer coatings have highly reduced adverse effects.[43] Therefore, NPs can bear a chance for therapeutic use.[44] They can be used as carriers for targeted drug delivery due to their ability to overcome certain protective membranes in the body such as the blood brain barrier.[45] NPs can be further used as nanosensors for early recognition and identification of diseases or as a new therapeutic method for the treatment of cancer. The signaling pathways associated with the engineered NP-mediated toxicity for either health related subjects or toxicity evaluation are still largely unknown [46] and need therefore detailed characterization by continuous single cell analysis.

## Overview of this Work

In the first results chapter of this thesis, a new patterning approach is introduced, which is capable of forming multifarious 2D-microstructures and which can be extended to a multicomponent pattern in combination with micro-contact printing. Based on this micropatterning technique, an alternative approach obtaining cell arrays via self-organization is presented in chapter 3. The underlying mechanisms of protein and cell interaction on cell repellent surfaces are analyzed via neutron reflectometry and cell motility measurements in chapter 4. In chapter 5, a first application of the cell array setup is introduced which uses time-resolved tracks of single cells on double microwell pattern. These double-well patterns allow to measure surface affinities and can further improve cell specific environments on the micropattern. A second application uses time resolved single cell analysis of NP-induced cell death, presented in the last two chapters (6 and 7). First

dose-response behavior are evaluated, a time-dependent effect of $\mathrm{EC}_{50}$ values is discussed, as well as correlation studies are performed. In chapter 7, selected key cell death events are fluorescently marked and characteristic time events are evaluated from phenomenological fit functions. The pairwise combination of markers with principal component analysis allows to identify sequences in cell death pathways.

# Chapter 2

## A Versatile Method to Generate Multiple Types of Micropatterns *

In the following chapter, a new approach of micropatterning is introduced, which features high versatility in the choice of substrate and protein coating, and can be combined with microcontact printing to produce complex patterns of up to three different proteins. The technique is used for all cell studies described in this thesis.

Most patterning protocols are based on one of the following three approaches: soft-lithography in form of micro-contact printing ($\mu$CP), [48–50] photo-lithography, [51–54] or plasma-based patterning. [55–59] Each of these techniques has its own advantages: $\mu$CP provides flexibility in the choice of transferred protein or geometry, and does not require advanced and expensive equipment. Photo-lithography-based protocols produce very homogeneous patterns and can be scaled up very easily. Plasma-based approaches enable strong and simple activation of the surface which can be exploited to directly cause increased cell attachment on elsewise cell repellent substrates [56, 59] or to spatially control polymer or protein deposition.[55, 57, 58] As micropatterning should be accessible to a broad range of labs, simple and cost-efficient working protocols are needed that can be adapted to different experimental conditions regarding geometry, protein and substrate. Here, an alternative plasma based micropatterning approach is presented, which is based on plasma-induced patterning in combination with PEGylation, and will be referred as micro-scale plasma-initiated protein patterning ($\mu$PIPP).

### Micro-Scale Plasma-Initiated Protein Patterning

In the following, the basic steps of $\mu$PIPP protocol are described: A polydimethylsiloxane (PDMS) stamp with the desired micropattern is placed on a surface (see Fig. 2.1a) and exposed to $O_2$ plasma which induces a partially negatively charged surface. Only patterns with no cavities (cf. pattern in Fig. 2.1 a and b) are applicable, so that the plasma can reach the spaces between the desired patterns which are going to be passivated. For the passivation, a droplet of a PLL(20kDa)-g[3.5]-PEG(2kDa) solution is drawn by capillary action between the open spaces of stamp and surface.

*Part of this chapter and figures are adopted from F. J. Segerer, P. J. F. Röttgermann, et al., 2016 [47] with permission of the American Institute of Physics Publishing.

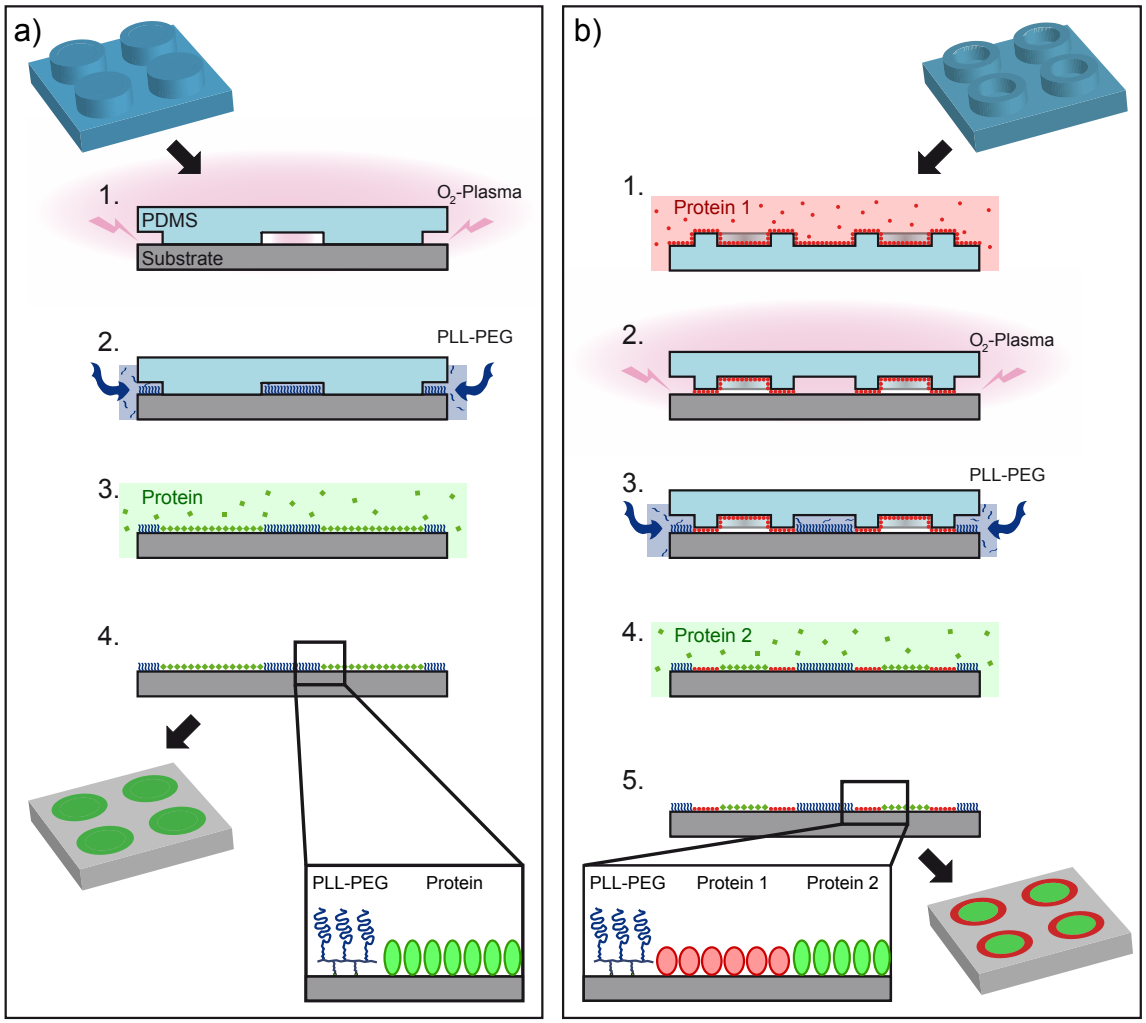


**Figure 2.1:** Patterning protocols. a) Patterning procedure for conventional $\mu$PIPP: (1.) The surface is partially covered by a PDMS stamp of the desired pattern and exposed to $O_2$ plasma (2.) A PLL-PEG solution is applied to the margins of the stamp and is drawn over the exposed surface by capillary action (3.) The stamp is removed and the surface is incubated with the protein. b) $\mu$PIPP combined with $\mu$CP: (1.) The UV-ozone activated PDMS stamp is incubated with Protein 1 for 1 h and (2.) printed on the surface, which is then exposed to $O_2$ plasma (3.) PLL-PEG solution is applied to the stamp edge and drawn between stamp and surface by capillary action (4.) The stamp is removed, and the surface is incubated with Protein 2.

PLL binds to the surface by electrostatic interaction and PEG brushes form a protein-repellent layer above. After 30 min incubation, the stamp is removed, and the sample is washed with PBS. Finally, a protein solution (e.g. 50 $\mu$g/ml fibronectin) is incubated for about one hour at room temperature and washed thrice with PBS. After exchange with cell culture medium, cells can be seeded on the patterned samples.

## Controlling Substrate and Protein Surface Concentration

The $\mu$PIPP technique implies many advantages in comparison to other common techniques. First, it can be applied to various substrates of different material properties with no adjustment of the

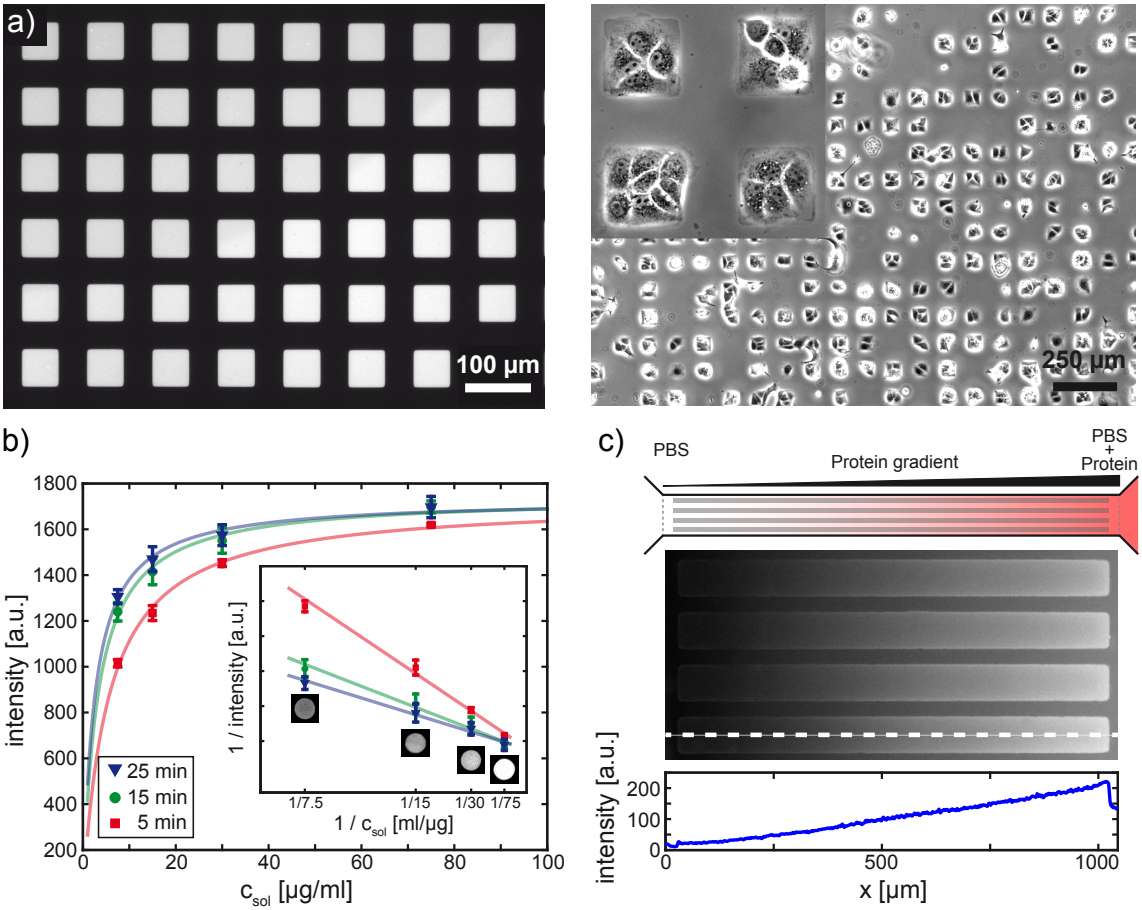


**Figure 2.2:** a) $\mu$PIPP on cyclic olefin copolymers. (Left) Fluorescence image of fibrinogen Alexa-488 pattern. Black areas are passivated with PLL-PEG. (Right) MDCK cells on fibronectin patterns 24 h after cell seeding (inset 5x magnified). b) Protein density within patterns can be adjusted by varying both the concentration in the incubation solution $c_{sol}$ or the incubation time $\tau$. Data is well fitted by a Langmuir isotherm (Eq. 2.1). The inset shows the corresponding linear scaling in inverse presentation. Error bars indicate the standard deviation. c) A gradient in the surface-bound protein density can be generated within the patterns by incubation in a protein concentration gradient formed in a chemotaxis chamber. Fluorescence image of micropatterned stripes obtained by incubation in a gradient of fibrinogen Alexa-488 and below measured intensity along the line shown in the middle panel.

protocol. Homogenous protein patterns could be generated on cyclic olefin copolymers (COC), see Fig. 2.2a), standard tissue cultured polystyrene (tc-PS), glass, which are all typical surfaces for cell culture, on parylene C, which is often used as biocompatible coating for electronic devices, and on PDMS with variable stiffnesses, which find application in mechanosensing cell experiments. Cell adhesion and stable confinement were achieved on all substrates several hours after seeding (Fig. 2.2a). The adsorption of the protein as well as the stable passivation confinement depends on the material properties of the substrate. On COC, for example, stable confinement over a period of several days was observed.

Protein coating via incubation rather than stamping has the advantage that the protein as well as the concentration can be easily varied without any tedious adjusting of the protocol. Fluorescence intensities are shown in dependence of different bulk concentrations $c_{sol}$ and incubation times $\tau$ in

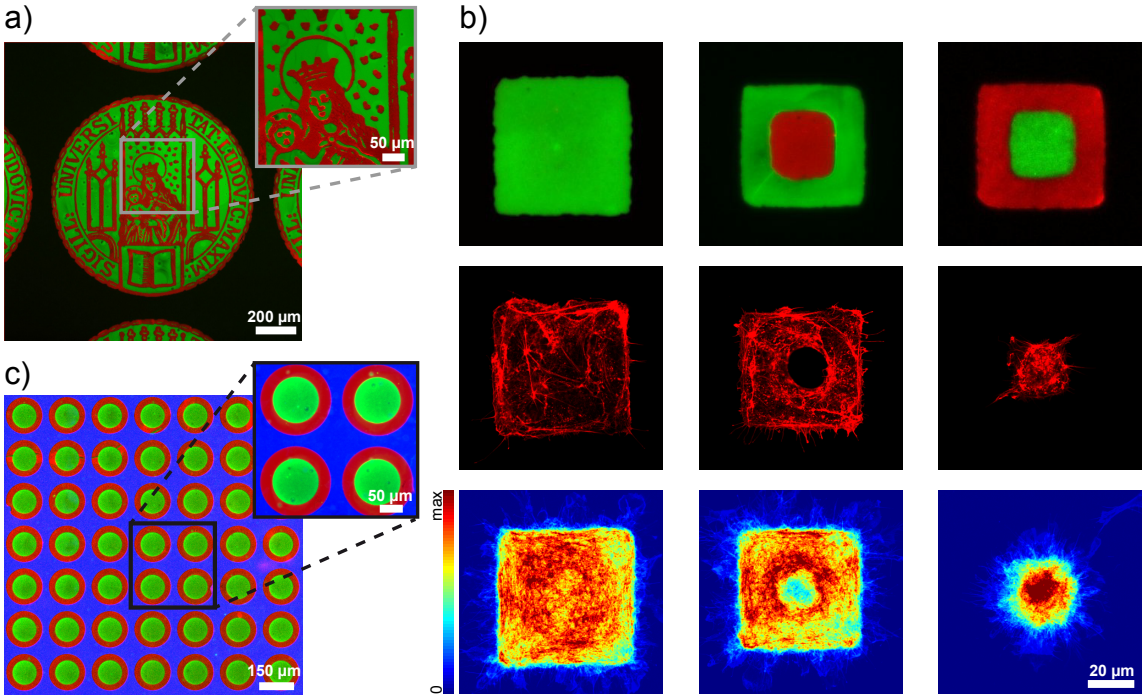


**Figure 2.3:** Multicomponent patterning. By combining $\mu$PIPP with $\mu$CP, patterns consisting of three different functionalizations can be formed. a) A complex pattern consisting of PLL-PEG (black) and fibrinogen labeled with Alexa-488 (green) and Alexa-647 (red), respectively. b) Fluorescence image of patterns composed of fluorescently labeled fibronectin (green) and laminin (red) (top row). A representative confocal fluorescence image of the actin cytoskeleton of HUVECs arranged in such patterns (middle row), and a heat map of the actin cytoskeleton distribution of cells on over 20 evaluated patterns (bottom row). c) Framed circle pattern consisting of fibronectin Alexa-488 (red), fibrinogen Alexa-594 (blue) and laminin Alexa-647 (green), respectively.

Fig. 2.2b. The adsorption behavior as a function of $c_{sol}$ is well fitted by the Langmuir expression for the adsorption isotherm:

$$c_{surf} = c_{max} \times \frac{\alpha \times c_{sol}}{1 + \alpha \times c_{sol}} \tag{2.1}$$

where $c_{surf}$ denotes the surface concentration of the protein, $c_{max}$ the saturated surface concentration and $\alpha$ the equilibrium constant. Short incubation times ($\tau$ = 5 and 15 min) are obviously not in the in equilibrium but still can be approximated with the Langmuir expression. The concentration-dependent adsorption can be used to create surface-gradient patterns using chemotaxis slides (ibidi) (see Fig. 2.2c). Protein surface gradients can have a guiding effect on cell motion [60, 61] and therefore might be a powerful tool to trigger cell motion. Besides the pattern and surface gradient, a soluble protein gradient can be applied in the chemotaxis slides. Such multicue environments of surface and solution gradients can further facilitate the step from *in-vitro* to *in-vivo* conditions.

## Multicomponent Patterning

$\mu$PIPP can also be combined with conventional $\mu$CP in order to create patterns consisting of up to three different proteins. Fig. 2.1b shows the procedure of the combined protocol. In the first step,

a stamp with enclosed cavities (e.g. donut structures) is inked with a first protein and transferred onto a UV-ozone activated COC surface. The enclosed cavities shield the surface from plasma and allow for coating of a second protein according to the $\mu$PIPP protocol. In this way, complex patterns can be created, as depicted in Fig. 2.3a. In order to obtain patterns of three proteins, a third protein is incubated instead of adding PLL-g-PEG for passivation (see Fig. 2.3c). In contrast to iterative methods of creating multiple component patterns, the advantage of creating all functionalizations with the same stamp (and working iteration) is that the individual components can be placed directly adjacent to each other and their relative positioning can hence be accurately controlled.

Such multi-component patterns can be used to directly measure cell response to different surfaces. A first simple experiment is shown in Fig. 2.3b, in which patterns of "framed" squares connected of two different extracellular matrix proteins fibronectin and laminin-1 were used. Increased or decreased adhesion affinity for laminin has been reported before.[62, 63] In our experiment, human umbilical vein endothelial cells (HUVEC) are strongly affected by the different proteins, as they avoid the laminin coated parts and only adhere on the fibronectin. It did not matter whether the laminin was coated via printing or incubated via protein solution (column 2 and 3 in Fig. 2.3b).

In summary, the novel $\mu$PIPP technique allows for simple and fast fabrication of micropatterned protein coated surfaces for cell studies. It features a compatibility with a wide range of substrates and proteins. The adsorbed protein concentration can be readily controlled, and gradients of surface bound proteins can be created. In combination with $\mu$CP, patterns of three different components can be achieved from the design of a single stamp obtaining high accuracy in the relative positioning of all components while still maintaining a relatively simple protocol. Different surface functionalizations can therefore be directly compared. The simplicity and versatility of the protocol paves the way for a standard micropatterning tool in cell science labs.

# Chapter 3

## Cellular Self-Organization on Micro-Structured Surfaces*

The latter described $\mu$PIPP technique can be used to generate micropatterns for single-cell arrays. There exist various ways to obtain arrays with single cell occupation: Most prominently, cells are seeded in excess on chemically functionalized micropatterns. The pattern is rinsed after a defined incubation time in order to remove non-adherent cells.[65–67] The challenging step lies in the right incubation time as well as in the initial cell density. Other approaches use microfluidic wells to trap cells by shear stress or by varying the flow rate. [68–70] However, optimizing the occupancy level can be tedious. A third common approach uses inkjet printing.[16, 71] The shear stress during cell transfer can rupture cells and hence reduces viability.

Here, a new approach is introduced which is based on cellular self-organization on surfaces with different adhesion affinities. This technique avoids any washing step and therefore does not bias a population as, e.g., weakly adherent cells are not washed away. The self-organization process is shown exemplary for three different cell lines A549, HuH7, MDA-MB-436 for various geometries in the following.

### Cellular Self-Organization on Microstructured Surfaces

The pattern created with $\mu$PIPP consists of 30$\times$ 30 $\mu$m, fibronectin-coated adhesion squares with various lattice spacings, surrounded by PLL-g-PEG passivated areas. Fig. 3.1a shows selected images of a time-lapse series over 24 h. Cells are seeded at a surface-concentration equal to the number of available adhesion sites (e.g. 50,000 cells per $\mu$-dish (ibidi) or 10,000 cells per channel of a 6channel slide (ibidi)). Directly after seeding, cells are randomly distributed on the micropattern. Cells which attach directly onto a FN square spread immediately, whereas cells which are located on the PLL-PEG parts are partially adherent and begin to migrate in a random manner (Fig. 3.1b 0-210min). Upon contact with the edge of an adhesion site, the cell spreads onto it and fills the entire adhesion area within 30 min. (Fig. 3.1b 220-250min). Cells remain captive resulting in an occupation of more and more adhesion sites with time (Fig. 3.1a 2-24h). Deviations

*Part of this chapter and figures are adopted from Röttgermann et al., 2014[64] with permission of The Royal Society of Chemistry.

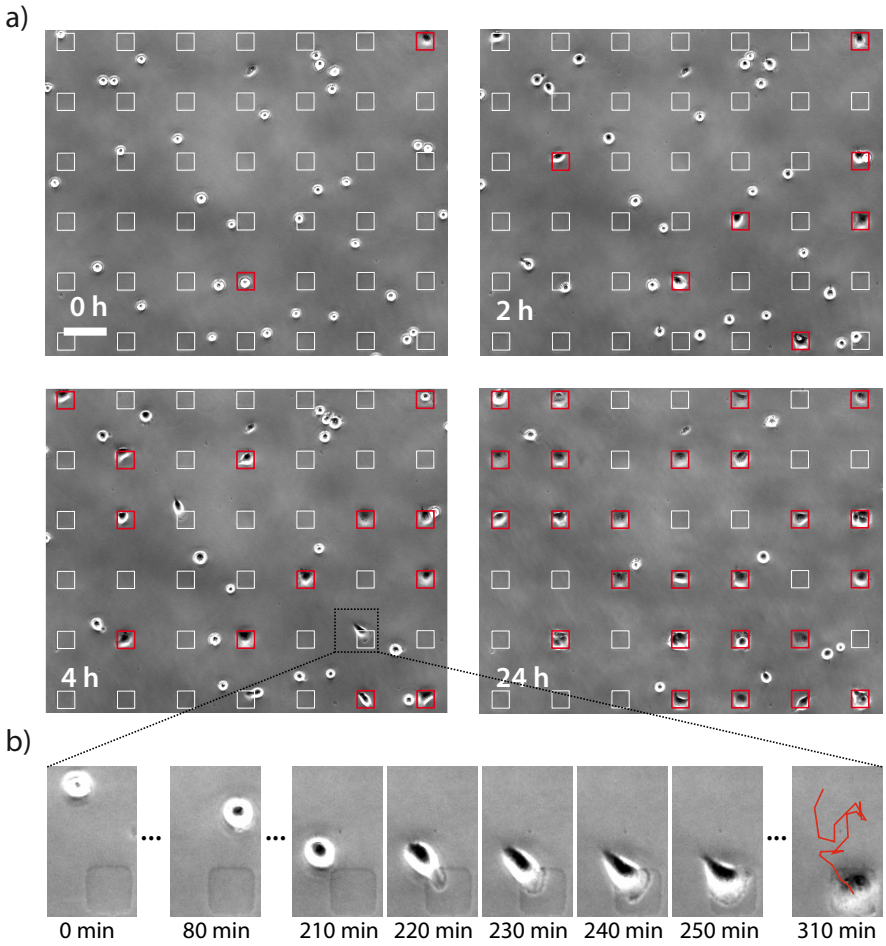


**Figure 3.1:** Dynamics of cellular self-organization. a) Selected images of the self-organization process during a time-lapse measurement. After cell seeding, cells are randomly distributed. They start to migrate randomly until they find adhesion sites. Gradually, an ordered distribution is obtained. Occupied sites are highlighted in red. Scale bar: 100 $\mu$m b). Detailed view of an adhesion process (3X magnification). The red track represents the trajectory of the cell.

from the ideal case of a singly occupied array occur in form of multiple occupancies, unoccupied sites (vacancies) and interstitial cells (see Fig. 3.2a). Multiple occupancies are caused by either settling of several individual cells in one site or by cell division.

## Quantification via Order Parameters

In order to assess the dependence of the ordering process on elapsed time the occupancy is quantified by a filling factor $F(t)$ which is defined by the ratio of occupied sites $N_{OC}$ to the total number of sites $N_S$: $F(t) = N_{OC}/N_S$. In Fig. 3.2b the filling factor is plotted against time for various lattice distances $d_l$ 70, 90, 110, 130 and 230 $\mu$m. The initial occupation numbers are in good agreement with a random deposition model described by a Poisson distribution with an expected value of 0.5. High fillings of 80% are obtained for small $d_l$ (70 and 90 $\mu$m), the poorest occupancy

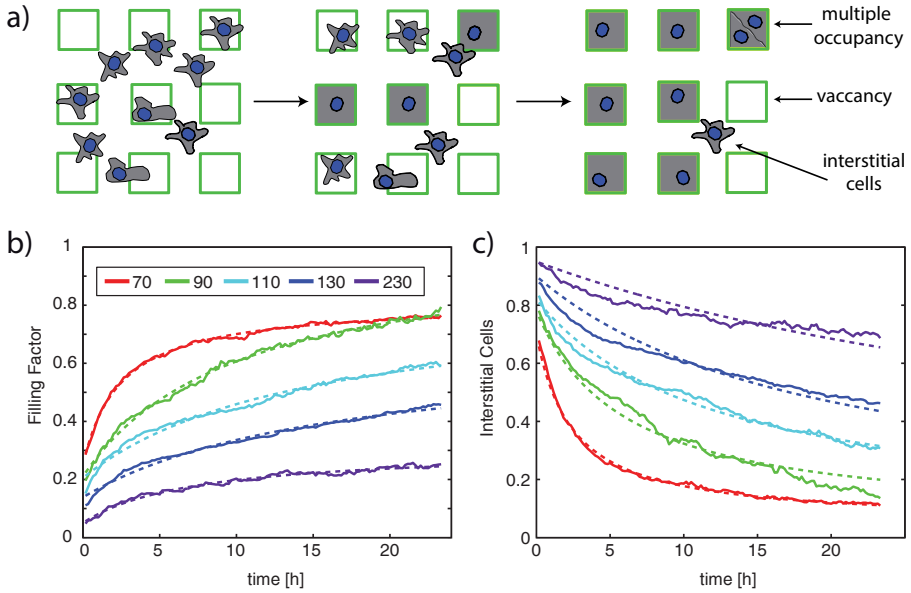


**Figure 3.2:** Dependence of order parameters on lattice spacing. a) During the self-organization process, optimal filling is compromised by defects such as multiple occupancies, vacancies and interstitial cells. Occupancy is quantified via order parameters: b) The *Filling Factor* describes the ratio of occupied lattice sites to the total number of sites. For A549 the highest filling of 80 % for a lattice distance of $d_l$ = 90 $\mu$m is obtained. c) The parameter *Interstitial Cells* denotes the ratio of misplaced to total cells. Misplaced cells after 24 h are either dead cells or cells which have not yet found a site.

level of 25% is obtained for $d_l$= 230 $\mu$m after 24h. In order to get a rough estimate about the filling rate, the time courses of the filling factor can be fitted by the phenomenological expression: $F(t) = F_0 + F_{max} \times (1 + t_{1/2}/t)^{-1}$ with a mean filling time $t_{1/2}$, an initial filling $F_0$ (initial occupation of the Poisson distribution) and a saturation filling $F_{max}$. Whereas vacancies are accounted for in the filling factor, the number of interstitial cells, which have not yet found an adhesion sites or have died, can be quantified as well. This is described by the defect parameter $I(t)$ which is defined as the ratio of interstitial cells $N_{IS}$ to the total number of cells $N_C$: $I(t) = N_{IS}/N_S$. For large distances, the number of interstitial cells increases drastically as cells which do not find an adhesion site within a day have a low survival rate (see Fig. 3.2c). In order to demonstrate that the self-organization is a generic behavior, order parameters were also analyzed for HuH7 and MDA-MB-436 cells. The phenomenon of cellular self-organization for these cell lines remains unchanged. However, as these cells have different properties with respect to adhesion strength, motility and viability, differences in the order parameter were measured.

## Model for Mean-Time to Settle

In order to understand how cells find a lattice site depending on lattice spacing and cell motility, a simple model that reveals the time-to-order on a cell chip is adapted from a model of chemoreception from Berg and Purcell.[72, 73] It describes the time needed for a freely diffusing ligand to find a cell surface receptor on a two dimensional membrane (circular patch). In our case, cells migrate in a random manner (with a motility constant $D$) on the microstructure $A_{IMG}$ (the field

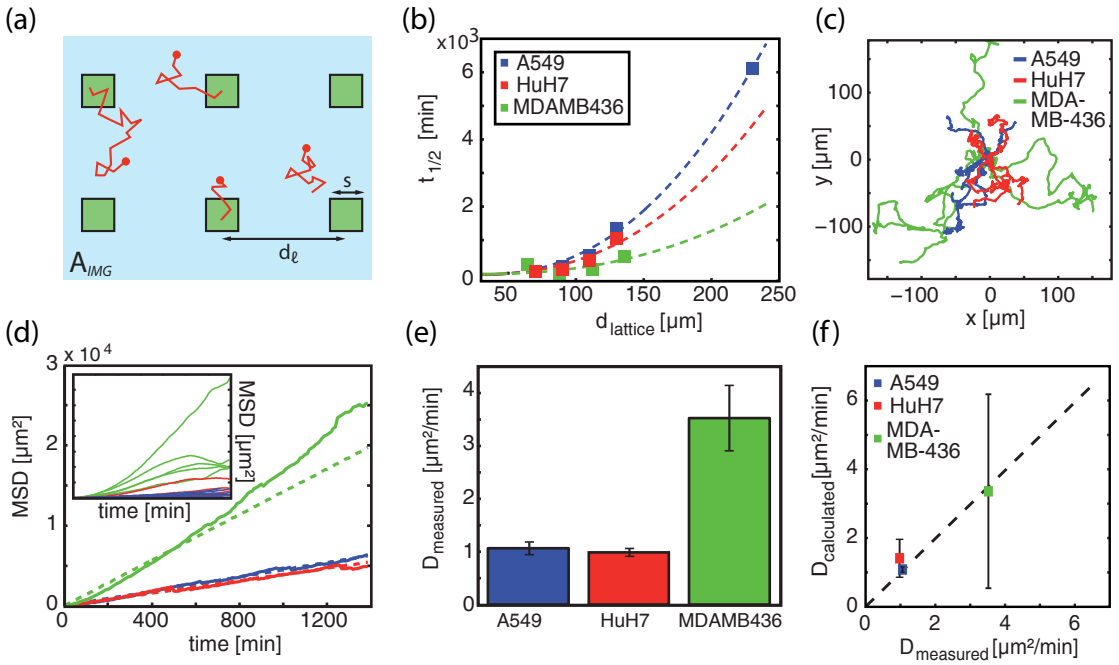


**Figure 3.3:** a) On an image area $A_{IMG}$ (light blue), adhesion sites of size $s$ (green) are distributed in a rectangular lattice with spacing $d_l$. The search process for single cells is depicted by the red trajectories. b) The best fit $t_{1/2}$ values obtained by fitting the decay curves for the parameter *Interstitial Cells* to Eq. 3.2 are plotted as a function of spacing $d_l$. The cell settling process, as described by a model adapted from Berg and Purcell (Eq. 3.1), is in good agreement with these data (dashed lines). c) Representative trajectories for all three cell lines migrating on non-patterned PLL-g-PEG are shown. d) Inset: MSDs of the trajectories in d) are plotted against time. The averaged MSDs of 100 cell tracks per cell line can be described by a 2D random walk. e) Fitting $D_{measured}$ reveals motilities of $1.1 \pm 0.1 \mu m^2\ min^{-1}$ (A549), $1.0 \pm 0.05 \mu m^2\ min^{-1}$ (HuH7) and $3.5 \pm 0.6 \mu m^2\ min^{-1}$ (MDA-MB-436). f) The motilities $D_{calc}$ from b) are plotted against the motilities $D_{measured}$ in e). The model is in good agreement with the measured motilities (correlation of 0.987), error bars correspond to 95 % confidence limits of the fit in b). Note that the error interval for MDA-MB-436 is big as the low number of points for the fit results in a high uncertainty.

of view), until they contact adhesion sites of length $s$ (Fig. 3.3a). Square adhesion sites are treated as circular shapes and the analytical expression ($Ns^2 \ll A_{IMG}$) is employed for the mean-time to settle:

$$\overline{t_{1/2}(d_l)} = \frac{1.1 A_{IMG}}{8\pi N(d_l) D}\, ln\left(\frac{1.2 A_{IMG}}{4 N(d_l) s^2}\right) \tag{3.1}$$

with the number of adhesion sites $N(d_l)$ depending on the lattice spacing.

The calculated $t_{1/2}$ values can be compared with the experimentally measured time-dependent decay curves for interstitial cells from Fig. 3.2c:

$$I(t) = I_0 + \frac{I_0 - I_{min}(d_{70})}{1 + t_{1/2}/t} \tag{3.2}$$

$I_0$ is the offset at t=0. In order to compare the $t_{1/2}$ values for all lattice distances, the same ratio of interstitial cells $I_{min}$ for $d_l$=70 $\mu$m was assumed neglecting different saturation levels due to

cell death. The $t_{1/2}$ values from the fits to Eq. 3.2 are plotted as a function of the lattice spacing for the three cell lines A549, HuH7 and MDA-MB-436 (see Fig. 3.3b) . The dashed lines are the fits from the adapted Berg and Purcell model (Eq. 3.1) which is found to be in good agreement with the data. The calculated motility constants $D_{calc}$ of the model can be compared with directly measured motilities. For this reason about hundred single cell tracks on PLL-PEG surfaces were recorded (Fig. 3.3 c) and mean square displacements (MSDs) (Fig. 3.3d) were calculated as

$$MSD(t) = \left\langle \left\langle \mathbf{X}_i(t+t_0) - \mathbf{X}_i(t_0))^2 \right\rangle_{t_0} \right\rangle_i \tag{3.3}$$

where $\mathbf{X}_i(t)$ denotes the center of cell $i$ at time $t$. $\langle\cdot\rangle_{t_0}$ designates the time averaging over all times $t$ with starting time $t_0$ and $\langle\cdot\rangle_i$ the ensemble average over all tracked cells. Cell motility could be extracted by the following expression $MSD(t) = 4Dt$, neglecting persistent motion or other biased random walks [74–76]. The motilities $D_{measured}$ obtained by the diffusion expression (see Fig. 3.3e) are in excellent agreement with the motilities derived from the adapted model Fig. 3.3f. This demonstrates that this simple model allows one to calculate the mean time to order $t_{1/2}$ for any given lattice distance using a single parameter, the motility value for the cell line of interest.

## Optimal Lattice Geometry

Finally, the optimal lattice geometry is discussed. Taking all order parameters into account, the best single cell filling can be achieved for a geometry of $d_l$=90 $\mu$m. For the analyzed cell lines a 2 to 3.5 fold increase in the filling rate of single cell occupancy could be achieved after 24h, e.g. for A549 cells an initial filling of 20% rises to 45% after 5h and to 75% after 24h. Based on the time course of occupation, it should be possible to reduce the incubation time to 5 h and still obtain reasonable filling. Shorter incubation periods are desirable in order to prolong the available time window for single-cell measurements. Common approaches require similar incubation times between 2 to 15h to allow cells to adhere completely to the substrate.[77–79] Decreasing the lattice spacing further than $d_l$=90 $\mu$m favors the formation of artifacts of bridge forming between two adhesion sites as well as constant movement between the sites, as the lammelipodia are in reaching distance to sense neighboring sites.

In summary, we have shown that creating single cell arrays by cellular self-organization offers several advantages in comparison to common procedures. All input cells can be analyzed, as this method avoids a washing step after seeding. This might be especially be useful for rare stem cells, that are available in limited numbers. The self-ordering phenomenon was observed for various cell lines and should be applicable for a wide range of cells. Optimal single-cell filling can be preferably achieved with small distances due to faster filling rates. A theoretical model based on a random-walk search process was presented. The model allows for optimization of the time-to-order for a specific cell type by rescaling the distances between the adhesion sites, taking the measured motility into account.

# Chapter 4

## Cell Motility on PEG Block Copolymers Correlates to Fibronectin Surface Adsorption*

Protein repellence of PEG has been subject of many studies investigating the influence of chain length, grafting density and chain mobility.[81–84] There is a remarkable difference in protein resistance between differently designed PEG polymers both for grafted and self-assembled monolayers. For example, for PEG covalently and densely bound on silicon, both proteins and cells are found to be strongly repelled.[85] In contrast to that, we observed partial cell adhesion on the cell repellent PEG polymers in the last chapter. It is therefore important to probe whether FN adsorbs to PLL–PEG coatings and if so, where it is located. Experimental access to localize FN within the PEG is difficult. Thus, we employ neutron reflectometry[86] to analyze the structure of different PEG layers and to determine the amount and distribution of FN in these PEG layers. We correlate the structural information with cell adhesion and motility using fluorescence time-lapse microscopy.

### Surface Passivation

The study focuses on two different PEG copolymers constructs: PEG grafted to a hydrophobic and to a hydrophilic polymer anchor. In Fig. 4.1, the chemical structure is displayed: The amphiphilic copolymer Pluronic (F-127) consists of a polypropylene oxide (PPO) backbone and two PEG chains of 4.4 kDa grafted to it. In water, the hydrophobic PPO chain readily physisorbs on hydrophobic surfaces. The copolymer PLL-PEG consists of a PLL chain and PEG chains with either 2 or 5 kDa length (referred as PLL-PEG(2) and PLL-PEG(5), respectively) grafted to that (in a ratio of one PEG chain per 3.5 lysine monomer units in average). The positively charged PLL can adsorb on negatively charged surfaces. All experiments were performed at physiological conditions and compared to a FN coated surfaces as reference.

*Part of this chapter and figures are adopted from Röttgermann et al., 2014b [80] with permission of John Wiley & Sons.

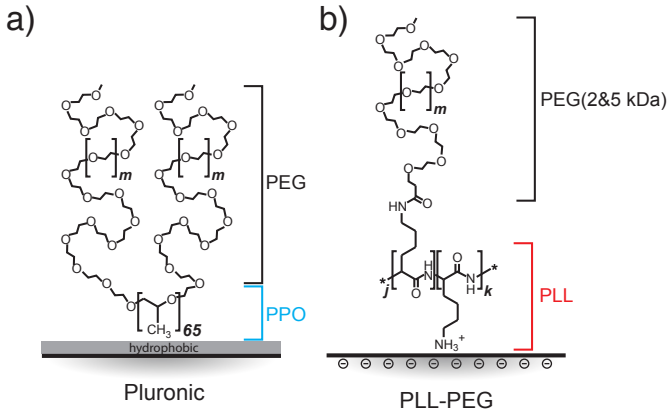


**Figure 4.1:** Schematics of the polymer architecture of Pluronic and PLL-PEG. a) Two PEG chains of 4.4 kDa (m = 99) are linked to a 65-mer of polypropylene oxide. b) On a PLL chain of 20 kDa, PEG chains of various lengths (2 and 5 kDa, m = 45 and 114) are linked in a grafting ratio of k/j = 3.5 (Lysine units per PEG chain).

## Cell Morphology and Motility

The cell behavior on the various passivated surfaces was characterized by measurements of cell morphology, in particular average cell area, and cell motility. The passivated areas were incubated for one hour with FN, rinsed and cells were seeded onto the surfaces. For determination of the cell morphology, cell contour areas of A549 cells were analyzed after 1 h and 24h by fluorescently marking the plasma membrane. Fig. 4.2a exemplarily shows the cell morphology on Pluronic and PLL-PEG(5). On Pluronic, all cells occupy a small area (mean = 250 $\mu$m$^2$ and standard deviation = 65$\mu$m$^2$) and are round shaped, indicating that cells are not attached. On PLL-PEG(2), cells adhere partially and their shape is more elongated with an area of 365$\pm$100$\mu$m$^2$. On PLL-PEG(5), cells are completely spread similar to pure FN surfaces (510$\pm$200$\mu$m$^2$ *vs.* 500$\pm$240$\mu$m$^2$) (Fig. 4.2a). The formation of lamellipodia as well as noticeable cell proliferation is observed on the latter two surfaces.

Besides the morphology, cell motility was determined by measuring cell trajectories of fluorescently labeled cell nuclei over a period of 24 h. Fig. 4.2b shows exemplary cell trajectories on PLL-PEG(2), PLL-PEG(5), and FN (on Pluronic no cell migration could be observed). From the trajectories, the MSD was calculated according to Eq. 3.3 and plotted in a log-log scale against time (Fig. 4.2b). Cell motion can be described by a persistent random walk.[87] Initially, on PLL-PEG(2 and 5) and FN cells show indications of ballistic motion (shown with green dotted lines). On the longer time scale, the MSD data approaches a diffusive behavior, shown with red dashed lines. A further parameter of cell migration can be determined by the cell speed, which is the contour length of the trajectory divided by the overall tracking time (see Fig. 4.2c). Whereas the velocity for the Pluronic surface is nearly zero with 1.2 $\mu$m h$^{-1}$ (detection limit of the setup), cell velocities are of 21.2$\pm$2.5 $\mu$m h$^{-1}$ for PLL-PEG(2), 29.1 $\pm$0.7 $\mu$m h$^{-1}$ for PLL-PEG(5), and 24.1 $\pm$2$\mu$m h$^{-1}$ for FN.

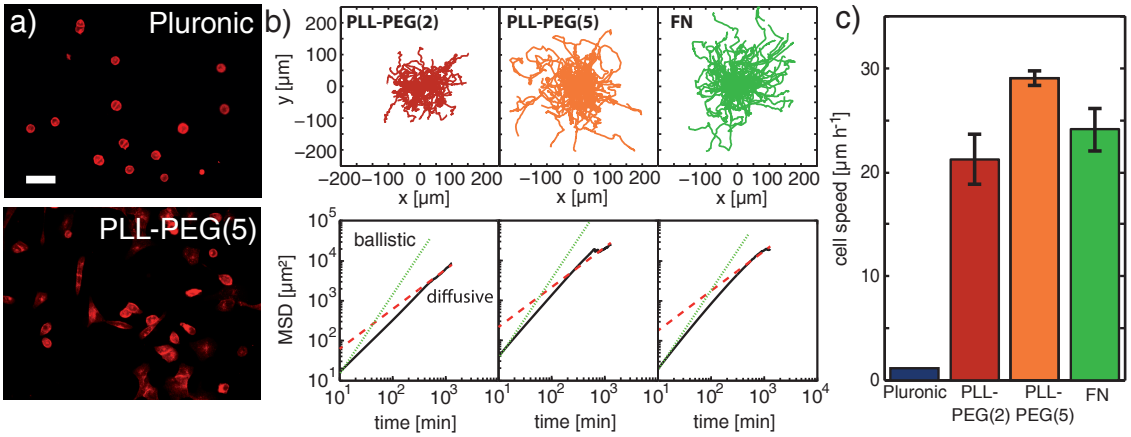


**Figure 4.2:** a) Fluorescence micrographs of plasma membrane stained A549 cells on Pluronic and PLL-PEG(5) after 24 h. Scale bar 100 $\mu$m. b) Upper row, representative cell trajectories over a period of 24 h: PLL-PEG(2) (red), PLL-PEG(5) (orange), and FN (green). Lower row, mean square displacements (black curves) are plotted against time for the various substrates. As a guide to the eye, the MSD dependence for directed motion (dotted green curve, slope 2) and diffusive motion (dashed red curve, slope 1) are indicated. c) Bar plot of single cell speed for the various substrates. Error bars represent the standard deviation of three experiments.

## Neutron Reflectivity on Polymer Layers

In order to investigate the location and amount of protein as well as the conformation of the block-copolymers for the different passivations, neutron reflectivity measurements were conducted.[86] Two measurements were performed on each system, first in $D_2O$ and second in a mix of $D_2O$ and $H_2O$ (with the scattering length density (SLD) matching to that of $SiO_2$). The contrast matching of those measurements allows for separate determination of hydration and composition of the films. The different passivated surfaces were measured before and after incubation with protein. Neutron reflectivity $R(q)$ is shown in dependence of the scattering vector $q = 4\pi/\lambda sin(\theta)$ in Fig. 4.3a (for better visualization the y-axis is multiplied by $q^4$); the typical oscillations are caused by the underlying oxide layer of the silicon block. The neutron data is fitted using different models. Starting from a one-layer model, the number of layers is increased, and thickness and roughness are adjusted until the model fits best the measured data. The Pluronic data could be fitted with one 28 Å thick layer with a hydration of 45% (see Fig. 4.3b), PPO and PEG could not be distinguished in the reflectivity data as they have similar SLDs. The addition of FN did not significantly change the layer thickness and composition. The PLL-PEG samples are described by a two layer model, one for the PLL and one for the PEG layer, whereas the longer PEG (5 kDa) is fitted by an exponentially decreasing profile towards the bulk in contrast to a linear profile for PLL-PEG(2). Both PLL-PEG systems exhibit with 90% and 84% water in the PEG a high hydration. As indicated by the green areas in Fig. 4.3b, the PLL layer increases in thickness after addition of FN (as the SLD of FN and PLL are indistinguishable, the increase is most likely due to accumulation of FN). From the change in thickness and the SLD, one can calculate the amount of FN which is 0.4 $\mathrm{mg\,m^{-2}}$ for PLL-PEG(2) and 0.7 $\mathrm{mg\,m^{-2}}$ for PLL-PEG(5).

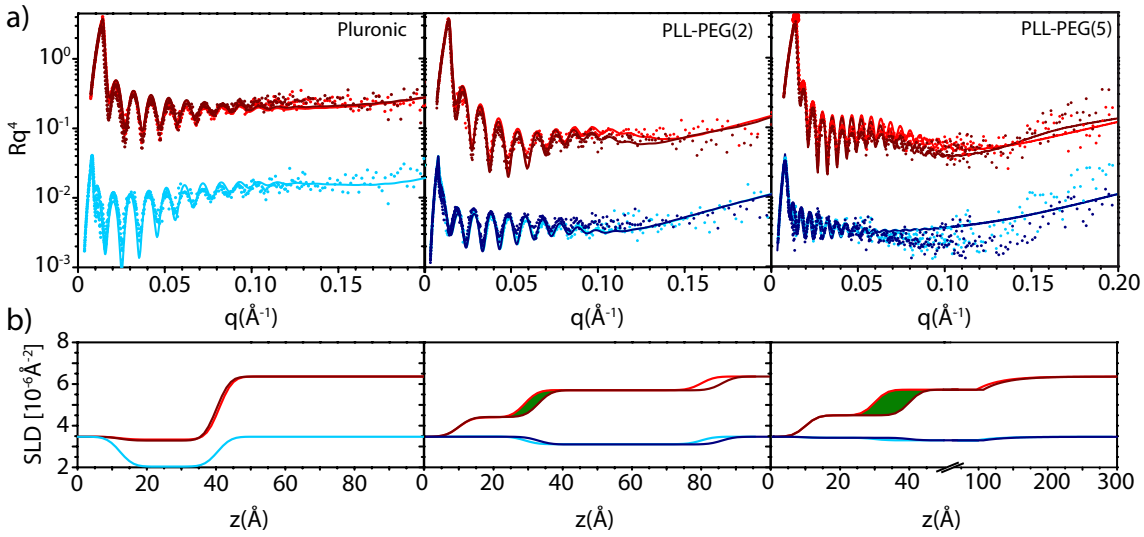


**Figure 4.3:** Reflectivity data and fits for Pluronic, PLL-PEG(2) , and PLL-PEG(5). a) Samples before the addition of FN are shown in light red for the $D_2O$ contrast and light blue for the $D_2O$ / $H_2O$ mix contrast. After the addition of FN, the data is shown in dark red for the $D_2O$ contrast and dark blue for the $D_2O$ / $H_2O$ mix contrast. The measurements in the $D_2O$ / $H_2O$ mix buffer are offset by a factor 0.1 for clarity. b) SLD profiles: The effect of FN is visible in the change in thickness indicated by the green area shown for PLL-PEG (2 and 5). The x-axis for PLL-PEG(5) is differently scaled for improved visualization. The much longer PEG chains are decaying exponentially towards the bulk.

| Surface | N | $\sigma_{exp}\,10^{-3}$ [Å$^{-2}$] | $L_{exp}$ [Å] | $L_{theo}$ [Å] | $R_F$ [Å] | $\sigma^{-1}{R_F}^{-2}$ | Conformation |
|---|---|---|---|---|---|---|---|
| PLL-g(3.5)-PEG(2) | 45 | 1.54 | 51 | 42 | 34 | 0.55 | Brush |
| PLL-g(3.5)-PEG(5) | 114 | 1.99 | 68+33 | 116 | 60 | 0.14 | Brush |
| PPO-g(32.5)-PEG(4.4) | 99 | 1.72 | >28 | 96 | 55 | 0.19 | Pancake |

**Table 4.1:** Comparison of AdG theory and neutron data with $N$ monomer units, measured surface density $\sigma_{exp}$, measured and calculated PEG layer thickness $L_{exp}$ and $L_{theo}$, Flory radius $R_F$, relation of $\sigma^{-1}{R_F}^{-2}$, and type of conformation.

## Interpretation of PEG-Protein Interface

A brief theoretical description of how and in which conformation grafted PEG layers adsorb is compared to our experimental findings. Depending on the adsorbed density of PEG chains, they can arrange in brush, mushroom or pancake conformation. For the dense brush conformation, the scaling theory of polymer adsorption is described by Alexander and de Gennes (AdG) [88, 89] with the following relation of polymer height $L$ and grafting density $\sigma$:

$$L = Na\left(a^2\sigma\right)^{1/3} \tag{4.1}$$

with the monomer size a=0.35nm for PEG [90] and the polymerization degree N. The AdG theory is valid if the product of the grafting density and the squared Flory radius $R_F = aN^{3/5}$ is smaller than 1.

In table 4.1 predicted and experimentally assessed values are compared. For PLL-PEG(2 and 5) the experimental length $L$ is in good agreement with a deviation of only about 15%. For the

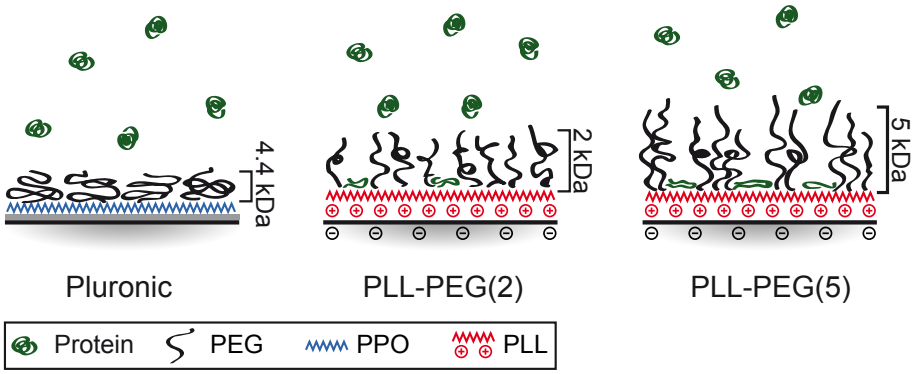


**Figure 4.4:** Interpretation based on the neutron SLD profiles of the adsorption of FN in the three different polymer coatings Pluronic, PLL-PEG(2) and PLL-PEG(5). In the first case, FN is not adsorbed on the pancake-like Pluronic layer, while on the PLL-PEG samples, small amounts of FN penetrate the extended brushed PEG layers to attach to underlying PLL. The higher PEG density leads to stiffer chains and therefore to higher protein adsorption.

Pluronic film, the AdG model is not valid as in that case the polymer extension is ruled by the hydrophobic interaction with the surface. Thus, PEG adopts a much thinner pancake structure and shields the hydrophobic surface from the water.[83, 91] This is also underlined by the low hydration of 45%. This and the high PEG density in the film do not allow for FN intercalation within the sensitivity of the experiment (see Fig. 4.4). On the contrary, FN adsorption was found in both PLL-PEG films, specifically in the vicinity of the PLL layer. The adsorbed PLL on silicon leaves a net positive charge, whereas FN under physiological conditions is negatively charged and hence primarily binds to the PLL.

Longer PEG chains lead normally to higher PEG densities and higher protein repellence. The higher protein adsorption for the PLL-PEG(5) system is in contrast to that finding. This anomaly could be explained due to the very high PEG density (0.14) caused by the high grafting ratio. Therefore, a uniform layer cannot form, and the PEG chains are rather stretched out as illustrated in Fig. 4.4. A disordered configuration may offer less protection compared to well ordered chains allowing more FN to diffuse through to the PLL.[92]

## Interpretation Cell Behavior on Polymer Layers

Having shed light on protein PEG interaction, the cell behavior on these surfaces is discussed. Due to the absence of protein for Pluronic, no cell adhesion can be mediated, as cells need ECM matrix proteins to bind via integrins, such as FN or present in FCS. In contrast, small amounts of protein are present in the PLL-PEG films. Massia and Hubbell [93] showed that an amount of $1\,\mathrm{fmol\,cm^{-1}}$ is already sufficient for complete cell spreading (corresponding to a ligand spacing of 440 nm). Our data for the FN reveals amounts of 72 $\mathrm{fmol\,cm^{-1}}$ for PLL-PEG(2), 127 $\mathrm{fmol\,cm^{-1}}$ for PLL-PEG(5) which is above the predicted minimal ligand density. As the protein is shielded underneath a PEG moiety, the binding sites of FN should be harder accessible.

Apart from the different spreading, cell migration also correlates with the different surface properties. The longest persistence time is observed on pure FN, whereas the highest velocity is observed

on PLL-PEG(5). A cell which polarizes in one direction (randomly in absence of a chemoattractant) has a higher probability to move forward in the same direction instead of turning towards any other direction.[94–96] As protein is isotropically distributed on the FN surface, the highest persistence is measured on this surface, whereas on PLL-PEG(2 and 5) fewer adhesion points lead to more frequent interruption but also to faster movement due to faster detachment.[97]

In summary, we performed neutron reflectivity on different PEG copolymers and studied the composition as well as protein intercalation. PEG grafted to a hydrophobic anchor (Pluronic) shows no protein adsorption due to the shielding effect of PEG from the hydrophobic moiety, and hence also no cell interaction. For PLL-PEG layers brush-like structure of the PEG layer is found which allows still some adsorption underneath the PEG close to the proximity of PLL. Cells exhibit the fastest speed on PLL-PEG(5) compared to that on pure FN. These findings suggest that the combination of partial adsorption of cell adhesive proteins and cell repellent properties of PEG are suited to elevate cell motility.

# Chapter 5

## Stochastic Transitions and Relative Affinity of Single Cells on Two-Adhesion Site Micropatterns*

The mechanism behind cell motion on PEGylated surfaces as well as strategies how to achieve good single cell occupation with optimal lattice geometry have been shown. Confining cells onto adhesion sites is an important step towards a precise quantification of fluorescent cell signals. However, cells are still motile on these sites, which can lead to small fluctuations in the fluorescence time tracks. These fluctuations can become problematic for quantitative analysis. In order to overcome these limitations, it is important to further minimize these cell fluctuations within the sites. Thus, it is necessary to determine the optimal adhesion area for single cells as well as to provide sufficiently large adhesion areas.[98] Different surface protein coatings can have a strong influence on cell adhesion as well.[99, 100] Further, new strategies could be followed, e.g. designing adhesion sites with nano-sized clustered arrays.[101, 102] In order to detect small differences and to quantify the best conditions of protein types and adhesion size, a platform of interconnected adhesion site is favorable. As a first step, we designed a two-adhesion site system to accurately measure relative surface affinities between two differently designed sites. In the following chapter, the guiding of the bridge is discussed including some preliminary results about the driving force to transit between the two sites. First examples of different double-sites with respect to area, protein coating, and nano-ligand-clusters within micropatterns are shown.

### Phenomenon of Cell Hopping

The micropatterns are designed in a dumbbell shape, with a narrow 5 $\mu$m bridge of length $d_l$ terminating into square sites of $A$=35x35 $\mu\mathrm{m}^2$ (see Fig. 5.1a). The guiding bridge is varied from 7.5 to 47.5 $\mu$m in length. The patterns are fabricated by the $\mu$PIPP protocol, low cell concentrations are seeded to obtain singly occupied dumbbell sites. Fig. 5.1b illustrates a time series of a fluorescently labeled breast cancer cell (MDA-MB-231). After adhesion, the cell starts sensing their environment by lamellipodial protrusion. Once the lamellipodium has sensed the opposite site,

*Part of this chapter and figures are adopted from the manuscript A. Fink†, P.J.F. Röttgermann†, et al. "Occupancy and stochastic transitions of single cells on double-well micropatterns", to be submitted to PNAS.

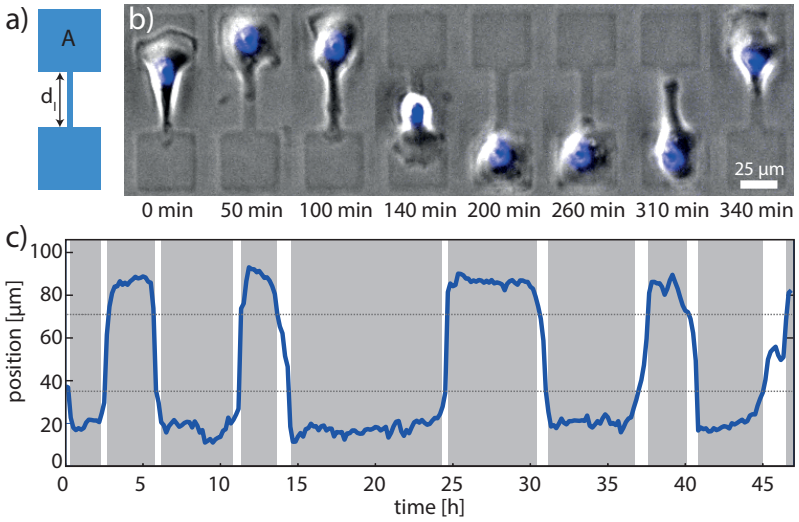


**Figure 5.1:** a) Schematic of dumbbell pattern with area $A$ and bridge distance $d_l$ b) Exemplary time series of a single cell transitioning from top to bottom, and back. c) Exemplary cell track (positions along the major axis) of the nucleus plotted against time. The nuclear center-of-mass tracks clearly show the observed transitions between resting states on the sites (gray stripes) and fast transitions from one adhesion site to the other (white stripes).

the whole cell transmigrates and spreads again. The distinct transitions between two sites will be referred to as "hops". The periodic motion involving spreading, sensing and hopping is sustained upon cell division and shown by an exemplary trajectory in Fig. 5.1c.

## Dependence of Cell Migration on Geometry

First, the effect of a variable bridge length is studied by alternating the bridge length from 7 to 47.5 $\mu$m. For each geometry, the cumulative distribution function of stay times - the time the center of a cell stays within the boundaries of a site - is evaluated (survival probability) , shown exemplarily for 16 $\mu$m in Fig. 5.2a. The exponential function ($f(t) = \lambda \cdot exp(-\lambda t)$ with time $t$ and the inverse mean stay time $\lambda$ are fitted to the distributions. For statistical reasons, the survival function is used ($S(t) = 1 - F(t)$ with the cumulative density function $F(t)$) and also plotted on a semi-log scale (shown in the inset of Fig. 5.2a). The hopping rates $\lambda_{hopp}$ can be plotted in relation to the bridge length (Fig. 5.2b). It can be seen that with increasing bridge length $L$ the rate decreases exponentially. In analogy to Arrhenius law [103] of particle diffusion in a double-well potential we use the following expression:

$$\lambda_{hopp}(L) = \nu \cdot exp(-\kappa L) \tag{5.1}$$

with attempt frequency $\nu$ , "bridging-length" factor $\kappa$ , and bridge length $L$, which is analogous to a thermal energy barrier in the particle diffusion system. The attempt frequency $\nu$ might depend on cell-typical properties such as adhesion strength and motility.

A first example for the measurement of affinities is a setup with variable adhesion areas. Therefore,

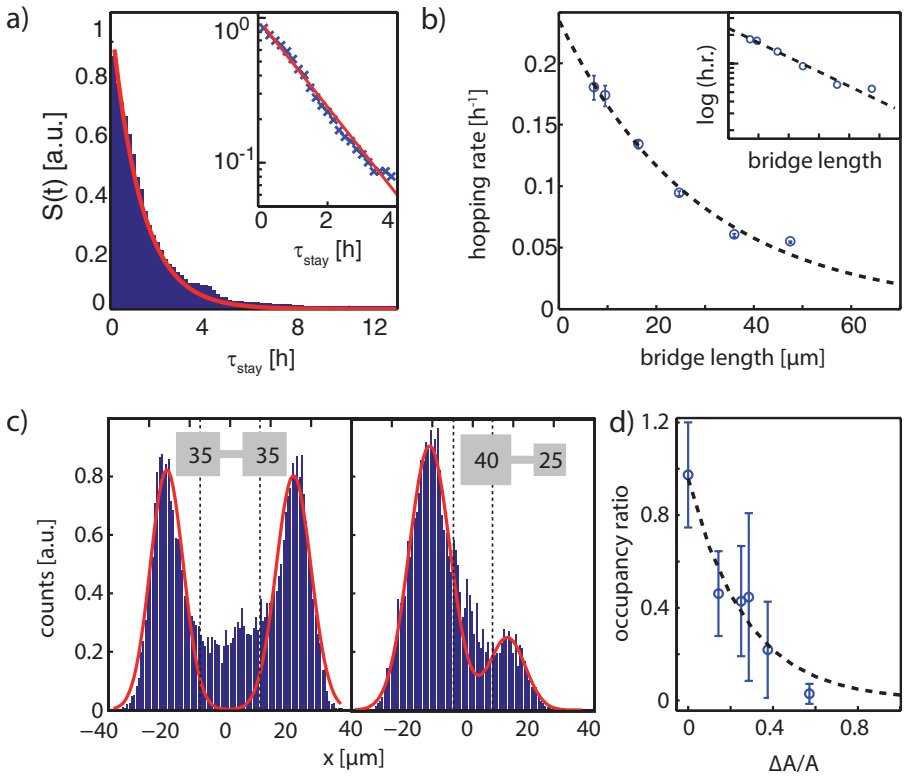


**Figure 5.2:** Geometry dependence of stay times a) Survival function of stay times $S(t)$ for a geometry of 16 $\mu$m bridge length. An exponential decay is fitted to the distributions. Inset: Data is shown on a semi-logarithmic scale. b) Extracted time constants from the exponential fits are plotted against bridge lengths. An exponential decay analogous to Arrhenius law approximates the data. c) Asymmetry in adhesion site areas leads to asymmetry in island occupation probabilities. Occupancies are plotted against the horizontal position on the dumbbell for a symmetric (35-35 $\mu$m$^2$) and an asymmetric (40-25 $\mu$m$^2$) micropattern. A sum of two Gaussians is fitted to the distributions. d) Time ratios of the individual occupancies on each side of the asymmetric patterns are plotted against the difference in island area scaled by the area of the larger square. Error bars display the variance of all cell systems. The curve scaling with $x^{-2}$ is a guide for the eye.

we prepared differently sized square sites of the dumbbell, which will be referred to as asymmetric dumbbells. In Fig. 5.2c the occupancy for the symmetric dumbbell ($A = 35^2$ $\mu$m$^2$) is compared to the occupancy time of the asymmetric dumbbell ($A = 40^2$ and $25^2$ $\mu$m$^2$, respectively). Instead of the hopping rate, the occupation times are compared. Occupation time is defined as the time the center of a cell is located in an adhesion site. In the shown case, the occupancy distribution shifts from a symmetric 50/50 to an 80/20 ratio. In Fig. 5.2d the occupancy probabilities, which are evaluated from two-Gaussian fits, are plotted against different area ratios, in particular the ratio of area difference $\Delta A$ to area $A$ of the larger square. The occupancy ratio decreases with increasing asymmetry of adhesion areas. As a guide for the eye, a curve proportional to $1/x^2$ is plotted. An explanation of the occupancies might be described by the energy functional in the cellular Potts model.[33] The Hamiltonian takes the surface tension $\sigma$ of a cell, which scales with the area $A$, as well as the line tension $\lambda$ of a cell, which scales with the cell perimeter $U$, into account ($\mathcal{H} = \sigma A + \lambda U$). Experiments with inhibitors could further study if also force-generation plays a role. For example, latrunculin or cytochalasin block actin polymerization in the front of a cell, and

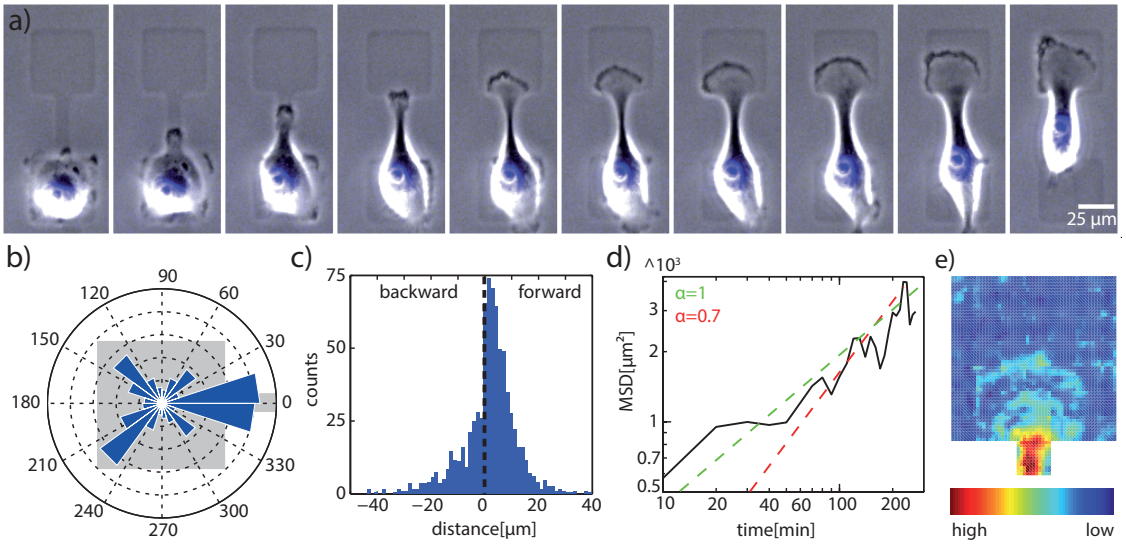


**Figure 5.3:** Filopodia growth on dumbbells a): Time series showing the extension of a lamellipodium along the connecting bridge, the growth of its tip to a fan-like shape and the onset of a transition over a period of 100 min (time interval between images 10 min). b) *De novo* formation of lamellipodia displayed in an angle histogram plot. Most lamellipodia are formed along the bridge. Increased lamellipodial activity is also observed for the corners of the adhesive squares. c) Frequency distribution of filopodia growth. The forward growth of lamellipodia differs from the backward retraction, which has a bigger step size. d) MSD of lamellipodia growth is plotted against time on a log-log scale (statistics over five double-site systems). The growth reveals no diffusive (slope $\alpha$=1) but a sub-diffusive regime ($\alpha = 0.7$), indicating that the time resolution is too coarse and the motion of the filopodia consists of more than one state. e) Close up of the growth process of the lamellipodial tip on an adhesion site. Heat plot: Overlay of brightfield images showing continuous growth and wave-like spreading of the tip.

hence a decrease in cell motility should be measured.[104] In contrast, blebbistatin inhibits myosin II in a cell front and hence would lead to lower traction force generation of the lamellipodium.[105, 106] Further evaluation could be done with traction force microscopy, where the displacement of particles in the substrate is a direct measure of the pulling and pushing forces.[107]

## Relation between Cell Transition and Lamellipodium Protrusion

A closer look on the formation of the lamellipodium can give additional information on the hopping phenomenon. In Fig. 5.3a, a detailed view on the formation of the lamellipodium is given. The hopping cycle starts with sensing. Dark spots in phase-contrast images are a sign of flat cell structure and could therefore indicate cell protrusions. In the first phase of sensing, the cell randomly repolarizes, also referred to as *de novo* formation of lamellipodia.[108] If a protrusion is orientated along the direction of the bridge, the second phase of sensing is initiated, by forming a lamellipodium and extending it randomly forwards and backwards. If the opposite site is sensed, a fan-like front is formed. In terms of the force argument, it means that if enough force is generated, the cell is most likely to detach from the initial site and move the center of mass to the opposite site. The center of mass movement usually starts when the opposite site is covered partially by the lamellipodium front. Fig. 5.3b shows the orientation of the *de novo* formation of manually tracked protrusions (center of the dark spots at the cell edges were tracked for each time point)

in an angular histogram. The lamellipodium mainly grows along the free space of the bridge but an increased number of protrusions towards the corners is also observed. The orientation of the actin-rich protrusions in the corners of a square is in accordance with literature.[109] In order to increase the hopping the squares could be rotated through $\pi/4$ so that the corners are connected by the bridge.

For the second step, the step length (measured in 10-min intervals) of the lamellipodial growth along the bridge is evaluated (see Fig. 5.3c). The plot shows two different step-size distributions for the forward and backward movement. Whereas the formation in forward direction mostly happens in many smaller steps, the retraction of the lamellipodium occurs in fewer but bigger steps. In order to determine the growth behavior of the lamellipodium (e.g. persistent random walk) along the bridge, the MSD is analyzed (see Fig. 5.3d). Although the number of tracked cells is low, the graph gives some first understanding. The lamellipodium growth does clearly not behave diffusive (red dashed lines). On this time scale, the step-wise protrusion exhibits sub-diffusive behavior (green dashed line). The sub-diffusive behavior can be explained firstly, by the step size not being equally distributed, and secondly, by the time resolution of 10 min being clearly insufficient. The lamellipodium formation happens at much smaller time-scales. Hence, the MSD may include two different growth states with run and rest states leading spuriously to a sub-diffusive regime.

The last step of lamellipodium growth is the spreading of the lamellipodium (contour of the front) on the opposite site which reveals an interesting phenomenon. Fig. 5.3e shows a heat plot of the tip of the cell, which is composed of an overlay of several brightfield images. In the heat plot, as well as in the time series (Fig. 5.3a and e), a circular shape is observed. Further analysis could evaluate if the front turns out to be always circular and if this can be disturbed in case of obstacles such as small gold dots are added. In order to gain a deeper understanding, it is necessary to fluoroescently mark the actin front of the cell. It is as well of interest to prove if the force argument holds. This could be realized by using inhibitors or using traction force microscopy as mentioned above.

### Affinities for Different Proteins and Nano-Patterned Sites

Further realizations of measuring surface affinities of different cell properties are outlined in Fig. 5.4a and b. In order to measure the adhesion affinity of a cell to a protein, different kinds of proteins can be printed using the combination of $\mu$PIPP and $\mu$CP, presented in chapter 2. Thereby, it is important to design the dumbbells in such a way that the frame is thin enough that on the one hand, microstructuring with stamping still works and on the other hand, it does not provide significant adhesion space for the cell. Possible protein variations would include ECM proteins such as fibronectin, laminin, vitronectin, and other proteins/peptides such as PLL or RGD. Different proteins could also be used to distinguish different modes of cancer migration using different types of cadherins (E-, N-, and P-cadherins).[110] The dumbbell patterns can also be used for measuring the influence of various ligand densities. For this application a different patterning method is necessary in order to generate pattern in the sub-micrometer range which is not possible with $\mu$PIPP. Gold lithography with a Pluronic backfill can generate such nanosized patterns as displayed in Fig. 5.4b. For these kind of patterns either the amount of gold (equal to possible adhesion area),

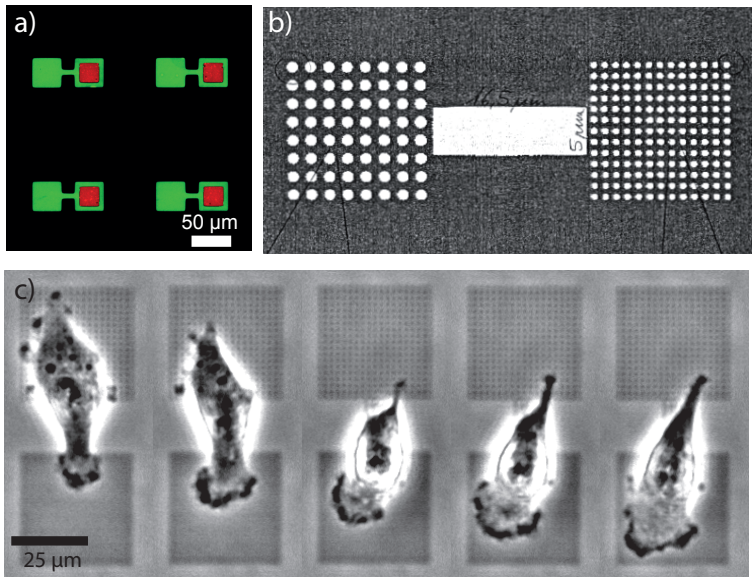


**Figure 5.4:** Surface affinities depending on ligand spacing and protein. a) A combined method of $\mu$PIPP with $\mu$CP provides double protein patterns, shown here for two differently labeled proteins. b) TEM image of gold microstructures, fabricated by photolithography. The amount of gold is kept constant whereas lattice spacing and gold dot size is varied ($d_l = 1.99\mu$m and ø=1.1 $\mu$m (left square) and $d_l = 1.18\mu$m and ø=0.64$\mu$m (right square)). c) Time series of a MDA-MB-231 cell. Cell front adapts the shape of the gold dots.

the ligand spacing, or the size of gold dots can be varied. As a proof of principle, a time series of a dumbbell nanopattern is shown in Fig. 5.4c with lattice spacing $d_l$=1.99 $\mu$m and a dot diameter $\oslash_{Au}$=1.1 $\mu$m (upper square) and with $d_l$=1.18 $\mu$m and $\oslash_{Au}$=0.64 $\mu$m (lower square), whereas the amount of gold is kept constant for both squares. The cell prefers the lower geometry with a smaller dot distance and a higher amount of dots. In addition, it can be observed that, due to the nanopattern, the lamellipodium is quantized which probably influences the migration behavior.

In this chapter, a two-adhesion site micropattern connected by a bridge was presented where cells hop between sites. Increasing bridge length showed an exponential decay of hopping. This was put into relation to lamellipodium formation. As a first proof of concept, adhesion area between the two sites were varied in order to show that small differences in migration behavior can be measured. This setup could also be used to distinguish between different cell types, as e.g. using different cadherins which causes different adhesion and hence different motility on mesenchymal and epithelial cells. The dumbbell-shaped micropatterns are therefore a versatile tool with potential applications in cancer diagnostics.

# Chapter 6

## Time-Resolved Study of Nanoparticle-Induced Toxicity *

The single cell time-lapse setup has been used for time-resolved cell migration studies as described in the last chapter. This setup is in particular relevant for quantitative studies of intracellular single cell responses. Quantitative mRNA transfection studies have been proven successfully on those patterns.[111] The heterogeneous cell death response is a further important application. So far, the majority of studies uses population-based toxicity assays, such as colorimetric assays for cell viability, [112, 113] and DNA fragmentation assays,[114] or techniques with single cell sensitivity such as flow cytometry, [115, 116] image cytometry, [117] or fluorescence microscopy [118] but data is taken at limited number of specific time points. In the following, we performed toxicity studies of $\mathrm{PS-NH_2}$ NPs as a proof of concept on hepato carcinoma cells (HuH7) (a relevant organ due to accumulation of NPs from the blood stream). The diverse onset timing of cell death, a perspective on dose dependence in relation to time, and a correlation analysis are described.

### Parallel Assessment of Cell Death Time Courses

For the toxicity experiment, HuH7 cells were exposed at different doses of $\mathrm{PS-NH_2}$, varying from 0.1 to 100 $\mu\mathrm{g/ml}$. In order to monitor the time point of cell death, two fluorescent markers were used: In an apoptotic cell, the phospholipid phosphatidylserine (PhS) is flipped to the outer leaflet of the cell membrane. The marker *polarity Sensitive Indicator for Viability and Apoptosis* (pSIVA, an annexin derivative) with an fluorescent tag N-((2-(iodoacetoxy)ethyl)-N-Methyl)amino-7-Nitrobenz-2-Oxa-1,3-Diazole (IANBD) binds specifically to PhS and fluoresces green upon binding. The second marker is the plasma membrane impermeant propidium iodide (PI) which stains the nucleus red if the plasma membrane looses the integrity. The loss of membrane integrity is also called secondary necrosis and happens *in-vitro* as no phagocytes can remove and recycle the apoptotic bodies. The two markers can be used to distinguish between apoptosis and necrosis. As long as a time difference between both onset times is observable, the cell death is induced by apoptosis. An exemplary time series is given in Fig. 6.1a, showing a brightfield image at the beginning and the corresponding fluorescence images of both markers at 0, 7, 14, 21 and 28

*Part of this chapter and figures are adopted from Röttgermann et al., 2016 [18] with permission of MDPI

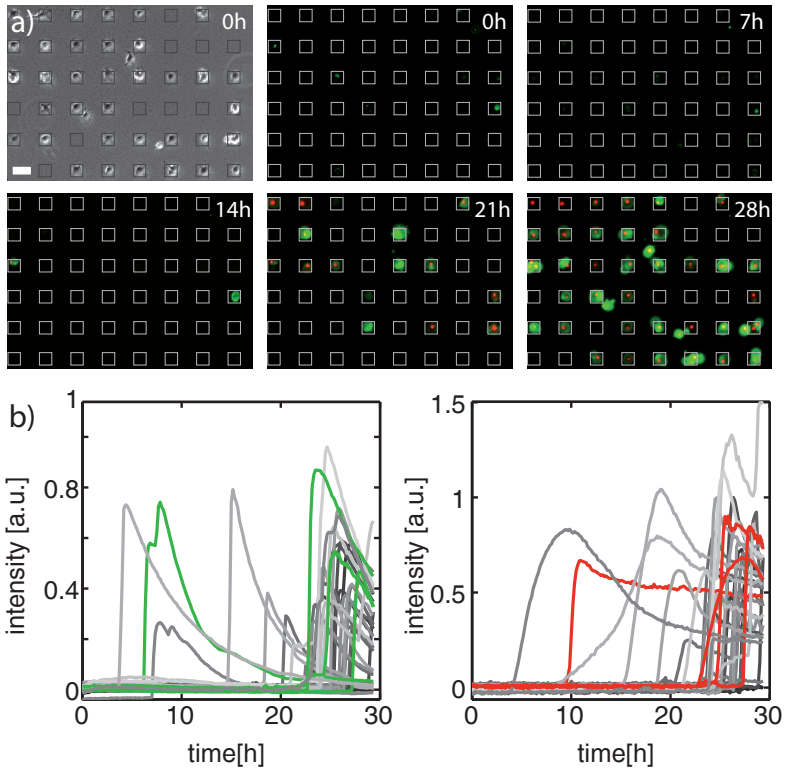


**Figure 6.1:** a) Time series of apoptosis induced with $PS-NH_2$-NPs monitored by bright-field and fluorescence microscopy at 0, 7, 14, 21 and 28 h after seeding. Green staining (pSIVA-IANBD) indicates exposure of phosphatidylserine on the outer leaf of the plasma membrane bilayer, the red nuclear staining (PI) indicates subsequent loss of plasma membrane integrity. The heterogeneity in the times of onset of apoptosis can be clearly seen. Square lattices are drawn for better visualization. Scale bar: 50 $\mu$m. b) Representative time traces of fluorescent signals monitored in the pSIVA (left) and PI (right) channels. A few typical traces are highlighted in green and red, respectively.

h. During the the first 14 h, few cells show green fluorescence, and fluorescence emission begins in earnest only after 20 h. The integrated fluorescence intensity over the adhesion sites is extracted for each single cell from the image stacks and shown in Fig. 6.1b. A heterogeneous response of the single cells is clearly visible. Change in membrane (pSIVA) as well as loss of the membrane integrity (PI) is indicated by the sharp increases of the signal. The dropping in the pSIVA signal after onset is due to photo bleaching, the dropping of the PI signal shortly after the onset is due to unspecific staining and degradation of RNA.[119] For the automated analysis, the onset times were determined as the times, at which the signal first exceeds a level equivalent to 25% of the maximum background intensity.

## Time-Dependent Dose Response Function

In order to assess the dynamic response of a cell population, the distribution of cell death onset times is analyzed. In Fig. 6.2a, normalized frequency distributions of onset times of the PI signal are plotted against time for increasing doses (0.1 to 100 $\mu g/ml$). The distributions $dc(t)$ are fitted by log-normal distributions:

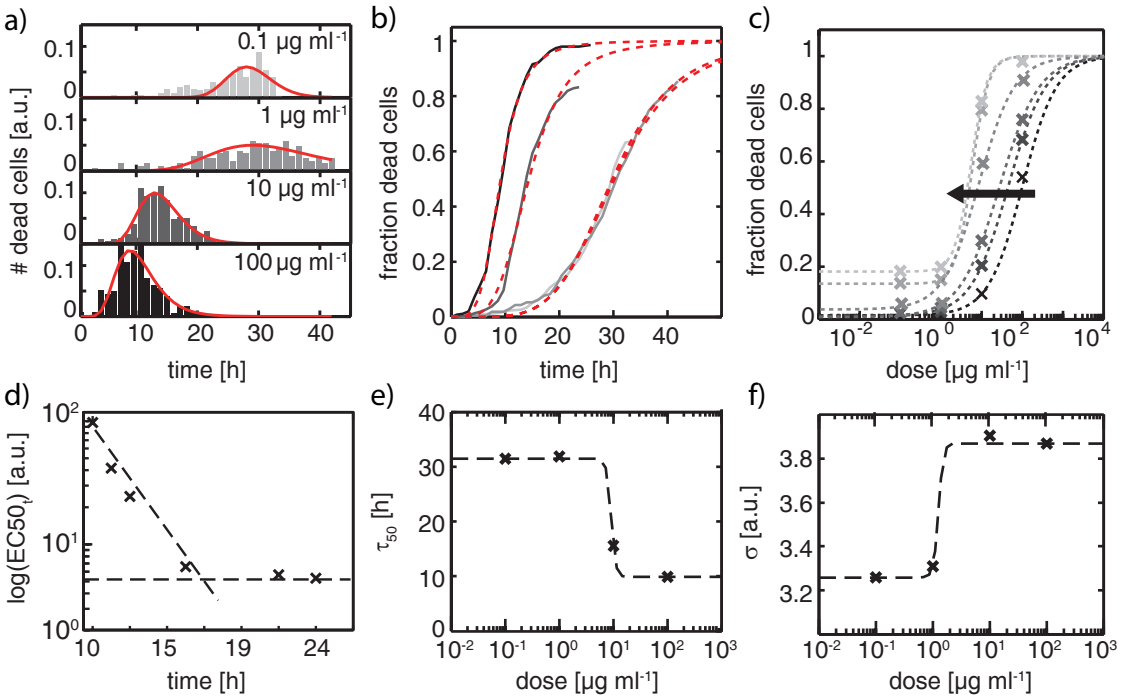


**Figure 6.2:** a) Normalized frequency distributions of cell death (onset times of the PI signal) are plotted against time for the indicated NP doses. The distributions shift to earlier time points and get narrower with increasing NP dose. They are fitted to log-normal functions (red curve). b) The cumulative fraction of dead cells is plotted against time for NP doses of 0.1 $\mu$g/ml (light gray), 1 $\mu$g/ml (medium gray), 10 $\mu$g/ml (dark gray), and 100 $\mu$g/ml (black). At the lowest dose, 20% of the cells die within 24 h, whereas at the highest dose all cells (100%) are dead by this point. The cumulative distributions are fitted to log-normal functions (red curve). c) Standard dose-response curves with fraction of dead cells which can be extracted from the distribution of b) for several different time points between 10 and 24 h (black to light gray). Data is fitted to dose-response functions (dashed lines). The $EC_{50}$ values shift towards lower dose with increasing late time endpoints (black arrow). d) The $EC_{50}$ values are plotted in logarithmic scale against the endpoints. At an end-point of 18 h, the $EC_{50}$ value approaches a constant value. e, f) Time points $\tau_{50}$ (e) and a rate-dependent $\sigma$ (f) for the cumulative distributions are plotted against dose. Both values exhibit dose-response behavior.

$$dc(t) = A \cdot exp\left(\frac{log(t) - \mu}{\sqrt{2\sigma}}\right)^2 \tag{6.1}$$

where $A$ denotes the amplitude, $t$ the time, $\sigma$ the standard deviation, and $\mu$ the mean. A log-normal distribution is applicable for a product of many independent processes. This is rational for multiplex cell pathway as will be shown later in the next chapter. The mean of the distribution shifts to earlier times (from 27.8$\pm$0.4 h at 0.1 $\mu$g/ml to 8.9$\pm$0.3 h at 100 $\mu$g/ml) and the distribution get narrower with higher dose. In order to assess the time-dynamic cell death of the whole population, the cumulative sum of cell death fraction is plotted against time in Fig. 6.2b. This "dynamic dose-response" is evaluated by plotting the time of 50% cell death $\tau_{50}$ (from Eq. 6.1) against dosage (Fig. 6.2e). The variance $\sigma$, i.e. the width of the log-normal distribution, increases with dose (Fig. 6.2f). For comparison, standard $EC_{50}$ are replotted for various "effective" endpoints (Fig. 6.2c), retrieved from the cell death distributions. The following dose response relation is

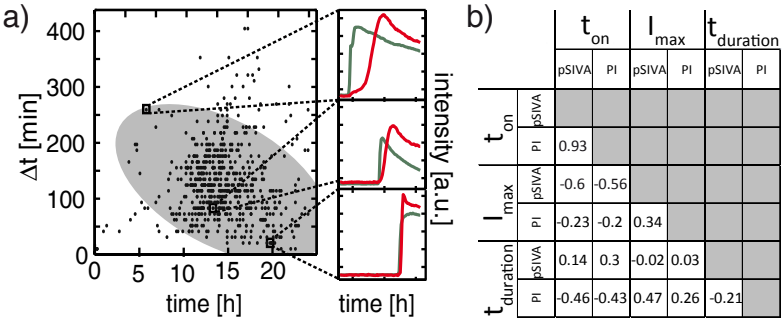


**Figure 6.3:** a) The interval separating early-stage apoptosis (only pSIVA) from secondary necrosis (pSIVA+PI) varies depending on the onset time of apoptosis. This time difference $\Delta$t is plotted against the onset time. The gray ellipse represents a $2\sigma$ interval of a PCA analysis. Three representative time traces of apoptotic cells are depicted for better visualization: Cells that die at later time-points transit faster into secondary necrosis. b) Different parameters of apoptotic cells are extracted from the time traces and displayed as a correlation matrix: onset times $\mathrm{t_{on}}$, maximum intensity $\mathrm{I_{max}}$ and duration of onset for pSIVA and PI. Maximal pSIVA intensity $\mathrm{I_{max}}$, and duration (spread) of onset time of PI $\mathrm{t_{duration}}$ are negatively correlated with the onset of apoptosis.

fitted to the data

$$F(dose) = y_0 + \frac{-y_0}{1 + (EC_{50}/dose)^2} \tag{6.2}$$

with rate $n$, the basal rate $y_0$, and the $EC_{50}$value where 50% of cells are dead.

The $\mathrm{EC_{50}}$ from the fits are plotted against the end-points in Fig. 6.2d. Here, a clear time dependence of the $\mathrm{EC_{50}}$ can be seen, which has been previously discussed. [120] A time-dependent $\mathrm{EC_{50}}$ becomes exceedingly problematic in the low-dose regime when toxicity occurs at time scale exceeding the window of experimental observation. [121, 122] In this case, a $\tau_{50}$ value would be more suitable. Using a too-early endpoint especially for weak toxic nanomaterials could be defective by under- or overestimating the toxic effect.

## Two Parameter Correlation of Cell Death

The time-dependent analysis cannot only be applied for a precise dose study but it can also elucidate dependencies and different cell behavior over time. The characteristic behavior of the early (pSIVA) and late (PI) marker can be correlated in time.

In Fig. 6.3a the delay time $\Delta$t between the onset of pSIVA and PI is plotted against the time of cell death of $t_{PI}$. Cells which die early (5-10 h) exhibit delay times of 100-300 min, while late events of cell death show no delay. The correlation is also quantified by the Pearsson's correlation coefficient $\rho(X, Y)$

$$\rho(X, Y) = \frac{Cov(X, Y)}{\sigma(X)\sigma(Y)} \tag{6.3}$$

with the covariance $Cov(X, Y)$ of two parameters X and Y and their related standard deviation. A value of 1 or -1 means fully correlated or anti-correlated, respectively, zero means not correlated. The time difference results in a correlation of 0.4 with a broad single cell distribution response. The correlation is underlined by a principal component analysis (PCA), which show

a tilted major axis, as indicated by the grey ellipse in the scatter plot (see Fig. 6.3a). The faster transition into secondary necrosis has different possible explanations: Firstly, omitted elimination of apoptotic bodies, due to missing phagocytes *in-vitro*, leads to transition of apoptotic to necrotic cell death.[123, 124] Secondly, cells that undergo apoptosis affect neighboring cells towards cell death.[125] Thirdly, accumulation of NPs in cell over time and concomitant decrease in fitness might contribute to the increase of necrosis.

Moreover, further parameters of the single cell tracks can be correlated such as the maximum intensity, onset and duration of the onset times. The dependencies are displayed in a correlation matrix in Fig. 6.3b for a dose of 10 $\mu\mathrm{g}/\mathrm{ml}$. Apart from some obvious parameters two correlation dependencies are picked: First, the maximal intensity $I_{max}$(pSIVA) negatively correlates with the onset of apoptosis (-0.6/-0.56). This could possibly indicate a connection to cell size, caspase activity or be related to fluorescence bleaching. Second, the maximal intensity $I_{max}$(PI) only weakly correlates with the maximal intensity $I_{max}$(pSIVA) (0.34). On the one hand, both the pSIVA and PI signal depends on cell size, on the other hand, there is a substantial cell-to cell variation in the size of the nucleus. The single cell fluorescence time correlations can be widened to multiple markers indicative for distinct cellular events, as shown in the next chapter.

In summary, single cell arrays enable the kinetic analysis of NP induced cell death. The time-resolved measurements reveal a heterogeneous onset distribution of NP induced apoptosis and a differentiated time-dependent picture of NP dose-response emerges. The kinetic investigation of cell death *in-vitro* can therefore complement toxicity risk assessment and could potentially scrutinize pathway and action of NPs using single-cell cross-correlation.

# Chapter 7

## Multiparameter and kinetic correlation analysis of apoptosis events on single cell arrays*

In the previous chapter, the dynamic evaluation of the single cell response of apoptosis as a useful tool for risk assessment has been shown. However, the setup can also be extended to study the timing of earlier cell death events using additional fluorescent markers. As shown in Fig. 1.4, the extent of apoptosis network bears high complexity, and the initial trigger of cell death cannot always be identified. Beyond that, crosstalk between apoptosis, necroptosis, and autophagy as well as feedback loops in the signaling can complicate the picture.[126, 127] Therefore, the analysis of only one single time point does not allow to evaluate the initiation or even the pathway of cell death. Thus, continuous single cell monitoring with the simultaneous use of several marker is advantageous. Previous studies of time-resolved markers have shown the potential of cell death correlations but still suffer from a very coarse time resolution.[38, 128, 129] There are common events/features in cell death which occur in many pathways: The mitochondrial outer membrane permeabilization (MOMP) is one key event in the intrinsic apoptosis pathway.[130] Also increased generation of reactive oxygen species (ROS) induces apoptosis. ROS generation occurs in the endoplasmatic reticulum upon stress, in the cytosol, or in the mitochondria.[131] Endosomes and lysosomes are further triggers of cell death, as for example the lysosomal break (LMP) can induce the release of cathepsin into the cytosol and trigger the initial pathway of apoptosis,[132] as shown in Fig. 7.1 and referred as the lysosomal pathway. Besides these early events, additional marker can give information on the further execution of the cell death pathway as well as for discrimination between different forms of cell death, as for example, initiation of apoptosis or transition into secondary necrosis. These markers stain the caspase 3/7 activation (CASP), the flipping of PhS to the outer plasma membrane (PhS-Flip) and the plasma membrane permeabilization (PMP). The latter two markers were already presented in the last chapter.

In the following study, the model NP $\mathrm{PS-NH_2}$ is used as a first proof of concept. Previous studies have shown that the cationic NPs cause a rupturing of the lysosomes and so induce the lysosomal

*Part of this chapter and figures are adopted from the manuscript P. J. F. Röttgermann†, A.-N. Murschhauser†, D. Garry†, M. F. Ober, D. Woschée, Y. Yan, K. A. Dawson, J. O. Rädler "Time-correlations of single cell dual fluorescence markers - a kinetic finger print in nanoparticle induced apoptosis" to be submitted to Nature Nanotechnology.

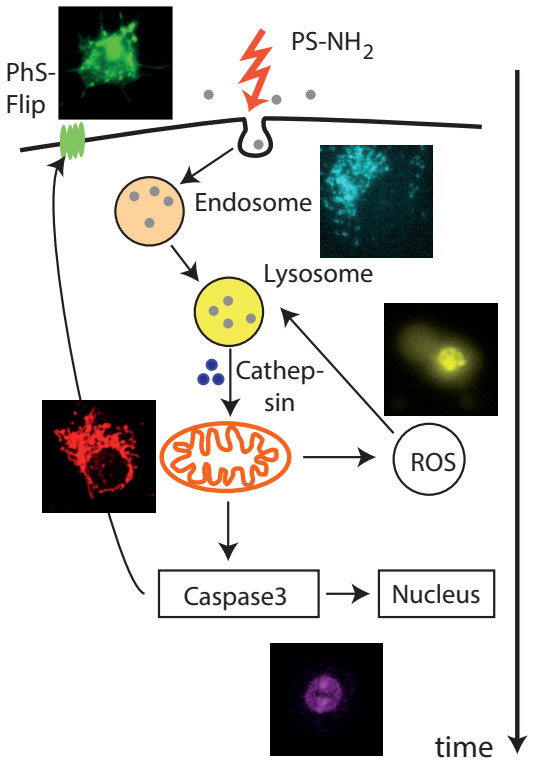


**Figure 7.1:** Schematic of lysosomal apoptotic pathway: The $\mathrm{PS-NH_2}$ NPs accumulate in the lysosome and cause the LMP. The released cathepsin initiates MOMP and leads to an increase of ROS. At point of no return, caspase-3 and -7 are activated, the PhS flips, and the plasma membrane gets compromised. The fluorescent images illustrate which cell compartments can be stained for time-lapse imaging.

pathway.[118, 129] These conclusions were drawn from $\mathrm{EC}_{50}$ values of specific cell markers. Here, we perform time-resolved single cell analysis with pairwise fluorescent marker combinations for different cell death events. The data is correlated in time by principal component analysis. An order of death events is then determined and compared to the positive control staurosporine. In addition, the NP dose-behavior on ROS generation is studied, and high content analysis is performed for the lysosomes.

## Marker Specific Phenomenological Time Courses

In order to follow the cell death events, the following markers were chosen: LysoTracker (orange, red) stains acidic organelles such as lysosomes, tetra-methyl rhodamine methyl ester (TMRM) fluoresces when the mitochondrium potential $\Delta\Psi_m$ is intact, CellRox (green, orange, red) fluoresces upon oxidation due to oxygen radicals, the CellEvent Caspase 3/7 marker stains the nucleus upon activation of caspase3/7, pSIVA-IANBD the PhS-flip at the plasma membrane, and the nucleus markers PI or Toto3-iodide upon loss of plasma membrane integrity. All these markers were used in low concentrations as well as were illuminated shortly to avoid (photo-)toxic effects.

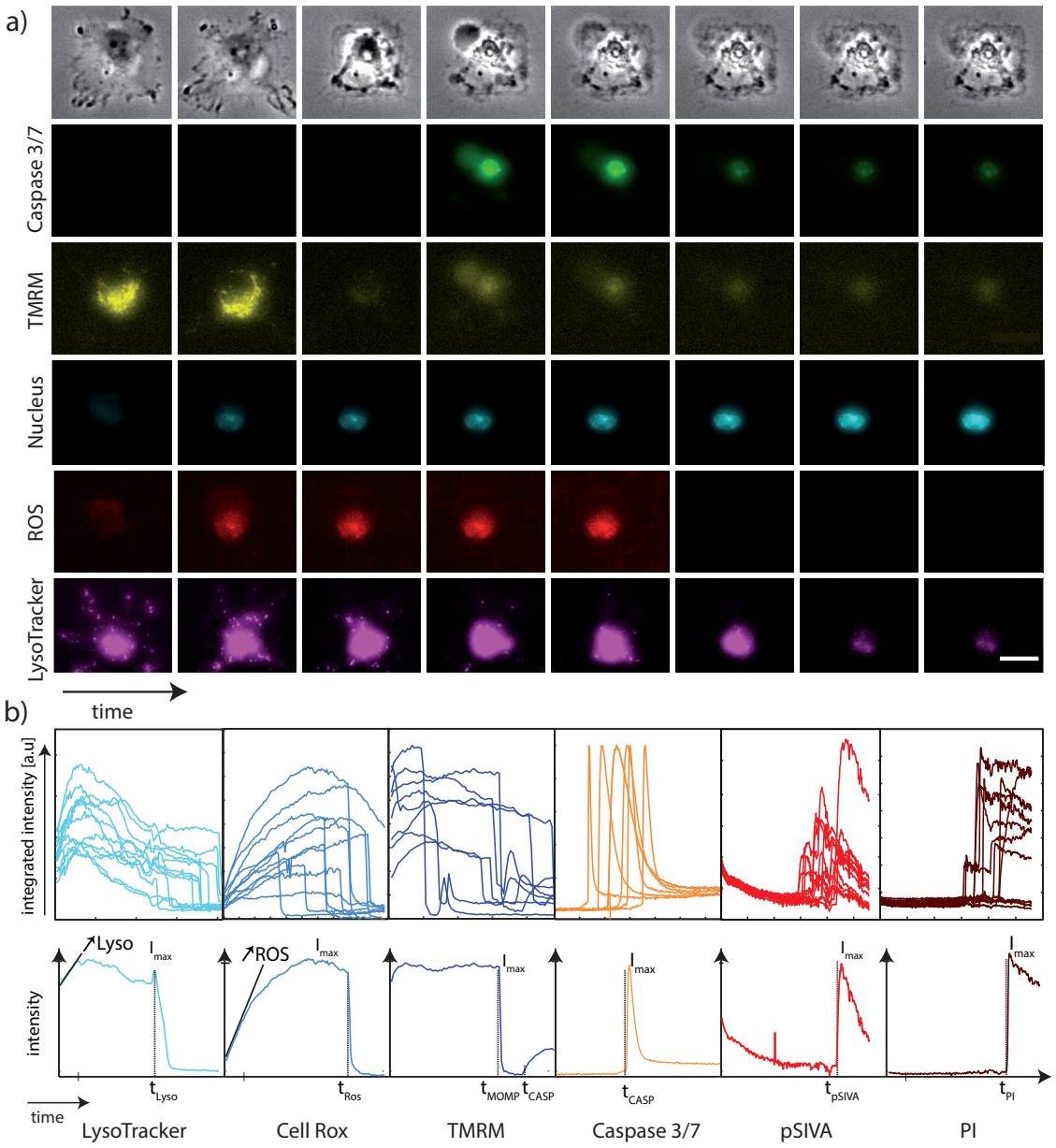


**Figure 7.2:** a) Time series of cell death at selected time points (0-24 h): Caspase3/7 (green) indicates caspase3/7 activation, TMRM marker (yellow) indicates the staining of mitochondrial potential, nucleus marker (cyan) stains plasma membrane permeabilization with subsequent staining of the nucleus, CellROX fluoresces red in presence of oxidative stress, and LysoTracker (purple) stains the lysosomes. Scale bar: 25 $\mu$m. b) Exemplary time traces of single cells: Lysosomes (LysoTracker), ROS-level (CellROX), MOMP (TMRM), Caspase3/7 activation (Cell Event Caspase3/7), PhS-Flip (pSIVA-IANBD), nucleus staining by PI or Toto3 (NUC). The early markers (first three graphs) and the late markers (last three graphs) show similar characteristic behavior. By fitting phenomenological functions to the single cell traces using a maximum likelihood fitting routine, characteristic parameters such as event times, slope of increase, and maximal intensity can be extracted.

Additionally, markers were chosen in such a way that there was no or low spectral overlap of the fluorophores. Fig. 7.2a shows exemplary time series of the different markers: Caspase3/7 (green), the nucleus (cyan), and pSIVA (not shown) show a clear onset of fluorescence, whereas the ini-

tial fluorescence of TMRM (yellow) and LysoTracker (magenta) fade out. For CellROX (red) the fluorescence intensity increases first and disappears then. 500 - 1000 single cell traces were extracted; a selection of characteristic time traces are displayed in Fig. 7.2b. While each individual time course is distinct and the overall onset times show a great variability, yet each fluorescent marker has defined characteristic features in the time courses. For example, each marker shows distinct discontinuities, which allow to determine defined event times. In the following, we describe the characteristic commons in the time lines and describe how to retrieve the event times by phenomenological functions using the maximum likelihood fitting routine.

The late apoptotic events are discussed first. The CellEvent Caspase 3/7 is a cell permeant marker with a DEVD peptide sequence (asparagine-glutamine-valine-asparagine) binding site. The peptide gets cleaved upon caspase-3 and -7 activity and hence fluoresces green by integration with nucleus DNA described by a sharp sigmoidal onset function. The exponential decay after the onset is caused by photo-bleaching.

The pSIVA-IANBD fluoresces only when bound to PhS, which is transposed to the outer leaflet of the plasma membrane at the execution phase of apoptosis. The fluorescence time courses are well described by the sigmoidal increase and decay as identically to the caspase signal.

The nuclear stain (PI/Toto3 iodide) binds specifically to DNA and unspecifically to RNA. The chromophore is non-fluorescent in the absence of nucleus acids as well as plasma membrane impermeable, and hence only fluoresces upon loss of plasma membrane integrity.

The late markers are fitted by

$$f(t) = A + B\sigma(t)(e^{\gamma(t_{step}-t)} + b) \tag{7.1}$$

with the global offset $A$, the scaling factor $B$ for the peak height, the sigmoid function $\sigma(t)$ at time $t_{step}$, and the exponential decay with a decay constant $\gamma$ and an offset $b$ between the initial level $A$ and the final level. The sigmoid function is defined by

$$\sigma(t) = \frac{1}{1 + e^{\alpha(t_{step}-t)}} \tag{7.2}$$

with the steepness $\alpha$ at time $t_{step}$.

The early markers show a more complex signal behavior. The lysosome marker consists on a pH dependent fluorophore which can enter vesicle-like particles such as lysosomes or endosomes. In the acidic environment of the lysosomes, the marker gets protonated which leads to fluorescence and hinders the marker to release the vesicle. The cell traces of LysoTracker show a small initial quadratic increase with a sigmoidal breakdown at $t_{Lyso}$. The increase may be associated with an increase of lysosomes (increase in acidification) and the breakdown most likely with the rupture of the lysosomes.

TMRM gets accumulated in active mitochondria with a membrane potential $\Delta\Psi_m$, more TMRM gets accumulated upon hyper-polarization whereas TMRM is released upon loss of the potential. Firstly, the fluorescence of TMRM weakly increases and subsequently decreases (sigmoidal) at

$t_{MOMP}$ which can be associated with MOMP. The fluorescence is followed by a plateau period and a small increase, likely associated with the increase of caspase induced fluorescence (due to the measurement with pairwise markers).

CellROX fluoresces upon oxidation in presence of oxygen radicals. The initial increase of the fluorescence time course can be directly correlated to the amount of generated ROS. The sigmoidal break down ($t_{ROS}$) is related to the oxidative burst which is the rapid release of superoxide radicals and hydrogen peroxides. This possibly is due to the transition into secondary necrosis as no phagocytes are available to take up the apoptotic bodies.[38] In the following, the oxidative burst will be defined as the characteristic time for the ROS generation.

The early markers are fitted by

$$f(t) = \sigma(t)(a_{const} + s\ a_{quad}(t - t_{vertex})^2) + (1 - \sigma(t))\ b \tag{7.3}$$

with the sigmoid function $\sigma(t)$, the constant $a_{const}$ and the quadratic coefficient $a_{quad}$, parabola vertex at time $t_{vertex}$, signum $s$ and the final saturation value $b$.

## Distribution of Apoptotic Event Times

The distribution of the characteristic times of the marker are extracted as follows: For the early markers, the breakdown events are determined by the times at which the curve deviate more than 3% from the initial parabola in relation to the amplitude. For the late markers, the onset event is determined by the intersection point between the basal fluorescence and the tangent of the fit parameter $t_{step}$. In Fig. 7.3, the frequency distributions of these event times are plotted for exposures of 25 $\mu\mathrm{g/ml\ PS-NH_2}$ NPs (Fig. 7.3a) and 2$\mu$M STS (Fig. 7.3b). The distributions show a broad heterogeneous response of the populations. In order to compare single cell distributions Gaussians were fitted. For the NP exposure, the mean times of the distributions are all within 2 hours around 24 h. For the STS exposure, more distinct differences in the timing can be recognized, but the statistic is not as high as for the NPs and could therefore be misleading. As the time differences are small compared to the width of the distributions, the mean times are an insufficient way for the determination of sequence of events.

## Two-Color Pair Correlation of Successive Events

While the characteristic times of each marker is broadly distributed, the time correlation of successive markers might be a better way for determination of sequences, as the time difference between two events can be assessed directly. In Fig. 7.4, the characteristic times are plotted for each pairwise marker combination where $t_n$ and $t_{n+1}$ are denoted as the times of two successive events. Early markers (upper row) and late markers (middle row) are plotted separately. The color encodes for the following different pairs of apoptotic markers: MOMP-ROS (light blue), LMP-MOMP (medium blue), LMP-ROS (dark blue), LMP/MOMP-PhS-Flip (yellow), PhS-Flip-Casp (red), and Casp-PMP (dark red) and LMP-PMP (dark brown). The ellipses display the correlations

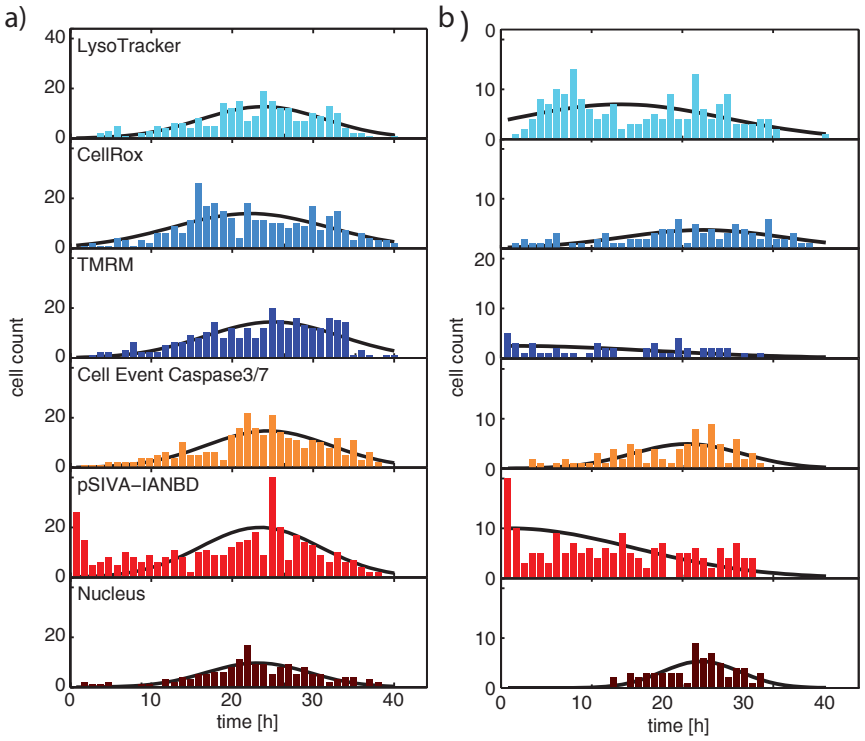


**Figure 7.3:** Frequency distributions of single cell event times for various markers: (LysoTracker (light blue), CellROX (medium blue), TMRM (dark blue) Caspase3/7 (orange), pSIVA-IANBD (red), and Nucleus (dark red) for an exposure of a) 25 $\mu g/ml$ $PS-NH_2$ and b) 2$\mu$M STS. In order to evaluate mean times, Gaussians were fitted to the distributions. The mean times of the distributions show no clear sequence. However, for STS the single cell responses are more broadly distributed.

obtained from a principal component analysis, whereas the axes of the ellipses correspond to the first two principal components for each combination with a one sigma interval (67% of data). The data shows the statistics of about 500 cells (note statistic is lower for some marker combinations). If the ellipse is above the dotted diagonal, marker $n+1$ follows marker $n$.

The pairwise correlation of LysoTracker and MOMP for the NP exposure shows a clear time delay and hence the sequence LMP before MOMP. This sequence would be expected for the lysosomal pathway. In contrast, the time difference between MOMP and ROS is very small. This means that the oxidative burst is directly correlated with the permeabilization of the mitochondria. For consistency, the combination of LMP and ROS breakdown is also measured. The result is similar to that of LMP and MOMP although broader distributed which can be explained by the low statistic and therefore high uncertainty.

The time correlation of STS is different in comparison to the one of the $PS-NH_2$-NP exposure. Two populations can be identified for the combination LMP-MOMP, on the one hand a population which dies early and where MOMP follows after LMP, and on the other hand a population where cells die at later time points and where *vice-versa* LMP follows shortly after MOMP. Furthermore, a distinct time difference between MOMP and ROS can be identified which indicates another ROS breakdown behavior than for the NPs. The time differences of MOMP-ROS are also more broadly

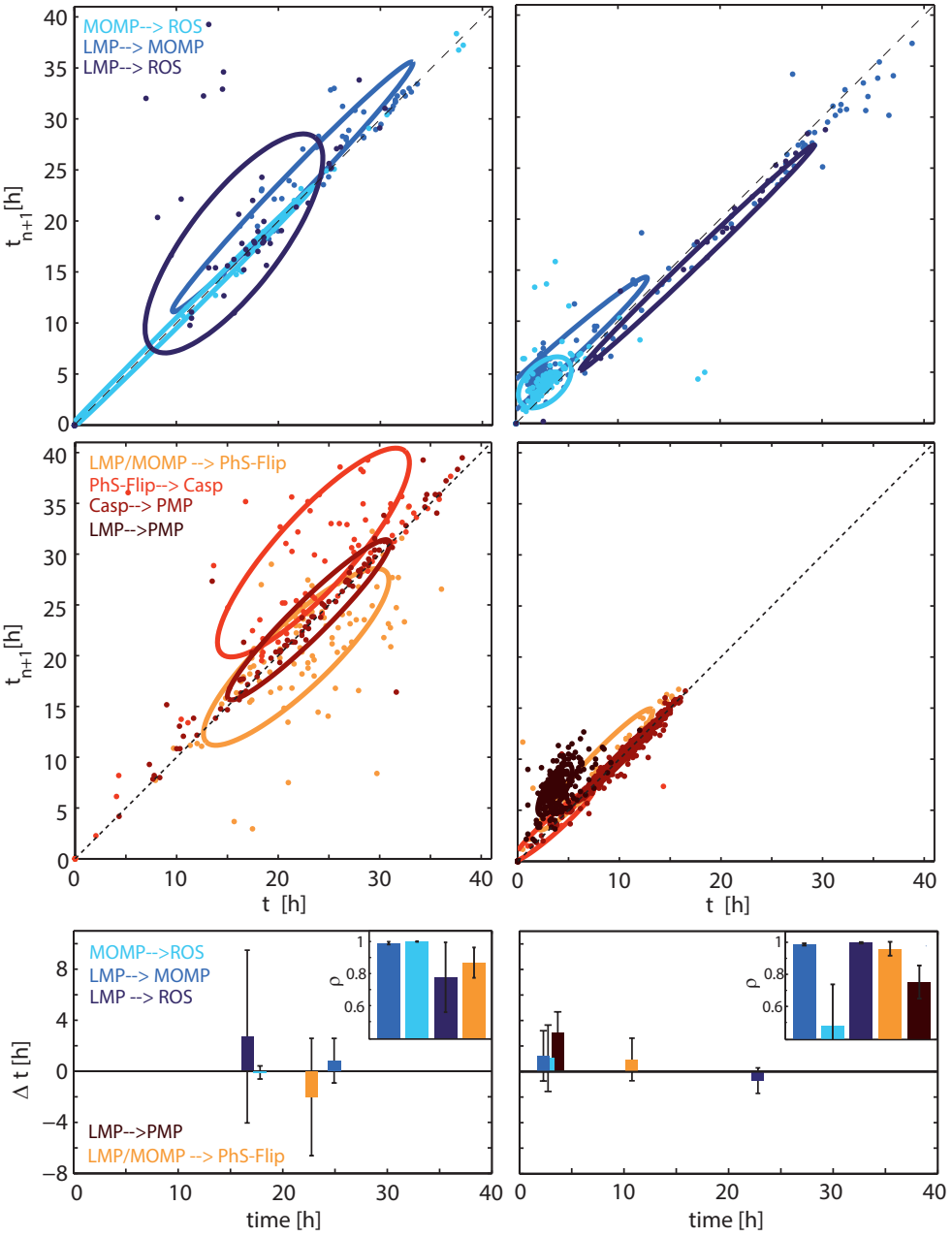


**Figure 7.4:** Two-dimensional representation of event times $t_n$ and $t_{n+1}$ of pairwise markers of NP ($PS - NH_2$) (left column) and STS (right column) induced cell death. The upper row shows the marker combinations of the early death events with MOMP - ROS (light blue), LMP – MOMP (blue), LMP – ROS (dark blue), the middle row the combinations of the late markers with LMP/MOMP - PhS-Flip (orange), PhS-Flip - Casp3 (red), Casp - PMP (dark red), and LMP - PMP (dark brown). The ellipses display a one sigma interval (67% of data) of the principal component analysis. Lower row: Bar plot of $\Delta t = t_{n+1} - t_n$ of successive events, in particular the time distance between the diagonal shown in the ellipse plots, vs. the mean event time $t_n$. The error bar corresponds to the width of the single cell distribution of marker $n$. Caspase3 was excluded from the analysis for the event order, as the event times occur after all the other markers and hence cannot be used for the time correlation. Insets show the Pearsson's correlation coefficients $\rho$ of the pairwise combinations in a bar plot with error bars corresponding to a 95% confidence interval.

distributed. The consistency check of the combination LMP-ROS suffers again from low statistic.

The late marker combinations do have some inconsistencies in their sequences of events. Most prominently, the onset event of caspase3 follows after the PhS-Flip and the PMP, whereas in the cell death pathway caspase3 is responsible for the execution pathway of PhS-Flip and the PMP. This discrepancy may be related to the indirect staining which probably causes a delay in fluorescence. Nevertheless, this marker can be used for discrimination when a cell has taken the caspase-dependent pathway or died via necrosis but cannot be used for the evaluation of time sequences. The ellipse with the combination LMP and PhS-Flip (orange) needs also further consideration, as this contradicts the observation of the early marker correlation. Here, additional experiments and increased statistic are necessary. Last, an early event (LMP) is compared with the latest event (PMP), shown for STS (dark brown). The control shows a higher time difference than the early distribution which is consistent with the data of the early markers.

By the principal components analysis, a sequence of events can be derived. This is displayed in the lower panel of Fig. 7.4, in which average delay times $\Delta t = \langle t_{n+1} - t_n \rangle$ of both markers are plotted as bars in relation to the mean event time of marker $n$. The error bars represent the width of the single cell distribution of marker $n$ and hence constitute a measure for the uncertainty of the mean event time (position of the bars). For the NPs, no clear sequence whereas for STS a sequence of LMP, MOMP, ROS, PhS-Flip and PMP can be determined. The events follow in short time intervals. Note that for simplicity's sake the bivalent LMP-MOMP behavior is not taken into account here. Another consistency check shows that the sum of $t_{LMP-MOMP}$ and $t_{MOMP-PhSFlip}$ is smaller than the total time difference $t_{LMP-PMP}$, whereas $t_{PhSFlip-PMP}$ is not evaluated yet. If all mean time distances of the pairwise combinations are known the bias of the individual fluorescent markers on the timing can be evaluated. The propagation of uncertainty should be calculated then by the square root of the sum of the squared pairwise marker time averages.

The insets in Fig. 7.4 (lower row) show the Pearsson's correlation coefficients $\rho$ (see Eq. 6.3) for the discussed marker combinations. Most of the $\rho$ values are near 1, meaning that the two pairwise events are highly correlated and that the ellipses are narrow. Low statistic of the combination LMP-ROS can be seen again in the high uncertainty of the correlation. For STS, the MOMP-ROS combination exhibit with 0.5 the lowest correlation, underlining again that these two events do not depend as strongly as the other successive events.

### NP-Dose Dependence of ROS

ROS plays a crucial role in apoptosis, as it is involved in different compartments of the cell. Thus, dose-dependent measurements were performed with ROS in combination with PI to check whether a different NP dose changes the cell behavior. Besides the event times, further parameters from the fit functions (see Eq. 7.1 and 7.3) are extracted, in particular the amplitude and the linear increase of the ROS level. In Fig. 7.5, the ROS activity (linear increase) is plotted against time point of cell death $t_{step}$(PI) for the negative control, STS, and different NP doses. Up to a dose of 25 $\mu\mathrm{g/ml}$,

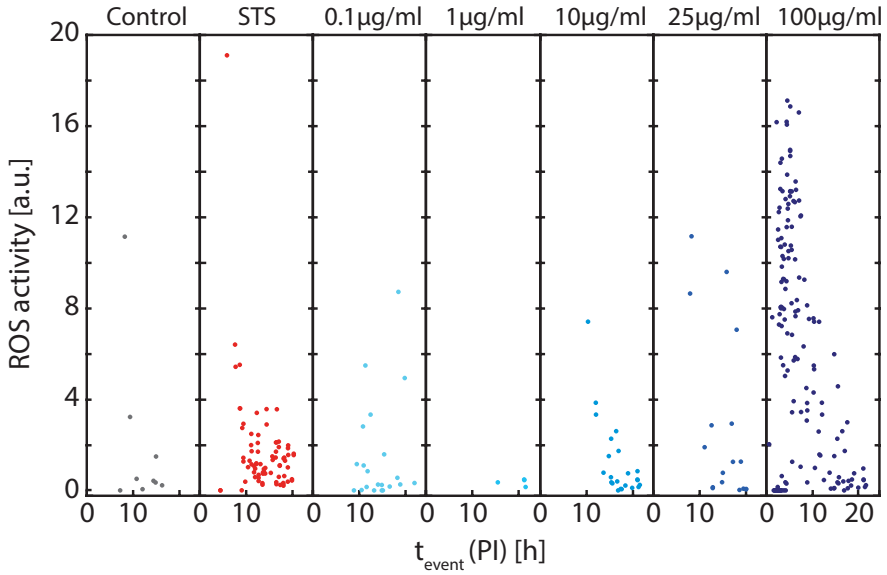


**Figure 7.5:** ROS activity was measured for different NP doses (0.1, 1, 10, 25, 100 $\mu$g/ml), for a negative control (cell culture medium), and for a positive control (STS). The ROS activity (linear increase of the fluorescence) is plotted against the time of death $t_{event}(PI)$. High ROS activity is observed for the highest NP dose. Cells which die early have a high ROS level, whereas cells which die late, similar to that of STS, exhibit a low level.

ROS activity is low as well as the fraction of dead cells. At 100 $\mu\mathrm{g}/\mathrm{ml}$, two populations can be discriminated: Cells which have a high ROS level die early (between 0 and 10 h), and cells which have a low ROS level die at later time points. In comparison to STS, ROS activity is moderate, and time response in cell death is broad. This dose-response analysis shows that cells respond differently upon NP dose. This has to be taken into account for further analysis.

## High Content Analysis of Lysosomal Break

Another important aspect is the study of the lysosomal signal. As each cell contains many single lysosomes, the mean signal, which is recorded in the time-lapse measurements, could lead to false conclusion, as especially the amount of uptaken NP could differ among the lysosomes. Thus, HCA analysis could give details on the lysosomal distribution in a cell. For the HCA measurements, cells were recorded with 60x resolution in a 10 min time interval. For each frame, ROIs of cells were determined and the number, total intensity, and total area of lysosomes were extracted. In Fig. 7.6 as insets, two distributions on the total number of lysosomes are displayed at the beginning (0h) and after 5h. A clear shift towards lower number of lysosomes can be observed. The mean signals from the distributions are plotted against time for the total intensity, total area and the number of lysosomes. The intensity and the area of the lysosomes decrease approximately at the same time, whereas the number of lysosomes decreases later. This could be interpreted as a sign that the lysosomes shrink before they rupture or by some bleaching artifacts. A shrinkage of the lysosomes are in contradiction to previous studies.[118, 133]

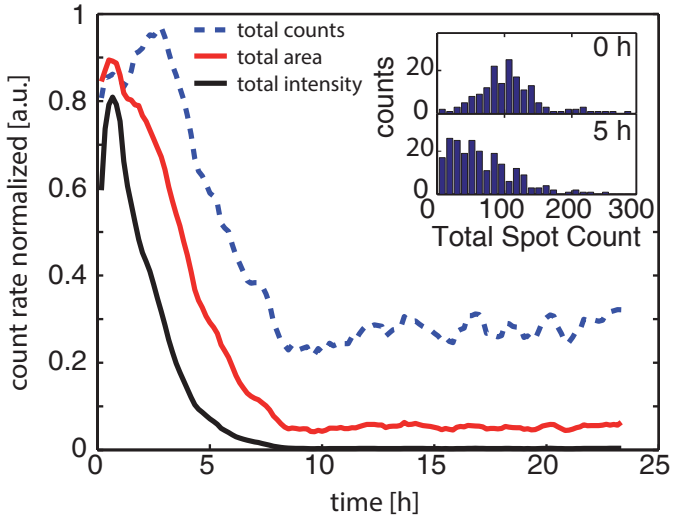


**Figure 7.6:** For the HCA analysis, the number of lysosomes per cell, the total area and the total intensity was measured over a period of 24 h. The inset shows a shift of the distributions of the total lysosome number at the beginning (0h) in comparison to the time after 5h. The averaged numbers of the total counts (blue dotted), the total lysosomal area (red) and the total lysosomal intensity (black) are plotted against time. A clear shift between number of lysosomes and area can be observed.

## Noise in Heterogeneous Timing of Apoptosis Signal Events

The correlation analysis gives a detailed view on heterogeneous timing. As mentioned in the introduction, heterogeneous timing is caused by stochastic fluctuations in either gene expression or more likely in protein levels. Non-genetic origins of cell-to-cell variability in cell death has been shown.[134, 135] This variability, the so-called noise, can be either ”intrinsic” (variation in identically-regulated quantities within a single cell) or ”extrinsic” (variation in identically-regulated quantities between different cells).[136] In Fig. 7.4, the ellipses are broader for the NP exposure as for STS. The broader ellipses are most likely due to extrinsic noise as it is expected that the quantity of uptaken NPs differ from cell to cell. Our setup allows us to determine the correlation of two events, the sequence, and the noise of the system. Based on this, simple regulatory circuits can be modeled to reproduce the experimental findings

In this chapter, we performed time-resolved measurements with multiple fluorescent cell death markers in pairwise combinations. Single cell traces were fitted by phenomenological functions which allowed to extract characteristic event times. The pairwise combination of the event times using principal component analysis allows precise determination of time differences. This can be used to determine the induction and signal pathway of cell death. First preliminary results could confirm that amino-modified polystyrene particle induce cell death via the lysosomal pathway. To underline the results so far, statistic will be increased as well as further positive controls will be applied. Candidates for a further control are death ligands such as FAS or TRAIL, which induce the external death pathway. These pathways should be more direct and hence give an unambiguous sequence of death events. The pairwise correlation analysis is a powerful tool which can pave the way for cell death signaling characterization.

# Chapter 8

## Conclusion and Outlook

In this thesis, a novel method for microstructuring has been introduced which allows to fabricate easily and fast homogenous patterns with a high flexibility with regard to substrate and protein composition obviating tedious adjustments of the protocol. The technique combines plasma-induced patterning with copolymer passivation. If extended with the Micro-Contact Printing, multicomponent patterns with up to three different proteins could be fabricated. This technique has been proven successful and reliable in all conducted cell experiments.

Based on this micropatterning, a single cell array approach has been presented, in which the occupation follows cellular self-organization: Cells randomly migrate on passivated areas and preferentially occupy with time the protein adhesion sites. The rinsing step after cell seeding is expendable and thus, all input cells can be analyzed. This is especially useful for rare and valuable stem cells. The self-organization is shown for various cell lines, and optimal lattice geometry is determined for each cell type. The self-organization phenomenon can be described by a reaction-diffusion model adapted from chemoreception, which is able to predict the single cell occupation if the motility of a specific cell line is known.

The fact, that cells can partially adhere on the passivated areas, has been investigated with neutron reflectometry and fluorescence microscopy. The protein adsorption in various PEG copolymers was studied. Copolymers with a hydrophobic (PPO) backbone and two 4.4 kDa PEG chains grafted to that showed no protein adsorption and hence no cell adhesion. The protein repellent effect is caused by the amphiphilic character, as hydrophilic PEG chains shield the backbone from water. In contrast to that, a hydrophilic (PLL) backbone with two different PEG chain lengths (2 and 5 kDa) revealed protein adsorption in the vicinity of the PLL. Besides adhesion ability, cell motility was compared on the different passivations. The highest speed was measured on a PLL-PEG(5) passivation, whereas the highest directed persistent motion on a pure fibronectin surface. This can be explained by the fact that fewer adhesion points of a cell on a passivated area lead to faster detachment and hence faster migration. In turn, fewer protein adhesion points in the passivation reduce the probability to continue migration in direction taken resulting in a lower persistent motion.

Next, a two-adhesion site with a connecting bridge, a so-called dumbbell pattern, was designed, on which cells periodically migrate between the sites. Experiments with different bridge lengths were conducted and the discrete transitions, so-called hops, were determined. An increase in bridge length exhibited an exponentially decrease in hopping. This was shown to be related to lamellipodium formation. By quantification of occupation times and transitions rates, this setup allows to measure relative affinities of two different sites. First experiments investigated the occupation times of asymmetric sized areas of the dumbbell. Affinities with regard to different proteins using a combination of $\mu$PIPP and $\mu$CP, as well as with regard to variable ligand spacing of gold adhesion spots using nanolithography can also be measured. The knowledge gained on the affinities allows for optimization of adhesion area and surface coating, but can also be used to phenotyping motility of different cell types.

A first application for time-resolved single cell analysis was introduced, in which the heterogeneous toxicity response induced by NPs was evaluated. As a model system, amino-functionalized PS NPs were exposed to hepato carcinoma cells at various doses. Cell death was marked via two fluorescent markers which indicate the PhS-flip in the plasma membrane and loss of plasma membrane integrity. The ratio of cell death was determined as a function of time. We showed that the half maximal effective concentration $\mathrm{EC}_{50}$ value depend on time and therefore introduced an average time-dependent $\tau_{50}$ value, which could especially be important for weak toxic nanomaterials. The time correlation between the onset of the cell death markers revealed a decrease in the time interval with the progression of the experiment.

The concept of time-correlation was extended in the last part of the thesis. Multiple fluorescent cell death markers were used which indicate apoptotic changes in the lysosomes, mitochondria, plasma membrane, oxidative burst, and caspase activity. Phenomenological functions were fitted to fluorescence single cell time traces, which allowed to extract characteristic event times and parameters such as signal intensity or initial increase in fluorescence. The time differences can be evaluated by pairwise measurements in order to get a kinetic fingerprint of the signal cascade in apoptosis. First preliminary results could confirm that amino-modified polystyrene particle induce cell death via the lysosomal pathway. Further correlation showed a dose-response dependence on ROS generation and time of cell death.

## Extension from Single to Oligo-Cell Analysis

All presented studies in this thesis have focused on single cells. As cells *in-vivo* grow in a sheet with contact to neighboring cells, it may be important to include cell-to-cell interaction as these results could differ from the single cell data. It has been shown that separate cells are more stressed than cells in a tissue. Also cell adhesion and cell survival molecules have an impact on their microenvironment and can be used, for example, to uncouple adhesion signaling from the tumor apoptosis.[137, 138] Cell-to-cell interactions can be addressed using an oligo-cellular cell array. Oligo-cell arrays could give answers to following questions: Do cells survive longer if connected to each other, are the onset times of death of two connected cells correlated to each other, and does this change if these are daughter cells? 3D environments in form of microslits for non-adherent

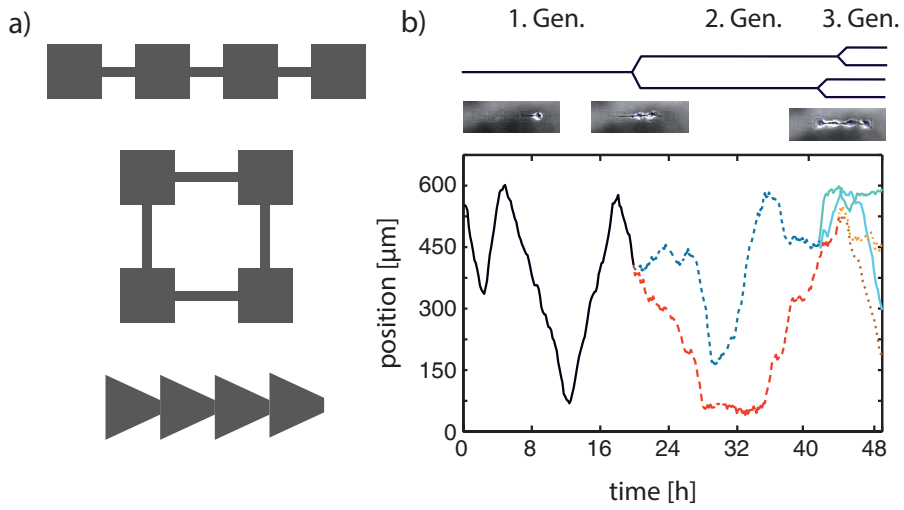


**Figure 8.1:** a) Possible geometries for an oligo-cell array setup: linear or in square shape arranged adhesion sites with interconnecting bridges, or ratchet shape geometry which may direct cell motion. b) Example for the tracking of two cell generations on a five interconnected adhesion site pattern. The geometry can provide the cell allocation as well as information on the cell cycle.

cells have been already implemented at our chair.[139] For adherent cells a 2D environment is needed. If the interest only lies in the response on the adhesion signaling of two connected cells, the adhesion site can be simply increased so that two or more cells fit on it, yet the allocation of the cells might be inaccurate. In order to follow the cell fate beyond cell division, the dumbbell pattern geometry, presented in chapter 5, can be used, which also involves an easier allocation of several cells. For example, in order to follow two cell generations, four sites can be either arranged linear or in a square format (see Fig. 8.1a). By using more sophisticated designs as e.g. ratchet geometries,[32] it may even be possible to influence the direction of movement after cell division. As a first proof of concept, a cell trace of two cell generations is shown on a pattern with five connected sites in Fig. 8.1b. Individual cells can easily be distinguished as well as the times of cell division. This allows the correlation of cell cycle and cell response which could provide useful insights for combinatorial drug therapy.

## Towards High-Throughput Screening and Analysis

So far, maximal 1000 single cells can be screened for one exposure condition, and up to eight different exposure conditions can be monitored in one experiment. In order to perform high-throughput screenings, the number of analyzed cells should reach the number of 10,000, especially if one wants to identify small sub-populations. In addition, the variation of up to eight parameters in one experiment is in terms of drug screening a small number. In order to overcome these limitations, the use of 96well plates instead of dish or slide samples are required. A 96well plate would allow to screen over ten times more parameters than an 8well. With 96 parameters, it is possible to test in one experiment different doses as well different marker combinations or different nanomaterials. The technical realization of single cell patterns on well plate format using photo-

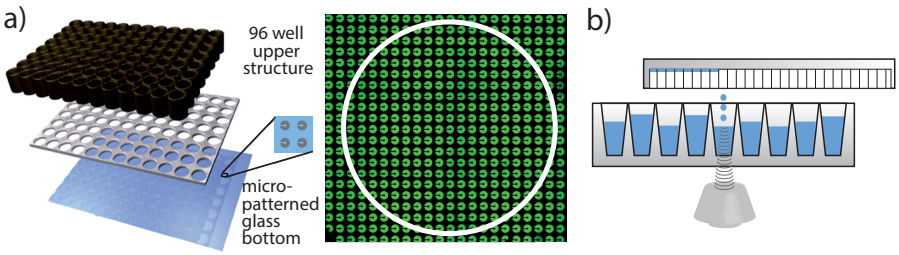


**Figure 8.2:** a) For up-scaling the single cell setup, a 96well plate from SCHOTT NEXTERION® can be used, which consists of a glass bottom, a frame, and an inset, which can be stuck to the plate. In this way, the flat bottom can be patterned either with conventional patterning or via photo-lithography (adapted from [65]). b) Instead of manual pipetting, an acoustic liquid transfer with source and the patterned target plate can be used. This allows high throughput transfer of various NPs and fluorescent markers at different concentrations.

lithography has been reported (see also Fig. 8.2a [65]). The use of the Schott NEXTERION® well plates (instead of sticky ibidi labware) allows to pattern the flat bottom with $\mu$PIPP or by photo-lithography. In the next steps, the bottom is set into a frame, and the inset for the 96well segmentation is stuck to the bottom of the plate. In order to avoid extensive pipetting, additional automation is essential. Here, one could use a robotic system such as the contact-free liquid handling system Echo550 instead of multi-pipettes (see Fig. 8.2b) to transfer in high-throughput the NPs and the fluorescent markers at different concentrations into the well plates.

Besides the up-scaling of the experimental setup, it is as well necessary to further automate the data analysis. Up to now, the geometry for each recorded position at the microscope is defined manually by the user. By using cluster analysis on fluorescence images, which is based on statistical moments, the cell positions can be automatically identified. Knowing the cell positions and the lattice geometry, the distance between cell locations and the lattice site positions needs only to be minimized. In order to identify, if a site is singly occupied, additional filter rules need to be applied, such as criteria of maximal size of a single cell or automated identification of fluorescent nuclei on an adhesion site.

In our time-resolved studies we are able to assess motility phenotypes by a comparative two-adhesion site setup and a kinetic fingerprint of cell death by correlating apoptotic markers which is not accessible in ensemble measurements. These new methods can contribute for drug screening and diagnostics for personalized medicine, as they provide patient-specific, individual single cell responses on external trigger such as chemostatic agents.

# List of Abbreviations

**AdG** Alexandre de Gennes

**BSA** Bovine Serum Albumine

**COC** Cyclic Olefin Copolymer

**DMEM** Dulbecco's Modified Eagle Medium

**DEVD** Asparagine-Glutamine-Valine-Asparagine

**ECM** Extra Cellular Matrix

**FN** Fibronectin

**FCS** Fetal Calf Serum

**HCA** High Content Analysis

**HEPES** 4-(2-HydroxyEthyl)-1-PiperazineEthaneSulfonic

**HUVEC** Human Umbilical Vein Endothelial Cell

**IANBD** N-((2-(iodoacetoxy)ethyl)-N-Methyl)amino-7-Nitrobenz-2-Oxa-1,3-Diazole

**L-15** Leibovitz's L-15

**LMP** Lysosomal Membrane Permeabilization

**MMP** Matrix-Metallo Proteases

**MOMP** Mitochondria Outer Membrane Permeabilization

**MSD** Mean Square Displacement

$\mu$**PIPP** Micro-Plasma-Induced Protein Patterning

$\mu$**CP** Micro-Contact Printing

**NP** Nanoparticle

**PBS** Phosphate-Buffered Saline

**PCA** Principal Component Analysis

**PCD** Programmed Cell Death

**PDMS** Polydimethylsiloxane

**PEG** Polyethyleneglycol

**PI** Propidium Iodide

**PLL** Poly-L-Lysine

**PMP** Plasma Membrane Permeabilization

**PPO** Polypropyleneoxide

**PhS** Phosphatidylserine

$\mathbf{PS-NH_2}$ polystyrene-amine functionalized

**pSIVA** polarity Sensitive Indicator for Viability and Apoptosis

**ROI** Region of Interest

**RGD** Arginyl-Glycyl-Aspartic acid

**ROS** Reactive Oxygen Species

**SLD** Scattering Length Density

**tc-PS** tissue cultured Polystyrene

**TEM** Transmission Electron Microscope

# List of Figures


1.1 Comparison of continuous single-cell *vs.* static population analysis . . . . . 2
1.2 Schematic overview: single cell analysis . . . . . 3
1.3 Schematic overview: cancer cell motion . . . . . 4
1.4 Schematic overview: apoptosis pathways . . . . . 5

2.1 Patterning procedure . . . . . 8
2.2 Versatile pattern on various substrates and protein concentrations/gradients . . . . . 9
2.3 Multicomponent patterning by combining $\mu$PIPP with $\mu$CP . . . . . 10

3.1 Dynamics of cellular self-organization . . . . . 14
3.2 Dependence of order parameters on lattice spacing . . . . . 15
3.3 Reaction-diffusion model in relation to cell motility . . . . . 16

4.1 Schematics of the polymer architecture of Pluronic and PLL-PEG . . . . . 20
4.2 Cell adhesion and motility on various PEG copolymers surfaces . . . . . 21
4.3 Neutron reflectivity data and fits for various PEG surfaces . . . . . 22
4.4 Interpretation of the adsorption of FN in the three different PEG surfaces . . . . . 23

5.1 Cell hopping on dumbbell patterns . . . . . 26
5.2 Geometry dependence of stay times . . . . . 27
5.3 Lamellipodia growth on dumbbells . . . . . 28
5.4 Surface affinities depending on ligand spacing and protein . . . . . 30

6.1 Time series of NP induced apoptosis . . . . . 32
6.2 Dose and time dependent cell death distributions . . . . . 33
6.3 Correlation analysis of pSIVA and PI . . . . . 34

7.1 Cell death pathway induced by PS-NH2 . . . . . 38
7.2 Time series of various cell death markers . . . . . 39
7.3 Frequency distributions of single cells for different cell death markers . . . . . 42
7.4 Pairwise correlation of cell death marker . . . . . 43
7.5 Correlation of ROS and dose dependence . . . . . 45

7.6 HCA on lysosomes . . . . . 46

8.1 Geometries for oligo-cell arrays . . . . . 49
8.2 Scaling up single cell array systems . . . . . 50

# Bibliography


[1] PHAN, J. H. ; MOFFITT, R. A. ; STOKES, T. H. ; LIU, J. ; YOUNG, A. N. ; NIE, S. ; WANG, M. D.: Convergence of biomarkers, bioinformatics and nanotechnology for individualized cancer treatment. In: *Trends Biotechnol* 27 (2009), no. 6, p. 350–8

[2] CORNETTA, K. ; BROWN, C. G.: Balancing personalized medicine and personalized care. In: *Acad Med* 88 (2013), p. 309–13

[3] FÜLLBECK, Melanie ; DUNKEL, Mathias ; HOSSBACH, Julia ; DANIEL, Peter T. ; PREISSNER, Robert: Cellular Fingerprints: A Novel Approach Using Large-Scale Cancer Cell Line Data for the Identification of Potential Anticancer Agents. In: *Chemical Biology & Drug Design* 74 (2009), no. 5, p. 439–448

[4] BAJORATH, J.: Integration of virtual and high-throughput screening. In: *Nat Rev Drug Discov* 1 (2002), no. 11, p. 882–94

[5] BUETTNER, F. ; NATARAJAN, K. N. ; CASALE, F. P. ; PROSERPIO, V. ; SCIALDONE, A. ; THEIS, F. J. ; TEICHMANN, S. A. ; MARIONI, J. C. ; STEGLE, O.: Computational analysis of cell-to-cell heterogeneity in single-cell RNA-sequencing data reveals hidden subpopulations of cells. In: *Nat Biotechnol* 33 (2015), p. 155–60

[6] KUANG, Y. ; WALT, D. R.: Monitoring "promiscuous" drug effects on single cells of multiple cell types. In: *Anal Biochem* 345 (2005), no. 2, p. 320–5

[7] WALLING, Maureen A. ; SHEPARD, Jason R. E.: Cellular heterogeneity and live cell arrays. In: *Chemical Society Reviews* 40 (2011), p. 4049–4076

[8] XIA, X. ; OWEN, M. S. ; LEE, R. E. ; GAUDET, S.: Cell-to-cell variability in cell death: can systems biology help us make sense of it all? In: *Cell Death Differ.* 5 (2014), p. e1261

[9] DAVEY, H M. ; KELL, D B.: Flow cytometry and cell sorting of heterogeneous microbial populations: the importance of single-cell analyses. In: *Microbiological Reviews* 60 (1996), no. 4, p. 641–96

[10] WEINBERGER, L. S. ; BURNETT, J. C. ; TOETTCHER, J. E. ; ARKIN, A. P. ; SCHAFFER, D. V.: Stochastic gene expression in a lentiviral positive-feedback loop: HIV-1 Tat fluctuations drive phenotypic diversity. In: *Cell* 122 (2005), no. 2, p. 169–82

[11] SUN, J. ; MASTERMAN-SMITH, M. D. ; GRAHAM, N. A. ; JIAO, J. ; MOTTAHEDEH, J. ; LAKS, D. R. ; OHASHI, M. ; DEJESUS, J. ; KAMEI, K. ; LEE, K. B. ; WANG, H. ; YU, Z. T. ; LU, Y. T. ; HOU, S. ; LI, K. ; LIU, M. ; ZHANG, N. ; WANG, S. ; ANGENIEUX, B. ; PANOSYAN, E. ; SAMUELS, E. R. ; PARK, J. ; WILLIAMS, D. ; KONKANKIT, V. ; NATHANSON, D. ; DAM, R. M. ; PHELPS, M. E. ; WU, H. ; LIAU, L. M. ; MISCHEL, P. S. ; LAZAREFF, J. A. ; KORNBLUM, H. I. ; YONG, W. H. ; GRAEBER, T. G. ; TSENG, H. R.: A microfluidic platform for systems pathology: multiparameter single-cell signaling measurements of clinical brain tumor specimens. In: *Cancer Res* 70 (2010), p. 6128–38

[12] PUSHKARSKY, I. ; LIU, Y. ; WEAVER, W. ; SU, T. W. ; MUDANYALI, O. ; OZCAN, A. ; DI CARLO, D.: Automated single-cell motility analysis on a chip using lensfree microscopy. In: *Sci Rep* 4 (2014), p. 4717

[13] ETZRODT, M. ; ENDELE, M. ; SCHROEDER, T.: Quantitative single-cell approaches to stem cell research. In: *Cell Stem Cell* 15 (2014), p. 546–58

[14] YOUSSEF, Simon ; GUDE, Sebastian ; RÄDLER, Joachim O.: Automated tracking in live-cell time-lapse movies. In: *Integr. Biol.* 3 (2011), p. 1095–1101

[15] WHITESIDES, George M. ; OSTUNI, Emanuele ; TAKAYAMA, Shuichi ; JIANG, Xingyu ; INGBER, Donald E.: SOFT LITHOGRAPHY IN BIOLOGY AND BIOCHEMISTRY. In: *Annual Review of Biomedical Engineering* 3 (2001), p. 335–373

[16] LIBERSKI, Albert R. ; DELANEY, Joseph T. ; SCHUBERT, Ulrich S.: "One Cell - One Well": A New Approach to Inkjet Printing Single Cell Microarrays. In: *ACS Combinatorial Science* 13 (2010), p. 190–195

[17] LOVE, Kerry R. ; BAGH, Sangram ; CHOI, Jonghoon ; LOVE, J. C.: Microtools for single-cell analysis in biopharmaceutical development and manufacturing. In: *Trends in Biotechnology* 31 (2013), p. 280–286

[18] RÖTTGERMANN, Peter J. ; DAWSON, Kenneth A. ; RÄDLER, Joachim O.: Time-Resolved Study of Nanoparticle Induced Apoptosis Using Microfabricated Single Cell Arrays. In: *Microarrays* (2016, accepted)

[19] SAHAI, E.: Mechanisms of cancer cell invasion. In: *Curr Opin Genet Dev* 15 (2005), no. 1, p. 87–96

[20] HANAHAN, Douglas ; WEINBERG, Robert A.: The Hallmarks of Cancer. In: *Cell* 100 (2000), no. 1, p. 57–70

[21] MOFFAT, J. G. ; RUDOLPH, J. ; BAILEY, D.: Phenotypic screening in cancer drug discovery - past, present and future. In: *Nat. Rev. Drug Discov.* 13 (2014), p. 588–602

[22] HULKOWER, K. I. ; HERBER, R. L.: Cell migration and invasion assays as tools for drug discovery. In: *Pharmaceutics* 3 (2011), no. 1, p. 107–24

[23] SOOD, Anil K. ; SEFTOR, Elisabeth A. ; FLETCHER, Mavis S. ; GARDNER, Lynn M. G. ; HEIDGER, Paul M. ; BULLER, Richard E. ; SEFTOR, Richard E. B. ; HENDRIX, Mary J. C.: Molecular Determinants of Ovarian Cancer Plasticity. In: *The American Journal of Pathology* 158 (2001), no. 4, p. 1279–1288

[24] PITTS, William C. ; ROJAS, Virginia A. ; GAFFEY, Michael J. ; ROUSE, Robert V. ; ESTEBAN, Jose ; FRIERSON, Henry F. ; KEMPSON, Richard L. ; WEISS, Lawrence M.: Carcinomas with Metaplasia and Sarcomas of the Breast. In: *American Journal of Clinical Pathology* 95 (1991), no. 5, p. 623–632

[25] POUJADE, M. ; GRASLAND-MONGRAIN, E. ; HERTZOG, A. ; JOUANNEAU, J. ; CHAVRIER, P. ; LADOUX, B. ; BUGUIN, A. ; SILBERZAN, P.: *Collective migration of an epithelial monolayer in response to a model wound*. October 9, 2007 2007

[26] MAREL, A. K. ; ZORN, M. ; KLINGNER, C. ; WEDLICH-SOLDNER, R. ; FREY, E. ; RÄDLER, J. O.: Flow and diffusion in channel-guided cell migration. In: *Biophys J* 107 (2014), no. 5, p. 1054–64

[27] ZORN, M. L. ; MAREL, A. K. ; SEGERER, F. J. ; RÄDLER, J. O.: Phenomenological approaches to collective behavior in epithelial cell migration. In: *Biochim Biophys Acta* 1853 (2015), no. 11 Pt B, p. 3143–52

[28] KUMAR, G. ; CO, C. C. ; HO, C. C.: Steering cell migration using microarray amplification of natural directional persistence. In: *Langmuir* 27 (2011), p. 3803–7

[29] MAIURI, P. ; TERRIAC, E. ; PAUL-GILLOTEAUX, P. ; VIGNAUD, T. ; MCNALLY, K. ; ONUFFER, J. ; THORN, K. ; NGUYEN, P. A. ; GEORGOULIA, N. ; SOONG, D. ; JAYO, A. ; BEIL, N. ; BENEKE, J. ; LIM, J. C. ; SIM, C. P. ; CHU, Y. S. ; PARTICIPANTS, W. C. R. ; JIMENEZ-DALMARONI, A. ; JOANNY, J. F. ; THIERY, J. P. ; ERFLE, H. ; PARSONS, M. ; MITCHISON, T. J. ; LIM, W. A. ; LENNON-DUMENIL, A. M. ; PIEL, M. ; THERY, M.: The first World Cell Race. In: *Curr Biol* 22 (2012), no. 17, p. R673–5

[30] SCHREIBER, Christoph ; SEGERER, Felix J. ; WAGNER, Ernst ; ROIDL, Andreas ; RÄDLER, Joachim O.: Ring-Shaped Microlanes and Chemical Barriers as a Platform for Probing Single-Cell Migration. In: *Sci. Rep.* (2016, submitted)

[31] LEE, R. M. ; KELLEY, D. H. ; NORDSTROM, K. N. ; OUELLETTE, N. T. ; LOSERT, W.: Quantifying stretching and rearrangement in epithelial sheet migration. In: *New J Phys* 15 (2013), no. 2

[32] MAHMUD, Goher ; CAMPBELL, Christopher J. ; BISHOP, Kyle J. M. ; KOMAROVA, Yulia A. ; CHAGA, Oleg ; SOH, Siowling ; HUDA, Sabil ; KANDERE-GRZYBOWSKA, Kristiana ; GRZYBOWSKI, Bartosz A.: Directing cell motions on micropatterned ratchets. In: *Nat Phys* 5 (2009), p. 606–612

[33] ALBERT, P. J. ; SCHWARZ, U. S.: Dynamics of cell shape and forces on micropatterned substrates predicted by a cellular Potts model. In: *Biophys J* 106 (2014), p. 2340–52

[34] CAMLEY, Brian A. ; ZHAO, Yanxiang ; LI, Bo ; LEVINE, Herbert ; RAPPEL, Wouter-Jan: Periodic Migration in a Physical Model of Cells on Micropatterns. In: *Physical Review Letters* 111 (2013), p. 158102(1–5)

[35] SHAO, D. ; LEVINE, H. ; RAPPEL, W. J.: Coupling actin flow, adhesion, and morphology in a computational cell motility model. In: *Proc Natl Acad Sci U S A* 109 (2012), no. 18, p. 6851–6

[36] XU, H. ; ZHAO, X. ; LIU, X. ; XU, P. ; ZHANG, K. ; LIN, X.: Antitumor effects of traditional Chinese medicine targeting the cellular apoptotic pathway. In: *Drug Des Devel Ther* 9 (2015), p. 2735–44

[37] LOWE, Scott W. ; LIN, Athena W.: Apoptosis in cancer. In: *Carcinogenesis* 21 (2000), no. 3, p. 485–495

[38] VANDEN BERGHE, T. ; VANLANGENAKKER, N. ; PARTHOENS, E. ; DECKERS, W. ; DEVOS, M. ; FESTJENS, N. ; GUERIN, C. J. ; BRUNK, U. T. ; DECLERCQ, W. ; VANDENABEELE, P.: Necroptosis, necrosis and secondary necrosis converge on similar cellular disintegration features. In: *Cell Death Differ* 17 (2010), p. 922–30

[39] NEL, A. ; XIA, T. ; MADLER, L. ; LI, N.: Toxic potential of materials at the nanolevel. In: *Science* 311 (2006), p. 622–7

[40] COLVIN, Vicki L.: The potential environmental impact of engineered nanomaterials. In: *Nat. Biotech.* 21 (2003), p. 1166–1170

[41] ZHANG, Haiyuan ; JI, Zhaoxia ; XIA, Tian ; MENG, Huan ; LOW-KAM, Cecile ; LIU, Rong ; POKHREL, Suman ; LIN, Sijie ; WANG, Xiang ; LIAO, Yu-Pei ; WANG, Meiying ; LI, Linjiang ; RALLO, Robert ; DAMOISEAUX, Robert ; TELESCA, Donatello ; MÄDLER, Lutz ; COHEN, Yoram ; ZINK, Jeffrey I. ; NEL, Andre E.: Use of Metal Oxide Nanoparticle Band Gap To Develop a Predictive Paradigm for Oxidative Stress and Acute Pulmonary Inflammation. In: *ACS Nano* 6 (2012), p. 4349–4368

[42] SENUT, Marie-Claude ; ZHANG, Yanhua ; LIU, Fangchao ; SEN, Arko ; RUDEN, Douglas M. ; MAO, Guangzhao: Size-Dependent Toxicity of Gold Nanoparticles on Human Embryonic Stem Cells and Their Neural Derivatives. In: *Small* 12 (2016), no. 5, p. 631–646

[43] YU, M. ; HUANG, S. ; YU, K. J. ; CLYNE, A. M.: Dextran and polymer polyethylene glycol (PEG) coating reduce both 5 and 30 nm iron oxide nanoparticle cytotoxicity in 2D and 3D cell culture. In: *Int J Mol Sci* 13 (2012), no. 5, p. 5554–70

[44] YILDIRIMER, L. ; THANH, N. T. ; LOIZIDOU, M. ; SEIFALIAN, A. M.: Toxicology and clinical potential of nanoparticles. In: *Nano Today* 6 (2011), no. 6, p. 585–607

[45] JAIN, Kewal K.: Nanobiotechnology-based strategies for crossing the blood–brain barrier. In: *Nanomedicine* 7 (2012), no. 8, p. 1225–1233

[46] GE, Y. ; BRUNO, M. ; WALLACE, K. ; WINNIK, W. ; PRASAD, R. Y.: Proteome profiling reveals potential toxicity and detoxification pathways following exposure of BEAS-2B cells to engineered nanoparticle titanium dioxide. In: *Proteomics* 11 (2011), no. 12, p. 2406–22

[47] SEGERER, Felix J. ; RÖTTGERMANN, Peter Johan F. ; SCHUSTER, Simon ; PIERA ALBEROLA, Alicia ; ZAHLER, Stefan ; RÄDLER, Joachim O.: Versatile method to generate multiple types of micropatterns. In: *Biointerphases* 11 (2016), no. 1, p. 011005

[48] WILBUR, James L. ; KUMAR, Amit ; BIEBUYCK, Hans A. ; KIM, Enoch ; WHITESIDES, George M.: Microcontact printing of self-assembled monolayers: applications in microfabrication. In: *Nanotechnology* 7 (1996), p. 452–457

[49] THÉRY, M. ; PIEL, M.: Adhesive micropatterns for cells: a microcontact printing protocol. In: *Cold Spring Harb. Protoc.* 4 (2009), p. pdb.prot5255

[50] ALOM RUIZ, Sami ; CHEN, Christopher S.: Microcontact printing: A tool to pattern. In: *Soft Matter* 3 (2007), p. 168

[51] AZIOUNE, Ammar ; STORCH, Marko ; BORNENS, Michel ; THÉRY, Manuel ; PIEL, Matthieu: Simple and rapid process for single cell micro-patterning. In: *Lab Chip* 9 (2009), p. 1640–1642

[52] NAKANISHI, Jun ; KIKUCHI, Yukiko ; TAKARADA, Tohru ; NAKAYAMA, Hidekazu ; YAMAGUCHI, Kazuo ; MAEDA, Mizuo: Photoactivation of a Substrate for Cell Adhesion under Standard Fluorescence Microscopes. In: *J. Am. Chem. Soc.* 126 (2004), p. 16314–16315

[53] KIM, Miju ; CHOI, Jong-Cheol ; JUNG, Hong-Ryul ; KATZ, Joshua S. ; KIM, Min-Gon ; DOH, Junsang: Addressable Micropatterning of Multiple Proteins and Cells by Microscope Projection Photolithography Based on a Protein Friendly Photoresist. In: *Langmuir* 26 (2010), p. 12112–12118

[54] BELISLE, J. M. ; KUNIK, D. ; COSTANTINO, S.: Rapid multicomponent optical protein patterning. In: *Lab Chip* 9 (2009), p. 3580–5

[55] CHENG, Q. ; KOMVOPOULOS, K.: Integration of plasma-assisted surface chemical modification, soft lithography, and protein surface activation for single-cell patterning. In: *Appl. Phys. Lett.* 97 (2010), p. 043705

[56] JUNKIN, Michael ; WONG, Pak K.: Probing cell migration in confined environments by plasma lithography. In: *Biomaterials* 32 (2011), p. 1848–1855

[57] LANGOWSKI, Bryan A. ; UHRICH, Kathryn E.: Microscale Plasma-Initiated Patterning ($\mu$PIP). In: *Langmuir* 21 (2005), p. 10509–10514

[58] *Kapitel* 5. In: PICONE, Remigio ; BAUM, Buzz ; MCKENDRY, Rachel: *Plasma Microcontact Patterning (P$\mu$CP): A Technique for the Precise Control of Surface Patterning at Small-Scale*. Bd. Volume 119. Academic Press, 2014, p. 73–90

[59] KIM, J. H. ; SEO, S. ; MIN, J.: Epithelial cell patterns on a PDMS polymer surface using a micro plasma structure. In: *J. Biotechnol.* 155 (2011), p. 308–11

[60] SMITH, Jason T. ; TOMFOHR, John K. ; WELLS, Matthew C. ; BEEBE, Thomas P. ; KEPLER, Thomas B. ; REICHERT, W. M.: Measurement of Cell Migration on Surface-Bound Fibronectin Gradients. In: *Langmuir* 20 (2004), p. 8279–8286

[61] LIU, Lingyun ; RATNER, Buddy D. ; SAGE, E. H. ; JIANG, Shaoyi: Endothelial Cell Migration on Surface-Density Gradients of Fibronectin, VEGF, or Both Proteins. In: *Langmuir* 23 (2007), p. 11168–11173

[62] EICHINGER, C. D. ; HSIAO, T. W. ; HLADY, V.: Multiprotein microcontact printing with micrometer resolution. In: *Langmuir* 28 (2012), p. 2238–43

[63] CARLSSON, R. ; ENGVALL, E. ; FREEMAN, A. ; RUOSLAHTI, E.: Laminin and fibronectin in cell adhesion: enhanced adhesion of cells from regenerating liver to laminin. In: *Proc. Natl. Acad. Sci. U.S.A.* 78 (1981), p. 2403–2406

[64] RÖTTGERMANN, Peter J. F. ; PIERA ALBEROLA, Alicia ; RÄDLER, Joachim O.: Cellular Self-Organization on Micro-Structured Surfaces. In: *Soft Matter* 10 (2014), p. 2397–2404

[65] AZIOUNE, Ammar ; STORCH, Marko ; BORNENS, Michel ; THÉRY, Manuel ; PIEL, Matthieu: Simple and rapid process for single cell micro-patterning. In: *Lab Chip* 9 (2009), p. 1640–1642

[66] ROLLI, C. G. ; NAKAYAMA, H. ; YAMAGUCHI, K. ; SPATZ, J. P. ; KEMKEMER, R. ; NAKANISHI, J.: Switchable adhesive substrates: revealing geometry dependence in collective cell behavior. In: *Biomaterials* 33 (2012), p. 2409–18

[67] PAN, Y. V. ; MCDEVITT, Todd C. ; KIM, Tae K. ; LEACH-SCAMPAVIA, Deborah ; STAYTON, Patrick S. ; DENTON, Denice D. ; RATNER, Buddy D.: Micro-Scale Cell Patterning on Nonfouling Plasma Polymerized Tetraglyme Coatings by Protein Microcontact Printing. In: *Plasmas and Polymers* 7 (2002), p. 171–183

[68] JEN, C. P. ; HSIAO, J. H. ; MASLOV, N. A.: Single-cell chemical lysis on microfluidic chips with arrays of microwells. In: *Sensors (Basel)* 12 (2012), p. 347–58

[69] RETTIG, Jacqueline R. ; FOLCH, Albert: Large-Scale Single-Cell Trapping And Imaging Using Microwell Arrays. In: *Analytical Chemistry* 77 (2005), p. 5628–5634

[70] CHUNG, K. ; RIVET, C. A. ; KEMP, M. L. ; LU, H.: Imaging single-cell signaling dynamics with a deterministic high-density single-cell trap array. In: *Analytical Chemistry* 83 (2011), p. 7044–52

[71] YUSOF, A. ; KEEGAN, H. ; SPILLANE, C. D. ; SHEILS, O. M. ; MARTIN, C. M. ; OLEARY, J. J. ; ZENGERLE, R. ; KOLTAY, P.: Inkjet-like printing of single-cells. In: *Lab on a Chip* 11 (2011), p. 2447–54

[72] BERG, H. C. ; PURCELL, E. M.: Physics of chemoreception. In: *Biophysical Journal* 20 (1977), p. 193–219

[73] ADAM, G. ; DELBRÜCK, M. ; RICH, Alexander (Hrsg.) ; DAVIDSON, Norman (Hrsg.): *Reduction of dimensionality in biological diffusion processes*. San Francisco, Calif. : W.H. Freeman & Company, 1968. – 198–215 S.

[74] POTDAR, A. A. ; LU, J. ; JEON, J. ; WEAVER, A. M. ; CUMMINGS, P. T.: Bimodal analysis of mammary epithelial cell migration in two dimensions. In: *Ann Biomed Eng* 37 (2009), p. 230–45

[75] CODLING, E. A. ; PLANK, M. J. ; BENHAMOU, S.: Random walk models in biology. In: *J R Soc Interface* 5 (2008), p. 813–34

[76] GAIL, Mitchell H. ; BOONE, Charles W.: The Locomotion of Mouse Fibroblasts in Tissue Culture. In: *Biophysical Journal* 10 (1970), p. 980–993

[77] MERODE, A. E. ; MEI, H. C. d. ; BUSSCHER, H. J. ; KROM, B. P.: Influence of culture heterogeneity in cell surface charge on adhesion and biofilm formation by Enterococcus faecalis. In: *J Bacteriol* 188 (2006), p. 2421–6

[78] GUPTA, Ajay K. ; GUPTA, Mona: Cytotoxicity suppression and cellular uptake enhancement of surface modified magnetic nanoparticles. In: *Biomaterials* 26 (2005), p. 1565–1573

[79] SATERBAK, A. ; KUO, S. C. ; LAUFFENBURGER, D. A.: Heterogeneity and probabilistic binding contributions to receptor-mediated cell detachment kinetics. In: *Biophysical Journal* 65 (1993), p. 243–252

[80] RÖTTGERMANN, P. J. ; HERTRICH, S. ; BERTS, I. ; ALBERT, M. ; SEGERER, F. J. ; MOULIN, J. F. ; NICKEL, B. ; RÄDLER, J. O.: Cell Motility on Polyethylene Glycol Block Copolymers Correlates to Fibronectin Surface Adsorption. In: *Macromol. Biosci.* 14 (2014), p. 1755–1763

[81] ALBEROLA, Alicia P. ; RÄDLER, Joachim O.: The defined presentation of nanoparticles to cells and their surface controlled uptake. In: *Biomaterials* 30 (2009), p. 3766–3770

[82] SEEHUBER, A. ; SCHMIDT, D. ; DAHINT, R.: Poly(acrylic acid)-poly(ethylene glycol) layers on positively charged surface coatings: molecular structure, protein resistance, and application to single protein deposition. In: *Langmuir* 28 (2012), p. 8700–10

[83] OCONNOR, S M. ; DEANGLIS, A P. ; GEHRKE, S H. ; RETZINGER, G S.: Adsorption of plasma proteins on to poly(ethylene oxide)/poly(propylene oxide) triblock copolymer films: a focus on fibrinogen. In: *Biotechnol. Appl. Biochem.* 31 (2000), p. 185–196

[84] HALPERIN, A. ; FRAGNETO, G. ; SCHOLLIER, A. ; SFERRAZZA, M.: Primary versus Ternary Adsorption of Proteins onto PEG Brushes. In: *Langmuir* 23 (2007), p. 10603–10617

[85] SHARMA, Sadhana ; JOHNSON, Robert W. ; DESAI, Tejal A.: Evaluation of the Stability of Nonfouling Ultrathin Poly(ethylene glycol) Films for Silicon-Based Microdevices. In: *Langmuir* 20 (2003), p. 348–356

[86] FRAGNETO-CUSANI, Giovanna: Neutron reflectivity at the solid/liquid interface: examples of applications in biophysics. In: *J. Phys.: Condens. Matter* 13 (2001), p. 4973

[87] MÉHES, Elöd ; MONES, Enys ; NÉMETH, Valéria ; VICSEK, Tamás: Collective Motion of Cells Mediates Segregation and Pattern Formation in Co-Cultures. In: *PLoS One* 7 (2012), p. e31711

[88] DE GENNES, P.G.: Scaling theory of polymer adsorption. In: *J. Phys. France* 37 (1976), p. 1445–1452

[89] ALEXANDER, S.: Adsorption of chain molecules with a polar head a scaling description. In: *J. Phys. France* 38 (1977), p. 983–987

[90] EFREMOVA, N. V. ; SHETH, S. R. ; LECKBAND, D. E.: Protein-Induced Changes in Poly(ethylene glycol) Brushes: Molecular Weight and Temperature Dependence. In: *Langmuir* 17 (2001), p. 7628–7636

[91] MCPHERSON, Timothy ; KIDANE, Argaw ; SZLEIFER, Igal ; PARK, Kinam: Prevention of Protein Adsorption by Tethered Poly(ethylene oxide) Layers: Experiments and Single-Chain Mean-Field Analysis. In: *Langmuir* 14 (1998), p. 176–186

[92] PASCHE, Stéphanie ; DE PAUL, Susan M. ; VÖRÖS, Janos ; SPENCER, Nicholas D. ; TEXTOR, Marcus: Poly(l-lysine)-graft-poly(ethylene glycol) Assembled Monolayers on Niobium Oxide Surfaces: A Quantitative Study of the Influence of Polymer Interfacial Architecture on Resistance to Protein Adsorption by ToF-SIMS and in Situ OWLS. In: *Langmuir* 19 (2003), p. 9216–9225

[93] MASSIA, S P. ; HUBBELL, J A.: An RGD spacing of 440 nm is sufficient for integrin alpha V beta 3-mediated fibroblast spreading and 140 nm for focal contact and stress fiber formation. In: *J. Cell. Biol.* 114 (1991), p. 1089–1100

[94] LI, Liang ; NØ RRELYKKE, Simon F. ; COX, Edward C.: Persistent Cell Motion in the Absence of External Signals: A Search Strategy for Eukaryotic Cells. In: *PLoS ONE* 3 (2008), p. e2093

[95] SAMBETH, R. ; BAUMGAERTNER, A.: Autocatalytic Polymerization Generates Persistent Random Walk of Crawling Cells. In: *Phys. Rev. Lett.* 86 (2001), p. 5196–5199

[96] VAN HAASTERT, Peter J. M.: A Model for a Correlated Random Walk Based on the Ordered Extension of Pseudopodia. In: *PLoS Comput Biol* 6 (2010), p. e1000874

[97] MAHESHWARI, Gargi ; WELLS, Alan ; GRIFFITH, Linda G. ; LAUFFENBURGER, Douglas A.: Biophysical Integration of Effects of Epidermal Growth Factor and Fibronectin on Fibroblast Migration. In: *Biophys. J.* 76 (1999), p. 2814–2823

[98] CHEN, Christopher S. ; MRKSICH, Milan ; HUANG, Sui ; WHITESIDES, George M. ; INGBER, Donald E.: Geometric Control of Cell Life and Death. In: *Science* 276 (1997), p. 1425–1428

[99] CLYMAN, R I. ; MCDONALD, K A. ; KRAMER, R H.: Integrin receptors on aortic smooth muscle cells mediate adhesion to fibronectin, laminin, and collagen. In: *Circulation Research* 67 (1990), p. 175–86

[100] LIBERIO, M. S. ; SADOWSKI, M. C. ; SOEKMADJI, C. ; DAVIS, R. A. ; NELSON, C. C.: Differential effects of tissue culture coating substrates on prostate cancer cell adherence, morphology and behavior. In: *PLoS One* 9 (2014), p. e112122

[101] CAVALCANTI-ADAM, E. A. ; AYDIN, D. ; HIRSCHFELD-WARNEKEN, V. C. ; SPATZ, J. P.: Cell adhesion and response to synthetic nanopatterned environments by steering receptor clustering and spatial location. In: *HFSP J* 2 (2008), p. 276–85

[102] COYER, S. R. ; SINGH, A. ; DUMBAULD, D. W. ; CALDERWOOD, D. A. ; CRAIG, S. W. ; DELAMARCHE, E. ; GARCIA, A. J.: Nanopatterning reveals an ECM area threshold for focal adhesion assembly and force transmission that is regulated by integrin activation and cytoskeleton tension. In: *J Cell Sci* 125 (2012), p. 5110–23

[103] A., Arrhenius S.: Über die Dissociationswärme und den Einflusß der Temperatur auf den Dissociationsgrad der Elektrolyte. In: *Z. Physik. Chem.* 4 (1889), p. 96–116

[104] HAYOT, C. ; DEBEIR, O. ; VAN HAM, P. ; VAN DAMME, M. ; KISS, R. ; DECAESTECKER, C.: Characterization of the activities of actin-affecting drugs on tumor cell migration. In: *Toxicol Appl Pharmacol* 211 (2006), no. 1, p. 30–40

[105] SAYYAD, W. A. ; AMIN, L. ; FABRIS, P. ; ERCOLINI, E. ; TORRE, V.: The role of myosin-II in force generation of DRG filopodia and lamellipodia. In: *Sci Rep* 5 (2015), p. 7842

[106] CHANG, S. S. ; GUO, W. H. ; KIM, Y. ; WANG, Y. L.: Guidance of cell migration by substrate dimension. In: *Biophys J* 104 (2013), no. 2, p. 313–21

[107] STYLE, R. W. ; BOLTYANSKIY, R. ; GERMAN, G. K. ; HYLAND, C. ; MACMINN, C. W. ; MERTZ, A. F. ; WILEN, L. A. ; XU, Y. ; DUFRESNE, E. R.: Traction force microscopy in physics and biology. In: *Soft Matter* 10 (2014), no. 23, p. 4047–55

[108] VAN HAASTERT, P. J.: A model for a correlated random walk based on the ordered extension of pseudopodia. In: *PLoS Comput Biol* 6 (2010)

[109] THÉRY, M. ; PEPIN, A. ; DRESSAIRE, E. ; CHEN, Y. ; BORNENS, M.: Cell distribution of stress fibres in response to the geometry of the adhesive environment. In: *Cytoskeleton* 63 (2006), p. 341–55

[110] PAWLIZAK, Steve ; FRITSCH, Anatol W. ; GROSSER, Steffen ; AHRENS, Dave ; THALHEIM, Tobias ; RIEDEL, Stefanie ; KIESSLING, Tobias R. ; OSWALD, Linda ; ZINK,

Mareike ; MANNING, M L. ; KÄS, Josef A.: Testing the differential adhesion hypothesis across the epithelial-mesenchymal transition. In: *New Journal of Physics* 17 (2015), no. 8, p. 083049

[111] FERIZI, M. ; LEONHARDT, C. ; MEGGLE, C. ; ANEJA, M. K. ; RUDOLPH, C. ; PLANK, C. ; RÄDLER, J. O.: Stability analysis of chemically modified mRNA using micropattern-based single-cell arrays. In: *Lab Chip* 15 (2015), p. 3561–3571

[112] FONSECA, Cristina ; SIMÕES, Sérgio ; GASPAR, Rogério: Paclitaxel-loaded PLGA nanoparticles: preparation, physicochemical characterization and in vitro anti-tumoral activity. In: *J. Control. Release* 83 (2002), p. 273–286

[113] KOMMAREDDY, Sushma ; AMIJI, Mansoor: Preparation and Evaluation of Thiol-Modified Gelatin Nanoparticles for Intracellular DNA Delivery in Response to Glutathione. In: *Bioconjugate Chem.* 16 (2005), p. 1423–1432

[114] JOSE, G. P. ; SANTRA, S. ; MANDAL, S. K. ; SENGUPTA, T. K.: Singlet oxygen mediated DNA degradation by copper nanoparticles: potential towards cytotoxic effect on cancer cells. In: *J. Nanobiotechnology* 9 (2011), p. 9

[115] BEXIGA, Mariana G. ; VARELA, Juan A. ; WANG, Fengjuan ; FENAROLI, Federico ; SALVATI, Anna ; LYNCH, Iseult ; SIMPSON, Jeremy C. ; DAWSON, Kenneth A.: Cationic nanoparticles induce caspase 3-, 7- and 9-mediated cytotoxicity in a human astrocytoma cell line. In: *Nanotoxicology* 5 (2011), p. 557–567

[116] WLODKOWIC, Donald ; SKOMMER, Joanna ; FALEY, Shannon ; DARZYNKIEWICZ, Zbigniew ; COOPER, Jonathan M.: Dynamic analysis of apoptosis using cyanine SYTO probes: From classical to microfluidic cytometry. In: *Exp. Cell Res.* 315 (2009), p. 1706–1714

[117] SUMMERS, Huw D. ; REES, Paul ; HOLTON, Mark D. ; ROWAN BROWN, M. ; CHAPPELL, Sally C. ; SMITH, Paul J. ; ERRINGTON, Rachel J.: Statistical analysis of nanoparticle dosing in a dynamic cellular system. In: *Nat Nano* 6 (2011), p. 170–174

[118] ANGUISSOLA, S. ; GARRY, D. ; SALVATI, A. ; OBRIEN, P. J. ; DAWSON, K. A.: High content analysis provides mechanistic insights on the pathways of toxicity induced by amine-modified polystyrene nanoparticles. In: *PLoS One* 9 (2014), p. e108025

[119] WARING, M. J.: Complex formation between ethidium bromide and nucleic acids. In: *Journal of Molecular Biology* 13 (1965), p. 269–282

[120] HUBER, M. D. ; GERACE, L.: The size-wise nucleus: nuclear volume control in eukaryotes. In: *J. Cell Biol.* 179 (2007), p. 583–4

[121] VANDENBERG, L. N. ; COLBORN, T. ; HAYES, T. B. ; HEINDEL, J. J. ; JACOBS, Jr. D. R. D. R. ; LEE, D. H. ; SHIODA, T. ; SOTO, A. M. ; SAAL, F. S. ; WELSHONS, W. V. ; ZOELLER, R. T. ; MYERS, J. P.: Hormones and endocrine-disrupting chemicals: low-dose effects and nonmonotonic dose responses. In: *Endocr Rev* 33 (2012), p. 378–455

[122] YEDJOU, Clement ; MOORE, Pamela ; TCHOUNWOU, Paul: Dose- and Time-Dependent Response of Human Leukemia (HL-60) Cells to Arsenic Trioxide Treatment. In: *International Journal of Environmental Research and Public Health* 3 (2006), p. 136–140

[123] SILVA, M. T.: Secondary necrosis: the natural outcome of the complete apoptotic program. In: *FEBS Lett* 584 (2010), p. 4491–9

[124] VANDEN BERGHE, T. ; GROOTJANS, S. ; GOOSSENS, V. ; DONDELINGER, Y. ; KRYSKO, D. V. ; TAKAHASHI, N. ; VANDENABEELE, P.: Determination of apoptotic and necrotic cell death in vitro and in vivo. In: *Methods* 61 (2013), p. 117–29

[125] GREGORY, Christopher D. ; POUND, John D. ; DEVITT, Andrew ; WILSON-JONES, Megan ; RAY, Parthasarathi ; MURRAY, Ruth J.: Inhibitory effects of persistent apoptotic cells on monoclonal antibody production in vitro: Simple removal of non-viable cells improves antibody productivity by hybridoma cells in culture. In: *mAbs* 1 (2009), p. 370–376

[126] MARINO, G. ; NISO-SANTANO, M. ; BAEHRECKE, E. H. ; KROEMER, G.: Self-consumption: the interplay of autophagy and apoptosis. In: *Nat Rev Mol Cell Biol* 15 (2014), no. 2, p. 81–94

[127] FULDA, S.: Cross talk between cell death regulation and metabolism. In: *Methods Enzymol* 542 (2014), p. 81–90

[128] YANG, Y. H. ; JOHNSON, J. D.: Multi-parameter single-cell kinetic analysis reveals multiple modes of cell death in primary pancreatic beta-cells. In: *J Cell Sci* 126 (2013), p. 4286–95

[129] WANG, F. ; BEXIGA, M. G. ; ANGUISSOLA, S. ; BOYA, P. ; SIMPSON, J. C. ; SALVATI, A. ; DAWSON, K. A.: Time resolved study of cell death mechanisms induced by amine-modified polystyrene nanoparticles. In: *Nanoscale* 5 (2013), p. 10868–76

[130] GARRIDO, C. ; GALLUZZI, L. ; BRUNET, M. ; PUIG, P. E. ; DIDELOT, C. ; KROEMER, G.: Mechanisms of cytochrome c release from mitochondria. In: *Cell Death Differ* 13 (2006), p. 1423–1433

[131] CIRCU, M. L. ; AW, T. Y.: Reactive oxygen species, cellular redox systems, and apoptosis. In: *Free Radic Biol Med* 48 (2010), p. 749–62

[132] REPNIK, U. ; CESEN, M. H. ; TURK, B.: The endolysosomal system in cell death and survival. In: *Cold Spring Harb Perspect Biol* 5 (2013), no. 1, p. a008755

[133] KIM, Jong A. ; ÅBERG, Christoffer ; CÁRCER, Guillermo de ; MALUMBRES, Marcos ; SALVATI, Anna ; DAWSON, Kenneth A.: Low Dose of Amino-Modified Nanoparticles Induces Cell Cycle Arrest. In: *ACS Nano* 7 (2013), no. 9, p. 7483–7494

[134] SPENCER, Sabrina L. ; GAUDET, Suzanne ; ALBECK, John G. ; BURKE, John M. ; SORGER, Peter K.: Non-genetic origins of cell-to-cell variability in TRAIL-induced apoptosis. In: *Nature* 459 (2009), p. 428–432

[135] GAUDET, S. ; SPENCER, S. L. ; CHEN, W. W. ; SORGER, P. K.: Exploring the contextual sensitivity of factors that determine cell-to-cell variability in receptor-mediated apoptosis. In: *PLoS Comput. Biol.* 8 (2012), p. e1002482

[136] ELDAR, Avigdor ; ELOWITZ, Michael B.: Functional roles for noise in genetic circuits. In: *Nature* 467 (2010), p. 167–173

[137] WARD, Carol ; ROSSI, Adriano G. ; HASLETT, Christopher ; DRANSFIELD, Ian: Apoptosis: future perspectives. In: *Essays In Biochemistry* 39 (2003), p. 155–162

[138] SAVILL, J. ; DRANSFIELD, I. ; GREGORY, C. ; HASLETT, C.: A blast from the past: clearance of apoptotic cells regulates immune responses. In: *Nat Rev Immunol* 2 (2002), no. 12, p. 965–75

[139] SEKHAVATI, Farzad: *Dynamic response of individual cells in heterogeneous population*, Ludwig-Maximilians-Universität, Thesis, 2015

## Associated Publications

1. Cellular Self-Organization on Microstructured Surfaces
   **P. J. F. Röttgermann, A. Piera Alberola, J. O. Rädler**
   Soft Matter, 2014, 10, 2397-2404, doi 10.1039/C3SM52419A

2. Cell Motility on Polyethylene Glycol Block Copolymers Correlates to Fibronectin Surface Adsorption.
   **P. J. F. Röttgermann[†], S. Hertrich[†], I. Berts, M. Albert, F. J. Segerer, JF. Moulin, B. Nickel, J. O. Rädler**
   Macromoleular Biosciences, 2014, 14, 1755–1763, doi 10.1002/mabi.201400246

3. Polyethylene Glycol Polymer Layers - Studies from Tethered Lipid Bilayers to Protein-Cell Interactions
   **P. J. F. Röttgermann, S. Hertrich, I. Berts, J. O. Rädler, B. Nickel**
   MLZ Report 2015

4. Versatile method to generate multiple types of micropatterns
   **F. J. Segerer, P. J. F. Röttgermann, S. Schuster, A. Piera-Alberola, S. Zahler and J. O. Rädler**
   Biointerphases, 2016, 11, 011005, doi 10.1116/1.4940703

5. Time-Resolved Study of Nanoparticle Induced Apoptosis Using Microfabricated Single Cell Arrays
   **P. J. F. Röttgermann, K. A. Dawson and J. O. Rädler**
   Microarrays, 2016, 2, 8, doi 10.3390/microarrays5020008

6. Highly Stable and Biocompatible DNA-Functionalized Gold Nanorods and their Use for Ultrafast Sequence-Selective DNA Melting
   **V. Baumann, P. J. F. Röttgermann, F. Haase, K. Szendrei, P. Dey, K. Lyons, R. Wyrwich, M. Gräßel, J. Stehr, L. Ullerich, F. Bürsgens, J. Rodríguez-Fernández**
   RSC Advances, 2016, under review

7. Stochastic Transitions and Relative Affinity of Single Cells on Double-Well Micropatterns
   **A. Fink[†], P. J. F. Röttgermann[†], C. P. Broedersz, J. O. Rädler,**
   in preparation

8. Time-Correlations of Single Cell Dual Fluorescence Markers - a Kinetic Fingerprint in Nanoparticle Induced Apoptosis
   **P. J. F. Röttgermann[†], A.-N. Murschhauser[†], D. Garry[†], M. F. Ober, D. Woschée, Yan Yan, K. A. Dawson, J. O. Rädler**
   in preparation

[†] equally contributed

# Publication1:
# Cellular Self-Organization on Microstructured Surfaces


http://dx.doi.org/10.1039/C3SM52419A

Soft Matter

PAPER

View Article Online
View Journal | View Issue



Cite this: *Soft Matter*, 2014, **10**, 2397

# Cellular self-organization on micro-structured surfaces†

Peter J. F. Röttgermann,* Alicia Piera Alberola and Joachim O. Rädler*

Received 13th September 2013
Accepted 23rd December 2013

DOI: 10.1039/c3sm52419a

www.rsc.org/softmatter

Micro-patterned surfaces are frequently used in high-throughput single-cell studies, as they allow one to image isolated cells in defined geometries. Commonly, cells are seeded in excess onto the entire chip, and non-adherent cells are removed from the unpatterned sectors by rinsing. Here, we report on the phenomenon of cellular self-organization, which allows for autonomous positioning of cells on micro-patterned surfaces over time. We prepared substrates with a regular lattice of protein-coated adhesion sites surrounded by PLL-*g*-PEG passivated areas, and studied the time course of cell ordering. After seeding, cells randomly migrate over the passivated surface until they find and permanently attach to adhesion sites. Efficient cellular self-organization was observed for three commonly used cell lines (HuH7, A549, and MDA-MB-436), with occupancy levels typically reaching 40–60% after 3–5 h. The time required for sorting was found to increase with increasing distance between adhesion sites, and is well described by the time-to-capture in a random-search model. Our approach thus paves the way for automated filling of cell arrays, enabling high-throughput single-cell analysis of cell samples without losses.

## Introduction

Important biological processes such as stem cell differentiation, gene expression and cell death are intrinsically stochastic as revealed by single-cell experiments.[1–6] Any given stimulus induces a broad distribution of responses in a cell population. The dynamics of these distributions amongst a population of individual cells under uniform conditions[7,8] can be quantified *via* single-cell arrays in which cells are positioned at regularly spaced sites in micro-wells or on chemically modified surfaces. These arrays allow automated acquisition of time-lapse series and efficient image analysis. Various ways of generating single-cell arrays have been reported. Most prominently, chemically micro-structured surfaces are used.[9,10] Cells are seeded on the substrate in excess and, after a short incubation time, the pattern is rinsed in order to remove non-adherent cells.[11–14] The difficulty resides in adjusting the initial cell concentration so that a single cell is left on each adhesive spot. The initial distribution of trapped cells per adhesive island is highly dependent on the seeding density. Another approach to create cell arrays uses micro-fluidic wells,[15–17] and the cell number per well is tuned by varying flow rate[18] or shear stress.[19] However, optimising occupancy levels by adjusting these parameters is tedious. Inkjet printing has also been used to create cell arrays.[20,21] However, this method suffers from low throughput[22,23] and low viability rates, as cells can be ruptured due to shear forces.[20,24] All these techniques try to achieve a higher occupancy rate than that given by the inherently stochastic process of sedimentation. The number of trapped cells per adhesive spot follows a Poisson distribution.[25–28] As a result, such arrays exhibit a broad distribution of cell numbers on the adhesive islands. For an expected value of $\lambda = 1$ (one cell per site), the maximal single-cell occupancy achievable is 37%.

In this article, we present a novel approach to the generation of single-cell arrays, utilizing cellular self-organization. Cells are seeded onto substrates patterned with protein-coated islands and separated by PLL-*g*-PEG passivated zones. The cells migrate to the passivated areas and spread onto the protein-coated sites upon contact. Thus, cells are sorted according to surface affinity and the population undergoes a transition from a spatially random distribution to an ordered array. Here, the phenomenon of cellular self-organization on micro-structured surfaces is systematically addressed. We quantify the time courses of occupancy levels using automated cell tracking. In addition, the correlation between lattice distance (distance between the centres of neighbouring sites) and filling rate is analysed, and the influence of cell motility is studied for three different cell lines (A549, HuH7, and MDA-MB-436). Finally, we describe the time-to-order onto the lattice sites by a simple model adapted from the physics of chemoreception.

## Materials and methods

### Cell culture

The A549 cell line (ATCC) was cultured in modified Eagle's medium with Earle's salts (c-c-pro) and 4 mM L-glutamine, the

*Fakultät für Physik, Ludwig-Maximilians-Universität, Geschwister-Scholl-Platz 1, 80539 Munich, Germany. E-mail: peter.roettgermann@physik.lmu.de; raedler@lmu.de; Fax: +49 89 2180 3182; Tel: +49 89 2180 2438*

† Electronic supplementary information (ESI) available. See DOI: 10.1039/c3sm52419a

HuH7 cell line (I.A.Z Toni Lindl GmbH) was cultured in Dulbecco's modified Eagle's medium with 4.5 g $L^{-1}$ glucose, 110 mg $L^{-1}$ sodium pyruvate (c-c-pro) and 2 mM L-glutamine, and MDA-MB-436 (ATCC) cells were grown in modified Eagle's medium and Ham's F12 (c-c-pro) with 2.5 mM L-glutamine. All cell media were supplemented with 10% fetal calf serum (FCS). The cells were cultured at 37 °C, with 5% $CO_2$ in an incubator. Cells were grown to 70–80% confluence, trypsinized (A549 and HuH7) or scraped off (MDA-MB-436) and centrifuged at 1000 rpm for 3 min. Cell pellets were resuspended in either cell medium or, for the experiments, in Leibovitz's L15 medium with GlutaMAX (Gibco) and 10% FCS to provide optimal growth conditions. The seeding density was determined using a Neubauer counting chamber. To track nuclei, cells were stained with the permeable fluorescent dye Hoechst 33342 (Life Technologies) by adding 25 nM dye to the suspension (incubation at 37 °C for 20 min).

### Surface patterning and sample preparation

The micro-structured surfaces were produced by selective oxygen plasma treatment (Femto Diener, 40 W for 3 min) on a Topas substrate (μ-dishes ibidi GmbH) with subsequent passivation. Selectivity was achieved using a polydimethylsiloxane (PDMS) stamp (cast from a master produced by photolithography) as a mask. The parts exposed to plasma were passivated with PLL(20k)-*g*(3.5)-PEG(2k) (SuSoS AG) at 1 mg $ml^{-1}$ in aqueous buffer (10 mM HEPES pH 7.4 and 150 mM NaCl). The remaining sectors were rendered cell adherent by exposure to 50 μg $ml^{-1}$ fibronectin (YoProteins) for 1 h. The probes were thoroughly rinsed with PBS; before cell seeding the samples were stored in cell medium at room temperature.

PLL-*g*-PEG surfaces without patterns were treated in the same way. 30 μm × 30 μm square adhesion sites were used, as this size turned out to be reasonable for single-cell adhesion of all three cell lines. Cells were seeded to achieve a filling of roughly one cell per adhesion site (*e.g.* for a lattice distance of 90 μm, 65 000 cells were seeded into a μ-dish). The micropattern shown in Fig. 1B was formed using a mixture of 20 μg $ml^{-1}$ fibronectin and 30 μg $ml^{-1}$ fibrinogen conjugated with Alexa Fluor 488 (Life Technologies).

### Time-resolved fluorescence microscopy

Images were taken with an iMIC digital microscope with phase contrast (TILL Photonics) and a Zeiss objective (10× Ph1 0.3 EC Plan Neofluar). Samples were kept at a constant temperature of 37 °C with an ibidi heating system (ibidi GmbH). Fluorescently labelled nuclei were imaged with an oligochrome light source (TILL Photonics) in combination with a single-band long-pass DAPI HC filter set (AHF Analysetechnik). Pictures were recorded every 10 min over a period of 24 h.

### Image and data analysis

Raw images were pre-processed in ImageJ: the background was subtracted with a built-in function. To highlight the nuclei, a band-pass filter was applied. Images were binarized by setting a global threshold. Binarized images were clustered and tracked with a cell evaluator.[29] Coordinates of the centre of mass and the area of nuclei were extracted and analysed in MATLAB. The position of the micro-structured lattice was evaluated from the bright-field images for every marker position. Every experiment was repeated at least twice. 20 to 50 image positions were evaluated for each distance and cell line. The mean of all positions was used for the occupancy statistics. The filling factor in Fig. 3B was normalized to the cell density to compare the different lattice distances.

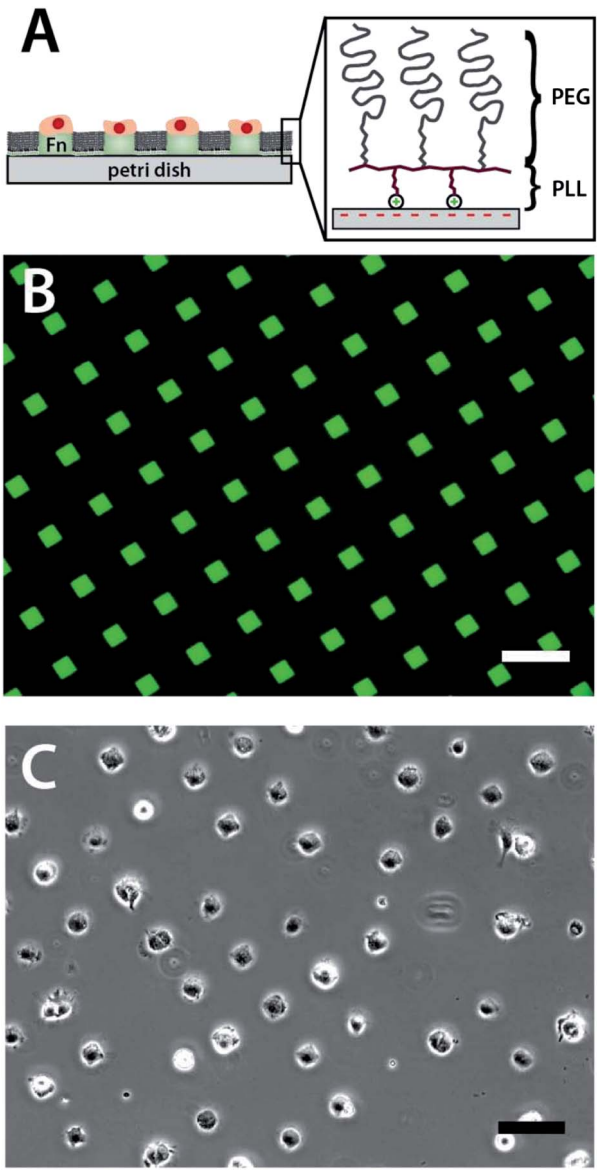


Fig. 1 Patterning technique. (A) A micro-structured surface was created by plasma-induced patterning with a backfill on a Topas surface. Plasma-treated areas were incubated with PLL(20k)-*g*(3.5)-PEG(2k) (A). PEG-free areas were coated with fibronectin (Fn, green). (B) Homogeneous square pattern of fibronectin and labelled Alexa Fluor 488 fibrinogen. (C) After seeding, cells arrange themselves onto the protein-coated islands, obviating the need for any washing steps. Scale bars: 100 μm.

 

### Cell motility analysis

The mean square displacement was calculated as

$$\mathrm{MSD}(t) = \langle\langle(\boldsymbol{X}_i(t + t_0) - X_i(t_0))^2\rangle_{t_0}\rangle_i \quad (1)$$

where $\boldsymbol{X}_i(t)$ denotes the centre of cell $i$ at time $t$. $\langle\cdot\rangle_{t_0}$ designates the mean of the reference frame $t_0$ over all times $t$. $\langle\cdot\rangle_i$ is the average over all tracked cells. Dead cells, as well as nuclei exceeding a maximal area (indication of two fused cells), were excluded from analysis. For every cell line at least 100 tracks were analysed. Cell motility was defined by the effective diffusion constant $D$ in two dimensions defined as

$$\mathrm{MSD}(t) = 4Dt. \quad (2)$$

The standard deviation was calculated from the cell motility of different fitted endpoints.

### Poisson distribution analysis

The Poisson distribution is stated as:

$$P(k) = \frac{\lambda^k}{k!}\, e^{-\lambda} \quad (3)$$

where $k$ is the occupation number ($k = 0, \ldots, 4$) and $\lambda$ the expected value. The initial number of cells in one image position was counted. Division of this number by a mesh-grid of 45 × 45 μm (adhesion site + cell radius) defines the expected value $\lambda$. The added deviation from the calculated distribution was averaged over all measured positions.

## Results and discussion

### Cell migration on micro-structured surfaces

We generated patterns of fibronectin-coated square adhesion sites (30 μm × 30 μm) and passivated PLL-*g*-PEG spacings on a Petri dish as described in the Materials and methods Section and schematically shown in Fig. 1A. The coating procedure described here yields an essentially homogeneous protein distribution, as revealed by the homogeneity of the fluorescent spots obtained using an Alexa 488-labelled fibrinogen coating as can be seen in Fig. 1B. Cells were seeded onto micro-patterned sites with various lattice spacings, and time-lapse series were recorded using fluorescence and phase-contrast microscopy. After 3–5 h, and without any washing steps, a regular single-cell array with a negligible number of misplaced cells was obtained (Fig. 1C).

To illustrate the self-organization process we describe it step by step for the adenocarcinoma cell line A549 as a representative example (see also Movie S7†): the sedimentation process after seeding takes about 20 min, and the cells are randomly distributed at this stage (Fig. 2A, 0 h). Cells that initially settle on PLL-*g*-PEG passivated areas begin to migrate in a random manner (Fig. 2B, 0–210 min). When a cell makes contact with the edge of an adhesion site (Fig. 2B, 210 min), it spreads onto it and fills the entire adhesion area within 30 min (Fig. 2B, 220–250 min). In the absence of perturbations, such as cell division events or intruding cells, cells remain captive on the adhesion sites (Fig. 2B, 310 min). With time, more and more adhesion sites are occupied (Fig. 2A, 2–24 h). Ideally, each cell would find a free adhesion site and all sites would eventually be singly occupied. Experimentally, we find certain deviations from this ideal scenario: multiple occupancies, unoccupied sites (vacancies) and interstitial cells. Multiple occupancies can be caused if a single cell, already occupying an adhesion site, divides or different cells arrive at the same adhesion site. We observe that multiple occupancies can be self-corrected by the cells if the lattice distance is less than the cells' specific reaching distance, which is defined as the maximal distance to which cells can extend the filopodia without leaving their adhesion site (Fig. S1A†). If the next available site lies beyond this distance, the defect cannot be self-corrected and cells are likely to stay on the same site (Fig. S1C†). We observe up to four cells occupying a single site. The reduced accessibility to the proteins on the substrate causes such cells to increase in height. Other rare events are described in the ESI.†

### Quantifying cellular self-organization *via* order parameters

In order to assess the dependence of the ordering process on elapsed time, we quantify the occupancy level. The fraction of maximally occupied sites depends on the initial number of cells per area and the lattice spacing. In the following, the initial cell density is roughly adjusted to the number of available sites. The lattice distance $d_l$ is varied from 70 μm to 230 μm. If a cell is positioned on a site, this site is identified as "filled", as illustrated in Fig. 3A. The occupancy level can now be described by a filling factor $F(t)$, which is the ratio of occupied sites $N_{OC}$ to the total number of sites $N_S$: $F(t) = N_{OC}/N_S$. For the A549 cells, we observed the highest filling rate, about 80%, for $d_l = 90$ μm after 24 h and the poorest occupancy level was obtained for $d_l = 230$ μm (25% after 24 h). However, the shortest filling time of 15 h was measured for the smallest distance $d_l = 70$ μm. For all lattices the initial occupation numbers are in good agreement with a random deposition model as described by a Poisson distribution (eqn (3)). The measured occupancy deviates by only 2–6% from the theoretically calculated Poisson distribution (Fig. S2†).

In the following, we describe the frequency of array irregularities, *i.e.* vacancies, interstitial cells and multiple occupations, as they occur during the self-ordering process (Fig. 3A).

Vacancies (unoccupied sites) are accounted for in the filling factor. Cells which have not yet found an adhesion site or have died are defined as interstitial. For the interstitial cells we introduce a defect parameter $I(t)$, which defines the ratio of interstitial cells $N_{IS}$ to the total number of cells $N_C$: $I(t) = N_{IS}/N_C$. As shown in Fig. 3C, where the time course of the interstitial cell number is plotted, the curves saturate at different values: for $d_l = 70$ μm, only 10% of the cells are misplaced after 24 h. For larger lattice distances, the ratio of misplaced cells increases drastically, reaching 80% for $d_l = 230$ μm. In addition, the number of dead cells strongly increases with the lattice size, as cells that do not find an adhesion site within a day have a low survival rate.

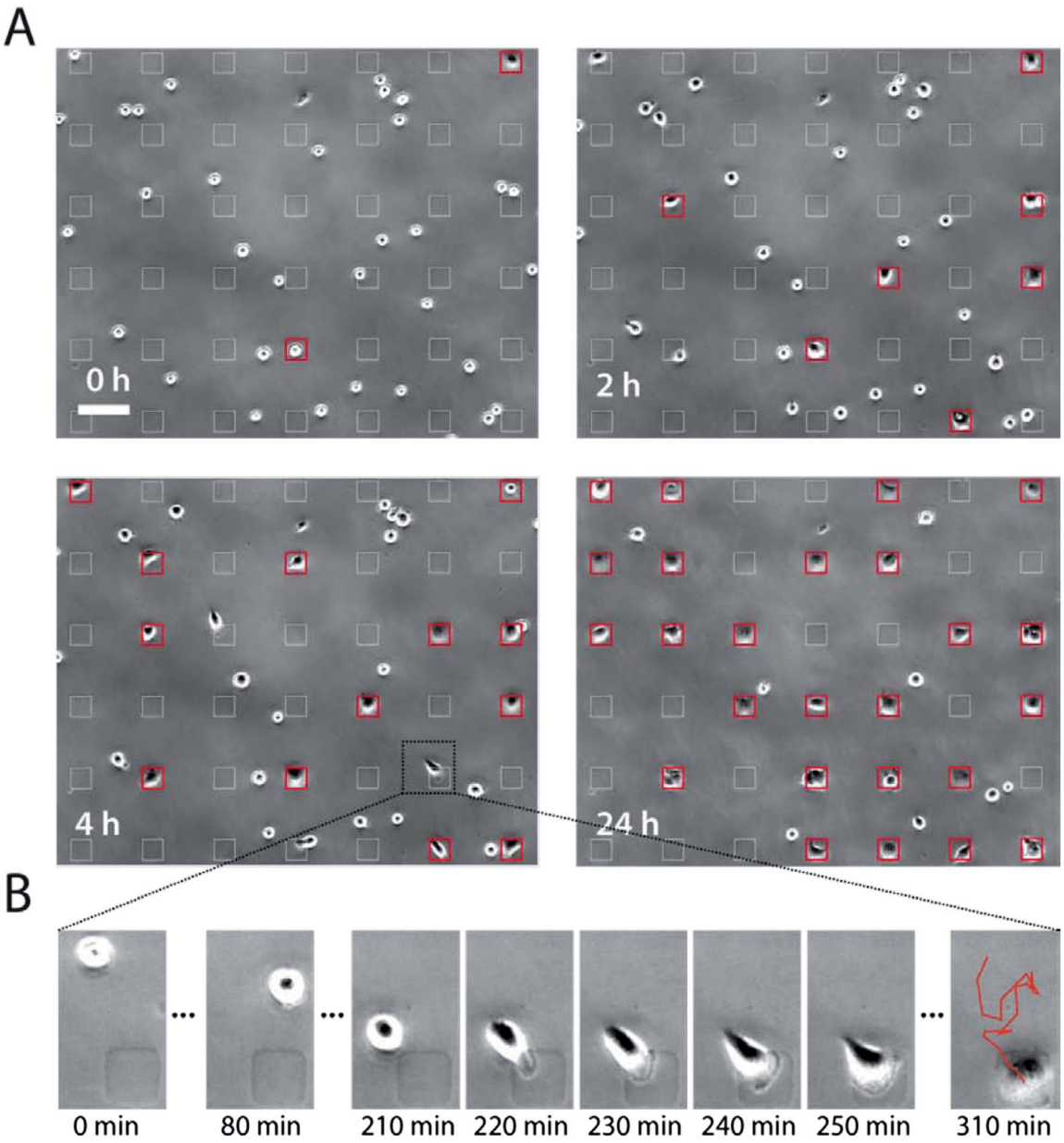


Fig. 2 Dynamics of cellular self-organization. (A) Selected images of the self-organization process during a time-lapse measurement. After cell seeding, cells are randomly distributed. They start to migrate randomly until they find adhesion sites. Gradually, an ordered distribution is obtained. Occupied sites are highlighted in red. Scale bar: 100 μm (B). Detailed view of an adhesion process (3× magnification). The red track represents the trajectory of the cell.

Our second defect parameter, $M(t)$, describes the case of multiple occupancies, which is defined as the ratio of multiply occupied sites $N_{MOC}$ to the total number of occupied sites $N_{OC}$: $M(t) = N_{MOC}/N_{OC}$. No clear dependency of $N_{MOC}$ on the lattice distance was observed (Fig. 3D). For all lattice sizes, $N_{MOC}$ is rather low, ranging from 10 to 20%. For $d_l = 70$ μm, a slight decrease over time can be observed. For this short lattice distance, cells are most probably able to explore their environment with their filopodia. Thus, the cells can more easily find and invade empty neighbouring sites, which reduces multiple occupancies. After 24 h, $N_{MOC}$ can be expected to increase strongly due to cell proliferation.

### Universal cell behaviour of self-organization

To demonstrate that the self-organization process is a generic behaviour of different cell types, we evaluated the aforementioned order parameters for two further cell lines: the hepatocellular carcinoma cell line HuH7 and the mammary-gland cancer cell line MDA-MB-436. As the spreading areas for these cell lines are basically comparable, the same sizes for the square adhesion sites are used. The phenomenon of cellular self-organization remains unchanged (Fig. S3†). However, as these cells have different properties with regard to adhesion strength, motility and viability, differences in the order parameters were

 

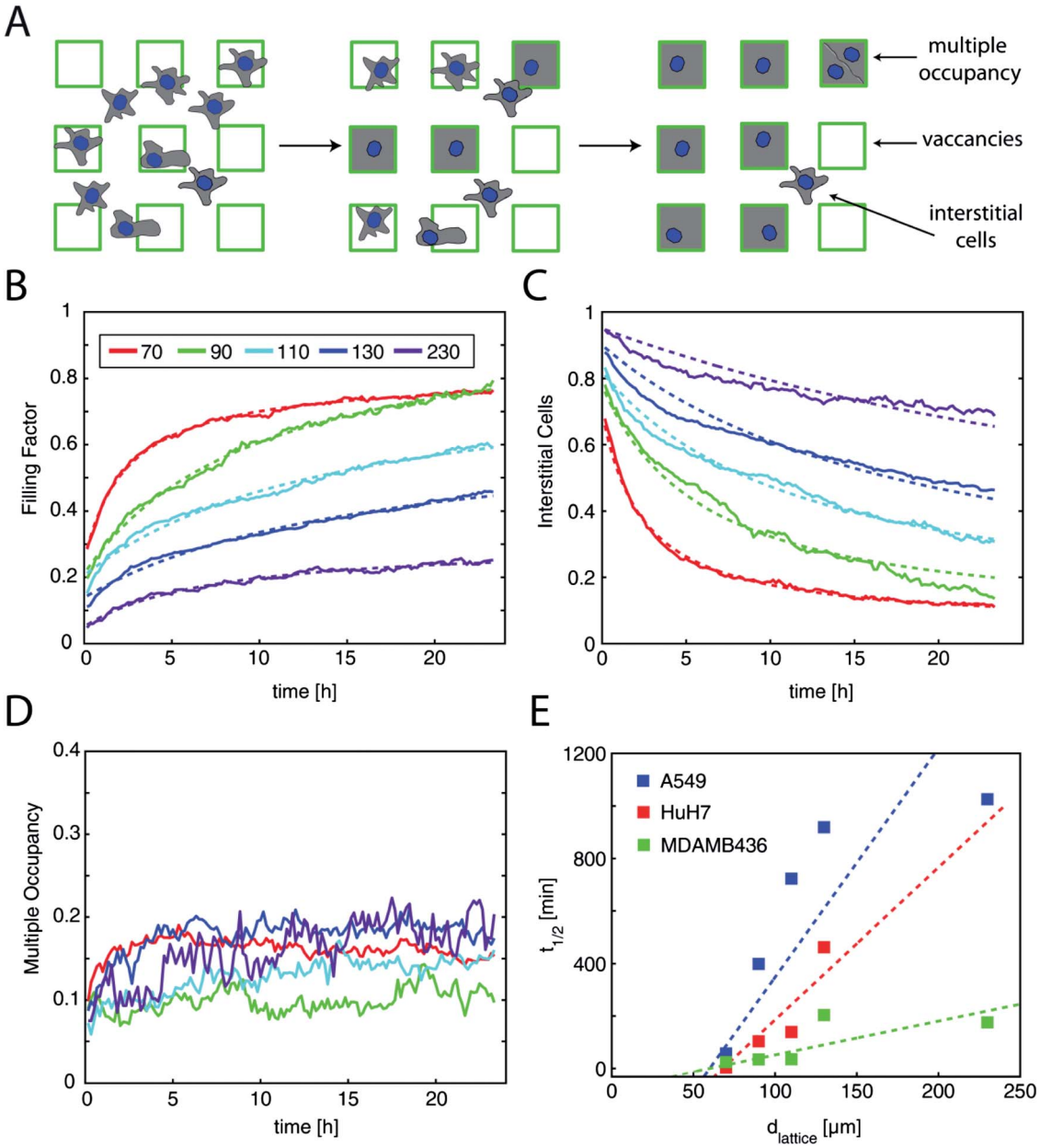


Fig. 3 Dependence of order parameters on lattice spacing. (A) During the self-organization process, optimal filling is compromised by defects such as multiple occupancies, vacancies and interstitial cells. Occupancy is quantified *via* order parameters: (B) the filling factor describes the ratio of occupied lattice sites to the total number of sites. For A549 the highest filling of 80% for a lattice distance of $d_l = 90$ µm is obtained. (C) The parameter interstitial cells denote the ratio of misplaced to total cells. Misplaced cells after 24 h are either dead cells or cells which have not yet found a site. (D) The ratio of multiply occupied sites to total occupied sites is denoted by the multiple occupancy parameter. No clear correlation with the lattice distance was observed. (E) Times for half-maximal filling ($t_{1/2}$, eqn (4)) are plotted against the lattice distance for three different cell lines (A549, HuH7, and MDA-MB-436) with dashed guidelines for the eye. MDA-MB-436 cells showed the smallest $t_{1/2}$ values.

measured. HuH7 showed the lowest initial number of interstitial cells (Fig. S3B†). This can be explained by faster adhesion and spreading to the surface compared to the other cell lines. In Fig. S4,† the distribution of the initial distance covered by motile cells is illustrated after 50 min. On average, HuH7 cells have migrated further than A549, although both exhibit similar cell motilities. Thus, HuH7 must start to migrate earlier, and this can be attributed to their faster adhesion. Apart from this, HuH7 behaved very similarly to A549. For MDA-MB-436, the overall filling was lower than for A549 (Fig. S3D†). A lattice distance of 70 µm was too small for MDA-MB-436, as cells tended to form bridges adhering to two sites simultaneously (Fig. S1B†). Small distances also favoured constant cell migration from one site to another. A larger number of defects (interstitial cells) was observed for MDA-MB-436, and may be attributable to their lower viability on PEG surfaces (Fig. S3E†). Furthermore, a higher incidence of multiple occupancies was found for MDA-MB-436 from the beginning of the experiment

(Fig. S3F†). This observation can be explained by the fact that these cells could not be trypsinized, but were scraped from plates prior to seeding, and thus were not individualized as efficiently, resulting in only 73% separated single cells *vs.* 90% for A549 (Fig. S5†). To compare the different cell line's filling rates, the time courses of the filling factors $F(t)$ were fitted to the following phenomenological expression:

$$F\ (t) = F_0 + \frac{F_{\max}}{1\ +\ t_{1/2}/t} \tag{4}$$

The offset $F_0$ quantifies the sites already occupied at $t = 0$. The coefficient of $F_{\max}$ describes the lattice-dependent saturation value of the filling factor. $t_{1/2}$ denotes the time at which $F$ reaches half of $F_{\max}$. The fitted $t_{1/2}$ values for all lattice distances are plotted in Fig. 3E. The data points show a clear tendency towards increasing filling rates as a function of increasing lattice spacing $d_l$. The shortest $t_{1/2}$ values are obtained for MDA-MB-436, which is consistent with their high motility.

To assess if cell size differences have an influence on filling, cell spreading on the PLL-*g*-PEG surface was analysed (Fig. S6†). The major diameter rather than the spreading area was taken into account, as it better reflects the reaching distance of elongated cells. In comparison to a fibronectin-coated surface the major diameter is decreased twofold for A549 and HuH7 and nearly fourfold for MDA-MB-436. Since the adhesion spots are limited, all cell types can only occupy comparably small and similar areas. Thus, the cell specific spreading area has no impact on the filling of the lattice.

## Mean time to settle

Since the self-organization process is a generic phenomenon that depends on the lattice spacing and cell motility, we set out to find a simple model that reveals the time-to-order on a cell chip. How do cells find a lattice site? We adapted the model of chemoreception from Berg and Purcell,[30,31] which describes the time needed for a ligand to find a cell surface receptor. Once ligands are attached to the surface of a cell they are assumed to diffuse freely within a membrane until they encounter receptors that are modelled as circular patches. In our case, cells migrate in a random walk on the micro-structured surface $A_{IMG}$, the field of view of the camera, until they contact adhesion sites of length $s$ (Fig. 4A). We treat our square adhesion sites as circular shapes and employ the analytical expression ($Ns^2 \ll A_{IMG}$) for the mean-time to capture derived by Berg and Purcell:

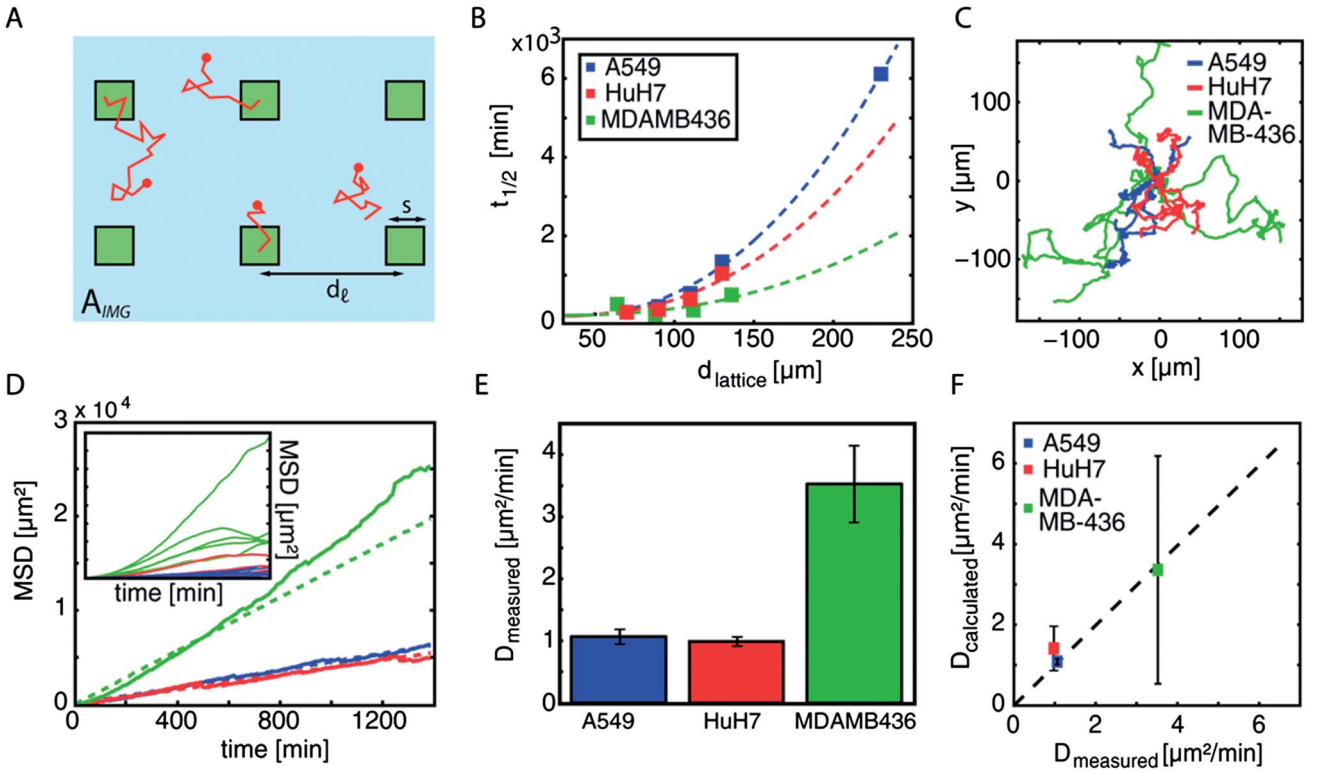


Fig. 4 Mean time to settle. (A) On an image area $A_{IMG}$ (light blue), adhesion sites of size $s$ (green) are distributed in a rectangular lattice with spacing $d_l$. The search process for single cells is depicted by the red trajectories. (B) The best fit $t_{1/2}$ values obtained by fitting the decay curves for the parameter interstitial cells to eqn (6) are plotted as a function of spacing $d_l$. The cell settling process as described by a model adapted from Berg and Purcell (eqn (5)) is in good agreement with these data (dashed lines). (C) Representative trajectories for cells of all three lines migrating on non-patterned PLL-*g*-PEG are shown. (D) Inset: MSDs of the trajectories in (C) are plotted against time. The averaged MSDs of 100 cell tracks per cell line can be described by a 2D random walk. (E) Fitting $D_{measured}$ reveals motilities of 1.1 ± 0.1 µm$^2$ min$^{-1}$ (A549), 1.0 ± 0.05 µm$^2$ min$^{-1}$ (HuH7) and 3.5 ± 0.6 µm$^2$ min$^{-1}$ (MDA-MB-436). (F) The motilities $D_{calculated}$ from (B) are plotted against the motilities $D_{measured}$ in (E). The model is in good agreement with the measured motilities (correlation of 0.987), error bars correspond to 95% confidence limits of the fit in (B).

 

$$\overline{t_{1/2}(d_l)} = \frac{1.1\ A_{IMG}}{8\pi\ N(d_l)\ D} \ln\left(\frac{1.2\ A_{IMG}}{4\ N(d_l)\ s^2}\right) \quad (5)$$

To compare experiment and theory, the $t_{1/2}$ values were derived from the experimentally measured, time-dependent decay curves for the interstitial cell number (Fig. 3C, S3B and E†):

$$I(t) = I_0 + \frac{I_0 - I_{min}(d_l = 70)}{1\ +\ t_{1/2}/t} \quad (6)$$

$I_0$ is the offset at $t = 0$. To compare the $t_{1/2}$ values for all lattice distances, the same ratio of interstitial cells, $I_{min}$ of $d_l =$ 70 μm, was assumed, neglecting different saturation levels due to cell death. In Fig. 4B, the $t_{1/2}$ values, obtained by the fits to eqn (6), are plotted as a function of the lattice spacing. The model is found to be in good agreement with the data.

To check that the motilities evaluated from the model are consistent with the measured values, single cell tracks were recorded on PLL-*g*-PEG coated surfaces without patterns. The mean square displacements (MSD) were calculated assuming diffusive behaviour, neglecting persistent cell motion or biased random walk[32–34] (Fig. 4D). Eqn (2) yielded motilities of 1.1 ± 0.1 μm$^2$ min$^{-1}$ for A549, 1.0 ± 0.05 μm$^2$ min$^{-1}$ for HuH7 and 3.5 ± 0.6 μm$^2$ min$^{-1}$ for MDA-MB-436 (Fig. 4E). For all cell lines, these values are in excellent agreement with the motilities derived from the model adapted from Berg and Purcell (Fig. 4F). This result could be expected since we assumed diffusive behaviour of the cells in the first place, but it nevertheless demonstrates that our model allows one to calculate the mean time to order, $t_{1/2}$ for any given lattice distance using a single parameter, the motility value for the cell line of interest.

### Optimal lattice geometry

Having modelled the settling of cells as a diffusive search process, we can finally address which lattice geometry is optimal. Taking all order parameters into account, the best filling can be achieved for a geometry with $d_l = 90$ μm. Here, a single-cell occupancy level of 20% at the beginning, 45% after 5 h and 75% after 24 h was obtained for A549 – a 3.5-fold increase in filling rate over 24 h. Similar values were measured for HuH7, with an initial occupancy of 31%, rising to 54% at 5 h and 59% after 24 h. The initial occupancy for MDA-MB-436 was 24%, rising to 40% after 5 h and 42% at 24 h. For both cell lines, the final filling rates are approximately twice as high as the initial ones. Based on the time course of occupation, it should be possible to reduce the incubation time to 5 h and still obtain reasonable filling. A shorter incubation period is desirable because it prolongs the available time window for single-cell measurements before cell division occurs. This is especially important for cells with high proliferation rates.

Given the motility of a certain cell line, an initial estimate of the best lattice spacing can be made. However, individual cell properties that can complicate the picture must also be taken into account in order to optimize the cell ordering process. These factors include the strength of cell adhesion, viability and cell area on the PEG surface. For example, the largest occupancy and fastest filling for highly motile cells like MDA-MB-436 is obtained for $d_l = 70$ μm, albeit at the cost of more defects. These cells tend to form bridges between two adhesion sites and are in constant movement. In addition, the transfer of cells between neighbouring sites is favoured for small distances. Conversely, if the lattice distance becomes too large, self-ordering becomes inefficient, as filling time as well as cell death increases. Thus, to obtain a single cell array *via* self-organization under reasonable conditions, the lattice distance has to be chosen in an appropriate range.

## Conclusion

In comparison to common procedures used to create single-cell arrays, we have shown here that seeding by cellular self-organization offers several advantages. All input cells can be analysed, as this method avoids a washing step after seeding. The cellular self-organization procedure is especially useful for cell types, *e.g.* rare stem cells, that are available only in limited numbers.[35,36] As an example, in preliminary experiments we have also observed the self-organising process with mesenchymal stem cells (data not shown). Since a washing step might selectively influence the heterogeneity of surface adhesion,[37–39] our assay can also be applied to weakly adherent cells that need more time to settle down. Having to wait several hours for self-organization might seem to be incompatible with high-throughput studies, but commonly used approaches also require 2 to 15 h to allow cells to adhere on the substrate.[13,40]

We presented a theoretical model that describes the generic cell ordering behaviour. The occupation of a regular lattice of adhesion sites follows a random-walk search process. The time-to-order describes the characteristic time-scale needed for a randomly seeded population of cells to arrange themselves on the predefined lattice. High-throughput, single-cell time-lapse analysis requires chips on which isolated cells are positioned at defined sites to facilitate automated image analysis. Hence, a high level of site occupancy and a small number of displaced cells must be achieved after short incubation. For optimal single-cell filling, small distances should be preferred because of faster filling rates. In principle the model allows for optimization of the time-to-order for a specific cell type by rescaling the distances between the adhesion sites, taking the measured cell motility into account.

Beyond that, we reported on several phenomena, such as bridging and multiple occupancies, that limit the densities of adhesion sites that can be achieved in practice. The short-scaled behaviours are interesting in their own rights in terms of cell-to-cell communication and open opportunities for further studies in the future. We also showed that various cell lines are capable of self-ordering in our system. Hence, we believe that cellular self-organization is a robust procedure and is applicable in a variety of cell-based assays.

## Acknowledgements

Financial support by the Deutsche Forschungsgemeinschaft (DFG) *via* project B1 within the SFB 1032, the Excellence Cluster

'Nanosystems Initiative Munich (NIM)', the Center for Nano-Science (CeNS), FP7 EU grants NanoTransKinetics and Nano-MILE is gratefully acknowledged. We would like to thank Susanne Seidel and Paul Hardy for critical reading and correcting the manuscript.

## Notes and references

1 D. Muzzey and A. van Oudenaarden, *Annu. Rev. Cell Dev. Biol.*, 2009, **25**, 301–327.
2 D. D. Carlo and L. P. Lee, *Anal. Chem.*, 2006, **78**, 7918–7925.
3 M. P. Lutolf, P. M. Gilbert and H. M. Blau, *Nature*, 2009, **462**, 433–441.
4 M. Halter, A. Tona, K. Bhadriraju, A. L. Plant and J. T. Elliott, *Cytometry, Part A*, 2007, **71**, 827–834.
5 M. Théry, *J. Cell Sci.*, 2010, **123**, 4201–4213.
6 T. Eißing, F. Allgöwer and E. Bullinger, *IEE Proc.: Syst. Biol.*, 2005, **152**, 221.
7 M. L. Yarmush and K. R. King, *Annu. Rev. Biomed. Eng.*, 2009, **11**, 235–257.
8 M. A. Walling and J. R. E. Shepard, *Chem. Soc. Rev.*, 2011, **40**, 4049–4076.
9 G. M. Whitesides, E. Ostuni, S. Takayama, X. Jiang and D. E. Ingber, *Annu. Rev. Biomed. Eng.*, 2001, **3**, 335–373.
10 G. Csucs, R. Michel, J. W. Lussi, M. Textor and G. Danuser, *Biomaterials*, 2003, **24**, 1713–1720.
11 C. G. Rolli, H. Nakayama, K. Yamaguchi, J. P. Spatz, R. Kemkemer and J. Nakanishi, *Biomaterials*, 2012, **33**, 2409–2418.
12 A. Azioune, M. Storch, M. Bornens, M. Thery and M. Piel, *Lab Chip*, 2009, **9**, 1640–1642.
13 Y. V. Pan, T. C. McDevitt, T. K. Kim, D. Leach-Scampavia, P. S. Stayton, D. D. Denton and B. D. Ratner, *Plasmas Polym.*, 2002, **7**, 171–183.
14 J. Fink, M. Thery, A. Azioune, R. Dupont, F. Chatelain, M. Bornens and M. Piel, *Lab Chip*, 2007, **7**, 672–680.
15 C. P. Jen, J. H. Hsiao and N. A. Maslov, *Sensors*, 2012, **12**, 347–358.
16 J. R. Rettig and A. Folch, *Anal. Chem.*, 2005, **77**, 5628–5634.
17 K. Chung, C. A. Rivet, M. L. Kemp and H. Lu, *Anal. Chem.*, 2011, **83**, 7044–7052.
18 H. Yin, X. Zhang, N. Pattrick, N. Klauke, H. C. Cordingley, S. J. Haswell and J. M. Cooper, *Anal. Chem.*, 2007, **79**, 7139–7144.
19 H. Lu, L. Y. Koo, W. M. Wang, D. A. Lauffenburger, L. G. Griffith and K. F. Jensen, *Anal. Chem.*, 2004, **76**, 5257–5264.
20 A. Yusof, H. Keegan, C. D. Spillane, O. M. Sheils, C. M. Martin, J. J. O'Leary, R. Zengerle and P. Koltay, *Lab Chip*, 2011, **11**, 2447–2454.
21 A. R. Liberski, J. T. Delaney and U. S. Schubert, *ACS Comb. Sci.*, 2010, **13**, 190–195.
22 D. J. Odde and M. J. Renn, *Biotechnol. Bioeng.*, 2000, **67**, 312–318.
23 D. J. Odde and M. J. Renn, *Trends Biotechnol.*, 1999, **17**, 385–389.
24 B. R. Ringeisen, C. M. Othon, J. A. Barron, D. Young and B. J. Spargo, *Biotechnol. J.*, 2006, **1**, 930–948.
25 K. Ino, M. Okochi, N. Konishi, M. Nakatochi, R. Imai, M. Shikida, A. Ito and H. Honda, *Lab Chip*, 2008, **8**, 134–142.
26 S. Gobaa, S. Hoehnel, M. Roccio, A. Negro, S. Kobel and M. P. Lutolf, *Nat. Methods*, 2011, **8**, 949–955.
27 S. Kobel and M. Lutolf, *BioTechniques*, 2010, **48**, ix–xxii.
28 L.-I. Lin, S.-h. Chao and D. R. Meldrum, *PLoS One*, 2009, **4**, 1–5.
29 S. Youssef, S. Gude and J. O. Rädler, *Integr. Biol.*, 2011, **3**, 1095–1101.
30 H. C. Berg and E. M. Purcell, *Biophys. J.*, 1977, **20**, 193–219.
31 G. Adam and M. Delbrück, ed. A. Rich and N. Davidson, *Reduction of dimensionality in biological diffusion processes* in *Structural chemistiy and molecular biology*, W.H. Freeman & Company, San Francisco, Calif., 1968, pp. 198–215.
32 A. A. Potdar, J. Lu, J. Jeon, A. M. Weaver and P. T. Cummings, *Ann. Biomed. Eng.*, 2009, **37**, 230–245.
33 E. A. Codling, M. J. Plank and S. Benhamou, *J. R. Soc. Interface*, 2008, **5**, 813–834.
34 M. H. Gail and C. W. Boone, *Biophys. J.*, 1970, **10**, 980–993.
35 S. Roy, P. Gascard, N. Dumont, J. Zhao, D. Pan, S. Petrie, M. Margeta and T. D. Tlsty, *Proc. Natl. Acad. Sci. U. S. A.*, 2013, **110**, 4598–4603.
36 G. Shi, W. Cui, M. Benchimol, Y. T. Liu, R. F. Mattrey, R. Mukthavaram, S. Kesari, S. C. Esener and D. Simberg, *PLoS One*, 2013, **8**, 1–9.
37 A. E. van Merode, H. C. van der Mei, H. J. Busscher and B. P. Krom, *J. Bacteriol.*, 2006, **188**, 2421–2426.
38 J. Y. Park, M. A. Arnaout and V. Gupta, *J. Biomol. Screening*, 2007, **12**, 406–417.
39 A. Saterbak, S. C. Kuo and D. A. Lauffenburger, *Biophys. J.*, 1993, **65**, 243–252.
40 J. Nakanishi, Y. Kikuchi, T. Takarada, H. Nakayama, K. Yamaguchi and M. Maeda, *Anal. Chim. Acta*, 2006, **578**, 100–104.

 

# Supplementary Information:

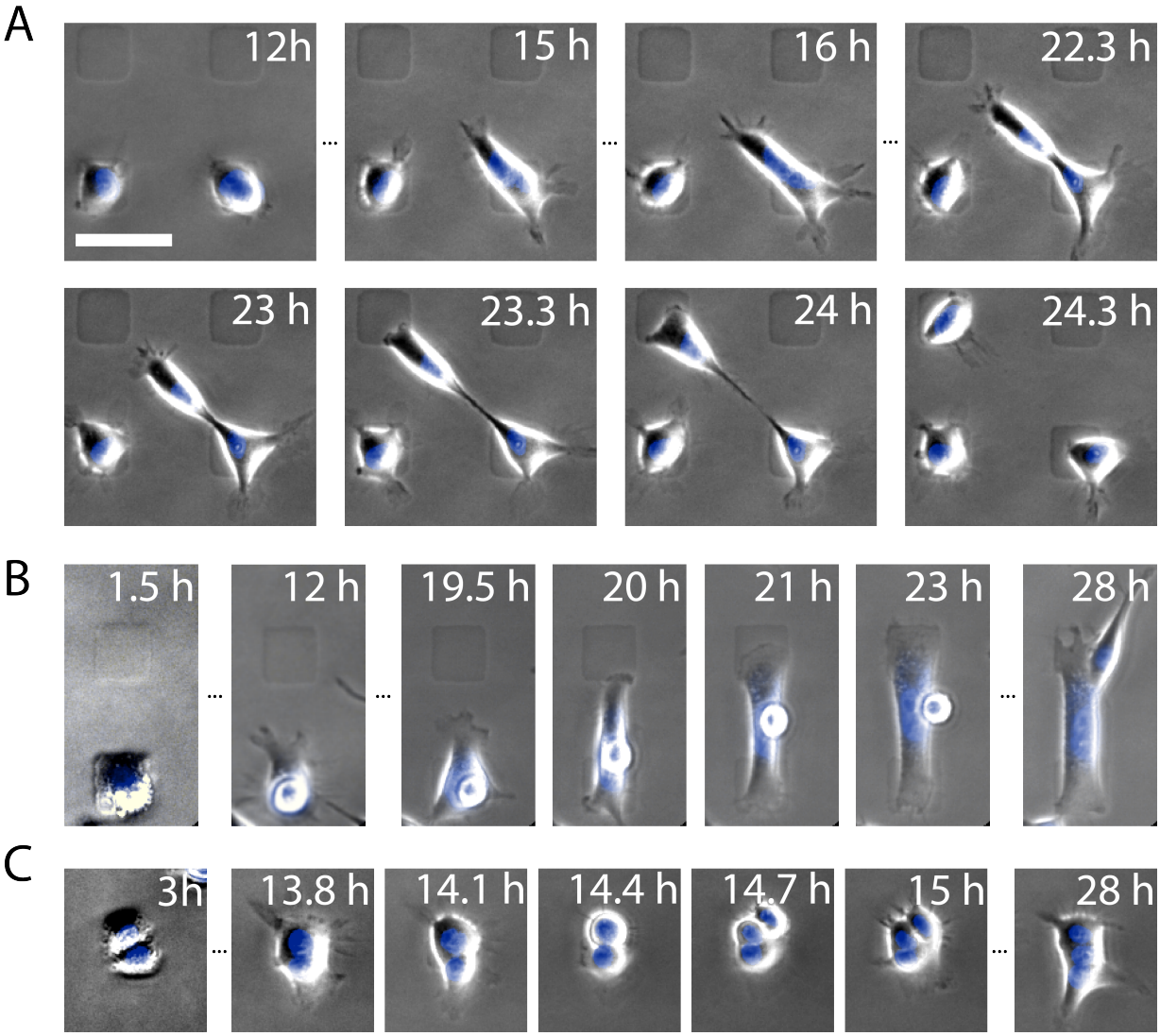


**Fig. S1 Events during the self-organization process**. (A) Two cells occupy the lower right adhesion site (12 h). As the adhesion site is optimized for one cell and the tension of the cell-cell junction is low in comparison to their mobility, the cells try to explore adjacent adhesion sites by stretching out their filopodia (15-23 h). After 23 h one of the cells has sensed a neighboring site. It moves away from the other cell and relocates to the upper left site. (B) A cell forms a bridge between two adhesion islands: This was observed for the smallest lattice distance $d_l$ = 70 µm. (C) Cell division on a double occupation site (3-15 h): As there are no other sites in reaching distance, cells share the space on the same site by reducing the contact area to the surface and getting increased in height. Scale bar for all images: 100 µm.

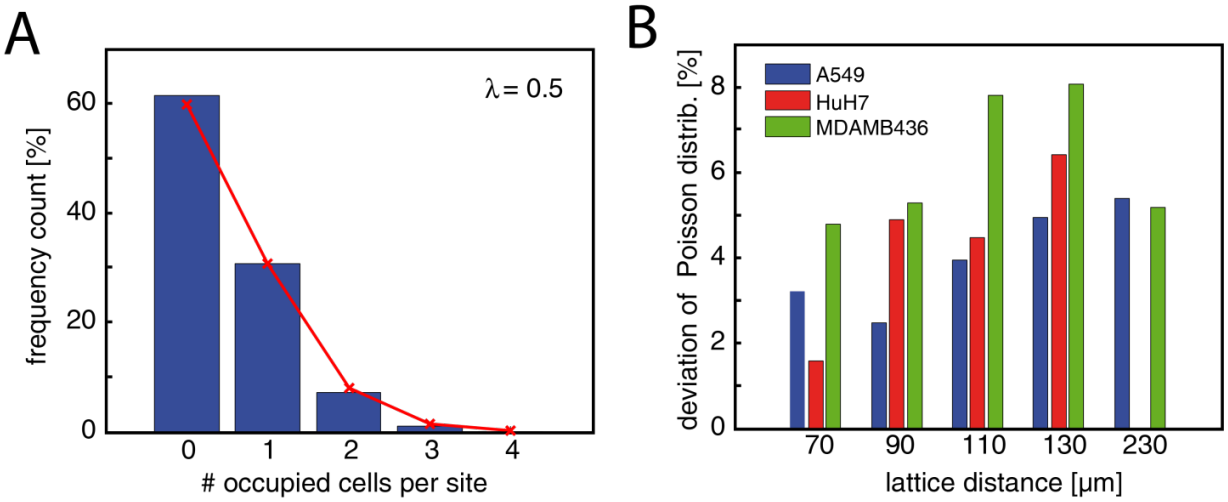


**Fig. S2 Initial occupation after seeding**. (A) Poisson distribution of an exemplary image position. Blue bars represent the percentage of occupied sites, the red curve displays the calculated distribution (see Eq. 3) for an expected value of $\lambda = 0.5$. The initial occupation is in good agreement with a Poisson distribution. (B) For all cell types and lattice distances, the measured occupation numbers deviates by ≤8 % from the calculated Poisson distribution.

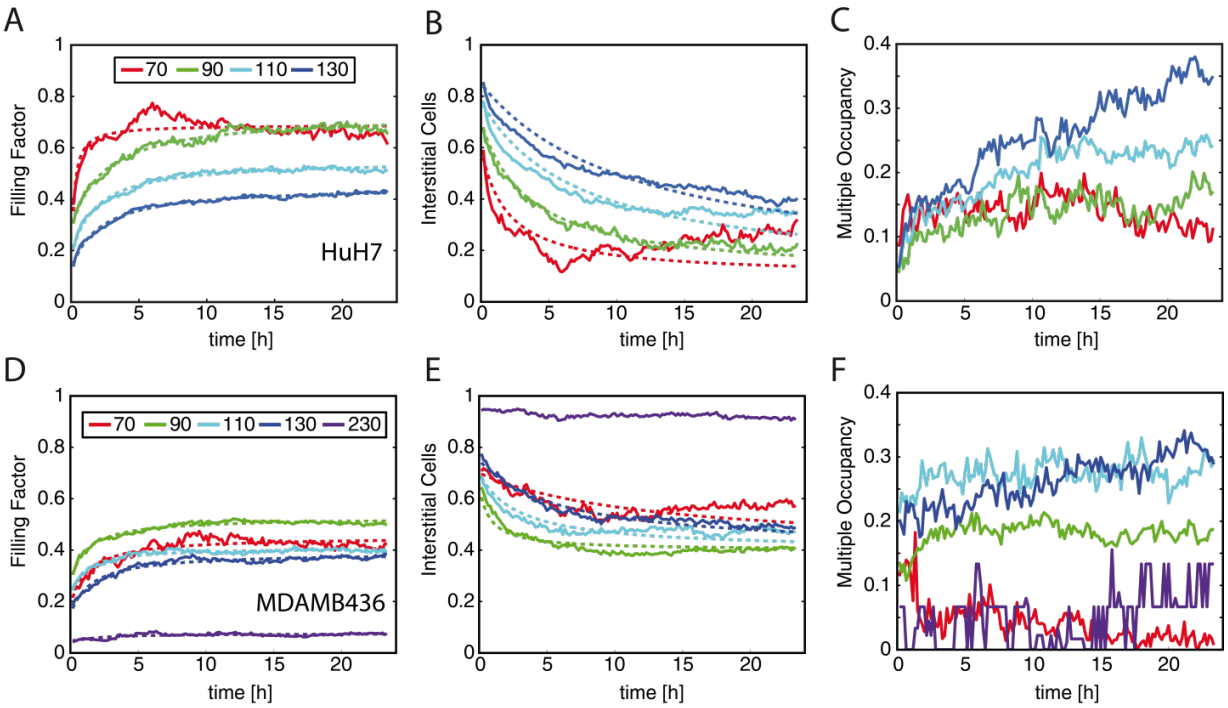


**Fig. S3 Dependence of order parameters on lattice spacing**. HuH7 (A-C) and MDA-MB-436 (D-F) are different in cell adhesion, motility and viability. Nevertheless the generic phenomenon of cellular self-organization was observed for all three cell lines. (A) Due to faster adhesion and spreading, HuH7 features higher initial occupation numbers than A549. (B) The time course of the "Interstitial Cells" and (C) the "Multiple Occupancy" parameters of HuH7 are similar to A549 (cf. Fig. 3). (D) The total filling of MDA-MB-436 is lower compared to A549 and (E) also the number of misplaced cells is higher since the MDA-MB-436 are less viable. Eq. 6 is fitted only to $d_I$ = 70-130 µm ($d_I$ = 200 µm did not converge properly; it is not included in further analysis). (F) Values of "Multiple Occupancy" are higher for MDA-MB-436 than for A549, as the cells could not be separated as efficiently before seeding.

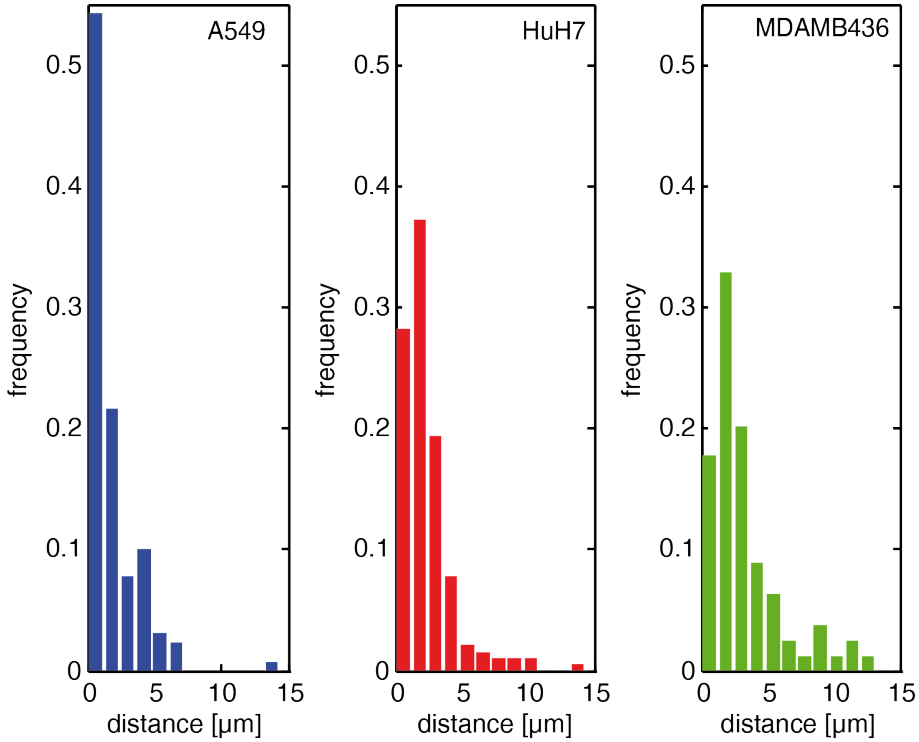


**Fig. S4 Covered Distance after Adhesion**. Frequency distribution of the initial covered distance represented in a bar plot for the three cell lines A549 (blue), HuH7 (red) and MDA-MB436 (green) after 50 min after seeding. The distribution for HuH7 is shifted towards longer distances in contrast to A549. As both cell lines have similar cell motilities, this shift can be explained by the faster adhesion to the substrate, followed by an earlier start of migration.

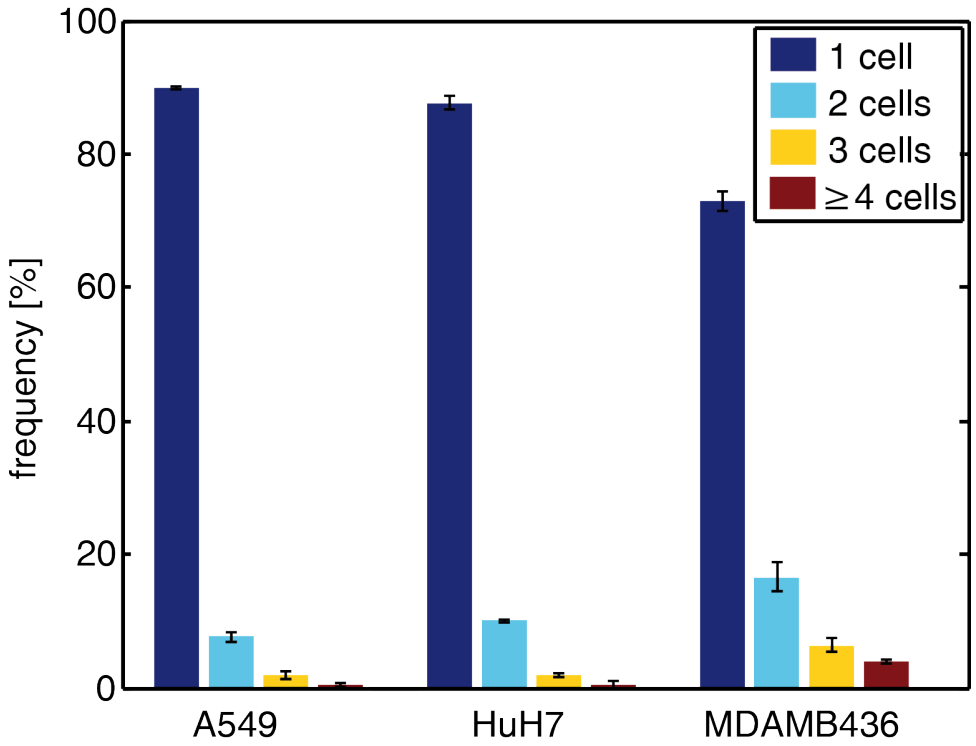


**Fig. S5 Distribution of cell clusters.** Frequency distribution for single cells (dark blue) and cell clusters (2 cells (light blue), 3 cells (yellow) and ≥ 4 cells (red)) is represented in a bar plot for the three cell lines A549, HuH7 and MDA-MB-436. The ratio of separated single cells for A549 and HuH7 (90 % and 88 %) is similar, whereas for the MDA-MB-436 only 73 % of the cells are separated and 27 % are clustered. As the MDA-MB-436 could not be trypsinized but only scraped prior to seeding, they were not separated as efficiently.

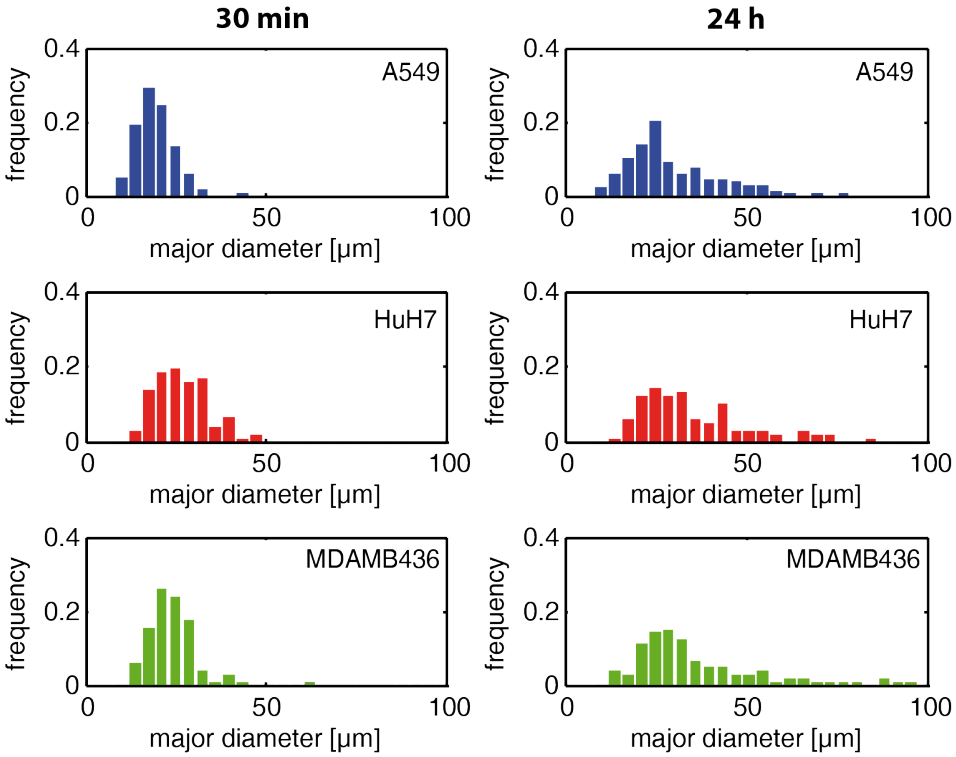


**Fig. S6 Spreading area on PLL-g-PEG surface.** Frequency distribution for the major diameter of elongated, spread cells on a PLL-g-PEG surface are visualized in bar plots for the three cell lines A549 (blue), HuH7 (red) and MDA-MB-436 (green) after 30 min (left) and after 24 h (right). Since A549 and MDA-MB-436 are often elongated in shape the major diameter reveals these cell types' larger reaching distances of these cells. The number of cell adhesion points is drastically decreased compared to culture treated surfaces: 24 µm (mean diameter after 24 h) vs. 55 µm (mean diameter on culture treated surface) for A549, 29 µm vs. 65 µm for HuH7 and 28 µm vs. 105 µm for MDA-MB-436. Thus, the spreading area does not play a significant role regarding the filling of the lattice. In general, cells are more spread on the PLL-g-PEG surface after 24 h than after 30 min.

# Publication 2:
# Cell Motility on Polyethylene Glycol Block Copolymers Correlates to Fibronectin Surface Adsorption


http://dx.doi.org/10.1002/mabi.201400246

# Cell Motility on Polyethylene Glycol Block Copolymers Correlates to Fibronectin Surface Adsorption

Peter J. F. Röttgermann,[a] Samira Hertrich,[a] Ida Berts, Max Albert, Felix J. Segerer, Jean-François Moulin, Bert Nickel, Joachim O. Rädler*

Adhesion and motility of cells on polyethylene glycol (PEG) engineered surfaces are of fundamental interest for the development of biotechnological devices. Here, the structure of PEG block copolymers physisorbed to surfaces by polyLlysine (PLL) or polypropylene oxide (PPO) is studied. Cell behavior on such surfaces incubated with fibronectin (FN) is analyzed via time-lapse microscopy, the amount and the location of FN is determined via neutron reflectivity. While FN does not adsorb onto PPOPEG, 0.4–0.7 mg m$^{-2}$ of FN is found in the vicinity of the PLL moiety of PLLPEG. Cells exhibit 21% increased motility on PLLPEG (5 kDa PEG chains) compared to pure FN layers, and 12% decreased motility for PLLPEG (2 kDa PEG chains). These findings suggest that by design of PEGylated surfaces cell migration can be controlled.

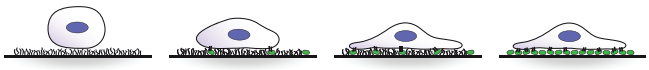


## 1. Introduction

In biomedical engineering and biotechnology, cell adhesion and motility on artificially engineered surfaces are of great importance. In a natural environment, cells interact with the extracellular matrix which determines cell shape and collective motion.[1] On artificial substrates, cells are solely confronted with the mechanical and chemical properties of the underlying surface. For example, stiffness as well as roughness of surfaces increases the spreading of cells.[2–4] Over the past few years, the functionalization of engineered polymer surfaces has advanced significantly. Lithographic techniques have been developed to generate micropatterned surfaces for protein immobilization and controlled cellular growth.[5–7] In these approaches, the attachment and movement of cells is controlled by patterning the surface with cell adhesion promoting proteins on the one hand and cell repellent polymers on the other hand. In particular, the protein fibronectin (FN) and the polymer polyethylene glycol (PEG) are commonly used.[8–10] FN is an adhesive glycoprotein of the extracellular matrix[11] and its primary function is to mediate cell attachment.[12–14] PEG is a multifaceted neutral polymer, soluble both in water and many organic solvents. It is well known for its non-adhesive properties with regard to protein adsorption as well as attachment of microorganisms. This protein repellence of surface grafted PEG has been the subject of many studies investigating the influence of chain length, grafting density, and chain mobility.[15–18] Grafting of PEG to solid surfaces can be achieved by various chemical linkages, e.g., thiols or silanes for gold and oxide surfaces, yielding highly stable and well defined monolayers.[19,20] Alternatively, PEG block copolymers are used to form stable monolayers by physisorption from solution.[21] In particular, electrostatic

P. J. F. Röttgermann, S. Hertrich, Dr. I. Berts, M. Albert, F. J. Segerer, Dr. B. Nickel, Prof. J. O. Rädler
Faculty of Physics and Center for NanoScience (CeNS), Ludwig-Maximilians-University, Geschwister-Scholl-Platz 1, 80539 Munich, Germany
E-mail: raedler@lmu.de
Dr. J.-F. Moulin
Helmholtz Zentrum Geesthacht, Institut für Werkstoffforschung, FRM II, Lichtenbergstr. 1, 85747 Garching, Germany

[a]Peter J. F. Röttgermann and Samira Hertrich contributed equally to this work.




DOI: 10.1002/mabi.201400246

surface anchoring via poly-L-lysine-grafted PEG (PLL–PEG) has found widespread application in cell patterning.[7,22]

There is a remarkable difference in protein resistance between differently designed PEG polymers both for grafted and self-assembled monolayers.[19,20,23,24] For example, for PEG covalently and densely bound on silicon, both proteins and cells are found to be strongly repelled.[25] In contrast, we have showed in previous work that cells are capable of migrating from PLL–PEG passivated areas to adhesion sites coated with FN and thus self-organize into ordered arrays.[7] In this case, however, the last step in the surface preparation involves the incubation of the PLL–PEG with FN. It is hypothesized that the exposure of the PLL–PEG layer to FN renders the PLL–PEG coating partially cell adhesive.

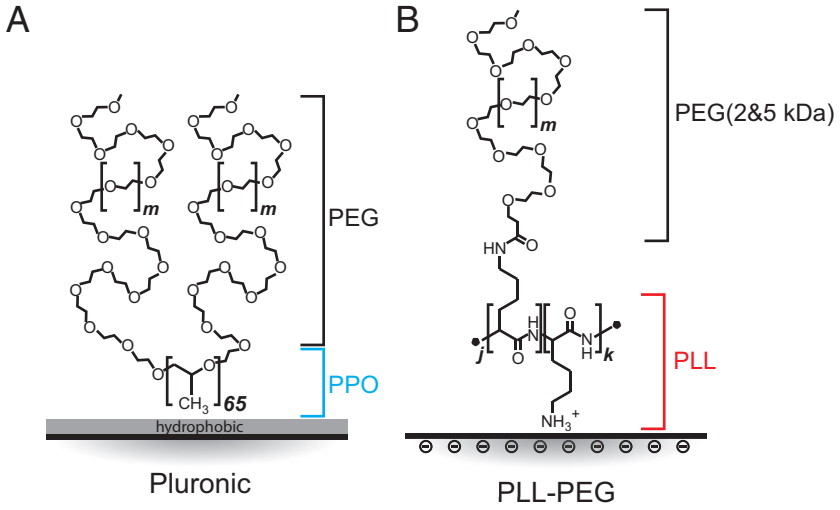


*Figure 1.* Schematics of the polymer architecture of Pluronic and PLL–PEG. A) Two PEG chains of 4.4 kDa ($m = 99$) are linked to a 65-mer of polypropylene oxide. B) On a PLL chain of 20 kDa, PEG chains of various lengths (2 and 5 kDa, $m = 45$ and 114) are linked in a grafting ratio of $k/j = 3.5$ (lysine units/PEG chain).

It is therefore important to probe whether FN adsorbs to PLL–PEG coatings and if so, where it is located. Experimental access to localize FN within the PEG is difficult. Thus, we employ neutron reflectometry[26] to analyze the structure of different PEG layers and to determine the amount and distribution of FN in these PEG layers. We focus our study on two polymer constructs: first, the PEG grafted to a hydrophobic polymer anchor PPO and second, the PLL–PEG with PEG chains of both 2 and 5 kDa length. The structural information is then correlated with cell morphology and cell motility on these surfaces.

## 2. Results

### 2.1. Surface Passivation

Cellular adhesion and motility properties are studied on three different PEG surfaces and on an unpassivated surface as reference. The PEG layers are formed using two different polymer coatings, Pluronic, and PLL–PEG. Pluronic (F-127) is a PEG–PPO–PEG triblock-copolymer, consisting of two end-attached PEG (4.4 kDa) polymers on a 65-mer PPO. The PPO chain is hydrophobic; thus in water it physisorbs readily on hydrophobic surfaces. In contrast, the PLL chain of the PLL–PEG construct is positively charged, which results in a spontaneous adsorption on clean silicon oxide surfaces. In summary, both surface passivations are based on a physisorbed polymer coating. All experiments were performed at physiological salt concentration and pH. Figure 1 illustrates the chemical structure of the samples. Two different chain lengths of PEG (2 and 5 kDa) on PLL are compared, herein denoted as PLL–PEG (2) and PLL–PEG (5). Finally, all substrates are incubated with FN.

### 2.2. Cell Morphology on Different Polymer Layers

To evaluate the morphology and spreading behavior on the different surfaces, cell contour areas were analyzed. Note that the microscopy images only show the projection areas of the cells, however, the cell contact area might be even smaller. Cell morphology and area give a first indication of how cells attach to the underlying surface, i.e., strong adhesion is commonly identified by flat cell shape while round cells indicate weak or no adhesion. Figure 2A shows fluorescence micrographs of plasma membrane stained adeno carcinoma cells (A549) on the different surfaces after 24 h. On Pluronic, all cells occupy a small area and are round shaped, i.e., cells do not spread. On PLL–PEG (2), cells partially adhere as their shape is more elongated. For PLL–PEG (5) and for FN (on the unpassivated culture dish), the spread out cell shape is even more distinct. Here, hardly any round shaped cells can be observed except for dividing cells. Furthermore, cells form filopodia on both substrates, and also start to proliferate during the first 24 h. This proliferation can be identified by cell junctions of several neighboring cells (Figure 2A).

In Figure 2B, the distributions of the contour area per cell for the different surfaces are plotted. One hour after seeding, the distributions are already distinguishable from each other. On Pluronic, the mean contour area is 225 $\mu m^2$ with a relatively small standard deviation of 50 $\mu m^2$. On the other coatings, the contour area is higher. This observation

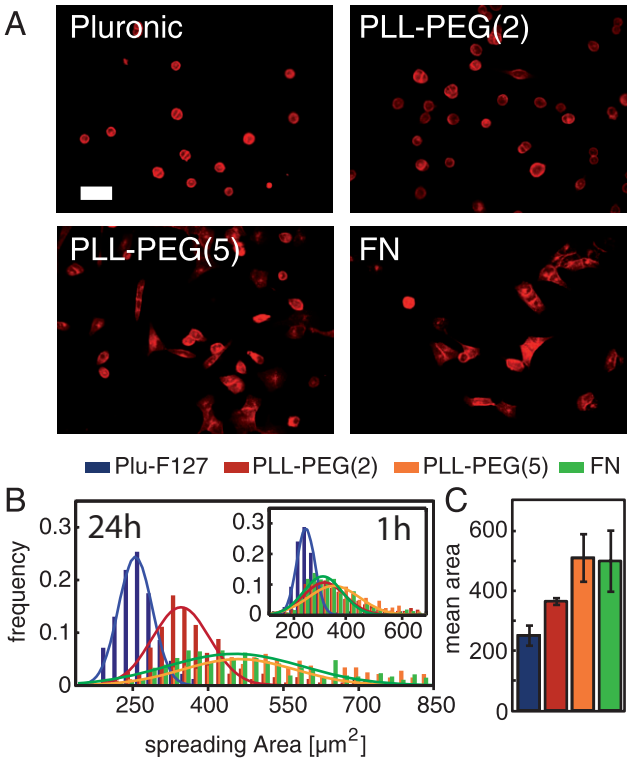


*Figure 2.* A) Fluorescence micrographs of plasma membrane stained A549 cells on Pluronic, PLL–PEG (2), PLL–PEG (5), and unpassivated surface, all incubated with FN, after 24 h. Scale bar 100 μm. B) Distribution of the cell contour area for Pluronic (blue), PLL–PEG (2) (red), PLL–PEG (5) (orange), and FN (green) at 24 and 1 h (inset) after seeding. C) Mean contour area per cell of A549 cells after 24 h. Error bars represent the standard deviation of three experiments.

becomes more obvious after 24 h. The contour area per cell reaches values of $365 \pm 100\ \mu m^2$ (mean ± standard deviation) for PLL–PEG (2), $510 \pm 200\ \mu m^2$ for PLL–PEG (5), and $500 \pm 240\ \mu m^2$ for FN (see Figure 2C). Only on Pluronic, the contour area stays low with $250 \pm 65\ \mu m^2$ indicating that cells are still not adherent.

### 2.3. Cell Motility

To access cell motility on the different surfaces, cell trajectories were extracted from fluorescence time-lapse microscopy images. Figure 3A shows several exemplary cell trajectories on Pluronic, on both PLL–PEG, and on pure FN surfaces over a period of 24 h. No cell migration was observed on the Pluronic surface, while on all other surfaces cells did migrate. Different populations of resting and persistently migrating cells were not observed, as cells were moving continuously. One way to quantify migration is to evaluate the mean squared displacement (MSD) with respect to the initial position. On PLL–PEG (2), the MSD is 125 μm, i.e., less than the 200 μm on PLL–PEG (5) after 1 d. The displacement on FN is similar, but slightly lower than on PLL–PEG (5).

To assess motility in a quantitative way the time evolution of the MSD is calculated by taking the ensemble average over all cells, as illustrated in Figure 3B. Typical cell migration can be described by a persistent random walk.[27] Initially, cells on PLL–PEG (2 and 5) and FN show indications of directed motion (shown with green dotted lines). On the longer time scale, the MSD data in Figure 3B approach a diffusive migration (random walk), shown with red dashed lines. A common way to determine cell speed is to calculate the contour length of the trajectory for all cells and divide this by the overall tracking

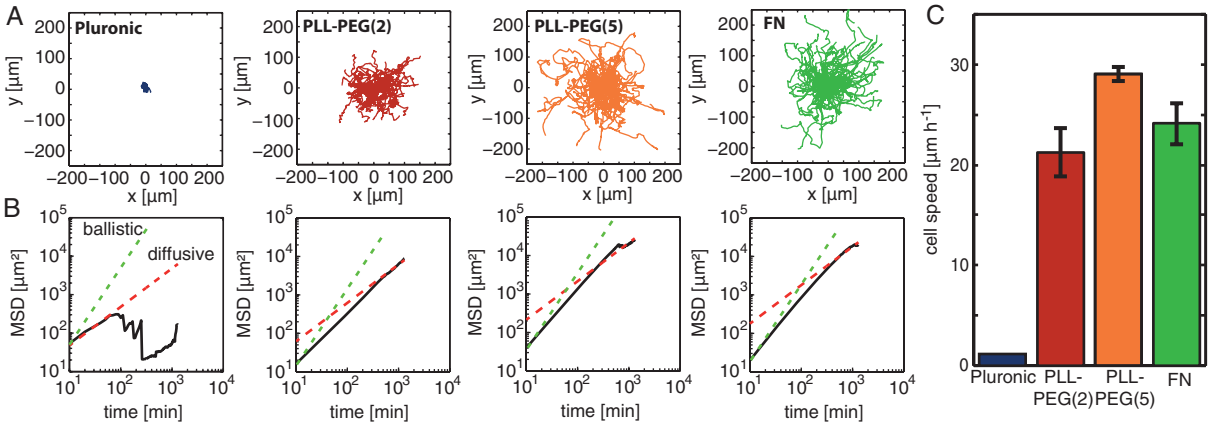


*Figure 3.* A) Representative cell trajectories on the four different substrates over a period of 24 h: Pluronic (blue), PLL–PEG (2) (red), PLL–PEG (5) (orange), and FN (green). B) Mean square displacements (black curves) are plotted against time for the various substrates. As a guide to the eye, the MSD dependence for directed motion (dotted green curve, slope 2) and diffusive motion (dashed red curve, slope 1) are indicated. C) Bar plot of single cell speed for the various substrates. Error bars represent the standard deviation of three experiments.

time, see Figure 3C. Using this procedure, the lowest cell speed of 1.2 $\mu m\,h^{-1}$ is obtained for Pluronic surface; this is at the detection limit of our setup. For the other surfaces, cell velocities are $21.2 \pm 2.5\,\mu m\,h^{-1}$ for PLL–PEG (2), $29.1 \pm 0.7\,\mu m\,h^{-1}$ for PLL–PEG (5), and $24.1 \pm 2\,\mu m\,h^{-1}$ for FN.

### 2.4. Neutron Reflectivity on Polymer Layers

Neutron reflectometry measurements provide detailed information regarding the amount and distribution of protein in the different polymer layers. Two sets of measurements were performed on each system, first in $D_2O$ and second in a mix of $D_2O$ and $H_2O$ with the scattering length density (SLD) matched to that of $SiO_2$. From the combination of these two measurements, we obtain hydration and composition of the films. Experiments were carried out on $SiO_2$ film to enhance contrast. Fresnel corrected neutron reflectivity $R(q)q^4$ are shown in the inset of Figure 4A–C. All reflectivity curves show oscillations in the intensity caused by the oxide layer on the silicon block. Silicon substrate with an oxide layer thickness of $d = 580 \pm 4$ Å was used for both the Pluronic and the PLL–PEG (2) samples. The oscillations of the intensity are narrower for samples containing PLL–PEG (5) due to the much thicker $SiO_2$ layer ($1\,090 \pm 5$ Å). The signal caused by the film is visible as the broad fringe at about $q = 0.1$ $Å^{-1}$.

The neutron data are fitted using different models. Starting from a one-layer model, the number of layers is increased plus their thickness and roughness adjusted until the calculated reflectivity of the models fits best the measured data. The minimum model necessary to reproduce the data is always chosen. The Pluronic data, could be fitted with one 28 Å layer and a SLD of $3.3 \times 10^{-6}$ $Å^{-2}$ in $D_2O$ and $2.0 \times 10^{-6}$ $Å^{-2}$ in the $D_2O/H_2O$ mix, indicating a hydration of 45%. The dry SLD for the Pluronic layer is at the expected value of $\sim 0.45 \times 10^{-6}$ $Å^{-2}$, the theoretical values for pure PEG and PPO are $0.6 \times 10^{-6}$ and $0.35 \times 10^{-6}$ $Å^{-2}$, respectively. After incubation with FN, no significant change was observed for the neutron reflectivity data of the Pluronic sample measured in $D_2O$, see Figure 4A. Therefore, the protein causes no change for the Pluronic surface.

A two-layer model is needed for the interpretation of the PLL–PEG samples. Here, the layer adjacent to the $SiO_2$ has a SLD of $4.4 \times 10^{-6}$ $Å^{-2}$ (in $D_2O$) and $3.5 \times 10^{-6}$ $Å^{-2}$ ($D_2O/H_2O$ mix) for PLL–PEG (2), and $4.5 \times 10^{-6}$ and $3.42 \times 10^{-6}$ $Å^{-2}$ for PLL–PEG (5). This layer represents the PLL and increases in thickness after addition of FN. The hydrated PEG layer on top has a SLD of $5.7 \times 10^{-6}$ and $3.1 \times 10^{-6}$ $Å^{-2}$ for PLL–PEG (2), and $5.73 \times 10^{-6}$ and $3.3 \times 10^{-6}$ $Å^{-2}$ for PLL–PEG (5). The PLL–PEG (2) system shows a highly hydrated PEG layer with 90% water and a thickness of about 50 Å,

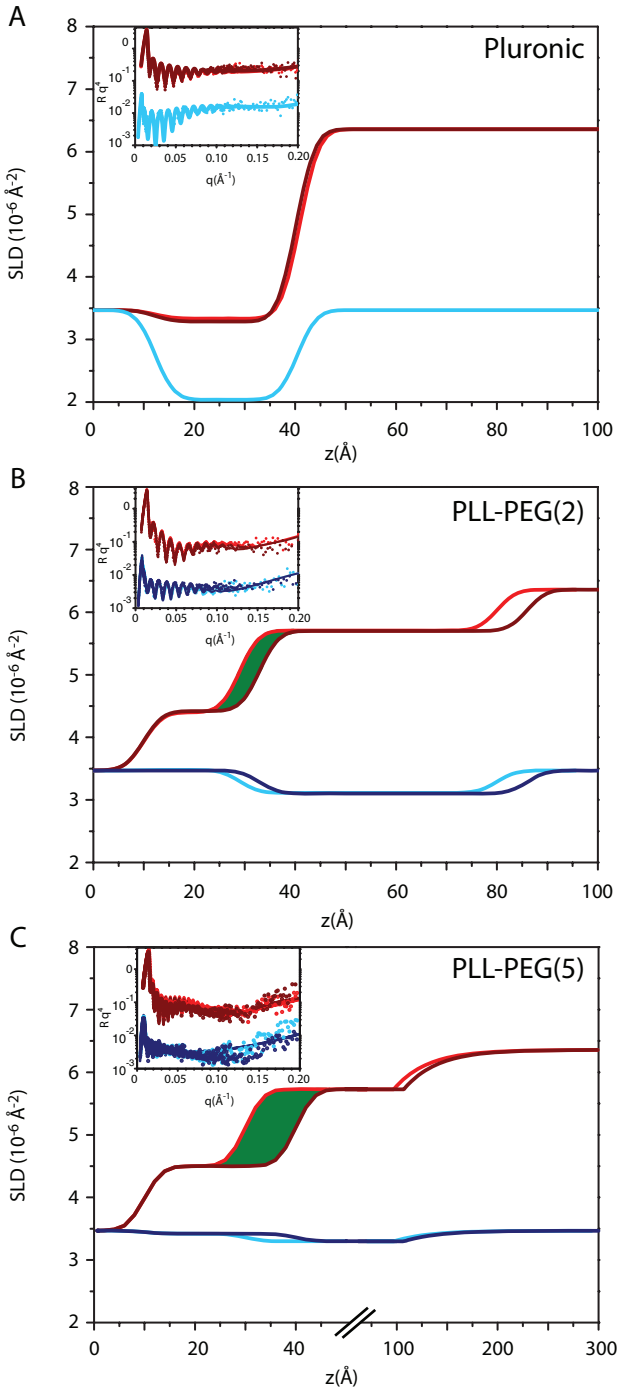


*Figure 4.* SLD profiles with the corresponding reflectivity data and fits (insets) for Pluronic A), PLL–PEG (2) B), and PLL–PEG (5) C). The samples before the addition of FN are shown in light red for the $D_2O$ contrast and light blue for the $D_2O/H_2O$ mix contrast. After the addition of FN, the data are shown in dark red for the $D_2O$ contrast and dark blue for the $D_2O/H_2O$ mix contrast. The measurements in the $D_2O/H_2O$ mix buffer are offset by a factor 0.1 for clarity. The effect of the FN is visible in the change in thickness indicated by the green area shown in B) and C). The *x*-axis in C) is differently scaled for improved visualization. The much longer PEG chains decay exponentially towards the bulk.

and underneath a PLL layer with hydration of 31% and a thickness of about 20 Å. The PLL–PEG (5) also shows a hydrated PEG layer (84% water) with the polymer density that can be fitted with an exponentially decreasing profile towards the bulk. The homogeneous part of the layer has a thickness of 68 Å, above, the PEG density decreases with a decay length of 33 Å. Its total length is almost double the thickness of PLL–PEG (2). The underlying PLL layer is 20 Å thick and contains 37% water, i.e., the layer is slightly less dense compared to PLL–PEG (2). After the incubation with FN, the reflectivity signal deviates for PLL–PEG (2) (Figure 4B dark red and dark blue) between $q = 0.08$ Å$^{-1}$ and $q = 0.15$ Å$^{-1}$ from the signal before (Figure 4B light red and light blue), indicating that FN changed the overall system. The same trend was observed for PLL–PEG (5), see Figure 4C.

Table 1 shows thickness, hydration and surface coverage extracted from the SLD model. While the SLD of both PLL and PEG layers remained unchanged, the underlying PLL layer increases in thickness by 4 Å for the shorter PEG. We conclude that the amount of material adsorbed to the surface increased after addition of FN. We evaluated the change in thickness to determine the amount of FN to be 0.4 mg m$^{-2}$. FN is affecting the PLL layer by an increase of 8 Å in layer thickness for the PLL–PEG (5). The amount of FN in this case is 0.7 mg m$^{-2}$.

## 3. Discussion

### 3.1. Description of Grafted PEG Layers

In our neutron reflectivity study, we showed that we can measure thickness, mass coverage, and thus PEG grafting density. Those values can be compared with theoretical descriptions. The relation of polymer height $L$ and grafting density $\sigma$ is $L = Na(a^2\sigma)^{1/3}$ with monomer size $a = 0.35$ nm[28] for PEG, and the polymerization degree $N$ as described by Alexander and de Gennes (AdG).[29,30] The AdG theory is valid for polymers in a brush conformation, i.e., the product of the grafting density and the squared Flory radius $R_F = aN^{3/5}$ is less than 1. The values predicted by this model are compared to our data in Table 2. Both PLL–PEG copolymers are clearly in the brush regime ($\sigma - 1$ $(R_F) - 2 = 0.55$ and 0.14). In case of the PLL–PEG (2), the thickness of the PEG layer is 16% higher than predicted by the model. Nevertheless, the thickness of PEG is

*Table 1.* Fit parameters of Pluronic and PLL–PEG with calculated surface coverage from the neutron reflectivity experiment.

| Sample | Layer description | Thickness [Å] | % Water in layer | Surface coverage [mg · m$^{-2}$] |
|---|---|---|---|---|
| Pluronic | PPO + PEG | 28 ± 1 | 45 ± 1 | 1.8 ± 0.1 |
| After FN incubation | PPO + PEG | 28 ± 1 | 45 ± 1 | 1.8 ± 0.1 |
| PLL–PEG (2) | PLL | 19 ± 1 | 31 ± 2 | 1.8 ± 0.1 |
| | PEG | 51 ± 1 | 90 ± 1 | 0.51 ± 0.02 |
| After FN incubation | PLL + FN | 23 ± 1 | 31 ± 5 | 2.2 ± 0.1 |
| | PEG | 53 ± 1 | 90 ± 3 | 0.53 ± 0.03 |
| PLL–PEG (5) | PLL | 20 ± 1 | 37 ± 3 | 1.76 ± 0.1 |
| | PEG | 68 ± 3 | 84 ± 1 | 1.65 ± 0.04 |
| After FN incubation | PLL + FN | 28 ± 1 | 37 ± 2 | 2.47 ± 0.1 |
| | PEG | 68 ± 3 | 84 ± 1 | 1.65 ± 0.04 |

*Table 2.* Comparison of AdG theory and neutron data with $N$ monomer units, measured surface density $\sigma_{exp}$, measured and calculated PEG layer thickness $L_{exp}$ and $L_{theory}$, Flory radius $R_F$, relation of $\sigma^{-1}$ $(R_F)^{-2}$, and type of conformation.

| Surface | $N$ | $\sigma_{exp}$ $10^{-3}$ [Å$^{-2}$] | $L_{exp}$ [Å] | $L_{theory}$ [Å] | $R_F$ [Å] | $\sigma^{-1}$ $(R_F)^{-2}$ | Conformation |
|---|---|---|---|---|---|---|---|
| PLL-g (3.5)–PEG (2) | 45 | 1.54 | 51 | 42 | 34 | 0.55 | Brush |
| PLL-g (3.5)–PEG (5) | 114 | 1.99 | 68 + 33 | 116 | 60 | 0.14 | Brush |
| PPO-g (32.5)–PEG (4.4) | 99 | 1.72 | <28 | 96 | 55 | 0.19 | Pancake |

consistent with previous measurements of PEG cushions[31] and PEG-tethered lipid bilayers.[32] In case of the PLL–PEG (5), the theoretical thickness of 116 Å is also in good agreement with the data fit, that produced a homogeneous layer of 68 Å and on top an exponential layer with a decay length of 33 Å. For the Pluronic film, the AdG model is not valid, as in that case the polymer extension is ruled by hydrophobic interaction with the surface. Thus, PEG adopts a much thinner pancake structure and shields the hydrophobic surface from the water.[33]

### 3.2. Surface Passivation and Protein Interaction

The anchor polymers, PLL and PPO, as well as the PEG chain length and density affect the degree of surface passivation. The Pluronic coating consists of 4.4 kDa PEG chains while the PLL–PEG film consists of 2 and 5 kDa PEG chains, respectively. Despite the long PEG chains of the Pluronic coating, the overall polymer layer is thinner and less hydrated (45% water), shown by the reflectivity data in Figure 4. The low water content and high PEG density in the Pluronic film does not allow for FN intercalation within the sensitivity of the neutron reflectometry experiment. This is in line with the above-described shielding effect of the PEG for the underlying hydrophobic PPO layer, blocking the adsorption sites to the protein. Similar behavior was also observed experimentally by O'Connor[17] and McPherson.[33]

On the contrary, the PEG layers of both PLL–PEG films contain more than 80% water and are not dense enough for complete protein repellence. In our work, we can specify both the location and the amount of protein by neutron reflectometry: FN was found in small amounts in the vicinity of the PLL layer. This indicates primary adsorption, which is the adsorption of proteins at the substrate surface of a polymer brush. The SLD of FN, with the majority of the exchangeable protons replaced with the ones from the solvent, is very close to the one of PLL (FN fully exchanged in $D_2O$ is $3.12 \times 10^{-6}$ Å$^{-2}$ compared to $3.4 \times 10^{-6}$ Å$^{-2}$ for PLL in $D_2O$). Due to this fact, it is not possible to distinguish between the PLL and the FN in the layer. Adsorption of FN in the PLL region is driven by electrostatics, in contrast to the theoretical prediction of protein adsorption into polymers by Halperin.[34] The adsorbed PLL on the silicon oxide leaves a net positive charge[35] and FN is negatively charged in physiological solution (isoelectric point 5.2).[36] Despite the big protein size, FN in the unfolded state is flexible and rod-like with a diameter (20 Å) comparable to a small protein.[37] Hence, it can penetrate the brushes and absorb primarily to a surface. Comparable results were presented by Pasche et al.[38] where the incubation of serum in a systematic series of PLL–PEG coatings with varying PEG molecular weights and grafting ratios revealed protein adsorption. Moreover, a study of the adsorption of myoglobin (diameter of 40 Å) onto PEG brushes using neutron scattering revealed similar behavior.[39] The protein layer closest to the polymer surface has a low thickness compared to the protein dimensions, which is interpreted as denaturation of the protein. In our case, we suggest that this effect is combined with a mixing of the FN with the PLL, thus resulting in the small layer thickness assigned to the FN.

Figure 5 illustrates the surfaces and their respective interaction with FN. Longer PEG chains of 5 kDa did not form a uniform layer but were rather stretched out. A disordered configuration may offer less protection compared to well ordered chains allowing more FN to diffuse through to the PLL.[38] This may be the reason why the 2 kDa PEG chains show better FN repellence compared to 5 kDa chains.

### 3.3. PEG Interface and Cell Behavior

In the following, we compare the surface properties with cell behavior. Firstly, cells do not adhere to Pluronic, as indicated by the round shape of the cells. This is caused by the absence or in sufficient accessibility of FN binding sites in the Pluronic film. In contrast, cells spread on PLL–PEG where FN adsorption was observed. Thus, small amounts of surface bound FN seem to be essential for cell spreading. Indeed, Massia and Hubbell[40] showed that 1 fmol cm$^{-2}$ is already sufficient for complete spreading of cells on a bare surface, which corresponds to a ligand spacing of 440 nm. Our data for the FN underneath a PEG moiety reveal amounts of 72 fmol cm$^{-2}$ for PLL–PEG (2), 127 fmol cm$^{-2}$ for PLL–PEG (5) and none for Pluronic (detection limit of

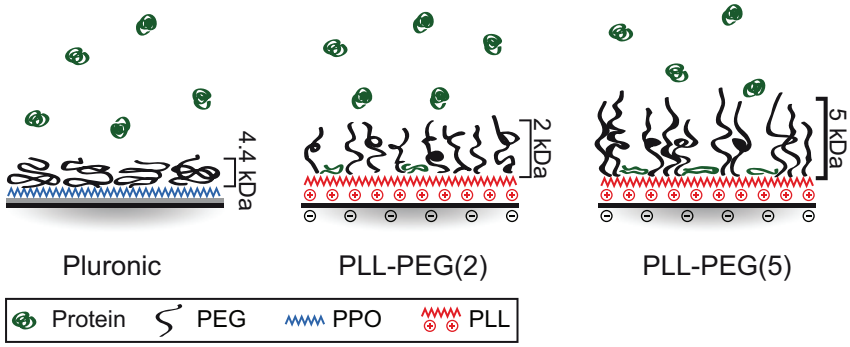


*Figure 5.* Interpretation based on the neutron SLD profiles of the adsorption of FN in the three different polymer coatings Pluronic, PLL–PEG (2), and PLL–PEG (5). In the first case, FN is not adsorbed on the pancake-like Pluronic layer, while on the PLL–PEG samples small amounts of FN penetrate the extended brushed PEG layers to attach to underlying PLL. The higher PEG density leads to non-ordered chains and therefore to higher protein adsorption.

18 fmol cm$^{-2}$). All these values are considerably above the predicted minimal ligand density most likely due to the fact that FN is bound primarily to the PLL and shielded by the PEG layer. Cells have to form protrusions through the PEG layer to bind to the FN. In addition, the conformation of FN in our system plays a role as it exists probably in the unfolded rod-like state which minimizes the accessibility of the RGD binding site.[41] Aggregates might further increase the average spacing of two binding sites for cells and also favor the formation of focal adhesions.

Apart from the different spreading, also cell migration correlates with the different surface properties. The longest persistence time is observed for the pure FN surface whereas the highest velocity is observed on PLL–PEG (5). As cells polarize in one direction (mostly random in absence of a chemo-attractant) they have a higher probability to move forward in the same direction instead of turning towards any other direction.[42–44] The protein on the pure FN surface is isotropically distributed and the process of the directed motion is only interrupted by intracellular processes resulting in the highest persistent time of motion. PLL–PEG (5) exhibits fewer adhesion points which leads on the one hand to more frequent interruption in the migration and on the other hand to faster movement, possibly due to faster detachment.[45] PLL–PEG (2) exhibits even fewer anchor points, the amount of FN is further decreased, and the cell movement cannot be sustained at such high speed. It seems the cells have to repolarize more often, which is time consuming and results in a much slower movement. A similar behavior with a maximum in the velocity distribution has been observed before.[43,46]

These findings indicate that there is an optimal FN density with regard to the maximal covered distance. This is best met by the PLL–PEG (5) layer. If the density is lower, e.g., on PLL–PEG (2), cells may not find anchor points to advance as fast. On the other hand, a too high anchor point density as for the pure FN surface slows the cells due to detachment time. It is likely that cell attachment to PEG could alter the underlying brush structure. The average distance of cell membrane and solid substrate is also likely to be tuned by FN and the PEG molecular weight and could be measured by neutron reflectivity.[47]

## 4. Conclusion

In this work, we have correlated the amount of FN adsorption into different PEG layers with cell adhesion and motility. PEG grafted to a hydrophobic PPO anchor suppresses cell adhesion and migration almost completely and shows no FN adsorption. This is most likely due to the shielding effect of the PEG from the hydrophobic moiety. For PLL–PEG layers, we find that the brush-like structure of the PEG layer still allows for adsorption of FN underneath the PEG layer, i.e., in close proximity to the PLL anchor. Cells exhibit faster speed on the PLL–PEG (5) compared to that of pure FN surface. These findings suggest that the combination of partial adsorption of cell adhesive proteins and the cell repellent properties of PEG are suited to elevate cell motility. Thus, artificially designed surfaces of PEG block copolymers and proteins could fine-tune cell motility properties.

## 5. Experimental Section

### 5.1. Sample Preparation

For the reflectometry measurements, silicon blocks were cleaned in an ultrasonic bath for 10 min in ethanol, 10 min in purified water (MiliQ, Millipore Corporation), and dried with nitrogen. The silicon blocks and the topas substrate (μ-dishes ibidi GmbH) for the cell experiments were then exposed to $O_2$ plasma (3 min at 40 W, Femto Diener). The samples were passivated with PLL (20 kDa)-g (3.5)–PEG (2 or 5 kDa) (SuSoS AG) at a 1 mg ml$^{-1}$ aqueous buffer solution (10 mM HEPES and 150 mM NaCl at pH 7.4) for 30 min at room temperature (RT). For Pluronic-F127 (Sigma–Aldrich), the silicon blocks were pre-coated with octadecyltrichlorosilane (Sigma–Aldrich) and/or untreated μ-dishes were taken, and passivated with 10 mg ml$^{-1}$ buffer aqueous solution for 1 h at RT. The samples were washed thrice with phosphate buffered saline (PBS). Subsequently, all samples were exposed to a 50 μg ml$^{-1}$ solution of FN (YoProteins) for at least 1 h. The pure protein coating was adsorbed on unpassivated μ-dishes for 1 h.

### 5.2. Neutron Reflectivity Measurements

Neutron reflectivity measurements were performed at the REFSANS horizontal time of flight reflectometer operated by the Helmholtz Zentrum Geesthacht at the Heinz Maier-Leibnitz Zentrum in Munich.[48] For this experiment, the relative $q$ resolution was set to $dq/q = 0.06$ and the incident wavelength spectrum ranged from $\lambda = 2$–10 Å. By combining the reflected intensities measured for five incident angles ($\theta = 0.15^\circ$, $0.3^\circ$, $0.6^\circ$, $1.4^\circ$, and $2.8^\circ$) the reflectivity $R(q) = I(\lambda,\theta)/I_0(\lambda)$ was obtained up to a scattering vector $q = 4\pi/\lambda \sin(\theta) = 0.2$ Å$^{-1}$ where $I_0$ denotes the primary beam intensity, and $I$ the reflected intensity.

In neutron measurements, the SLD can be adjusted by choosing different isotopes. Here, contrast variation of PBS buffer solution was used to determine the hydration of the film. Therefore, two reflectivity measurements on each sample were performed: one in $D_2O$ buffer, then the second in a mixture of 61% $D_2O$ and 39% $H_2O$, i.e., matched to the SLD of silicon oxide. From the difference in the SLD profile, the hydration and the SLD without the contribution of $D_2O$ or $H_2O$ (SLD dry) were calculated.[49] Finally, the protein was added to both the $D_2O$ buffer and the contrast matched buffer for a second set of measurements. Two measurements at different contrasts for each system ensure that changes in conformation or hydration can be differentiated from adsorption of new material on the surface.

The data for Pluronic and PLL–PEG (2) were analyzed with the MOTOFIT program.[50] The program allows us to define thin layers

on top of the substrate, which add up to the film. By matching the theoretical and measured reflectivity, the layer thickness and SLD can be determined. The data from PLL–PEG (5) were analyzed using CPROF.[51] This program fits multiple contrasts of data for a single sample in a similar way as the MOTOFIT program. In addition, it uses a model with smoothly varying density profiles appropriate for polymers and gels at interfaces.[52] The PEG layer of PLL–PEG (2) could also be fitted with a parabolic profile [53,54] without altering the agreement using a simpler box model with a low roughness. Parabolic and linear profiles were tested for the PLL–PEG (5) data but the agreement was not as good as for the exponential profile. This is due to either lower grafting density or higher polydispersity.[52,55] For the graphical representation of the data, the reflectivity was multiplied by $q^4$ to correct for the Fresnel decay at higher $q$ values. This allows for a better visualization of the small changes to the reflected intensity by ultrathin layers.

### 5.3. Cell Culture

The A549 cell line (ATCC) was cultured in modified Eagle's medium with Earle's salts (c-c-pro), 2 mM L-glutamine, and 10% fetal calf serum. Cells were grown to 70–80% confluence, trypsinized and centrifuged at 1 000 rpm for 3 min. Cell pellets were resuspended in either cell medium or, for the experiments in Leibovitz's L15 medium with GlutaMAX (Gibco) and 10% fetal calf serum. Equal cell densities were seeded on each surface. Cells were stained with CellMask Orange Plasma membrane Stain (Life Technologies) by adding 5 μM dye for 5 min to highlight the contour of the cells or with the permeable fluorescent dye Hoechst 33342 (Life Technologies) by adding 25 nM dye to the suspension (incubation at 37 °C for 20 min) to track the nuclei. Samples were not washed to avoid an influence on weakly adherent cells.

### 5.4. Time-Resolved Fluorescence Microscopy

Images were taken with an iMIC digital microscope with phase contrast (TILL Photonics) and an oligochrome fluorescent light source (TILL Photonics) in combination with a single-band long-pass DAPI HC filter set and a dualband GFP/mCherry ET filterset (AHF Analysetechnik). Samples were kept at a constant temperature of 37 °C with an ibidi heating system (ibidi GmbH).

### 5.5. Image and Data Analysis

Raw images were preprocessed in ImageJ: the background was subtracted with a built-in function. To highlight the nuclei or the contour of the cells, a band-pass filter was applied (colliding cells were excluded from analysis). Images were binarized by setting a global threshold. Binarized images were clustered and tracked with Cell Evaluator.[56] Coordinates of the center of mass and the area of the nuclei were extracted and analyzed in MATLAB.

### 5.6. Cell Motility and Morphology Analysis

The mean square displacement was calculated as $\mathrm{MSD}(t) = \left\langle \left\langle (X_i(t+t_0) - X_i(t_0))^2 \right\rangle_{t_0} \right\rangle_i$ where $X_i(t)$ denotes the center of cell nucleus $i$ at time $t$. $\langle\cdot\rangle t_0$ designates the average over all times $t$ with starting time $t_0$. $\langle\cdot\rangle_i$ is the average over all tracked cells. Dead cells, as well as nuclei exceeding a maximal area (indication of two fused cells), were excluded from analysis. At least 200 tracks were analyzed for each experiment. All experiments have been repeated thrice. The MSD data were fitted on the short time scale for the first 40 min with the function $\mathrm{MSD}(t) = 4Dt^2$ and for the long-term behavior with $\mathrm{MSD}(t) = 4Dt$.

For the evaluation of the spreading area, only single cells have been taken into account. The frequency distributions of the spreading area have been fitted to Gaussian functions.

The single cell speed was calculated by dividing the contour length by the tracking time for a single cell and then averaging over all tracked cells. The contour length is determined by summing the nucleus displacement for each frame.

Acknowledgments: Financial support by the Deutsche Forschungsgemeinschaft (DFG) via project B1 and A7 within the SFB 1032, the Excellence Cluster "Nanosystems Initiative Munich (NIM)", FP7 EU grants NanoTransKinetics and NanoMILE, and by BMBF 05K13WM1 is gratefully acknowledged.

Received: May 19, 2014; Revised: August 13, 2014; Published online: September 10, 2014; DOI: 10.1002/mabi.201400246

Keywords: cell motility; cell morphology; fibronectin adsorption; neutron reflectivity; polyethylene glycol

[1] T. E. Angelini, E. Hannezo, X. Trepat, J. J. Fredberg, D. A. Weitz, *Phys. Rev. Lett.* **2010**, 104.
[2] B. C. Isenberg, P. A. DiMilla, M. Walker, S. Kim, J. Y. Wong, *Biophys. J.* **2009**, *97*, 1313.
[3] A. Zemel, F. Rehfeldt, A. E. X. Brown, D. E. Discher, S. A. Safran, *Nat. Phys.* **2010**, *6*, 468.
[4] E. Biazar, M. Heidari, A. Asefnejad, N. Montazeri, *Int. J. Nanomed.* **2011**, *6*, 631.
[5] R. S. Kane, S. Takayama, E. Ostuni, D. E. Ingber, G. M. Whitesides, *Biomaterials* **1999**, *20*, 2363.
[6] A. S. Blawas, W. M. Reichert, *Biomaterials* **1998**, *19*, 595.
[7] P. J. F. Röttgermann, A. Piera Alberola, J. O. Rädler, *Soft Matter* **2014**, *10*, 2397.
[8] G. Csucs, R. Michel, J. W. Lussi, M. Textor, G. Danuser, *Biomaterials* **2003**, *24*, 1713.
[9] M. Théry, *J. Cell. Sci.* **2010**, *123*, 4201.
[10] A. Azioune, M. Storch, M. Bornens, M. Théry, M. Piel, *Lab Chip* **2009**, *9*, 1640.
[11] S. Stenman, A. Vaheri, *J. Exp. Med.* **1978**, *147*, 1054.
[12] D. L. Elbert, J. A. Hubbell, *Annu. Rev. Mater. Sci.* **1996**, *26*, 365.
[13] K. Sekiguchi, S. Hakomori, *Proc. Natl. Acad. Sci. USA* **1980**, *77*, 2661.
[14] R. Hynes, *Annu. Rev. Cell Biol.* **1985**, *1*, 67.
[15] R. Michel, S. Pasche, M. Textor, D. G. Castner, *Langmuir* **2005**, *21*, 12327.
[16] A. Seehuber, D. Schmidt, R. Dahint, *Langmuir* **2012**, *28*, 8700.
[17] S. M. O'Connor, A. P. Deanglis, S. H. Gehrke, G. S. Retzinger, *Biotechnol. Appl. Biochem.* **2000**, *31*, 185.

[18] A. Halperin, G. Fragneto, A. Schollier, M. Sferrazza, *Langmuir* **2007**, *23*, 10603.
[19] J. Jung, K. Na, B. Shin, O. Kim, J. Lee, K. Yun, J. Hyun, *J. Biomater. Sci. Polym. Ed.* **2008**, *19*, 161.
[20] M. Gabi, A. Larmagnac, P. Schulte, J. Vörös, *Colloids Surf. B* **2010**, *79*, 365.
[21] N.-P. Huang, J. Vörös, S. M. De Paul, M. Textor, N. D. Spencer, *Langmuir* **2001**, *18*, 220.
[22] J. Fink, M. Théry, A. Azioune, R. Dupont, F. Chatelain, M. Bornens, M. Piel, *Lab Chip* **2007**, *7*, 672.
[23] T. A. Desai, *Med. Eng. Phys.* **2000**, *22*, 595.
[24] B. Zhu, T. Eurell, R. Gunawan, D. Leckband, *J. Biomed. Mater. Res.* **2001**, *56*, 406.
[25] S. Sharma, R. W. Johnson, T. A. Desai, *Langmuir* **2003**, *20*, 348.
[26] G. Fragneto-Cusani, *J. Phys.: Condens. Matter* **2001**, *13*, 4973.
[27] E. Méhes, E. Mones, V. Németh, T. Vicsek, *PloS ONE* **2012**, *7*, e31711.
[28] N. V. Efremova, S. R. Sheth, D. E. Leckband, *Langmuir* **2001**, *17*, 7628.
[29] P. G. de Gennes, *J. Phys. France* **1976**, *37*, 1445.
[30] S. Alexander, *J. Phys. France* **1977**, *38*, 983.
[31] T. L. Kuhl, D. E. Leckband, D. D. Lasic, J. N. Israelachvili, *Biophys. J.* **1994**, *66*, 1479.
[32] S. Hertrich, F. Stetter, A. Ruhm, T. Hugel, B. Nickel, *Langmuir* **2014**.
[33] T. McPherson, A. Kidane, I. Szleifer, K. Park, *Langmuir* **1998**, *14*, 176.
[34] A. Halperin, *Langmuir* **1999**, *15*, 2525.
[35] Y. Duval, J. A. Mielczarski, O. S. Pokrovsky, E. Mielczarski, J. J. Ehrhardt, *J. Phys. Chem. B* **2002**, *106*, 2937.
[36] N. M. Tooney, M. W. Mosesson, D. L. Amrani, J. F. Hainfeld, J. S. Wall, *J. Cell. Biol.* **1983**, *97*, 1686.
[37] H. P. Erickson, N. Carrell, J. McDonagh, *J. Cell. Biol.* **1981**, *91*, 673.
[38] S. Pasche, S. M. De Paul, J. Vörös, N. D. Spencer, M. Textor, *Langmuir* **2003**, *19*, 9216.
[39] E. Schneck, A. Schollier, A. Halperin, M. Moulin, M. Haertlein, M. Sferrazza, G. Fragneto, *Langmuir* **2013**, *29*, 14178.
[40] S. P. Massia, J. A. Hubbell, *J. Cell. Biol.* **1991**, *114*, 1089.
[41] E. Klotzsch, I. Schoen, J. Ries, A. Renn, V. Sandoghdar, V. Vogel, *Biomater. Sci.* **2014**, *2*, 883.
[42] L. Li, S. F. Nørrelykke, E. C. Cox, *PloS ONE* **2008**, *3*, e2093.
[43] R. Sambeth, A. Baumgaertner, *Phys. Rev. Lett.* **2001**, *86*, 5196.
[44] P. J. M. Van Haastert, *PLoS Comput. Biol.* **2010**, *6*, e1000874.
[45] G. Maheshwari, A. Wells, L. G. Griffith, D. A. Lauffenburger, *Biophys. J.* **1999**, *76*, 2814.
[46] S. Wu, A. Wells, L. G. Griffith, D. A. Lauffenburger, *Biomaterials* **2011**, *32*, 7524.
[47] L. Pocivavsek, A. Junghans, N. Zebda, K. Birukov, J. Majewski, *Am. J. Physiol. Lung Cell Mol. Physiol.* **2014**, *306*, L1.
[48] R. Kampmann, M. Haese-Seiller, V. Kudryashov, B. Nickel, C. Daniel, W. Fenzl, A. Schreyer, E. Sackmann, J. Rädler, *Physica B* **2006**, *385-386*, Part 2, 1161.
[49] S. Stanglmaier, S. Hertrich, K. Fritz, J. F. Moulin, M. Haese-Seiller, J. O. Rädler, B. Nickel, *Langmuir* **2012**, *28*, 10818.
[50] A. Nelson, *J. Appl. Cryst.* **2006**, *39*, 273.
[51] A. R. Rennie, "http://material.fysik.uu.se/Group_members/adrian/cprof.htm", accessed: August, **2014**.
[52] I. Berts, G. Fragneto, J. Hilborn, A. Rennie, *Eur. Phys. J. E* **2013**, *36*, 1.
[53] S. T. Milner, T. A. Witten, M. E. Cates, *Macromolecules* **1989**, *22*, 853.
[54] W. M. de Vos, F. A. M. Leermakers, *Polymer* **2009**, *50*, 305.
[55] E. P. K. Currie, M. Wagemaker, M. A. C. Stuart, A. A. van Well, *Physica B* **2000**, *283*, 17.
[56] S. Youssef, S. Gude, J. O. Rädler, *Integr. Biol.* **2011**, *3*, 1095.

# Publication 3:
# PEG - Studies from Tethered Lipid Bilayers to Protein-Cell Interactions

# Polyethylene Glycol Polymer Layers – Studies from Tethered Lipid Bilayers to Protein-Cell Interactions

P. J. F. Röttgermann1, S. Hertrich1, I. Berts1, J.O. Rädler1, B. Nickel1

Fakultät für Physik & CeNS, Ludwig-Maximilians-Universität, Geschwister-Scholl-Platz 1, 80539 München, Germany

Structural design and analysis of bio-mimicking surfaces is of great importance for the design of artificial environments for cell adhesion. Such bioavailable surfaces can be mimicked by tethered, solid-supported lipid bilayers (TBL) using polyethylene glycol (PEG) as a cushion. PEG can also be used for spatial organization of proteins and PEG linked as copolymer on a surface. Thus, cell motility can be tuned by variation of the surface parameters.

## PEG-Tethered Lipid Bilayers

Solid-supported lipid bilayer can act as a workbench for the study of membrane processes. The realization of tethered lipid bilayers is difficult. Here, we designed TLBs with a cushion thickness comparable to a bilayer dimension.[1] LipoPEG was used, as PEG is a weakly interacting cushion material. The PEG end is grafted to the solid surface and the lipid end can anchor a lipid bilayer (Fig. 1).

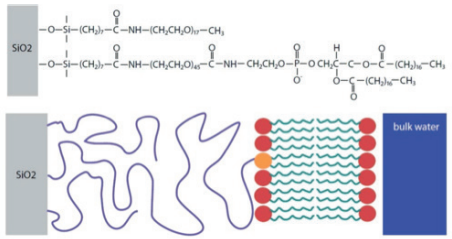


Fig. 1. Structure of the tethered lipid bilayer (TLB): (a) Chemical composition of the silane and PEG–lipid cushion. (b) Cartoon of the structure of the TLB consisting of the silicon oxide surface, the PEG cushion, one tethered lipid (yellow head), and several lipids in the bilayer (red heads). Bulk water is represented in blue. [1]

With FRAP measurements, we determined a diffusion constant of 2.1± 0.1 µm²s-1 for the TBL which is only 12% lower than diffusion constants of supported lipid bilayers (SLB). This suggests that the bilayer exhibits only a small immobile fraction without any grafted lipids as obstacles. Xray- and neutron scattering (N-REX+ at FRM2, instrument supervisor: A. Rühm) were performed to determine the structural layer composition of the TBL. A three layer model consisting of a silicon oxide layer, a PEG layer and a lipid chain region could fit the neutron measurements (Fig. 2). The PEG interlayer of the TLB is highly hydrated with a water content of 90±3%.

AFM indentation measurements proved the softness of the PEG layer perpendicular to the surface. As the TLB ruptures only after deformation of about 40 Å compared to 20 Å for a SLB, the additional deformation can be referred to the compression of the PEG cushion. Possible applications of such elevated lipid bilayers are, for example, the study of membrane-perforating proteins or binding studies of membrane-associated proteins.

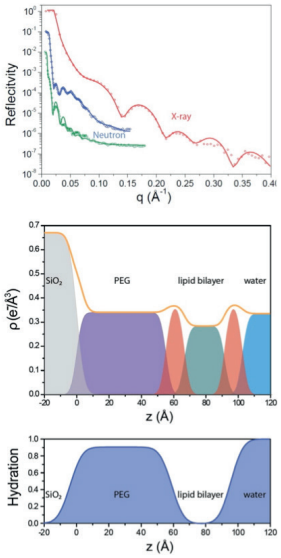


Fig. 2. (a) Normalized neutron and X-ray reflectivity data and fit (b) Electron density of the different layers of the system, extracted from the X-ray measurement. (c) Hydration of lipid bilayer and PEG cushion extracted from the difference of the neutron models at different contrasts (D2O and D2O/H2O mix with SLD 4.0 × 10–6 Å–2). [1]

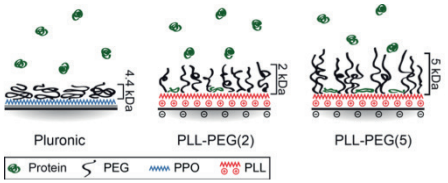


Fig. 3. Interpretation based on the neutron SLD profiles of the adsorption of FN in the three different polymer coatings Pluronic (PPO-PEG), PLL PEG(2) and PLL PEG(5). In the first case, FN is not adsorbed on the Pluronic, while on the PLL PEG samples FN penetrates the extended PEG layers to attach to underlying PLL. The higher PEG density leads to stiffer chains and therefore higher protein adsorption. [3]

## Cell Motility on PEG-Copolymers

To understand how cells and proteins interact on PEG copolymer surfaces, structural analysis is needed. It has been previously observed that cells are able to migrate on passivated PEG areas which were exposed to proteins such as fibronectin (FN). [2] Here, we employed neutron scattering (REFSANS at FRM2, instrument supervisor: J. F. Moulin) to probe the structure of different PEG layers and to determine the amount and distribution of FN in these PEG layers.[3] We focused our study on two polymer constructs, first the PEG grafted to a hydrophobic polymer anchor polypropylene oxide (PPO), and second the poly-L-lysine (PLL) PEG with PEG chains of both 2 kDa and 5 kDa. The REFSANS data revealed that PEG repellence is mainly influenced by the underlying polymer-layer and secondly by the PEG density. Hydrophobic layers such as PPO are shielded by the PEG chains and therefore are highly protein repellent. In the moiety of hydrophilic layers (PLL) protein adsorption of 0.4 mg/cm² for PLL-PEG(2) and 0.7 mg/cm² for PLL-PEG(5) was found. A too low PEG density leads to more protein adsorption as well as a too high grafting density of PEG on PLL as PEG brushes get stiffer and are not that flexible anymore (Fig.3).

Surface properties were compared with cell behavior. No cell adhesion was noticed as no protein is adsorbed on the PEG linked PPO polymer (Pluronic). In contrast, cell spreading was observed on PLL-PEG. Cell spreading on PLL-PEG(5) is comparable to on pure FN surfaces. Apart from different spreading, cell motility correlates with different surface properties as well. Cell motion was tracked by time-lapse fluorescence microscopy (Fig. 4). The longest persistence time of cell motion is observed on a pure FN surface whereas the highest velocity is observed on PLL PEG(5)(Fig. 4). As cells polarize in one direction (mostly random in absence of a chemo-attractant) they have a higher probability to move forward in the same direction instead of turning towards any other direction if the amount of protein is high. The highest speed is measured on PLL PEG(5). It exhibits fewer adhesion points than pure FN layers which leads on the one hand to more frequent interruption in the migration and on the other hand to faster movement, possibly due to faster detachment.

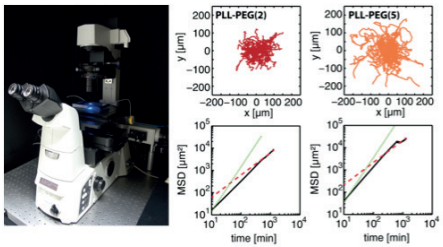


Fig. 4. (a) Setup for time-lapse fluorescence microscopy for cell tracking. (b) Representative cell trajectories on the two different substrates over a period of 24 h: PLL PEG(2) (red), PLL PEG(5) (orange) (c) Mean square displacements (MSD) (black curves) are plotted against time for the various substrates. As a guide to the eye, the MSD dependence for directed motion (dotted green curve, slope 2) and diffusive motion (dashed red curve, slope 1) are indicated. [3]

We generated artificial surfaces with TLB which could provide a more natural and cell like surrounding. Further studies on membrane interaction of living cells on solid surfaces containing FN and PEG are needed using neutron reflectivity. The knowledge about surface interaction of macromolecular biomolecules paves the way for more advanced micro-structured surfaces which can be used for cell migration assays or high-throughput single cell analysis.

## Acknowledgements

Financial support by the Deutsche Forschungs-gemeinschaft (DFG) via project B1 within the SFB 1032, the Excellence Cluster ‘Nanosystems Initiative Munich (NIM)’, the Center for NanoScience (CeNS), FP7 EU grants NanoTransKinetics and NanoMILE, and by BMBF-05K13WM1 and 05K10WM1 is gratefully acknowledged.

[1] S. Hertrich, F. Stetter, A. Ruhm, T. Hugel and B. Nickel, Langmuir, 2014, 30, 9442-9447.

[2] P. J. F. Röttgermann, A. Piera Alberola and J. O. Rädler, Soft Matter, 2014, 10, 2397-2404.

[3] P. J. Röttgermann, S. Hertrich, I. Berts, M. Albert, F. J. Segerer, J. F. Moulin, B. Nickel and J. O. Rädler, Macromol. Biosci., 2014,14, 1755-1763.

# Publication 4:
# Versatile Method to Generate Multiple Types of Micropatterns


http://dx.doi.org/10.1116/1.4940703

Biointerphases
A Journal of Biomaterials and Biological Interfaces

# Versatile method to generate multiple types of micropatterns

Felix Jakob Segerer, Peter Johan Friedrich Röttgermann, Simon Schuster, Alicia Piera Alberola, Stefan Zahler, and Joachim Oskar Rädler

Citation: Biointerphases **11**, 011005 (2016); doi: 10.1116/1.4940703
View online: http://dx.doi.org/10.1116/1.4940703
View Table of Contents: http://scitation.aip.org/content/avs/journal/bip/11/1?ver=pdfcov
Published by the AVS: Science & Technology of Materials, Interfaces, and Processing

# Versatile method to generate multiple types of micropatterns

Felix Jakob Segerer and Peter Johan Friedrich Röttgermann
*Faculty of Physics and Center for NanoScience, Ludwig-Maximilians-Universität München, Geschwister-Scholl-Platz 1, D-80539 Munich, Germany*

Simon Schuster
*Department of Pharmacy - Center for Drug Research, Pharmaceutical Biology, Ludwig-Maximilians-Universität München, Butenandtstr. 5-13, D-81377 Munich, Germany*

Alicia Piera Alberola
*Faculty of Physics and Center for NanoScience, Ludwig-Maximilians-Universität München, Geschwister-Scholl-Platz 1, D-80539 Munich, Germany*

Stefan Zahler
*Department of Pharmacy - Center for Drug Research, Pharmaceutical Biology, Ludwig-Maximilians-Universität München, Butenandtstr. 5-13, D-81377 Munich, Germany*

Joachim Oskar Rädler[a)]
*Faculty of Physics and Center for NanoScience, Ludwig-Maximilians-Universität München, Geschwister-Scholl-Platz 1, D-80539 Munich, Germany*

(Received 18 November 2015; accepted 13 January 2016; published 22 January 2016)

Micropatterning techniques have become an important tool for the study of cell behavior in controlled microenvironments. As a consequence, several approaches for the creation of micropatterns have been developed in recent years. However, the diversity of substrates, coatings, and complex patterns used in cell science is so great that no single existing technique is capable of fabricating designs suitable for all experimental conditions. Hence, there is a need for patterning protocols that are flexible with regard to the materials used and compatible with different patterning strategies to create more elaborate setups. In this work, the authors present a versatile approach to micropatterning. The protocol is based on plasma treatment, protein coating, and a poly(L-lysine)-grafted-poly(ethylene glycol) backfill step, and produces homogeneous patterns on a variety of substrates. Protein density within the patterns can be controlled, and density gradients of surface-bound protein can be formed. Moreover, by combining the method with microcontact printing, it is possible to generate patterns composed of three different components within one iteration of the protocol. The technique is simple to implement and should enable cell science labs to create a broad range of complex and highly specialized microenvironments. © *2016 American Vacuum Society*. [http://dx.doi.org/10.1116/1.4940703]

## I. INTRODUCTION

Micropatterning techniques have become an established tool for researchers interested in single-cell functions and dynamics[1–7] and the collective behavior of small cell assemblies and tissues.[8–10] Their significance for today's cell science arises from the fact that they provide direct control over the shape and functionality of the cell's environment on a microscopic scale.

How a cell adapts to the structure and composition of its microenvironment can give considerable insight into its intrinsic mechanical and functional properties.[11–13] In addition, micropatterns can be exploited to actively manipulate cell behavior. For instance, it has been found that the size and geometry of the accessible area can alter and direct the axis of cell polarization and division,[2,3,5] the positions and orientation of pseudopodia,[4] or the locations of junctions between adjacent cells.[14] Cell adhesion and migration depends in large part on the protein composition of a cell's surroundings,[15–17] but the relative density of adhesion sites,[18–20] as well as density gradients of surface-bound proteins, can influence and bias its spreading and motion.[21,22]

Micropatterning techniques should therefore provide for precise control over the shape of the cell's microenvironment, i.e., the distribution and concentration of surface-bound proteins. In addition, it should be compatible with a large variety of proteins and be capable of producing patterns composed of multiple protein species.

Most current micropatterning protocols are based on one of the following three approaches. Soft lithography in form of microcontact printing ($\mu$CP) involves protein transfer from a polymeric stamp, while the remaining surface is often passivated by PEGylation.[23–25] In photolithography, the properties of a surface or a precoated matrix are locally altered by photocleavage with a laser device or by exposing it to light through a photomask.[26–29] In plasma lithography, a surface that is partially protected by a shadow mask or stamp is modified/activated by exposure to a plasma (e.g., oxygen).[30–35] Protein deposition in the latter protocols is mainly achieved by surface adsorption from an aqueous solution. Each of these approaches has its own specific advantages. $\mu$CP provides flexibility with respect to the molecules that

[a)]Electronic mail: raedler@lmu.de

are transferred to the surface, and does not require advanced or expensive equipment. Photolithography-based protocols produce very homogeneous patterns and have also been extended to enable formation of gradients in the surface-bound protein density.[28] Finally, plasma-based approaches profit from the strong activation of the surface by the plasma exposure which can be exploited (1) directly to cause increased cell attachment on elsewise cell repellent substrates,[31,35] (2) as a basis to spatially control polymer or protein deposition or conformation,[30,32] and (3) to selectively remove a layer of protein or polymer.[34] The plasma treatment itself is a robust and effective procedure that provides fast working protocols and is applicable to a large variety of substrates. However, the diversity of substrates, coatings, and patterns used in the field of cell science is so great that no single existing technique is capable of fabricating designs suitable for all experimental conditions. In particular, gradients in protein density or the accurate deposition of different proteins within a multicomponent pattern are often difficult to accomplish. Additionally, since micropatterning should ideally be accessible to a broad range of labs, patterning methods should also be preferably easy to handle and cost efficient. Therefore, simple working protocols, which are adaptable to different experimental conditions such as proteins and substrates and can be combined with other patterning approaches to create more complex microenvironments, can be expected to stimulate further progress in this field.

In this paper, we present an alternative plasma based and simple means of creating micropatterns on a broad range of substrates. The technique is based on plasma-induced patterning in combination with PEGylation and protein coating, and is therefore referred to here as microscale plasma-initiated protein patterning ($\mu$PIPP). It provides control over the final concentration of protein on the surface and produces homogeneous and stable patterns on various substrates such as glass, tissue culture polystyrene (tc-PS), cyclic olefin copolymers (COCs), and parylene C. We show that gradients in the surface-bound protein density can be generated via protein incubation within a chemotaxis chamber. Finally, we combine the $\mu$PIPP protocol with $\mu$CP to create complex patterns consisting of up to three different components while providing accurate and adjacent relative positioning. The method presented in this paper should prove useful as a facile and versatile approach to the fabrication of a wide variety of micropatterns.

## II. EXPERIMENT

### A. Preparation of masters

The desired patterns can be designed by a drawing software, e.g., AUTOCAD (Autodesk) or CIRCUITPRO PL (LPKF Laser & Electronics). Masters for stamp preparation can then be created by following established protocols (such as those provided by photoresist producers like MicroChem) or the protocol provided in Sec. S1 of the supplementary material.[36] Note that labs that do not have the means to create stamp masters can order them online (from HTS Resources, for example). Once prepared, each master can be used to make multiple stamps.

### B. Stamp preparation

Poly(dimethylsiloxane) (PDMS) was prepared by mixing ten parts silicone elastomer with one part crosslinker (Sylgard Elastomer Kit, Dow Corning), and poured as a 1–3 mm thick layer onto the master and degassed in a desiccator. The coated master was then cured overnight at a temperature of 50 °C.

### C. Patterning

Sections II C 1–II C 3 describe the patterning protocols. The proteins used for patterning in this work were: fibrinogen labeled with Alexa-488, Alexa-594, or Alexa-647 (Life Technologies), respectively, fibronectin (YO Proteins) with and without Alexa-488 label, and laminin-1 (bio-techne) with and without Alexa-647 label. Note, however, that the technique may be used with a broad range of different proteins.

#### *1. Conventional μPIPP*

A PDMS stamp of the desired pattern was placed on the surface to be patterned [see Fig. 1(a)]. The assembly was then exposed to $O_2$ plasma at a pressure of 2 mbar in a plasma cleaner (Diener Femto) at 40 W for 3 min, thus activating the exposed parts of the surface (in general, high power and at least 2 min plasma treatment is recommended for reproducible patterns). A droplet of a 2 mg/ml PLL(20 kDa)-g[3.5]-PEG(2 kDa) [poly(L-lysine)-grafted-poly(ethylene glycol) (PLL-PEG)] (SuSoS) solution in 10 mM 4-(2-hydroxyethyl)-1-piperazineethanesulfonic acid (*p*H 7.4) and 150 mM NaCl was then placed at the edge of the stamp, and was drawn into the spaces between surface and stamp by capillary action. After 30 min at room temperature, the stamp was removed, and the substrate was rinsed with phosphate-buffered saline (PBS). Finally, a (50 $\mu$g/ml) solution of the desired protein (e.g., fibronectin, fibrinogen) dissolved in PBS was added for 30–60 min (if not noted otherwise), and the substrate was rinsed three times with PBS.

#### *2. Gradient patterning*

To set up a protein density gradient in the final pattern, the $\mu$PIPP protocol was applied to a chemotaxis slide. Therefore, the surface of a chemotaxis slide (ibidi, sticky-Slide Chemotaxis) was first patterned with PLL-PEG according to the standard $\mu$PIPP protocol [steps 1 and 2 in Fig. 1(a)]. Afterwards, the "sticky chamber" was attached and filled with PBS. The PBS on one side of each chamber was then replaced by 45 $\mu$l of a 100 $\mu$g/ml solution of protein in PBS according to the manufacturer's instructions[37] to create a gradient in the concentration of the protein solution. The patterned surface was incubated in this gradient for 40 min. Finally, the surface was rinsed by flooding the chamber three times with PBS.

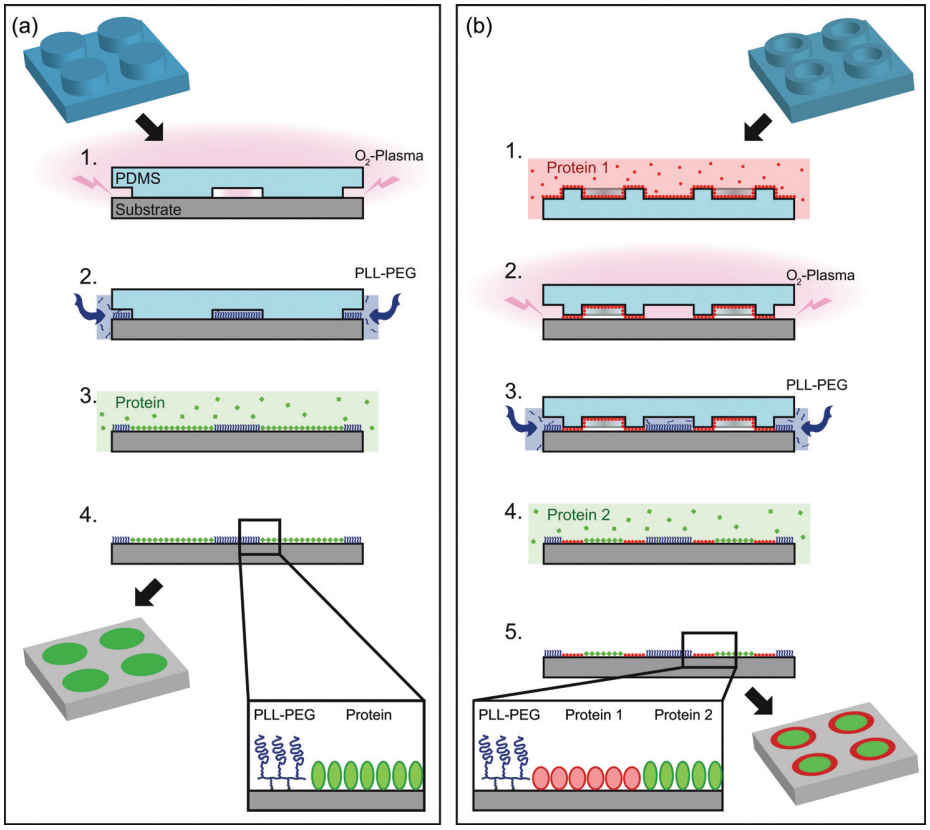


FIG. 1. Patterning protocols. (a) Patterning procedure for conventional $\mu$PIPP: (1) The surface is partially covered by a PDMS stamp of the desired pattern and exposed to $O_2$ plasma. (2) A PLL-PEG solution is applied to the margins of the stamp and is drawn over the exposed surface by capillary action. (3) The stamp is removed and the surface is incubated with the desired protein. (b) $\mu$PIPP combined with $\mu$CP: (1) Following UV-ozone activation (see Sec. II), the PDMS stamp is incubated with Protein 1. (2) The protein-coated stamp is inverted and Protein 1 is printed on the surface, which is simultaneously exposed to $O_2$ plasma. (3) PLL-PEG solution is applied to the stamp edge and drawn between stamp and surface by capillary action. (4) The stamp is removed, and the surface is incubated with Protein 2.

#### *3. Multicomponent patterning*

In order to obtain a pattern consisting of three different components, the basic $\mu$PIPP protocol was extended, as shown in Fig. 1(b). Note that this method works for all stamp geometries that provide enclosed cavities. The PDMS stamp was initially activated for 5 min in an UV-ozone cleaner (novascan) and incubated for about 1 h with a 50 $\mu$g/ml solution of the first protein. Incubated stamps were rinsed once with ultrapure water and dried for about 6 min. A COC substrate (ibidi) was then activated for 3 min in the UV-ozone cleaner before the stamp was set in place.[38] The subsequent procedure follows the standard $\mu$PIPP protocol. Note that if a third protein instead of PLL-PEG is used, no plasma treatment is necessary.

### D. Cell culture

#### *1. MDCK*

The Madin–Darby canine kidney (MDCK) cell line was cultured in minimum essential medium (c-c-pro) containing 2 mM L-glutamine and 10% fetal calf serum (FCS) at 37 °C in a 5% $CO_2$ atmosphere. Prior to experiments, cells were grown to 70%–80% confluence, trypsinized, and centrifuged at 1000 rcf for 3 min. Cell pellets were resuspended in Leibovitz's L15 medium with GlutaMAX (Gibco) and 10% FCS.

#### *2. HUVEC*

Human umbilical vein endothelial cells (HUVEC) were cultivated in endothelial cell growth medium 2 (ECGM) (Promocell) supplemented with 1% penicillin/streptavidin/amphotericin B (PAN-Biotech) and 10% FCS (PAA). Cells were incubated at 37 °C in a 5% $CO_2$ atmosphere. Prior to experiments, cells were overlaid with 1× trypsin/ethylenediaminetetraacetic acid (PAN-Biotech) to detach the cell layer. Subsequently, trypsin was inactivated by adding Dulbecco's modified Eagle's medium supplemented with 10% FCS. After inactivation, cells were centrifuged and the cell pellet was diluted in ECGM to desired concentration. For all experiments, cells were used in their third passage.

### E. Fluorescence staining

After a 24 h incubation on micropatterned plates, cells were washed twice with PBS and fixed with 4% paraformaldehyde for 10 min. After a second washing step with PBS, cells were permeabilized for 10 min using 0.2% Triton in PBS. Before staining, samples were exposed to 1% bovine serum albumin

(BSA) in PBS for 30 min to saturate nonspecific protein-binding sites, and then stained with a 1:400 dilution of rhodamine-phalloidin (Invitrogen/Thermo Scientific) and 0.5 $\mu$g/ml Hoechst 33342 (Sigma) diluted in 1% BSA in PBS. After 30 min, fixed cells were washed three times for 5 min each with PBS containing 0.2% BSA and sealed with FluorSave Reagent (Merck Millipore) and a coverslip.

### F. Microscopy

Phase-contrast and fluorescence images were taken on a Nikon TI Eclipse inverted microscope. Confocal microscopy was performed using a Leica SP8 microscope.

## III. RESULTS AND DISCUSSION

In the first set of experiments, we created grids of fibronectin-coated squares using $\mu$PIPP as described in Sec. II. Note that in this set of experiments, we used squares of 60 $\mu$m width, but in principle, pattern resolution is limited by the accuracy of the stamp master ($\sim$2 $\mu$m in our experiments). To test whether $\mu$PIPP is compatible with commonly used cell-culture substrates, we applied the procedure to standard tc-PS, glass, COC, parylene C, and PDMS. As depicted in Fig. 2, the method produces homogeneous protein patterns on all these surfaces. The method could be applied to these substrates without the need of any surface pretreatment or adjustment of the protocol. Cell adhesion and confinement to the patterned surfaces was achieved on tc-PS, as well as on glass and COC. Pattern quality was also high on parylene C, which is often used as a biocompatible coating for electronic devices. Although patterns were successfully produced on PDMS, confinement of cells within these patterns was not stable over time. (To vary the stiffness of the PDMS surface, monomer to crosslinker ratios of 1:5, 1:10, and 1:20, respectively, were used. The different stiffness had no influence on the confinement.) With the standard $\mu$PIPP protocol, the protein is physisorbed via hydrophobic effect on hydrophobic surfaces and via electrostatic interaction on charged surfaces. FN organization plays a key role in cell adhesion. The FN adsorption can be influenced by self-assembled monolayers with different terminal -OH, -$CH_3$, and -$NH_2$.[39,40] Such functionalization possibly can be realized via silanization on glass or plasma activated COC, tc-PS, or PDMS in a preliminary step. Due to the plasma treatment, the silane with the desired functional end groups would be removed at the areas where the PLL-PEG binds and only remain at the areas where protein gets bound later.

Notably, patterns produced by treatment with plasma can be visualized by phase-contrast as well as differential interference contrast microscopy (see Fig. S2 of the supplementary material[36]), owing to the fact that exposure to plasma slightly alters the altitude and degree of roughness of the surface (in the order of a few hundred nanometers), and hence changes its optical properties.[41,42] This feature simplifies working with the final pattern, as patterned regions can be located and identified without any need for fluorescence microscopy. In order to test whether the patterns produced are suitable for cell confinement over long timescales, we carried out time-lapse measurements of cells on patterned surfaces over extended time periods. As shown in Fig. S3 of the supplementary material[36] (and seen in earlier studies[7,10,43]), the patterns are stable and capable of confining cells over periods of up to several days. These results are in accordance with the work of Lussi *et al.*[44] which found good stability of PEGylation based cell confinements over time periods of three days; depending on the surface (e.g., tc-PS) stable confinements of up to 2 weeks could be observed.[36]

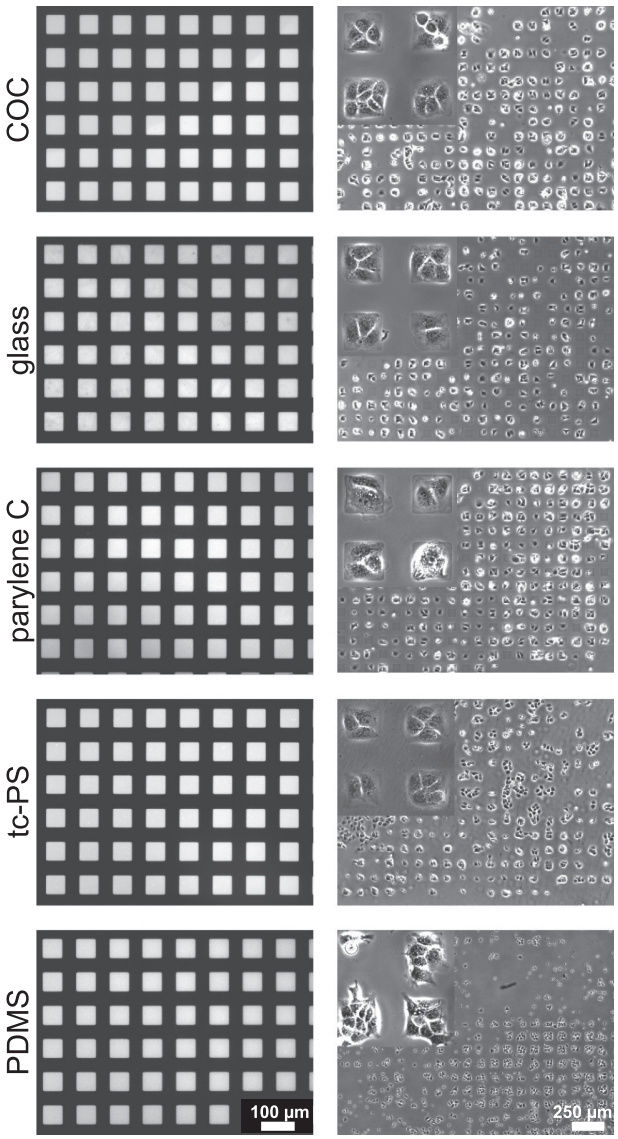


FIG. 2. $\mu$PIPP on different substrates. (Left column) Fluorescence images of fibrinogen Alexa-488 patterns on different substrates: COC, glass, parylene C, tc-PS, and PDMS (ratio 1:10). Black areas are passivated with PLL-PEG. (Right column) MDCK cells on fibronectin patterns 24 h after cell seeding (insets 5× magnified).

Protein coating by incubation (rather than stamping) has the advantage that the concentration of protein attached to the surface can be easily varied, either by adjusting the concentration of the protein solution $c_{sol}$ or the time of incubation $\tau$. The results of a series of experiments in which both parameters were systematically varied are shown in Fig.

3(a). Here, for three different incubation times $\tau = 5$, 15, and 25 min, the concentration of fibrinogen Alexa-488 in the solution was also varied as $c_{sol} = 7.5$, 15, 30, and 75 $\mu$g/ml. For each combination of $\tau$ and $c_{sol}$, we evaluated the fluorescence intensities of over 1500 patterns from four experiments. The low standard deviation of the measured distribution indicates that very homogeneous and reproducible patterns were generated. The mean values show that an increase in the incubation time $\tau$ or protein concentration in solution $c_{sol}$ leads to an increase in fluorescence intensity, and thus, assuming a linear dependence of protein density to fluorescence intensity, in the surface density of protein.

The adsorption behavior as a function of $c_{sol}$ is well fitted by the Langmuir expression for the adsorption isotherm[45]

$$c_{surf} = c_{max} \times \frac{\alpha \times c_{sol}}{1 + \alpha \times c_{sol}}. \quad (1)$$

Here, $c_{surf}$ denotes the surface concentration of the protein, $c_{max}$ the saturated surface concentration, and $\alpha$ the equilibrium constant in the case of Langmuir adsorption. Note, however, that in our experiments, adsorption to and desorption of protein from the surface depends on the time of incubation and hence is clearly not in equilibrium (at least not for $\tau = 5$ and 15 min, as $c_{surf}$ increases further for longer incubation times $\tau$). The data suggest, though, that an equilibrium regime may be asymptotically reached for longer incubation times $\tau$. Still, in the context of this paper, we use the Langmuir expression solely as an estimate for the adsorption behavior for different incubation concentrations. The dependence of $c_{surf}$ on $c_{sol}$ can be exploited to generate gradients in the density of the surface-bound protein within the micropatterns. To this end, we used a chemotaxis chamber to create a gradient in the concentration of the protein solution $c_{sol}$ in the protein incubation step of $\mu$PIPP. Using this method, we succeeded in creating gradients in the density of the surface-bound proteins within the micropatterns, which show approximately a linear profile, as can be seen in Fig. 3(b). The linear profile could be the result of theoretical linear diffusion gradient of the bulk concentration $c_{sol}$. Additional time-dependent effects of protein surface adsorption should play a minor role in low bulk concentration regime. Gradients in the concentration of proteins like fibronectin or vascular endothelial growth factor are known to have a guiding effect on cell migration and could therefore be exploited to orchestrate cell motion within the micropatterns.[21,22] After the pattern and a surface gradient have been prepared, the chemotaxis chamber can be used to set up an additional gradient of protein in the solution bathing the attached cells. In such a setup, the guidance cues of a gradient in the surface-bound protein density, a soluble protein gradient, and the cues provided by the micropattern are combined. Since *in vivo* cells are often confronted with such multicue situations, their implementation *in vitro* is a useful tool for cell sciences.[46]

In addition to single protein patterns, the technique is also capable of forming patterns consisting of three components. Such multicomponent patterning can be achieved by combining $\mu$PIPP with $\mu$CP. A simple and versatile implementation of this combination is available for all geometries that are designed in such a way that the PDMS stamp used provides enclosed cavities [Fig. 1(b)]. Using such geometries, the embossed parts of the stamp are directly used for $\mu$CP whereas the enclosed cavities which shield the surface from plasma without direct stamp contact allow for protein coating according to the standard $\mu$PIPP protocol. In this way, complex multicomponent patterns, such as those depicted in Fig. 4(a), can be created. Passivation with PLL-PEG is not essential in this procedure, and patterns consisting of three different types of proteins are possible as well [Fig. 4(c) and Fig. S4 of the supplementary material[36]]. In contrast to iterative methods of creating patterns of multiple components, the advantage of creating all functionalizations with the aid of the same stamp (and working iteration) is that the individual components can be placed directly adjacent to each other

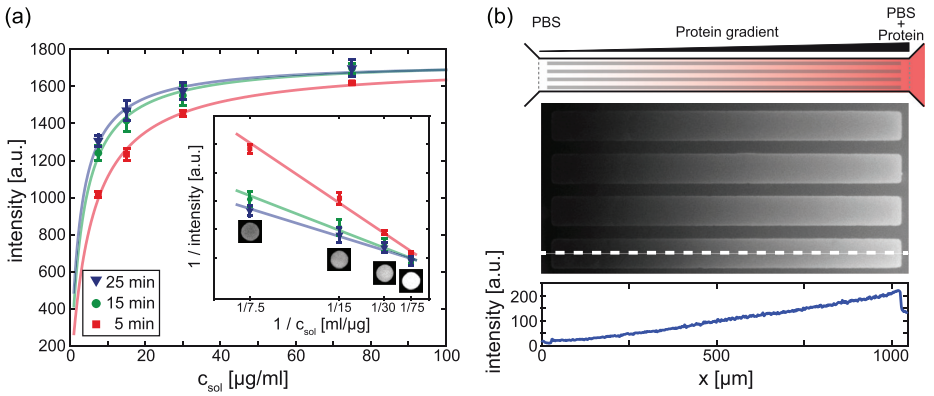


FIG. 3. Controlling the surface concentration of the protein. (a) Protein density within patterns can be adjusted by varying both the concentration in the incubation solution $c_{sol}$ and the incubation time $\tau$. We analyzed the fluorescence intensity of Alexa-488-labeled fibrinogen in micropatterns after incubation with $c_{sol}$ = 7.5, 15, 30 or 75 $\mu$g/ml for 5, 15, and 25 min. The data are well fitted by a Langmuir isotherm [Eq. (1)] with equilibrium constants $\alpha_\tau$ of $\alpha_5 = 0.18 \pm 0.06$, $\alpha_{15} = 0.31 \pm 0.16$, and $\alpha_{25} = 0.39 \pm 0.18$ for the different incubation times $\tau$, respectively ($\pm$ errors indicate confidence bounds of 95% within the fits). The inset shows the corresponding linear scaling in inverse presentation. Error bars indicate the standard deviation. (b) A gradient in the surface-bound protein density can be generated within the patterns by incubation in a protein concentration gradient formed in a chemotaxis chamber. Top down: (1) Formation of gradients on the chemotaxis slide. (2) Fluorescence image of micropatterned stripes obtained by incubation in a gradient of fibrinogen Alexa-488. (3) Measured intensity along the line shown in the middle panel.

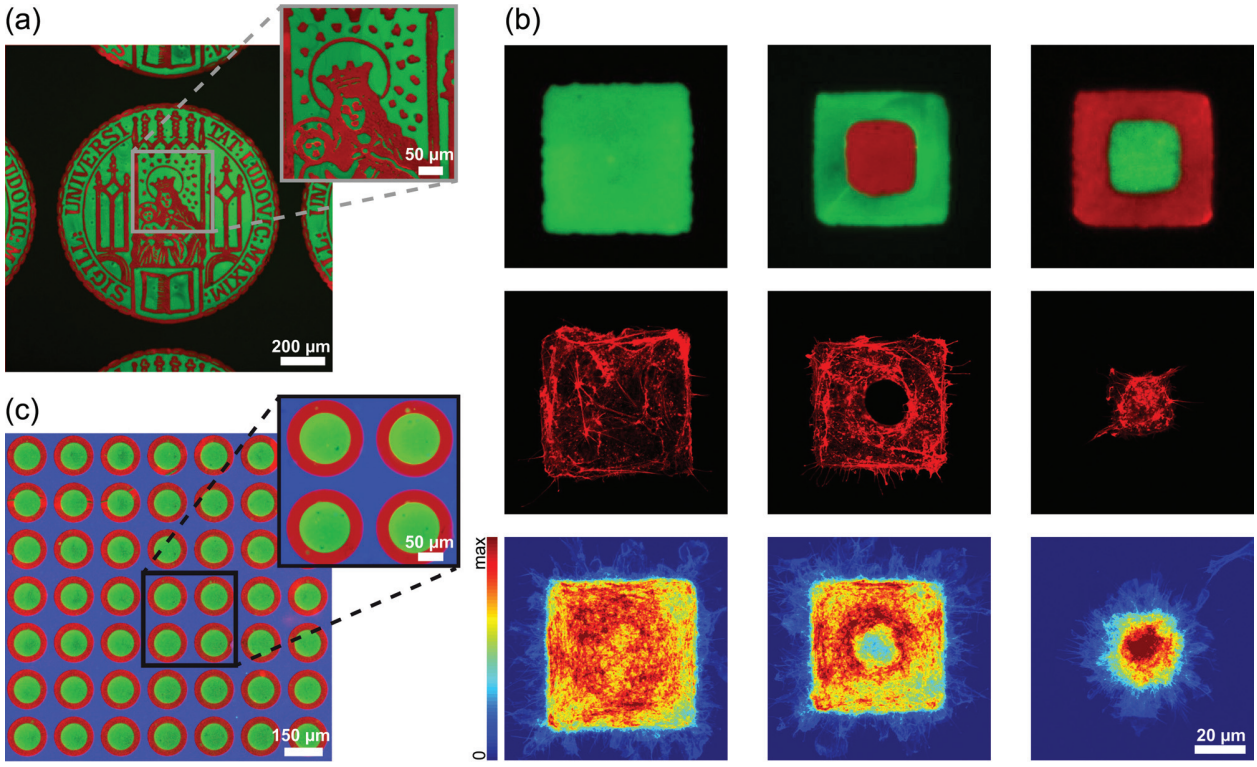


FIG. 4. Multicomponent patterning. By combining $\mu$PIPP with $\mu$CP, patterns consisting of three different functionalizations can be formed. (a) A complex pattern consisting of PLL-PEG (black) and fibrinogen labeled with Alexa-488 (green) and Alexa-647 (red), respectively. (b) Fluorescence image of patterns composed of fluorescently labeled fibronectin (green) and laminin (red) (top row). A representative confocal fluorescence image of the actin cytoskeleton of HUVECs arranged in such patterns (middle row), and a heat map of the actin cytoskeleton distribution of cells on over 20 evaluated patterns (bottom row). (Note that all three patterns were created with the multicomponent pattern protocol; hence, the inner portions of the framed squares are the only regions available for passive protein attachment by incubation.) (c) Framed circle pattern consisting of fibronectin Alexa-488 (red), fibrinogen Alexa-594 (blue), and laminin Alexa-647 (green), respectively.

and their relative positioning can hence be accurately controlled. Precise interfaces and pattern geometries consisting of multiple coatings can therefore be guaranteed without the potentially problematic step of bringing one pattern generation in the relatively right position to the last one. Note that $\mu$PIPP can also be combined with $\mu$CP in a successive manner (see Sec. S5 of the supplementary material[36]). This alternative way of combining both techniques complements the protocol described above and is able to produce multicomponent patterns such as "dashed" stripe patterns similar to the ones created via stamp-off protocols[47,48] (see Fig. S5 of the supplementary material[36]). If two or more proteins are adsorbed sequentially to a surface, the Vroman effect has to be considered.[49,50] This effect describes the exchange of adhered proteins by proteins in solution which is caused by a difference in surface affinity. In our case, we did not observe a strong protein exchange for the double and triple protein patterns (possible due to the fact that the proteins are bound irreversible via the hydrophobic effect).

By seeding cells on such multicomponent patterns, cellular responses to different surface coatings can be directly compared. As a proof of principle, we studied cell adhesion on "framed" patterns consisting of a square area coated with one kind of protein surrounded by a rim area coated with a second type of protein. We chose a standard passivation with PLL-PEG and the two extracellular matrix proteins fibronectin and laminin-1, which are both known to play a role in cell adhesion.[51,52] We found the adhesion of HUVECs to be strongly affected by the different protein coatings within the patterns. The cells were well confined within framed squares. Within the patterns, however, they avoided the parts coated with laminin-1, while adhering to the fibronectin-coated areas [Fig. 4(b)]. Such a decreased or an increased adhesion on laminin compared to other proteins has been reported before.[17,51] In our setup, the preference of fibronectin over laminin did neither depend on the pattern geometry nor on which of the proteins was printed and which was applied by incubation, as it becomes evident from comparison of columns 2 and 3 in Fig. 4(b). This suggests that, in this method, the effects of the proteins on cell adhesion do not depend on the way they are affixed to the surface.

## IV. CONCLUSION

In this work, we have described $\mu$PIPP, a novel and simple technique for the fabrication of micropatterned protein-coated surfaces for cell studies. As shown, $\mu$PIPP is compatible with various substrates and proteins typically used in cell research. The concentrations of proteins adsorbed to the surface can be readily controlled and gradients in the density of

surface-bound proteins can be formed. Both parameters are known to influence on cell spreading and migration.[18–22] Since an additional gradient can be set up in the liquid medium bathing the cells with the aid of the chemotaxis chamber, multicue situations can be produced, in which the synergy or competition between the surface and solution gradients can be studied within the defined geometries provided by a micropattern. Furthermore, in combination with $\mu$CP, patterns consisting of three different components can be generated. The fact that the deposition areas of all three components emerge from the design of a single stamp brings the advantage of high accuracy in the relative positioning of all components while still maintaining a relatively simple protocol. This set of patterning techniques thus permits complex microenvironments to be created and allows for direct comparisons of the impact of different surface functionalizations on cell adhesion and migration. Due to the simplicity and versatility of the protocol, it should find wide application as a micropatterning tool in cell science labs.

## ACKNOWLEDGMENTS

Financial support from the Deutsche Forschungsgemeinschaft (DFG) via Projects B01 and B08 in Sonderforschungsbereich (SFB) 1032 and from the European Union's Seventh Framework Programme (FP7) for Research (Project NanoMILE) is gratefully acknowledged.

[1]G. Mahmud, C. J. Campbell, K. J. M. Bishop, Y. A. Komarova, O. Chaga, S. Soh, S. Huda, K. Kandere-Grzybowska, and B. A. Grzybowski, Nat. Phys. **5**, 606 (2009).
[2]M. Théry, V. Racine, A. Pépin, M. Piel, Y. Chen, J. B. Sibarita, and M. Bornens, Nat. Cell Biol. **7**, 947 (2005).
[3]M. Théry, V. Racine, M. Piel, A. Pépin, A. Dimitrov, Y. Chen, J.-B. Sibarita, and M. Bornens, Proc. Natl. Acad. Sci. U.S.A. **103**, 19771 (2006).
[4]K. K. Parker *et al.*, Faseb J. **16**, 1195 (2002).
[5]X. Jiang, D. A. Bruzewicz, A. P. Wong, M. Piel, and G. M. Whitesides, Proc. Natl. Acad. Sci. U.S.A. **102**, 975 (2005).
[6]S. H. Yoon, Y. K. Kim, E. D. Han, Y. H. Seo, B. H. Kim, and M. R. Mofrad, Lab Chip **12**, 2391 (2012).
[7]M. Ferizi, C. Leonhardt, C. Meggle, M. K. Aneja, C. Rudolph, C. Plank, and J. O. Rädler, Lab Chip **15**, 3561 (2015).
[8]C. G. Rolli, H. Nakayama, K. Yamaguchi, J. P. Spatz, R. Kemkemer, and J. Nakanishi, Biomaterials **33**, 2409 (2012).
[9]A. K. Marel, M. Zorn, C. Klingner, R. Wedlich-Söldner, E. Frey, and J. O. Rädler, Biophys. J. **107**, 1054 (2014).
[10]F. J. Segerer, F. Thüroff, A. Piera Alberola, E. Frey, and J. O. Rädler, Phys. Rev. Lett. **114**, 228102 (2015).
[11]I. B. Bischofs, F. Klein, D. Lehnert, M. Bastmeyer, and U. S. Schwarz, Biophys. J. **95**, 3488 (2008).
[12]Y. H. Tee *et al.*, Nat. Cell Biol. **17**, 445 (2015).
[13]M. Théry, A. Pepin, E. Dressaire, Y. Chen, and M. Bornens, Cytoskeleton **63**, 341 (2006).
[14]Q. Tseng, E. Duchemin-Pelletier, A. Deshiere, M. Balland, H. Guillou, O. Filhol, and M. Théry, Proc. Natl. Acad. Sci. U.S.A. **109**, 1506 (2012).
[15]J. L. Junker and U. I. Heine, Cancer Res. **47**, 3802 (1987).
[16]K. J. Tomaselli, C. H. Damsky, and L. F. Reichardt, J. Cell Biol. **105**, 2347 (1987).
[17]C. D. Eichinger, T. W. Hsiao, and V. Hlady, Langmuir **28**, 2238 (2012).
[18]G. Maheshwari, A. Wells, L. G. Griffith, and D. A. Lauffenburger, Biophys. J. **76**, 2814 (1999).
[19]G. Maheshwari, G. Brown, D. Lauffenburger, A. Wells, and L. Griffith, J. Cell Sci. **113**, 1677 (2000).
[20]P. Rajagopalan, W. A. Marganski, X. Q. Brown, and J. Y. Wong, Biophys. J. **87**, 2818 (2004).
[21]J. T. Smith, J. K. Tomfohr, M. C. Wells, T. P. Beebe, T. B. Kepler, and W. M. Reichert, Langmuir **20**, 8279 (2004).
[22]L. Liu, B. D. Ratner, E. H. Sage, and S. Jiang, Langmuir **23**, 11168 (2007).
[23]M. Théry and M. Piel, Cold Spring Harbor Protoc. **4**, pdb.prot5255 (2009).
[24]S. Alom Ruiz and C. S. Chen, Soft Matter **3**, 168 (2007).
[25]J. L. Wilbur, A. Kumar, H. A. Biebuyck, E. Kim, and G. M. Whitesides, Nanotechnology **7**, 452 (1996).
[26]A. Azioune, M. Storch, M. Bornens, M. Théry, and M. Piel, Lab Chip **9**, 1640 (2009).
[27]M. Kim, J.-C. Choi, H.-R. Jung, J. S. Katz, M.-G. Kim, and J. Doh, Langmuir **26**, 12112 (2010).
[28]J. M. Belisle, D. Kunik, and S. Costantino, Lab Chip **9**, 3580 (2009).
[29]J. Nakanishi, Y. Kikuchi, T. Takarada, H. Nakayama, K. Yamaguchi, and M. Maeda, J. Am. Chem. Soc. **126**, 16314 (2004).
[30]Q. Cheng and K. Komvopoulos, Appl. Phys. Lett. **97**, 043705 (2010).
[31]M. Junkin and P. K. Wong, Biomaterials **32**, 1848 (2011).
[32]B. A. Langowski and K. E. Uhrich, Langmuir **21**, 10509 (2005).
[33]A. Tourovskaia, T. Barber, B. T. Wickes, D. Hirdes, B. Grin, D. G. Castner, K. E. Healy, and A. Folch, Langmuir **19**, 4754 (2003).
[34]R. Picone, B. Baum, and R. McKendry, "Plasma microcontact patterning (pcp): A technique for the precise control of surface patterning at small-scale," in *Methods in Cell Biology*, edited by M. Piel and M. Théry (Elsevier, Amsterdam, 2014), Vol. 119, Chap. 5, pp. 73–90.
[35]J. H. Kim, S. Seo, and J. Min, J. Biotechnol. **155**, 308 (2011).
[36]See supplementary material at http://dx.doi.org/10.1116/1.4940703 for additional protocols (S1,S4) and microscope images for pattern contrast (S2) and long-term confinement (S3).
[37]ibidi, "Sticky-slide chemotaxis" (2016), http://ibidi.com/xtproducts/en/ibidi-Labware/sticky-Slides/sticky-Slide-Chemotaxis.
[38]This UV activation step was found to be critical, since the surface has to be sufficiently hydrophilic to allow the printed protein to be properly transferred from the stamp yet hydrophobic enough to ensure that the protein is adsorbed from the incubation solution.
[39]M. Lin, H. Wang, C. Ruan, J. Xing, J. Wang, Y. Li, Y. Wang, and Y. Luo, Biomacromolecules **16**, 973 (2015).
[40]E. Battista, F. Causa, V. Lettera, V. Panzetta, D. Guarnieri, S. Fusco, F. Gentile, and P. A. Netti, Biomaterials **45**, 72 (2015).
[41]I. Beaulieu, M. Geissler, and J. Mauzeroll, Langmuir **25**, 7169 (2009).
[42]A. U. Alam, M. M. R. Howlader, and M. J. Deen, J. Micromech. Microeng. **24**, 035010 (2014).
[43]P. J. F. Röttgermann, A. P. Alberola, and J. O. Rädler, Soft Matter **10**, 2397 (2014).
[44]J. W. Lussi, D. Falconnet, J. A. Hubbell, M. Textor, and G. Csucs, Biomaterials **27**, 2534 (2006).
[45]I. Langmuir, J. Am. Chem. Soc. **40**, 1361 (1918).
[46]L. Lara Rodriguez and I. C. Schneider, Integr. Biol. **5**, 1306 (2013).
[47]R. A. Desai, M. K. Khan, S. B. Gopal, and C. S. Chen, Integr. Biol. **3**, 560 (2011).
[48]N. M. Rodriguez, R. A. Desai, B. Trappmann, B. M. Baker, and C. S. Chen, Langmuir **30**, 1327 (2014).
[49]L. Vroman and A. L. Adams, J. Biomed. Mater. Res. **3**, 43 (1969).
[50]S. Milani, F. Baldelli Bombelli, A. S. Pitek, K. A. Dawson, and J. Rädler, ACS Nano **6**, 2532 (2012).
[51]R. Carlsson, E. Engvall, A. Freeman, and E. Ruoslahti, Proc. Natl. Acad. Sci. U.S.A. **78**, 2403 (1981).
[52]R. I. Clyman, K. A. McDonald, and R. H. Kramer, Circ. Res. **67**, 175 (1990).

# “Versatile method to generate multiple types of micropatterns” Supplementary Material

F. J. Segerer,[a] P. J. F. Röttgermann,[a] S. Schuster,[b] A. Piera Alberola,[a] S. Zahler,[b] and J. O. Rädler*[a]

## S1 Preparation of stamp masters

As for conventional $\mu$CP, a master of the desired pattern was prepared on silicone using photolithography. The accuracy of the pattern depends on the material of the photo mask: PET masks are cheap in production but have only an accuracy of some micrometers, chrome masks are more expensive but can provide accuracies in submicrometer range. For the master preparation, an adhesion promoter (TI-Prime, MicroChemicals GmbH) was applied to a silicon wafer (Si-Mat) by spin-coating, first at 500 rpm for 5 s and then accelerating to 5000 rpm for 30 s. The wafer was baked for 2 min at 120°C on a hot plate. Then, a 15 $\mu$m thick layer of negative photoresist (SU-8 100, micro resist technology GmbH) was applied by spin-coating first at 500 rpm for 5 s and then accelerating to 2000 rpm for 35 s. Next, the wafer was soft baked at 65°C for 2 min and then at 95°C for 5 min. In the following step, the wafer was exposed to UV light (wavelength peaks: 365 nm, 405 nm, 436 nm) which was passed through a photo mask (e.g. Zitzmann GmbH) of the desired pattern (alternatively, a laser lithography device can be used to write the desired pattern directly in the photoresist). A 5 min post-exposure baking step was performed at 95°C in order to selectively crosslink the UV-exposed portions of the resist. Afterwards, the wafer was placed in a developer bath (mr-Dev 600, micro resist technology GmbH) for approximately 2 min. To inhibit crack formation in the photoresist layer, the wafer was baked again for 5 min at 95°C. Finally, the surface was silanized with perfluorotrichlorosilane (Sigma Aldrich) by silane evaporation.

## S2 Patterns viewed by phase-contrast and differential interference contrast microscopy

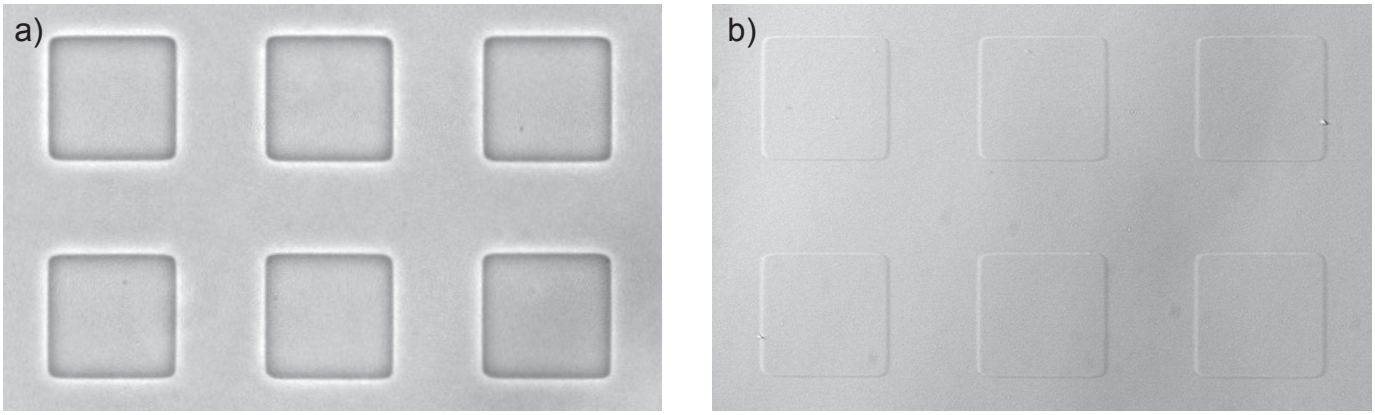


**Fig. S2** Pattern of squares (width 60 $\mu$m) created on COC by $\mu$PIPP imaged here by (a) phase-contrast and (b) differential interference contrast microscopy.

[a] *Faculty of Physics and Center for NanoScience, Ludwig-Maximilians-Universität München, Geschwister-Scholl-Platz 1, D-80539 Munich, Germany. Fax: +49 89 2180 3182; Tel: +49 89 2180 2438; E-mail: raedler@lmu.de*

[b] *Department of Pharmacy - Center for Drug Research, Pharmaceutical Biology, Ludwig-Maximilians-Universität München, Butenandtstr. 5-13, D-81377 Munich, Germany*

## S3 Long-term confinement of cells within the patterns

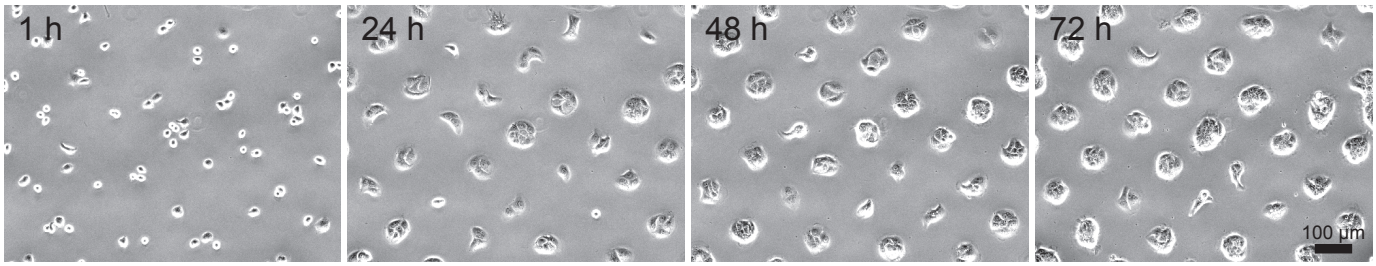


**Fig. S3** Patterns are stable and cells are confined to pattern elements for periods of several days. Cells confined in circle shaped micropatterns (radius 46 $\mu$m) at different time points after cell seeding.

## S4 Multicomponent patterning of fibrinogen with different labels

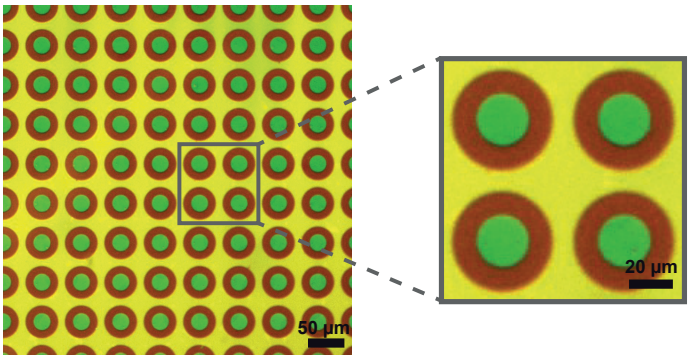


**Fig. S4** Framed circle pattern consisting of one protein with three different labels. First, fibrinogen Alexa-647 (red) printed via $\mu$CP, second, fibrinogen Alexa-594(yellow) drawn into the spaces between surface and stamp by capillary action, and third, fibrinogen Alexa-488 (green) attaching on the remaining areas via incubation in solution.

## S5 Multicomponent patterning by successive combination of $\mu$PIPP and $\mu$CP

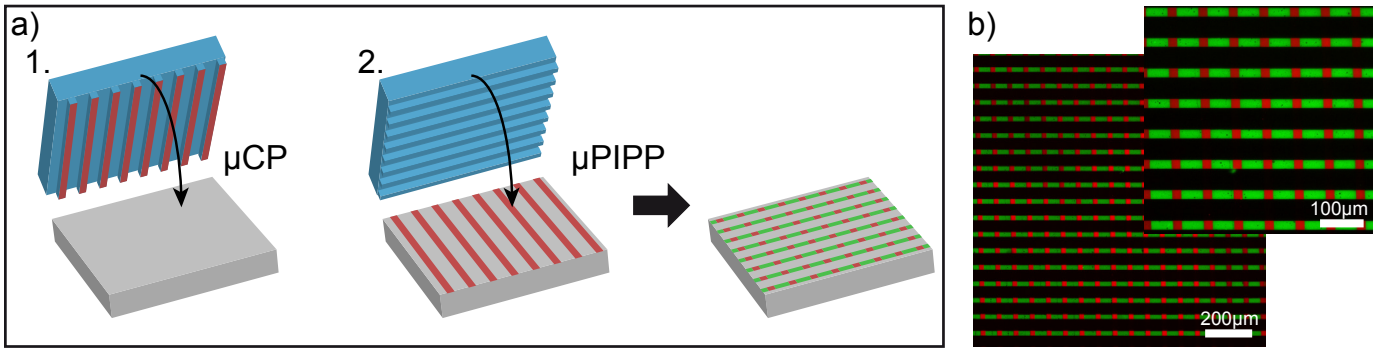


**Fig. S5** Alternative combination method of $\mu$PIPP and $\mu$CP. a) Patterning procedure: 1. A pattern of the first protein is transferred via $\mu$CP to a COC substrate. 2. For the $\mu$PIPP step, an untreated stamp is placed orthogonal to the pattern created via $\mu$CP. Due to the plasma the first protein is partially removed and replaced by areas coated with a second protein or PLL-PEG respectively. b) Dashed line pattern created via the successive combination of $\mu$CP and $\mu$PIPP. The pattern is composed of PLL-PEG (black), fibrinogen labeled with Alexa-488 (green) and Alexa-647 (red), respectively.

Additionally to the method described in the main text, $\mu$PIPP can also be combined with $\mu$CP in a successive way to create multicomponent patterns. Here, the pattern of the first protein created via $\mu$CP is partially removed by the plasma (Fig. S5a). Analogously to the already described protocol of multicomponent patterning, a PDMS stamp (in this case a stripe pattern) was initially activated in an UV-ozone cleaner (novascan) for 5 min and incubated with a 50 $\mu$g/ml solution of the first protein for about 1 h. The incubated stamp was rinsed once with ultrapure water and dried for about 6 min. The stamp is placed on a COC substrate (ibidi) that was activated with UV-ozone for 3 min. For better transfer of the protein to

the surface, a droplet of PBS was applied to the margins of the stamp which is drawn underneath by capillary action. The sample was incubated for 1 h. Afterwards, the stamp was removed and the surface was dried in an airflow. In the next step, for the $\mu$PIPP, a second untreated stamp (in our case the same stripe pattern geometry as used above) was placed as a mask in orthogonal direction to the stripes created via $\mu$CP. The subsequent procedure follows the standard $\mu$PIPP protocol with PLL-PEG passivation and incubation of a second protein. The plasma exposed parts of the $\mu$CP protein pattern get ablated and only the parts that are covered by the second stamp are preserved. This successive combination of both techniques can, for instance, be used to create stripe patterns composed of one kind of protein that are interrupted by fields of another protein type (Fig. S5b).

# Publication 5:
# Time-Resolved Study of Nanoparticle Induced Apoptosis Using Microfabricated Single Cell Arrays


http://dx.doi.org/10.3390/microarrays5020008

microarrays

MDPI

Article

# Time-Resolved Study of Nanoparticle Induced Apoptosis Using Microfabricated Single Cell Arrays

**Peter J. F. Röttgermann[1], Kenneth A. Dawson [2] and Joachim O. Rädler [1,*]**

[1] Faculty of Physics and Center for NanoSciene (CeNS), Ludwig-Maximilians-Universität, Geschwister-Scholl-Platz 1, 80539 Munich, Germany; peter.roettgermann@physik.lmu.de

[2] Centre for BioNano Interactions, School of Chemistry and Chemical Biology, University College Dublin, Belfield, Dublin 4, Ireland; Kenneth.A.Dawson@cbni.ucd.ie

* Correspondence: raedler@lmu.de; Tel.: +49-89-2180-2438; Fax: +49-89-2180-3182

Academic Editor: Holger Erfle

Received: 3 March 2016 / Accepted: 7 April 2016 / Published: 15 April 2016

**Abstract:** Cell fate decisions like apoptosis are heterogeneously implemented within a cell population and, consequently, the population response is recognized as sum of many individual dynamic events. Here, we report on the use of micro-patterned single-cell arrays for real-time tracking of nanoparticle-induced (NP) cell death in sets of thousands of cells in parallel. Annexin (pSIVA) and propidium iodide (PI), two fluorescent indicators of apoptosis, are simultaneously monitored after exposure to functionalized polystyrene ($PS-NH_2$) nanobeads as a model system. We find that the distribution of Annexin onset times shifts to later times and broadens as a function of decreasing NP dose. We discuss the mean time-to-death as a function of dose, and show how the $EC_{50}$ value depends both on dose and time of measurement. In addition, the correlations between the early and late apoptotic markers indicate a systematic shift from apoptotic towards necrotic cell death during the course of the experiment. Thus, our work demonstrates the potential of array-based single cell cytometry for kinetic analysis of signaling cascades in a high-throughput format.

**Keywords:** single cell array; cytotoxicity; nanoparticle; dose-response; correlation studies; micropatterning

## 1. Introduction

The interactions of nanoparticles (NPs) with cells remain poorly understood and this has raised concerns about potential cytotoxicity and environmental risks [1,2]. In recent years, many *in-vitro* and *in-vivo* studies have probed the safety and biocompatibility of NPs. Evidence for cytotoxicity was found in particular cases of NPs, depending on the cell line and test conditions used [3–6]. The majority of studies uses population-based toxicity assays, such as colorimetric assays for cell viability [7,8] and DNA fragmentation assays [9], or techniques with single-cell sensitivity, such as flow cytometry [10,11], image cytometry [12], or fluorescence microscopy [3], but data are taken at limited number of specific time points. It has recently been noted that cell-to-cell variations, which are averaged out in populations measurements but are revealed in single cell analysis, have non-genetic origins and provide important information on noise in apoptosis regulating circuitry [13,14]. Naturally occurring fluctuations in the levels of regulatory proteins can lead to "fractional killing" and subpopulations of very sensitive or robust cells [14–16]. Moreover, time-lapse microscopy allows for fully time-resolved studies, in which every cell is tracked over time via brightfield and fluorescence microscopy [17–19]. These studies can directly assess the heterogeneous dynamic response of individual cells.

It has become clear that, in NP toxicity studies, the precise experimental conditions have a crucial bearing on the results, and great care is required in the preparation and administration of NPs. Depending on the biological media chosen, NPs may be coated with a protein corona that further facilitates their entry into cells and determines their effect on cells [20,21]. However, we still know little about the biochemical pathways that are affected by NPs and how NPs eventually induce cell death. In order to understand the internal signaling processes and discriminate between various pathways that lead to cell death, it is crucial to measure cellular responses to NPs at the single-cell level using quantitative readouts. Typical cell death markers used in microscopy are Annexin V and propidium iodide (PI). The Annexin V-based marker pSIVA shows increased fluorescence when bound to phosphatidylserine (PhS), and hence indicates the externalization of plasma-membrane PhS induced by activation of the caspase-dependent pathway. The impermeable dye PI stains the nucleus only when the integrity of the cell membrane is lost, and this can be related to the late stage of apoptosis, the so-called secondary necrosis [22,23]. The use of cells captured on microfluidic- [24] or micro-patterned cell arrays offers a route towards high-throughput analysis. We recently introduced micro-patterned substrates for time-resolved measurements on regularly arrayed cells, and showed that cells self-organize onto fibronectin-coated sites surrounded by boundaries passivated by treatment with poly-L-lysine- polyethylene glycol [25,26].

Here, we perform NP toxicity studies on single cell arrays which yield time-resolved data at single-cell resolution. For a first proof of concept, we choose hepato carcinoma derived HuH7 liver cells exposed to $PS-NH_2$ NPs, because liver cells are relevant in bio-accumulation and frequently used in toxicity studies. The timing of the onset of activation of two fluorescent markers — pSIVA, indicating the early apoptotic events and PI, the late stage of apoptosis or necrosis — was measured and the corresponding distribution function was analyzed as a function of dose. We show that the dynamics of NP-induced apoptosis is dose dependent, and relate the time-to-death value $\tau_{50}$ to the effective $EC_{50}$ value. Furthermore, we find that the timing and signal intensities of the different apoptosis events are correlated.

## 2. Results

### *2.1. Highly Parallel Assessment of the Kinetics of Cell Death*

Figure 1 shows the workflow for data acquisition in time-resolved single-cell measurements. Microstructured surfaces for the preparation of single cell arrays are fabricated by selective plasma-induced patterning on either dishes or 8 well slides. Cells are seeded onto the microstructures and are left for five hours to self-arrange and adhere to the fibronectin adhesion sites. Cells are then exposed to different doses (0.1 to 100 $\mu g \cdot mL^{-1}$) of $PS-NH_2$ NPs, and incubated together with the fluorescent markers pSIVA-IANBD (an Annexin B12 derivative) and PI. No further washing step is applied. NPs were obtained from the QualityNano project and were characterized by transmission electron microscopy (see Supplementary 1, Figure S1). The patterned cell samples are then scanned at 10-min intervals under physiological conditions for up to 48 h, using an automated microscope. Typically, 500 single cell traces of fluorescence intensities are extracted from image stacks using grid-based read-out software.

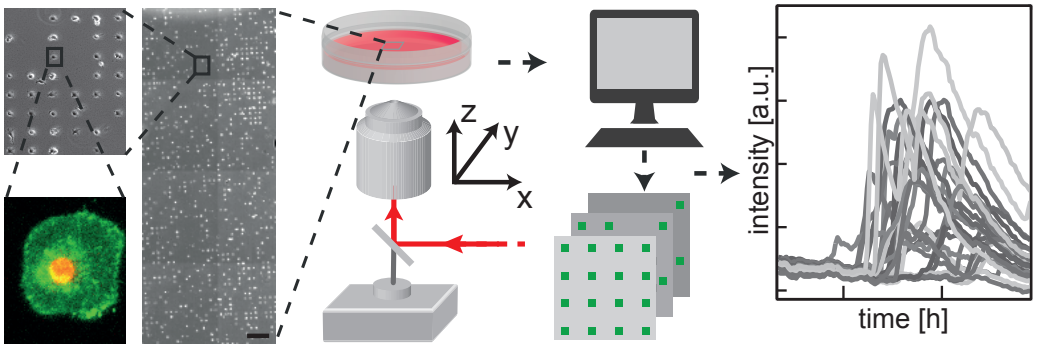


**Figure 1.** Protein-coated arrays are generated following plasma-induced patterning of μ-dishes. Cells distribute themselves on the patterned sites of an array after seeding. They are then exposed to NPs and monitored for activation of fluorescent markers of cell death for up to 72 h using an automated fluorescence microscope. The ease of automated image processing on the cell lattice enables high-throughput analysis of the kinetics of single-cell fluorescence. Scale bar: 500 μm (close-ups 5× and 25× magnified, respectively).

Figure 2 shows brightfield (left) and fluorescence (right) microscopy images taken at selected time-points (0, 7, 14, 21 and 28 h, see movie in Supplementary 2). Green fluorescing cells indicate the binding of pSIVA to the cell surface at an early stage of apoptosis. During the the first 14 h, few cells show green fluorescence, and fluorescence emission begins in earnest only after 20 h. A similar pattern is observed for the red PI signal, albeit with a somewhat later onset (see below). In the time series and in Movie S2, the subsequent onset times of the green and red signal is clearly visible. The fading of the green signal towards the end of the measurement (28 h) is due to bleaching of the IANBD fluorophore.

Fluorescence intensities integrated over the adhesion sites (indicated as squares in Figure 2) for each single cell can be extracted from the image stacks, and Figure 3 shows the time courses of single-cell intensities as a function of the NP exposure time. The plasma membrane transition of PhS in individual cells is readily detectable from the time course of the pSIVA signal (Figure 3A).

Loss of plasma membrane integrity is indicated by a sharp increase of the PI signal (Figure 3B). The times of onset of these changes in individual cells can be clearly seen for pSIVA as well as for PI. For an NP dose of 10 $\mu g \cdot mL^{-1}$, the first apoptotic events are seen after 3 h and most cell deaths occur about 20 h after administration of NPs. Although not discernible in Figure 3B, in any given cell the PI signal appears about 70 min on average after the onset of the pSIVA signal (see below). The pSIVA time courses typically reveal a sudden, sharp increase followed by an exponential decrease. The latter behavior is attributable to the bleaching of the fluorophores. Some pSIVA traces show a second peak after the onset. Morphological changes such as formation of apoptotic bodies can lead to an increase in area and hence cause a higher mean fluorescence signal. In contrast, the decrease in the PI signal after the onset of cell death is related to non-specific staining of RNA, which lowers the intensity of PI fluorescence [27]. Most notably the peak intensities of both pSIVA and PI time courses vary quite considerably. The peak intensity distribution are plotted in the Supplementary Figure S3A, and we will discuss this cell-to-cell variability later on. In the following we focus on the onset-times of the pSIVA and PI signals. In our automated data analysis these values were determined as the times at which the signal first exceeds a level equivalent to 25% of the maximum background intensity. Cells which were dead from the beginning (less than 5%) are excluded from analysis. Also cell sites showing multiple occupation were excluded. Multiple occupation occurs either by the attachment of two cells on the same site or by cell division. The exclusion of dividing cells could lead to a bias in the cell death population as cells in a late cell cycle are neglected. However, the percentage of dividing cells over 40 hours is relatively low, about 15% in the case of cell arrays without exposure to NPs. Addition of NPs even decreases the ratio to 10% for a dose of 0.1 $\mu g \cdot mL^{-1}$ and below 1% for

higher doses. This decreased cell division rate is due to cell-cycle arrest [28]. Hence, as the fraction of dividing cells is low, the restriction of our analysis to pure single cell events should not adversely bias the assessment of cell death timing.

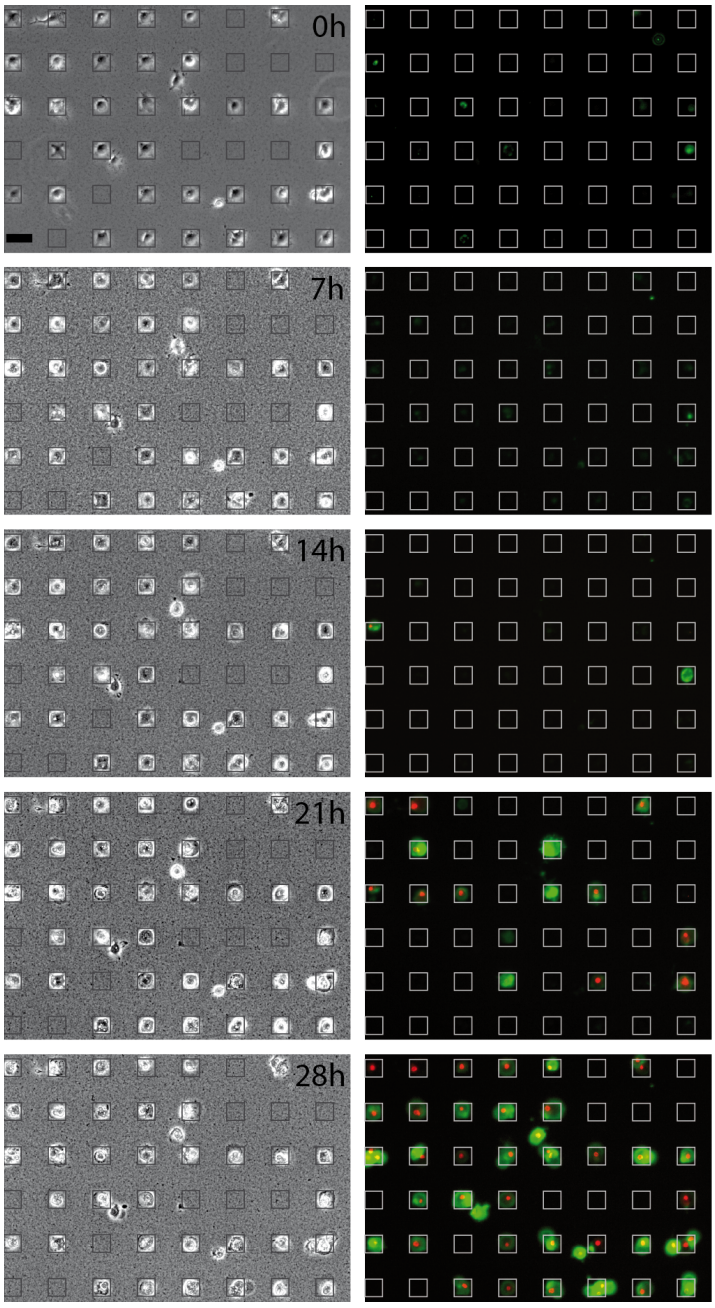


**Figure 2.** Time series of apoptotic events induced by PS − $NH_2$-NPs monitored by brightfield illumination and fluorescence imaging at 0, 7, 14, 21 and 28 h after seeding. The graininess seen in the brightfield images is attributed to sedimentation of nanoparticle (NP) aggregates. In the fluorescence images, green staining (pSIVA-IANBD) indicates exposure of phosphatidylserine (PhS) on the outer leaf of the plasma membrane bilayer, the red nuclear staining (PI) indicates subsequent loss of plasma membrane integrity. The heterogeneity in the times of onset of apoptosis can be clearly seen. Square lattices are drawn for better visualization. Scale bar: 50 µm.

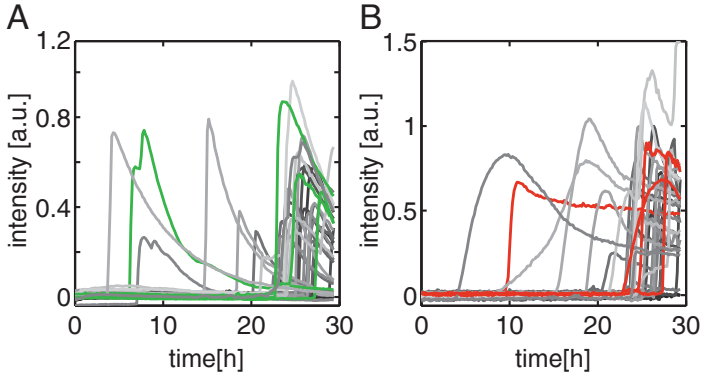


**Figure 3.** Representative time traces of fluorescent signals monitored in the polarity Sensor for Viability and Apoptosis (pSIVA) (**A**) and propidium iodide (PI) (**B**) channels. A few typical traces are highlighted in green and red, respectively. The first apoptotic events are observed after 3 h whereas the majority of induced cell deaths occur after 20 h. The decrease in the pSIVA signal at late times can be attributed to bleaching of the fluorophores. Fluorescent signals are background corrected.

### *2.2. Time Dependent Dose Response Function*

The distribution of times of apoptosis provides a measure for the dynamic response of a cell population. We studied the evolution of the onset distribution with increasing NP dosage (from 0.1 $\mu g \cdot mL^{-1}$ to 100 $\mu g \cdot mL^{-1}$). In Figure 4A, normalized frequency distributions of onset times of the PI signal are plotted against time for various doses. It can be seen that with increasing NP dose, cell death onset shifts to earlier times. The same behavior is found in the corresponding time distribution for the pSIVA signal (data not shown), which also exhibits the same characteristic broadness in the distribution. The distributions are fitted by log-normal distributions. A log-normal distribution describes a process which is the product of many independent processes and is found (in our case as well as in literature) to fit the cell death distribution better than Gaussians [29]. For the lowest dose (0.1 $\mu g \cdot mL^{-1}$), the mean onset time is 27.8 $\pm$ 0.4 h, and for the highest dose it is shifted to the markedly earlier time of 8.9 $\pm$ 0.3 h. In addition, the distributions become narrower as the dosage is increased. The fraction of cells that dies is given by the cumulative sum. Figure 4B shows the cumulative sum against time and the fits to the integrated log-normal function. The time-course of the fraction of dead cells highlights the dependence of the dynamic response on dosage. At the highest dose almost all cells are dead after 24 h, whereas only 20% of those exposed to the lowest dose have died by this time. We evaluate this "dynamic dose response" by plotting the time of 50% cell death, $\tau_{50}$, against dosage (Figure 4E). A drop in time-to-death with increasing dose can clearly be seen. The variance, $\sigma$, *i.e.*, the width of the log-normal distribution, in contrast, increases with dose (Figure 4F). In order to retrieve standard $EC_{50}$ values from the log-normal distributions shown in Figure 4A,B, we replotted the data as a whole as a function of dose rather than time (see Figure 4C). In this way, we obtain dose-response curves for various time points, *i.e.*, effective end-points. We find that with increasingly late end-point the dose-response curves shift to lower dose values as depicted in Figure 4C. As a consequence, the $EC_{50}$ value, *i.e.*, the dose that result in 50% cell death, appears to depend on the time point of examination (Figure 4D). After a sufficiently long time, the $EC_{50}$ values asymptotically approach a constant value. In our case, sufficiently long means 20 h, as is clearly seen in Figure 4D. However, it is not obvious *a priori* at which time point a reliable $EC_{50}$ value can be obtained. In order to test if the heterogeneous response is caused by the NPs negative controls were performed (see Supplementary S4, Figure S3A,D). The negative control for the time-lapse measurement as well as a viability assay showed a high viability (95%) after four days. Further, in order to show the applicability of the single cell assay to other toxic agents, a dose response measurement for the anti-cancer drug staurosporine was performed (see Supplementary 4, Figure S3A–C).

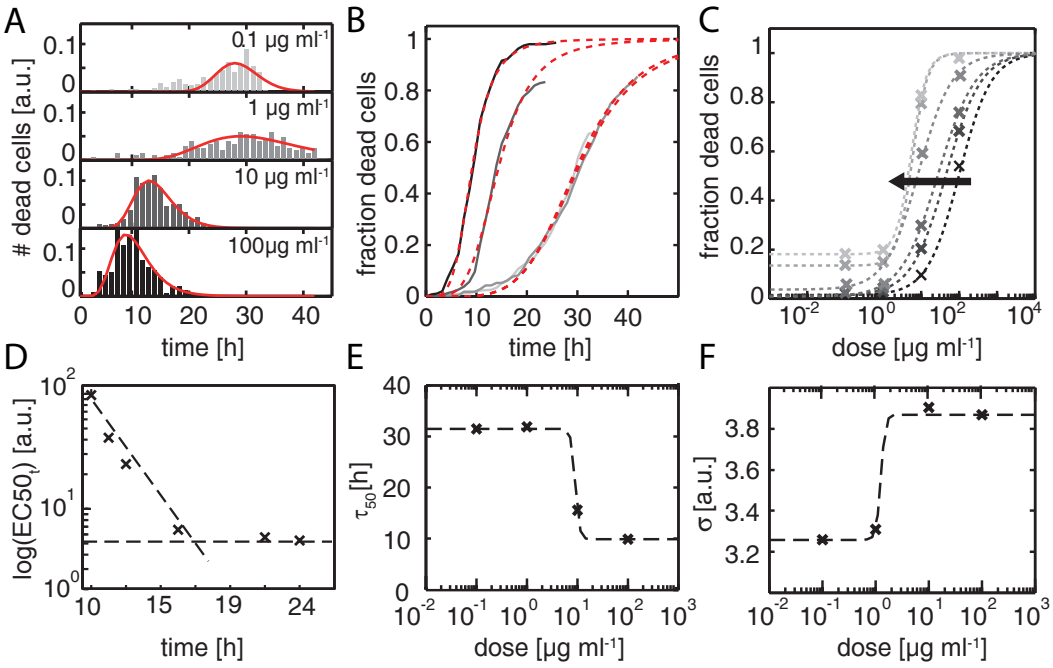


**Figure 4.** (**A**) Normalized frequency distributions of times of cell death (onset times of the PI signal) are plotted against time for the indicated NP doses. Note that the distributions shift to earlier time points and get narrower with increasing NP dose. The distributions are fitted to log-normal functions (red curve); (**B**) The cumulative fraction of dead cells is plotted against time for NP doses of 0.1 µg · mL$^{-1}$ (light gray), 1 µg · mL$^{-1}$ (medium gray), 10 µg · mL$^{-1}$ (dark gray), and 100 µg · mL$^{-1}$ (black). At the lowest dose 20% of the cells die within 24 h, whereas at the highest dose all cells (100%) are dead by this point. The cumulative distributions are fitted to log-normal functions (red curve); (**C**) Standard dose-response curves with fraction of dead cells which can be extracted from the distribution of (**B**) for several different time points between 10 and 24 h (black to light gray). Data are fitted to dose-response functions (dashed lines). The $EC_{50}$ values shift towards lower dose with increasing late time endpoints (black arrow); (**D**) The $EC_{50}$ values are plotted in logarithmic scale against the endpoints. At an end-point of 18 h, the $EC_{50}$ value approaches a constant value; (**E**, **F**) Time points $\tau_{50}$ (**E**) and a rate-dependent $\sigma$ (**F**) for the cumulative distributions are plotted against dose. Both values exhibit dose-response behavior

### *2.3. Two-Parameter Correlation of Cell Death*

Next, the degree of correlation between onset times of the early and late apoptotic markers was examined. In Figure 5A, the interval $\Delta t$ between the onset of the pSIVA signal $t_{pSIVA}$ and that of the PI signal $t_{PI}$ is plotted against the time of cell death, which we again define as $t_{PI}$. The scatter plot shows that there is a tendency for $\Delta t$ to decrease with time of death. In fact, cells that die earlier, *i.e.*, in the time window between 5 and 10 h exhibit a delay time of about 100 to 300 min while late events of cell death show almost no delays. The correlation is underlined by a principal component analysis (PCA), which shows a tilted major axis, as indicated by the grey ellipse in the scatter plot. The correlation between pSIVA and PI onset times is also well brought out by the Pearson's correlation coefficient (for details, see data analysis in Experimental Section). The Pearson's correlation in this case is 0.96, and hence clearly indicates a strong correlation at the scale from zero (no correlation) to one (full correlation). Extending this concept to all measurable parameters of the apoptotic time trace we also investigated the cross-correlations of the onset time $t_{on}$ with maximal intensity $I_{max}$, and duration of onset $t_{duration}$ (*i.e.*, the time of increase from background to maximum signal for both the pSIVA and PI fluorescence). The correlation matrix is shown in Figure 5B for a dose of 10 µg · mL$^{-1}$. Interestingly, the maximal intensity $I_{max}$(pSIVA) correlates negatively with the onset

of apoptosis (−0.6/−0.56). This possibly indicates a connection with cell size or caspase activity, or it may be related to fluorescence bleaching. Indeed, the heterogeneity of the pSIVA fluorescence intensity depends on the amount of PhS exposed, and hence depends on the level of activation of caspase3 [30,31]. Also the maximal intensity $I_{max}$ (PI) is negatively correlated, albeit weakly, with the onset of apoptosis $t_{on}$ (−0.23, −0.2). Likewise $I_{max}$ (PI) is weakly correlated with $I_{max}$(pSIVA) (0.34). Both pSIVA and PI signals depend on cell size, which is in turn cell-cycle dependent. However, there is also substantial intrinsic cell-to-cell variation in the size of the nucleus (see Supplementary Figure S2B) [32,33]. For completeness, we also show the correlation of the duration times of the onset. The duration $t_{duration}$(PI) is negatively correlated with the onset of apoptosis $t_{on}$ (−0.46/−0.43). $t_{duration}$(PI) moderately correlates with $I_{max}$ of pSIVA (0.47). Cells that die late undergo more rapid loss of membrane integrity, which leads to a faster increase in the PI signal. pSIVA $t_{duration}$ does not, or only weakly, correlates with other parameters (0.14, 0.3, −0.02, and 0.03).

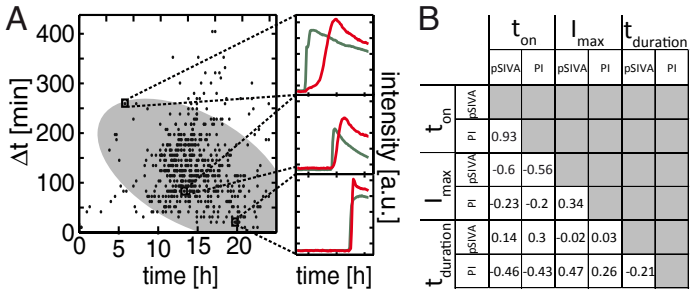


**Figure 5.** (**A**) The interval separating early-stage apoptosis (only pSIVA) from secondary necrosis (pSIVA+PI) varies depending on the onset time of apoptosis. This time difference $\Delta t$ is plotted against the onset time. The grey ellipse represents a $2\sigma$ interval of a principal component analysis (PCA). Three representative time traces of apoptotic cells are depicted for better visualization: Cells that die at later time-points transit faster into secondary necrosis; (**B**) Different parameters of apoptotic cells are extracted from the time traces and displayed as a correlation matrix: onset times $t_{on}$, maximum intensity $I_{max}$ and duration of onset for pSIVA and PI. Maximal pSIVA intensity $I_{max}$, and duration (spread) of onset time of PI $t_{duration}$ are negatively correlated with the onset of apoptosis.

## 3. Discussion

In this work, we demonstrate the advantages of time-resolved analysis of single cell arrays on microstructured substrates for studies of the dynamics of NP-induced cell death. The individual cell traces permit virtually continuous monitoring of apoptotic events indicated by the markers pSIVA and PI. The wealth of information provided by this approach, in comparison to standard population-based toxicity tests, is obvious. The technique has allowed us to demonstrate that the time distribution function of apoptosis onset is dose dependent, and to introduce the $\tau_{50}$ value as a measure for fast or slow toxic efficacy. Conversely, the $EC_{50}$ value is seen to depend on the time-point of measurement. The dependence of the $EC_{50}$ value has been discussed previously [34]. It has also been noted that a time-dependent $EC_{50}$ becomes exceedingly problematic in the low-dose regime, when toxicity occurs on time scales that exceed the duration of experimental observations [35,36]. In this case it can be argued that the $\tau_{50}$ value is the more useful measure. In the conventional approach, the evaluation of an $EC_{50}$ value for weakly toxic nanomaterials is complicated not only by the choice of end-point, but also involves the risk of under- or over-estimating the toxic effect. In contrast to highly time-resolved measurements of many cells, our methodology allows us to extrapolate from the behavior of the relevant measured curve in order to get a first indication of toxicity risk in *in-vitro* systems.

A second major advantage of single cell data with high time resolution lies in the fact that successive events can be correlated in time. As described earlier, single-cell time-courses yield distinct onset times showing that the pSIVA signal precedes the PI signal. It is generally accepted that a

difference in onset time between the two events is indicative of apoptosis-induced cell death. Hence in our case, as we clearly observe a pSIVA-PI time difference — at least in the early phase of NP exposure — cells death is induced via the apoptosis pathway. However, as the experiment proceeds, the delay between the onset of pSIVA and PI activation becomes shorter. Short delay times are interpreted as a signature of necrotic or necroptotic cell death. In our set-up, the number of necrotic cells rises with increasing duration of the experiment. This time-dependent upsurge in the incidence of necrosis in toxicity assays has been reported before, and has two possible causes. First, failure to eliminate apoptotic bodies, due to the lack of phagocytes *in-vitro*, promotes the transition from apoptotic to necrotic cell death [22,23]. Secondly, cells that undergo apoptosis affect neighboring cells towards cell death [37]. In addition, accumulation of NPs in cells over time, with a concomitant decrease in cell fitness, might contribute the increase of necrosis. At all events, the time-resolved single-cell approach quantifies the necrotic shift in the cell culture death with unprecedented directness. The utility of the single-cell strategy for exploring temporal correlations between fluorescent signals can also be extended by employing multiple markers indicative for distinct cellular events. As shown by the work of Wang et al. multiple markers can be used to elucidate the pathway induced by NPs [21].

## 4. Experimental Section

### *4.1. Cell Culture*

HuH7 cells were cultured in RPMI supplemented with 2 mM L-glutamine (c-c-pro) and 10% fetal calf serum. Cells were grown to 70%–80% confluence, trypsinized and centrifuged at 1000 rcf for 3 min. Cell pellets were re-suspended in either cell medium or, for the experiments in Leibovitz's L15 medium with GlutaMAX (Gibco), 10% fetal calf serum and 1 mM calcium chloride. Cells were stained with polarity Sensor for Viability and Apoptosis (pSIVA-IANBD, Novus Biologicals) [38,39] (the stock solution was diluted 1:50) and 1 μM propidium iodide (Novus Biologicals). Cell dyes were added without any further washing step. As a positive control for cell death staurosporine (Sigma Aldrich) was used at doses between 0.5 and 25 μM.

### *4.2. NP Preparation and Characterization*

Core size and shape of the $PS-NH_2$ NPs (provided by QualityNano, UCD) were determined with a transmission electron microscope (TEM). NPs were adsorbed onto a Formvar/carbon film-coated grid and were observed with a Jeol 1011 TEM. Sizes of the NPs were determined with ImageJ and further analyzed in MATLAB (see Supplementary 1 Figure S1). Further characterization was carried out in the context of the QualityNano project [10,40]. Prior to use, NPs were vortexed for 1 min to obtain maximal dispersity, although aggregates of >1 μm were still present. Cells were exposed either to $PS-NH_2$ (0.1 $\mu g \cdot mL^{-1}$, 1 $\mu g \cdot mL^{-1}$, 10 $\mu g \cdot mL^{-1}$, and 100 $\mu g \cdot mL^{-1}$, corresponding to a surface concentration of 14 $ng \cdot cm^{-2}$ to 14 $\mu g \cdot cm^{-2}$). NPs were kept in solution for the duration of the measurement.

### *4.3. Micropatterning*

The micro-structured surfaces were produced by selective oxygen plasma treatment (Femto Diener, 40 W for 3 min) on a topas substrate (μ-dishes ibidi GmbH) with subsequent passivation using either μ-dishes or 8 well slides. Selectivity was achieved using a polydimethylsiloxane (PDMS) stamp (cast from a master produced by photolithography) as a mask. The parts exposed to plasma were passivated with 1 $mg \cdot mL^{-1}$ PLL(20k)-g(3.5)-PEG(2k) (SuSoS AG) in aqueous buffer (10 mM HEPES pH 7.4 and 150 mM NaCl). The remaining sectors were rendered cell adherent by exposure to 50 $\mu g \cdot mL^{-1}$ fibronectin (YoProteins) for 1 h. The samples were thoroughly rinsed with PBS and stored in cell medium at room temperature prior to seeding (8000 cells per 8 well and 50,000 per μ-dish).

### *4.4. Time-Resolved Fluorescence Microscopy*

Images were taken with an inverted Nikon Ti Eclipse microscope with phase-contrast and a fluorescent lamp with multiple filter sets (GFP, propidium iodide). Samples were kept at a constant temperature of 37 °C with an ibidi heating system (ibidi GmbH). Pictures were recorded every 10 min over a period of between 24 and 48 h.

### *4.5. Image and Data Analysis*

Raw images were pre-processed in ImageJ. For the image analysis on the cell grid and a background correction the in-house plug-in Microwell Analysis was used. Multiple occupied sites, determined at the end of the measurement, were filtered out. The time of onset of apoptosis/secondary necrosis was defined as the point at which the pSIVA/PI signal first exceed the threshold of 25% of the basal background . This definition was in good agreement with manual tracking. The duration of the onset time was determined as the interval between the first local maximum of the smoothed curve and the crossing of the threshold. The dose-response of the log-normal distribution of dead cells $dc(t)$ was fitted by

$$dc(t) = A * exp\left(\frac{log(t) - \mu}{\sqrt{(2\sigma)}}\right)^2$$

and the fraction of dead cells $F(t)$, the cumulative sum of the distribution, by

$$F(t) = 0.5 * \left[1 + erf\left(\frac{log(t) - \mu}{\sqrt{(2\sigma^2)}}\right)^2\right]$$

where $A$ denotes amplitude, $t$ the time, $\sigma$ the standard deviation, and μ the mean. The dose-response curves for the fraction of dead cells $F(dose)$ in Figure 4C were fitted by

$$F(dose) = y_0 + \frac{-y_0}{1 + (EC_{50}/dose)^n}$$

with rate $n$, the basal rate $y_0$, and the $EC_{50}$ value at which 50% of cells are dead. Onset times of the two markers were analyzed, and the subsequent correlation analysis was carried out, in MATLAB. For the principal component analysis, the eigenvectors were calculated for the data set of $t_{PI}$ and Δt. In Figure 5A, the plotted axis of the ellipse correspond to those eigenvectors with lengths of two standard deviations $\sigma$. The ellipse is centered on the mean. The correlation coefficient was defined by Pearson's correlation :

$$\rho(X, Y) = \frac{Cov(X, Y)}{\sigma(X)\sigma(Y)}$$

with the covariance $Cov(X, Y)$ of the two parameters $X$ and $Y$ and their related standard deviation $\sigma$.

## 5. Conclusions

In summary, we provide the first kinetic analysis of NP-induced cell death based on single cell arrays. The resulting time-resolved measurements enable us to measure the onset distribution function of NP-induced apoptosis and a differentiated time-dependent picture of the NP dose-response relationship emerges. Future use of micro-arrays for high-throughput acquisition of single cell time-lapse data will pave the way to kinetic investigations of cell death in *in-vitro* and could potentially uncover aspects of the action NPs trapped within cells, thus allowing for the detailed characterization of nanomaterial pathways using single cell cross-correlation. Hence automated microscopy combined with micro-array technology might evolve into a potent platform for nanomaterial characterization and beneficially complement toxicity risk assessment.

**Supplementary Materials:** The following are available online at http://www.mdpi.com/2076-3905/5/2/8/s1.

**Acknowledgments:** We are grateful to Christian Meggle for writing the image analysis plug-in in ImageJ. Financial support from the FP7 EU grants NanoMILE and NanoTransKinetics, and the Excellence Cluster 'Nanosystems Initiative Munich (NIM)' is gratefully acknowledged.

**Author Contributions:** Peter J. F. Röttgermann and Joachim O. Rädler conceived and designed the experiments; Peter J. F. Röttgermann performed the experiments; Peter J. F. Röttgermann analyzed the data; Kenneth A. Dawson contributed reagents/materials/analysis tools; Peter J. F. Röttgermann and Joachim O. Rädler wrote the paper.

**Conflicts of Interest:** The authors declare no conflict of interest.

## References

1. Colvin, V.L. The potential environmental impact of engineered nanomaterials. *Nat. Biotech.* **2003**, *21*, 1166–1170.
2. Nel, A.; Xia, T.; Madler, L.; Li, N. Toxic potential of materials at the nanolevel. *Science* **2006**, *311*, 622–627.
3. Anguissola, S.; Garry, D.; Salvati, A.; O'Brien, P.J.; Dawson, K.A. High content analysis provides mechanistic insights on the pathways of toxicity induced by amine-modified polystyrene nanoparticles. *PLoS ONE* **2014**, *9*, e108025.
4. Elsaesser, A.; Howard, C.V. Toxicology of nanoparticles. *Adv. Drug Deliv. Rev.* **2012**, *64*, 129–137.
5. Love, S.A.; Maurer-Jones, M.A.; Thompson, J.W.; Lin, Y.S.; Haynes, C.L. Assessing nanoparticle toxicity. *Annu. Rev. Anal. Chem.* **2012**, *5*, 181–205.
6. Lu, X.; Liu, Y.; Kong, X.; Lobie, P.E.; Chen, C.; Zhu, T. Nanotoxicity: A growing need for study in the endocrine system. *Small* **2013**, *9*, 1654–1671.
7. Fonseca, C.; Simões, S.; Gaspar, R. Paclitaxel-loaded PLGA nanoparticles: preparation, physicochemical characterization and in vitro anti-tumoral activity. *J. Control. Release* **2002**, *83*, 273–286.
8. Kommareddy, S.; Amiji, M. Preparation and evaluation of thiol-modified gelatin nanoparticles for intracellular DNA delivery in response to glutathione. *Bioconjugate Chem.* **2005**, *16*, 1423–1432.
9. Jose, G.P.; Santra, S.; Mandal, S.K.; Sengupta, T.K. Singlet oxygen mediated DNA degradation by copper nanoparticles: potential towards cytotoxic effect on cancer cells. *J. Nanobiotechnology* **2011**, *9*, 9.
10. Bexiga, M.G.; Varela, J.A.; Wang, F.; Fenaroli, F.; Salvati, A.; Lynch, I.; Simpson, J.C.; Dawson, K.A. Cationic nanoparticles induce caspase 3-, 7- and 9-mediated cytotoxicity in a human astrocytoma cell line. *Nanotoxicology* **2011**, *5*, 557–567.
11. Wlodkowic, D.; Skommer, J.; Darzynkiewicz, Z. Flow cytometry-based apoptosis detection. *Methods Mol. Biol.* **2009**, *559*, 19–32.
12. Summers, H.D.; Rees, P.; Holton, M.D.; Rowan Brown, M.; Chappell, S.C.; Smith, P.J.; Errington, R.J. Statistical analysis of nanoparticle dosing in a dynamic cellular system. *Nat. Nano* **2011**, *6*, 170–174.
13. Xia, X.; Owen, M.S.; Lee, R.E.; Gaudet, S. Cell-to-cell variability in cell death: can systems biology help us make sense of it all? *Cell Death Differ.* **2014**, *5*, e1261.
14. Spencer, S.L.; Gaudet, S.; Albeck, J.G.; Burke, J.M.; Sorger, P.K. Non-genetic origins of cell-to-cell variability in TRAIL-induced apoptosis. *Nature* **2009**, *459*, 428–432.
15. Love, K.R.; Bagh, S.; Choi, J.; Love, J.C. Microtools for single-cell analysis in biopharmaceutical development and manufacturing. *Trends Biotechnol.* **2013**, *31*, 280–286.
16. Ware, M.J.; Godin, B.; Singh, N.; Majithia, R.; Shamsudeen, S.; Serda, R.E.; Meissner, K.E.; Rees, P.; Summers, H.D. Analysis of the Influence of Cell Heterogeneity on Nanoparticle Dose Response. *ACS Nano* **2014**, *8*, 6693–6700.
17. Aftab, O.; Nazir, M.; Fryknas, M.; Hammerling, U.; Larsson, R.; Gustafsson, M.G. Label free high throughput screening for apoptosis inducing chemicals using time-lapse microscopy signal processing. *Apoptosis* **2014**, *19*, 1411–1418.
18. Albeck, J.G.; Burke, J.M.; Aldridge, B.B.; Zhang, M.; Lauffenburger, D.A.; Sorger, P.K. Quantitative analysis of pathways controlling extrinsic apoptosis in single cells. *Mol. Cell* **2008**, *30*, 11–25.
19. Forrester, H.B.; Albright, N.; Ling, C.C.; Dewey, W.C. Computerized video time-lapse analysis of apoptosis of REC:Myc cells X-irradiated in different phases of the cell cycle. *Radiat. Res.* **2000**, *154*, 625–639.
20. Milani, S.; Baldelli Bombelli, F.; Pitek, A.S.; Dawson, K.A.; Rädler, J. Reversible *versus* irreversible binding of transferrin to polystyrene nanoparticles: Soft and hard corona. *ACS Nano* **2012**, *6*, 2532–2541.

21. Wang, F.; Yu, L.; Monopoli, M.P.; Sandin, P.; Mahon, E.; Salvati, A.; Dawson, K.A. The biomolecular corona is retained during nanoparticle uptake and protects the cells from the damage induced by cationic nanoparticles until degraded in the lysosomes. *Nanomedicine* **2013**, *9*, 1159–1168.
22. Silva, M.T. Secondary necrosis: The natural outcome of the complete apoptotic program. *FEBS Lett.* **2010**, *584*, 4491–4499.
23. Vanden Berghe, T.; Grootjans, S.; Goossens, V.; Dondelinger, Y.; Krysko, D.V.; Takahashi, N.; Vandenabeele, P. Determination of apoptotic and necrotic cell death in vitro and in vivo. *Methods* **2013**, *61*, 117–129.
24. Wlodkowic, D.; Faley, S.; Zagnoni, M.; Wikswo, J.P.; Cooper, J.M. Microfluidic single-cell array cytometry for the analysis of tumor apoptosis. *Anal. Chem.* **2009**, *81*, 5517–5523.
25. Röttgermann, P.J.; Hertrich, S.; Berts, I.; Albert, M.; Segerer, F.J.; Moulin, J.F.; Nickel, B.; Rädler, J.O. Cell motility on polyethylene glycol block copolymers correlates to fibronectin surface adsorption. *Macromol. Biosci.* **2014**, *14*, 1755–1763.
26. Röttgermann, P.J.F.; Piera Alberola, A.; Rädler, J.O. Cellular Self-Organization on Micro-Structured Surfaces. *Soft Matter* **2014**, *10*, 2397–2404.
27. Waring, M.J. Complex formation between ethidium bromide and nucleic acids. *J. Mol. Biol.* **1965**, *13*, 269–282.
28. Kim, J.A.; Åberg, C.; de Cárcer, G.; Malumbres, M.; Salvati, A.; Dawson, K.A. Low dose of amino-modified nanoparticles induces cell cycle arrest. *ACS Nano* **2013**, *7*, 7483–7494.
29. Furusawa, C.; Suzuki, T.; Kashiwagi, A.; Yomo, T.; Kaneko, K. Ubiquity of log-normal distributions in intra-cellular reaction dynamics. *Biophysics* **2005**, *1*, 25–31.
30. Frasch, S.C.; Henson, P.M.; Kailey, J.M.; Richter, D.A.; Janes, M.S.; Fadok, V.A.; Bratton, D.L. Regulation of phospholipid scramblase activity during apoptosis and cell activation by protein kinase C$\delta$. *J. Biol. Chem.* **2000**, *275*, 23065–23073.
31. Lee, S.H.; Meng, X.W.; Flatten, K.S.; Loegering, D.A.; Kaufmann, S.H. Phosphatidylserine exposure during apoptosis reflects bidirectional trafficking between plasma membrane and cytoplasm. *Cell Death Differ.* **2013**, *20*, 64–76.
32. Edens, L.J.; White, K.H.; Jevtic, P.; Li, X.; Levy, D.L. Nuclear size regulation: from single cells to development and disease. *Trends Cell Biol.* **2013**, *23*, 151–159.
33. Huber, M.D.; Gerace, L. The size-wise nucleus: Nuclear volume control in eukaryotes. *J. Cell Biol.* **2007**, *179*, 583–584.
34. Krippendorff, B.F.; Neuhaus, R.; Lienau, P.; Reichel, A.; Huisinga, W. Mechanism-based inhibition: Deriving K(I) and k(inact) directly from time-dependent IC(50) values. *J. Biomol. Screen* **2009**, *14*, 913–923.
35. Vandenberg, L.N.; Colborn, T.; Hayes, T.B.; Heindel, J.J.; Jacobs, D.R.J.; Lee, D.H.; Shioda, T.; Soto, A.M.; vom Saal, F.S.; Welshons, W.V.; *et al*. Hormones and endocrine-disrupting chemicals: Low-dose effects and nonmonotonic dose responses. *Endocr Rev.* **2012**, *33*, 378–455.
36. Yedjou, C.; Moore, P.; Tchounwou, P. Dose- and time-dependent response of human leukemia (HL-60) cells to arsenic trioxide treatment. *Int. J. Environ. Res. Public Health* **2006**, *3*, 136–140.
37. Gregory, C.D.; Pound, J.D.; Devitt, A.; Wilson-Jones, M.; Ray, P.; Murray, R.J. Inhibitory effects of persistent apoptotic cells on monoclonal antibody production in vitro: Simple removal of non-viable cells improves antibody productivity by hybridoma cells in culture. *mAbs* **2009**, *1*, 370–376.
38. Kim, Y.E.; Chen, J.; Chan, J.R.; Langen, R. Engineering a polarity-sensitive biosensor for time-lapse imaging of apoptotic processes and degeneration. *Nat. Meth.* **2010**, *7*, 67–73.
39. Kim, Y.E.; Chen, J.; Langen, R.; Chan, J.R. Monitoring apoptosis and neuronal degeneration by real-time detection of phosphatidylserine externalization using a polarity-sensitive indicator of viability and apoptosis. *Nat. Protoc.* **2010**, *5*, 1396–1405.
40. Wang, F.; Bexiga, M.G.; Anguissola, S.; Boya, P.; Simpson, J.C.; Salvati, A.; Dawson, K.A. Time resolved study of cell death mechanisms induced by amine-modified polystyrene nanoparticles. *Nanoscale* **2013**, *5*, 10868–10876.


# Supplementary Materials: Time-Resolved Study of Nanoparticle Induced Apoptosis Using Microfabricated Single Cell Arrays

**Peter Johan Friedrich Röttgermann[1], Kenneth Adrian Dawson [2] and Joachim Oskar Rädler [1,*]**

## Supplementary Material

### Supplementary 1

Core size and shape of the amine PS-NPs were characterized with TEM. NPs were adsorbed onto a Formvar/carbon film-coated grid and were observed with a Jeol 1011 TEM. The mean size of the particles was determined to be 35 $\mu m$ (Figure S1C). Note that aggregated particles were observed in the experiment as well as in TEM images (Figure S1B).

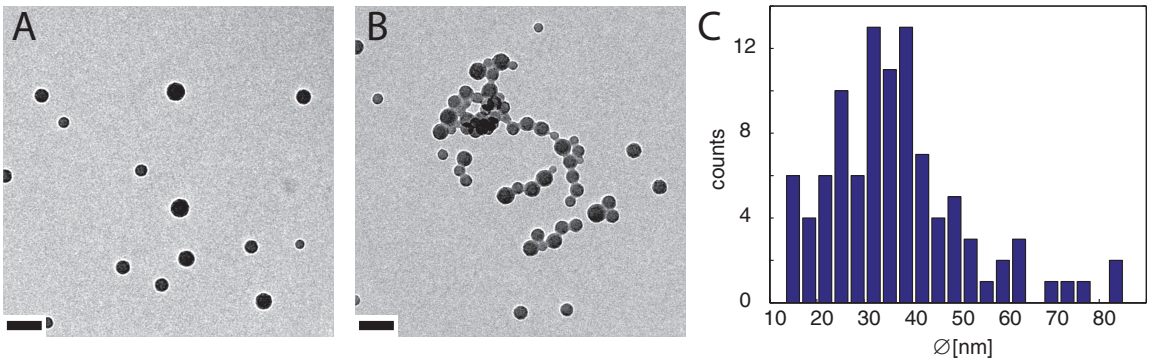


**Figure S1.** TEM images of monodispersed (**A**) and agglomerated (**B**) PS − $NH_2$ particles. Scale Bar: 100 $\mu$m. (**C**) Size distributions of the NPs with mean diameter particle size 35 $\mu$m.

### Supplementary 2

Time-lapse movie at 30 h of cells on a single-cell array. Cells are stained with pSIVA-IANBD, which fluoresces green upon binding to phosphatidylserine, and with propidium iodide, which fluoresces red when bound to nuclear DNA upon loss of plasma membrane integrity. After 8 h the first cells undergo cell death. The heterogeneity in time of onset of apoptosis can be clearly seen.

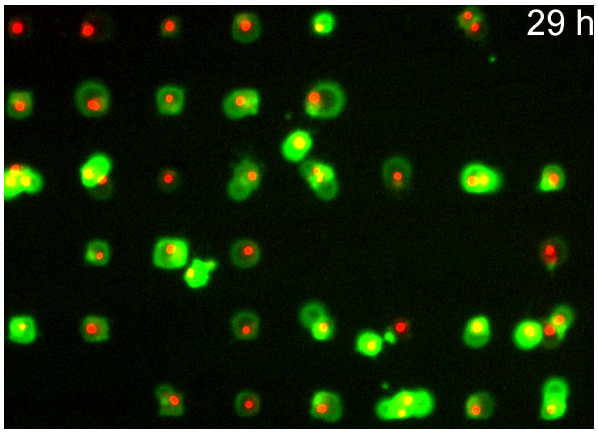

## Supplementary 3

The maximal signal intensity attained differs between single cells. Figure S2 shows the frequency distributions for the pSIVA signal (corrected for bleaching) and the PI signal for an NP dosage of 10 $\mu g \cdot mL^{-1}$. The plots are approximately Gaussian distributed. The differences in the maximal pSIVA signal can be explained by variation in the amount of exposed PS and by cell size, the differences in the PI signal by cell-cycle phase and the size distribution of the cell nuclei. The peak around zero is attributed to the healthy cells, which exhibit a low basal level of fluorescence.

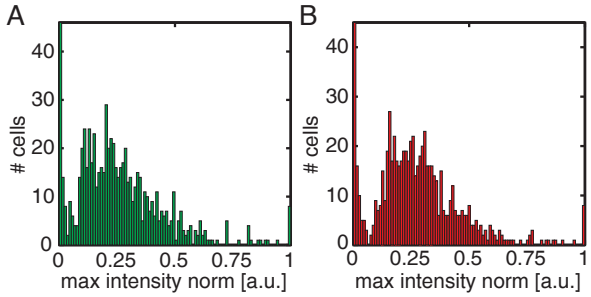


**Figure S2.** Frequency distribution of normalized maximum intensity for (**A**) pSIVA and (**B**) PI signal for a dose of 10 $\mu g \cdot mL^{-1}$. Signals are corrected for bleaching.

## Supplementary 4

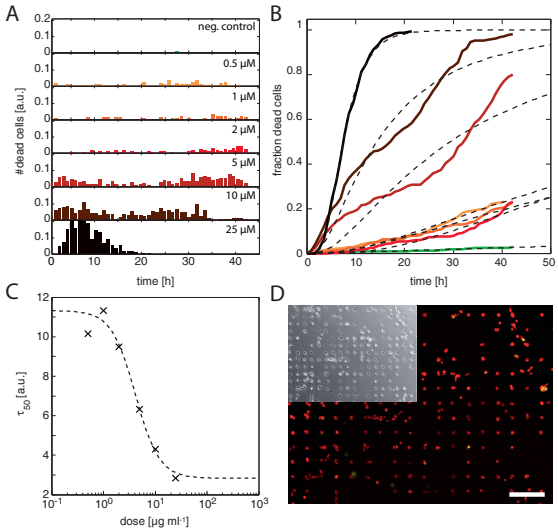


**Figure S3.** (**A**) Frequency distribution of dead cells for negative control (no treatment) and for STS at various doses (0.5 to 25 $\mu M$). A bimodal cell distribution can be determined. Doses higher than 5 $\mu m$ exhibit a second population of early cell death in the first 20 h. (**B**) Cumulative fraction of dead cells in relation to time are plotted for the negative control and STS. Regardless the bimodality, the cell distributions are fitted to log-normal functions. (**C**) Graph with time points $\tau_{50}$ for the cumulative distributions in dependence of dose. For STS, a dose-response behavior is observed. (**D**) Exemplary fluorescent image and brightfield image as inset of a viability test for the negative control (no addition of NPs and cell death markers). Red indicates viable cells (mitochondrial activity) and green compromised cell membranes (nucleus staining). Scale bar: 200 $\mu m$.

In order to show that the toxicity studies are not only limited to NPs we performed time-lapse measurements in which cells were treated with the anti-cancer drug staurosporine (STS) at doses of 0.5, 1, 2, 5, 10, and 25 $\mu M$. Figure S3 A show the cell death distributions for the various doses as well as for a negative control (with no STS or NP) over a period of 43 h. Depending on the dose, a bimodal distribution of cell death can be distinguished. For a dose regime of 0.5 to 2 $\mu M$ cells die toward late time points, whereas for 5 and 10 $\mu M$ two fraction of cell death can be distinguished: a fraction which die in the first 20 h and a fraction which induce cell death around 30 h. At the highest dose (25 $\mu M$), all cells die in the first 20 h. The fraction of cell death is plotted against time in Figure S3 B. The toxicity level for the negative control is with only 5% low. The cumulative distribution are fitted to log-normal functions neglecting the bimodal behavior at higher doses (see Figure S3 C). For STS, a time-dependent dose-response behavior is observed as also seen for the amino-modified PS NPs.

An additional test was performed to test if cells stay viable on the cell array over a period of 4 days. A live-dead assay with c12-resazurin and SYTOX green was used (see Figure S3D) which measures the metabolic activity as well as the integrity of the plasma membrane. A red color indicate a healthy metabolism whereas a green color (stained nucleus) indicate a compromised cell membrane and hence dead cells. After four days a high viability of 95% $\pm$ 0.6 % was observed showing that the micropattern has no adverse effect on the cells.

# Publication 6:
# Highly Stable and Biocompatible DNA-Functionalized Gold Nanorods and their Use for Ultrafast Sequence-Selective DNA Melting

# Highly stable and biocompatible gold nanorod-DNA conjugates as NIR probes for ultrafast sequence-selective DNA melting

*Verena Baumann,[1,3] Peter Johan Friedrich Röttgermann,[2,3] Frederik Haase,[1,3,#] Katalin Szendrei,[1,3,#] Priyanka Dey, [1,3] Katja Lyons,[1,3] Regina Wyrwich,[5] Matthias Gräßel,[1,3,4] Joachim Stehr,[4] Lars Ullerich,[4] Federico Bürsgens,[4] Jessica Rodríguez-Fernández[1,3]**

[1]Photonics and Optoelectronics Group, Department of Physics and Center for NanoScience (CeNS), Ludwig-Maximilians-Universität München, Amalienstr. 54, 80799 Munich (Germany)

[*]E-mail: jessica.rodriguez@lmu.de

[2]Soft Condensed Matter Group, Department of Physics and Center for NanoScience (CeNS), Ludwig-Maximilians-Universität München, Geschwister-Scholl-Platz 1 80539 Munich (Germany)

[3]Nanosystems Initiative Munich (NIM), Schellingstr. 4, 80799 Munich (Germany)

[4]GNA Biosolutions GmbH, Am Klopferspitz 19, 82152 Martinsried (Germany)

[5]Department of Chemistry, Ludwig-Maximilians-Universität München, Butenandtstr. 5-13 (E), 81377 Munich (Germany)

[#]Current address: Max Planck Institute for Solid State Research, Heisenbergstr. 1, 70569 Stuttgart, Germany.

KEYWORDS. Gold nanorods, DNA functionalization, colloidal stability, biocompatibility, plasmon resonance, plasmonic heating, DNA detection, DNA melting.

ABSTRACT. Here, we have prepared DNA-functionalized gold nanorods (Au NRs@HS-DNA) through a combination of stepwise ligand exchange, involving a sequential aqueous-organic-aqueous transfer, and subsequent oligonucleotide grafting. The as-prepared Au NRs@HS-DNA display a high and long-term colloidal stability in high ionic strength media, and they are proved very stable and biocompatible in cell culture media. We discuss important aspects in order to obtain a high DNA loading and to ensure colloidal stability during the functionalization process. We also demonstrate the high biocompatibility (>95% viability, low ROS activity, normal cell growth rate) of the DNA-functionalized Au NRs, which is mainly ascribed to the efficient removal of cetyltrimethylammonium bromide (CTAB) from their surface and to their high stability. These Au NR-DNA conjugates can be selectively addressed with a laser beam in a binary sample mixture comprising clusters of self-assembled DNA-functionalized spherical Au nanoparticles (NPs) and clusters of self-assembled DNA-functionalized Au NRs. We demonstrate that each colloidal cluster can be selectively disassembled by exciting the NPs close to their respective plasmon resonance maxima with microsecond laser pulses at 532 nm (for the spherical Au NPs) or 1064 nm (for the Au NRs). To the best of our knowledge this is the first report of an assay that allows to optically induce selective DNA melting of different sequences within one solution, regardless of their respective melting temperatures. As a proof of concept, we demonstrate that the Au NR-DNA conjugates can be used as NIR-addressable probes and

mediators for ultrafast and selective DNA melting and, in turn, for the selective detection of DNA.

## INTRODUCTION

The fast-paced development of nanoparticle-based nanoscience and biotechnology[1] has strongly benefitted from advances in the synthesis, understanding and control over the functional properties of several nanoparticle types.[2-5] Metal and semiconductor nanoparticles have played a remarkable role herein, especially those with near-infrared (NIR) plasmon resonances.[6-10] Gold nanorods stand out in this context and thanks to their plasmonic properties they have raised interest for metamaterials,[11, 12] sensing,[13] light-triggered actuation/release,[14-17] as photothermal agents,[18-20] and for *in vitro/in vivo*- imaging,[21, 22] among others. Of special interest is their deployment in the biomedical field, which requires rendering them biocompatible and colloidally stable in the high ionic strength conditions inherent to biological buffers and body fluids.[23] This can be achieved by interfacing their surface with biocompatible polymers, such as polyethyleneglycol (PEG),[24-26] or with biomolecules.[23, 27] Here, DNA is particularly advantageous due to its sequence-specific recognition capability that can be used to obtain nanoparticle assemblies of varying complexity and with optimized or new properties.[28-35]

Spherical gold nanoparticles can be easily functionalized with DNA oligonucleotides by direct grafting of thiol-ending oligonucleotides[36] or by direct adsorption of unmodified oligonucleotides[37-39] due to the accessibility of their surface and the straightforward displacement of citrate ions. In contrast, functionalization of gold nanorods with DNA is more challenging due to the stabilizing CTAB bilayer on their surface, needed for their growth.[40, 41] If NR functionalization is intended for DNA-directed self-assembly with other nanoparticles[42-44] or

DNA nanostructures[43, 45-50] containing complementary strands, it is plausible to functionalize the CTAB-capped Au NRs through direct grafting of thiol-ending oligonucleotides on their surface. This typically requires the addition of negatively charged surfactants (*e.g.* sodium dodecyl sulfate, SDS),[42, 45] non-ionic surfactants (*e.g.* tween), tween/polyethyleneglycol mixtures,[41] or negatively charged molecules with a hydrophobic aromatic region (*e.g.* 5-bromosalicylic acid)[51] prior to the actual DNA grafting step so as to not disrupt NR stability during the process. These approaches have been proven successful and certain improvements, such as a significant reduction in DNA grafting time at low pH,[42] have been reported. However, their main disadvantage is that the cationic surfactant can only be partially removed by the several washing cycles performed. Since CTAB monomers are primarily responsible for the toxic effect of gold nanorods,[52] surfactant removal is essential if the Au NR-DNA conjugates are intended for biomedical applications. Wijaya *et al.* demonstrated that CTAB-free DNA-functionalized Au NRs can be prepared by using a round-trip phase transfer process.[40] This approach consists of the extraction of CTAB-capped Au NRs from water into a dodecanethiol phase, followed by redispersion in a non-polar organic solvent (toluene) and subsequent back-transfer to water for oligonucleotide grafting. Here, the very strict experimental conditions needed for the direct exchange of CTAB molecules by the alkanethiol lead quite often to irreversible aggregation, as observed by our and other groups.[3, 53] This makes it difficult to reproducibly prepare surfactant-free Au NR-DNA conjugates.

In order to overcome this issue, here we show that biocompatible and highly stable DNA-functionalized Au NRs with a tailorable density of oligonucleotides can be routinely and reproducibly prepared through the combination of an aqueous-organic-aqueous transfer and subsequent oligonucleotide grafting. The introduction of an intermediate PEG layer prior to

redispersion in an organic polar solvent (THF) is found to be critical to ensure NR stability during the CTAB-removal process, while still enabling an efficient grafting of thiol-ending oligonucleotides in the subsequent steps. We discuss important key aspects to obtain Au NR-DNA conjugates, and demonstrate their long-term stability in stringent buffer conditions and cell culture media, as well as their biocompatible character (>95%). We also show that the ssDNA on the Au NRs retains its hybridization capacity. This is demonstrated by selectively addressing with a NIR laser nanoparticle clusters comprising DNA-functionalized Au NRs. As a proof of concept we demonstrate that these NIR-addressable probes can be used for the ultrafast detection of single-stranded DNA.

## EXPERIMENTAL

**Chemicals.** Hydrogen tetrachloroaurate trihydrate ($HAuCl_4 \cdot 3H_2O$), sodium borohydride ($NaBH_4$), silver nitrate ($AgNO_3$) and cetyltrimethylammonium bromide (CTAB, > 98%) were purchased from Sigma-Aldrich. Magnesium chloride ($MgCl_2$, > 99%) was procured from Roth, polyethylene glycol (PEG) α-methoxy-ω-mercapto (HS-PEG-OMe, MW 5000 Da), from Rapp Polymere and sodium oleate, from TCI America. Tetrahydrofuran (THF, > 99.9%) was ordered from Merck. 6-Carboxyfluorescein (6-FAM) modified (5'-thiol-$C_6$-TTTTTTTTTTTTTTTTTT-3'-6-FAM) and non-modified (5'-thiol-$C_6$-TTTTTTTTTTTTTTTTTT-3') thiolated DNA oligonucleotides (hereafter HS-DNA; 200 μM in water) were procured from Biomers.net. Tris-borate-EDTA buffer (1× TBE, pH 8.0) and tris-acetate-EDTA buffer (1× TAE, pH 8.0) were also used. All chemicals were used without further purification. In all preparations ultrapure Milli-Q water ($H_2O$, 18.2 MΩ cm) was used.

**Synthesis of Au NRs.** Short aspect ratio (AR=3.96) Au NRs with a length × width = 64 × 12 nm and with a longitudinal plasmon resonance centered at 821 nm were synthesized by the seed-mediated growth method.[54, 55] To prepare the Au seed solution in a total volume of 5 mL, 300 μL $NaBH_4$ were added at once to a stirring solution containing 9.94 μL $HAuCl_4$ 0.1257 M and 4.7 mL CTAB 0.1 M. After 2 min of vigorous stirring the solution was incubated in a water bath at 25 °C. In the meanwhile a growth solution consisting of 0.994 mL $HAuCl_4$ 0.1257 M, 250 mL CTAB 0.1 M and 4.65 mL HCl 1 M was prepared. This mixture was kept at 27 °C for 15 min. To induce Au nanorod formation the growth solution was first mixed with 300 μL $AgNO_3$ 0.1 M, then with 2 mL ascorbic acid 0.1 M and last with 600 μL of the Au seed solution. The mixture was incubated overnight at 30 °C. Chemicals from the synthesis were removed by centrifuging for 50 min at 7232x*g* and redispersing with the same volume of CTAB 0.1 M. Sample washing was carried out twice. Finally the 250 mL sample was centrifuged additionally two times and redispersed with water in order to obtain gold nanorods with final concentrations of [Au] = 0.920 mM ($2.56\times10^{-9}$ moles of particles / L) and [CTAB] = 0.75 mM. Thereafter, the brown-colored dispersion was stored in a water bath at 27 °C for later use.

High AR (6.65) Au NRs with a length × width = 93 × 14 nm, and with a longitudinal plasmon resonance centered at 1080 nm were synthesized by the seed-mediated growth approach described by Ye *et al.*[56] using a binary surfactant mixture consisting of CTAB and sodium oleate. First, the Au seeds were prepared by mixing 5 mL of $HAuCl_4\cdot3H_2O$ solution (0.5 mM, in water) and 5 mL of an aqueous CTAB solution (0.2 M), followed by the addition of 1 mL of a freshly prepared $NaBH_4$ solution (0.6 mL of 0.01 M of $NaBH_4$ were diluted to 1 mL with water) under vigorous stirring. After two minutes the stirring was stopped and the seed solution was allowed

to age for 30 minutes in a water bath at 27 °C. For the growth solution, 3.5 g CTAB and 617 mg sodium oleate were dissolved in 125 mL warm water (~50 °C). When the solution was cooled down to 30 °C, $AgNO_3$ (4 mM, 12 mL) was added and the solution was kept undisturbed for 15 minutes at 30 °C. Then, an aqueous $HAuCl_4 \cdot 3H_2O$ solution (1 mM, 125 mL) was added. The solution turned colorless after 90 minutes of moderate stirring. Subsequently, 3.111 mL of HCl (32 wt. % in water) were added and the moderate stirring was continued for additional 15 min. Thereafter, 0.625 mL ascorbic acid 64 mM were added and the solution was stirred vigorously for 30 s. Thereafter, 0.4 mL of the seed solution were added to the growth solution. After stirring for additional 30 s, the reaction mixture was stored overnight in a water bath at 30°C to allow for gold nanorod formation. The Au NRs were finally purified by centrifugation at 7000 rpm for 30 min (2×) and redispersed in 125 mL of a 5 mM CTAB solution.

**DNA functionalization of Au NRs.**

Here we provide a thorough experimental description of the experimental steps and conditions to functionalize the short AR (3.96) Au NR sample. The process is identical for the high AR (6.65) sample prior adjustment of the relative concentrations of Au NRs and grafting molecules according to the molecular grafting densities indicated below.

**1. PEGylation of Au NRs@CTAB (aqueous-to-organic transfer).** Based on the works from Thierry *et al.*[53] and Sánchez-Iglesias *et al.*,[3] a partial PEGylation of the CTAB-capped Au NRs was performed. For that, 800 µL of a $8.04\times10^{-5}$ mM aqueous HS-PEG-OMe solution (providing 20 molecules / Au $nm^2$) was added under strong stirring to a mixture of 11.2 mL of an Au NR dispersion [Au] = 0.920 mM, $2.56\times10^{-9}$ moles of particles / L; [CTAB] = 0.75 mM) and 36 µL CTAB 0.1 M. PEGylation was allowed to proceed for 3 h at room temperature under moderate

stirring. The PEGylated Au NRs were centrifuged (1643×*g*, 40 min) and redispersed in 12 mL ethanol under sonication. The centrifugation step was repeated and the particles were finally redispersed in 12 mL THF while sonicating.

**2. Surface modification of Au NRs@HS-PEG-OMe with MHA (organic-to-aqueous transfer).** For the functionalization of Au NRs with 6-mercaptohexanoic acid (MHA), 126.8 µL of a 100 mM MHA solution were added to 11.5 mL of Au NRs@HS-PEG-OMe in THF, in order to provide the Au surface with 300 molecules / Au $nm^2$. As described in the protocol of Thierry *et al.* particles were sonicated for 30 min at room temperature followed by sonication for 1 h at 55 °C.[53] The sample was left undisturbed overnight at room temperature. The next day the dispersion was centrifuged (1643×*g*, 40 min), the supernatant was discarded and 11.5 mL isopropanol were added in order to deprotonate the carboxy groups of the MHA ligands, as reported by Wijaya *et al.*[57] The sample was centrifuged once more (1643×*g*, 40 min) and the pellet was redispersed in 11.5 mL of 1× tris-borate-EDTA buffer (1× TBE, pH 8.0) containing 0.001 % tween 80 under sonication.

**3. Functionalization of Au NRs@MHA with thiolated DNA oligonucleotides.** To cleave the S-S bond of the stock thiolated DNA oligonucleotides a 100-fold molar excess of an aqueous tris(2-carboxyethyl)phosphine hydrochloride (TCEP) solution was added to the HS-DNA and kept undisturbed for 1 h at room temperature. The samples were stored in the freezer for later use.

For DNA functionalization of Au NRs@MHA, the reduced HS-DNA was added to a dispersion of 1.786 mM ($5\times10^{-9}$ moles of particles / L) Au NRs in 1× TBE containing 0.001 % tween 80 so as to theoretically functionalize the particles with 1 DNA strand / Au $nm^2$. After incubation for 15 min, charge screening was performed. In a typical experiment yielding

194 DNA strands / Au NR (0.05 DNA strands / Au $nm^2$), charge screening was performed in four salting steps until a final [NaCl] = 0.08 M was achieved (value taken from Zhang *et al.*[58]) by using a 2 M NaCl stock solution in 1× TBE containing 0.001 % tween 80. After each salting step the sample was sonicated for 15 s and subsequently allowed to stand undisturbed for 30 min. Once the last salting step was finished it was kept undisturbed overnight (17 h) at room temperature. To remove free HS-DNA oligonucleotides, the sample was centrifuged (1207×*g*, 40 min) and resuspended in 1× TAE, pH 8.0 containing 0.001 % tween 80. The same centrifugation / redispersion cycles were repeated two additional times.

**Quantification of DNA oligonucleotides on the Au NR surface**

The extinction spectra of the DNA functionalized Au NRs do not give information on the actual number of DNA strands bound to the Au NR surface. Hence, we used a DNA quantification method based on the work of Demers *et al.*,[59] to determine the total number of DNA strands bound to the Au NR surface by fluorescence spectroscopy.

**1. Oxidation of Au NRs@HS-DNA-6-FAM.** Au NRs functionalized with fluorescently labeled thiolated DNA (namely the fluorescein derivative label 6-FAM at the 3' end: 5'-thiol-$C_6$-TTTTTTTTTTTTTTTTTT-3'-6-FAM, HS-DNA-6-FAM hereafter).[i] The proximity of the fluorescein moieties to the Au NRs' surface leads to complete fluorescence quenching, in agreement with previous works,[60, 61] and thus no DNA quantification is possible. To overcome this issue we performed the selective oxidation of the Au NRs@HS-DNA-6-FAM through the addition of a mild and selective oxidizing mixture of $K_3[Fe(CN)_6]$ and KCN. Specifically, the

[i] Our experimental results showed that the presence of 6-FAM in the HS-DNA sequence did not affect the Au NR stability during functionalization: the UV-vis-NIR spectra of Au NRs@HS-DNA and Au NRs@HS-DNA-6-FAM are identical.

mixture was added to the DNA functionalized Au NRs to obtain final conditions of 0.08 M KCN, 0.8 mM $K_3[Fe(CN)_6]$ and 1.429 mM Au ($4\times10^{-9}$ moles of particles / L). The mixture oxidizes the Au NRs into $Au^I$, as previously reported for gold spheroids and gold nanorods,[62, 63] leading to the "release" into solution of the HS-DNA-6-FAM strands bound to the Au NRs' surface (see schematic depiction in Figure S1, ESI). Au NR oxidation was followed by vis-NIR spectroscopy through the disappearance of the Au NRs' plasmon bands. Their complete disappearance indicated the complete oxidation of the sample.

**2. DNA quantification.** We quantified the concentration of the HS-DNA-6-FAM strands released from the Au NRs' surface by measuring the photoluminescence (PL) intensity at 520 nm, which is the fluorescence emission maximum of HS-DNA-6-FAM upon excitation at 485 nm (see absorption and PL spectra in Figure S1B, inset). To determine the correspondence between the measured PL intensity and the actual concentration of HS-DNA-6-FAM we made a calibration curve. For this, we prepared a solution containing the same amount of buffer and oxidizing agents as present in the actual Au NR oxidation experiment (0.08 M KCN and 0.8 mM $K_3[Fe(CN)_6]$ in 1× TAE buffer containing 0.001 % tween 80). To this mixture a known concentration of the fluorescently labeled DNA was added. The recorded intensity values at 520 nm for each concentration were interpolated with a linear fit (see calibration curve in Figure S1B). It is important to note that with this quantification method not only the HS-DNA-6-FAM oligonucleotides released into solution as a consequence of Au NR oxidation contribute to the PL at 520 nm. Indeed, if the centrifugation / redispersion cycles performed after DNA functionalization (step 3.3, Figure 1A) are not carried out carefully (note that not all DNA strands added during the functionalization process graft on the Au NRs' surface), any remaining

(unbound) HS-DNA-6-FAM strands left will also contribute to the PL at 520 nm. This can lead to an "overestimation" of the number of DNA strands grafted on the NRs' surface. To minimize this effect, we determined the optimal number of centrifugation / redispersion cycles (namely 3×, in the presence of 0.001 % tween 80) that leads to a ratio of $[\text{HS-DNA-6-FAM}]_{free}$ / $[\text{HS-DNA-6-FAM}]_{total} < 0.01$. Here, $[\text{HS-DNA-6-FAM}]_{free}$ is the concentration of unbound HS-DNA-6-FAM, and it is determined from the PL emission at 520 nm from the corresponding supernatant solution. $[\text{HS-DNA-6-FAM}]_{total}$ is the total concentration of HS-DNA-6-FAM, that is, the concentration as determined from the PL emission at 520 nm of the solution after oxidation. Therefore, the $[\text{HS-DNA-6-FAM}]_{total}$ determined in this way includes the contribution from the unbound oligonucleotides and from the strands released upon Au NRs@HS-DNA-6-FAM oxidation. Ensuring that the ratio $[\text{HS-DNA-6-FAM}]_{free}$ / $[\text{HS-DNA-6-FAM}]_{total}$ remains low (< 0.01) in the final washed sample, allows us to confirm that the PL determined in the oxidized solution is essentially due to the surface-grafted DNA strands, with no significant contribution from the "free", unbound, DNA strands. For more details, see summarizing table (Table S4) in the ESI.

**Assessment of the time stability and DNA desorption of DNA-functionalized Au NRs in high ionic strength media.** We studied the stability of Au NRs@HS-DNA-6-FAM in 1× TAE containing 0.001 % tween 80 as a function of the medium ionic strength and time (for a total of 56 days). Specifically, we followed the spectral evolution (by means of vis-NIR spectroscopy) of Au NRs@HS-DNA-6-FAM in the presence of a final salt concentration of 5 mM $MgCl_2$, 2 M NaCl, and no salt.

In order to determine the occurrence of HS-DNA-6-FAM desorption from the Au NR surface, from the samples described above aliquots were taken after 0, 1, 2, 6, 14, 28, and 56 days, and oxidized as explained above. Ultimately, we determined the number of DNA strands grafted on the Au NRs by fluorescence spectroscopy.

**Biocompatibility Tests**

The biocompatibility of the DNA-functionalized Au NRs was investigated through four different tests: a viability assay on cell population and viability/membrane leakage assay, reactive oxygen species (ROS) activity assay, and a proliferation assay on single cell level.

1. **MTS assay**

For the population viability test, a 3-(4,5-dimethylthiazol-2-yl)-5-(3-carboxymethoxyphenyl)-2-(4-sulfophenyl)-2H-tetrazolium (MTS) assay was used. The method uses a colorimetric approach, where the MTS tetrazolium salt is metabolized by the mitochondria of viable cells to a blue-colored formazan product. Final extinction measurement of the produced dye at 490 nm allows for quantification of the living cells. The CellTiter 96 Aqueous One Solution Cell Proliferation Assay from Promega was used.

For the assay, adherent lung carcinoma A549 (from the Leibniz Institute DSMZ – German Collection of Microorganisms and Cell Cultures) cells were seeded in a flat-bottom 96 multi-well plate by adding in each well 200 μL of a $5\times10^4$ live cells/mL solution (containing DMEM with 10% fetal calf serum, FCS), and incubating at 37 °C in a 5% $CO_2$ atmosphere for 24 h. The wells in the periphery were filled with complete cell culture medium without cells, in order to prevent edge effects.

After a cell monolayer was formed in each well, 100 µL of the DNA functionalized Au NRs (sequence: 5'-thiol-$C_6$-TTTTTTTTTTTTTTTTTT-3'-6-FAM) were added to the cells in five serial dilutions in triplicate (1, 10, 25, 50 and 100 µg/mL). For background measurements, wells were filled with the same volume of medium but in the absence of cells. Other wells containing cells, but no Au NRs, were used as a positive control with staurosporine (2 µM, STS) from Sigma Aldrich. After incubation for 24 h, the medium was removed and 120 µL of the MTS reagent was added into each well. The cell plate was transferred into the incubator and left for 1 h at 37 °C in a humidified, 5% $CO_2$ atmosphere. Thereafter, the absorbance of formazan at 490 nm was recorded using a microtiter plate reader (FLUOstar OPTIMA from BMG Labtech).

Analysis of the absorbance measurements was carried out by subtraction of the average background value from each single replicate. Normalization to the average absorbance of the cells without Au NRs was performed in order to obtain the percentage of cell survival as shown in equation 1.

$$\% \text{ cell survival} = \left[\frac{A_{AuNR}}{A_{no\ AuNR}}\right]_c \times 100 \quad (1)$$

Here, *A* is the absorbance and *c* indicates the correction by the background value. The percentage of cell survival was calculated as the average of the three replicates and its standard deviation.

**2. Viability/membrane leakage assay**

For the single cell viability assay/membrane leakage test, a two-color fluorescence assay was applied using $c_{12}$-resazurin (Thermo Fisher) and SYTOX green (Thermo Fisher). In metabolically active cells, $c_{12}$-resazurin is reduced in the mitochondria to the red-fluorescent $c_{12}$-

resorufin. In cells with compromised plasma membrane, as well as in dead cells, the nucleus is green fluorescent.

A549 cells were seeded in an ibitreat 8well slide (ibidi GmbH) at a concentration of 6000 cells/well. After 16 h, cells were exposed to the different Au NRs@HS-DNA doses, to a negative control (only cell culture medium) and to 1 μM STS. After 24 h, the cells were treated with 0.5 μM $c_{12}$-resazurin and 10 nM SYTOX green in 200 μL PBS at 37°C and 5% $CO_2$ for 15 min, according to the manufacturer instructions. As a second additional control, ethanol (EtOH) was added to CCM to induce cell membrane permeabilization. Cells were imaged with an inverted TI Eclipse microscope (Nikon) and a fluorescence lamp SOLA LED (Lumencor) with 20× resolution. The fluorescence of $c_{12}$-resorufin was recorded with a PI filter (Ex. 540 nm / Em. 630 nm), and the SYTOX green, with an eGFP filter (Ex. 470nm / Em. 525 nm). Approximately 1000 cells were analyzed *per* exposure condition. The percentage of damaged cells was calculated by the ratio of total cell number to the number of nucleus-stained cells.

### 3. ROS activity

For the ROS activity assay, the fluorescent marker Cell ROX (Thermo Fisher) was applied. The cell-permeable marker is non-fluorescent in the reduced state, while it exhibits a strong fluorescent signal upon oxidation. The fluorescence intensity of CellROX is directly correlated to the amount of ROS activity.

A549 cells were seeded in an ibitreat 8well slide (ibidi GmbH) at a concentration of 6000 cells/well. After seeding for 16 h, the cells were exposed to the different doses of Au NRs@HS-DNA, to a negative control (CCM), and to a positive control (75 μM menadione, Alfa Aesar).

After 24 h, 100 nM CellROX orange and 100nM Hoechst33342 (Thermo Fisher) in DMEM + 10% FCS was incubated at 37°C and 5% $CO_2$ atmosphere for 30 min.

The fluorescence of CellROX orange was recorded with a PI filter (Ex. 540 nm / Em. 630 nm), and the Hoechst 33342, with a DAPI filter (Ex. 377nm / Em. 447 nm). For image analysis, regions of interest (ROI) for each single cell were extracted from the location of the stained nuclei. The ROIs were then applied to the CellROX fluorescence images and the mean fluorescence of each ROI was then calculated. Few hundred cells were analyzed *per* exposure condition.

**4. Proliferation assay**

For the proliferation assay, cells were recorded at single cell resolution by fluorescently labeling the nuclei with a cell membrane permeant marker. 3000 cells/well were seeded in an ibitreat 8 well (ibidi GmbH) slide. After 8 h of incubation, cells were exposed to 100, 50, 25, and 0 µg/mL DNA-Au NRs together with the fluorescent nucleus marker Hoechst33342 (25 nM) in $CO_2$ independent medium, Leibovitz L15 (c-c-pro), with 10% FCS. Note that as the L15 medium does not provide the optimal growth conditions, the cells exhibit a decreased growth rate in comparison to cell growth in DMEM medium. Cells were recorded with an inverted fluorescence microscope iMIC (L-FEI) every 30 min for 60 hours in bright field and DAPI channel (Ex. 377 / Em. 409). For the determination of the number of cells, a bandpass filter was applied to the fluorescent images, and then binarized using a dynamic cutoff threshold. Fused cell nuclei were split and recognized by the watershed algorithm. The number of clusters was then counted for each time step. For the growth curves the cell numbers were divided by the cell number of the first time point.

**Laser-assisted DNA melting experiments.** A thorough description of the experimental setup devised for the ultrafast laser-assisted melting and detection of DNA upon disassemcuvettbly of clusters of spherical or rod-like DNA-functionalized Au NPs is provided in the discussion associated with Figure 5.

**Characterization.** Optical absorption spectra were measured with a Cary 5000 UV-vis-NIR spectrophotometer in a 2 mm quartz cuvette. Photoluminescence measurements were performed with a Cary Eclipse Fluorescence Spectrometer in a 2 mm quartz fluorescence cuvette. For transmission electron microscopy characterization, we employed a JEOL JEM-1011 microscope operating at 100 kV. Zeta potential measurements were performed on a Zetasizer Nano S (Malvern Instruments, Malvern UK) with a 4 mW He-Ne laser operating at 633 nm and a detection angle of 173°. XPS measurements were carried out on an X-ray photoelectron spectrometer equipped with a VSW TA10 X-ray source and a VSW HA100 hemispherical analyser. To sputter clean the surface of the Au NRs@HS-DNA sample, a VSW AS10 argon ion gun was used. The samples for XPS analysis were prepared by drop-casting a dispersion of Au NRs@CTAB and a dispersion of Au NRs@HS-DNA bearing 700 DNA strands / NR (*i.e.*, 0.126 DNA strands / Au $nm^2$) on a silicon wafer.

## RESULTS AND DISCUSSION

CTAB-capped Au NRs (64±12 nm length (L), 16±3 nm width (W) and 3.96±0.76 aspect ratio (L / W)) were functionalized through a combination of stepwise ligand exchange, involving a

sequential aqueous-organic-aqueous transfer, and subsequent oligonucleotide grafting. Our approach was inspired by the method from Wijaya *et al.*[40] with modifications for the aqueous-organic-aqueous transfer and subsequent steps, as we describe further below. Figure 1A provides an overview of the process. It comprises a ligand exchange process involving three main steps. In the first one (aqueous-to-organic transfer), CTAB-stabilized Au NRs are transferred from water to THF *via* a gradual decrease in solvent polarity as described by *Thierry et al.*[53] The transfer is enabled by PEGylation with HS-PEG-OMe (step 1.1), subsequent redispersion in ethanol (step 1.2), and ultimately redispersion in THF (step 1.3). This process is known to allow a complete removal of the cytotoxic surfactant CTAB, which is demonstrated further below.[53] In the second step (organic-to-aqueous transfer), the Au NRs@HS-PEG-OMe in THF are functionalized with mercaptohexanoic acid (MHA, step 2.1). The ionization of the terminal carboxylic acid group of MHA is promoted by addition of a protic solvent (isopropanol in our case, step 2.2), as reported elsewhere.[57] This allows the redispersion of Au NRs@MHA in buffer medium, namely 1× TBE buffer containing 0.001 % tween 80 (step 2.3, see discussion below for details on the role and importance of tween). Finally, in step 3 the Au NRs@MHA are functionalized with thiolated oligonucleotides (HS-DNA) upon incubation for 15 min first (step 3.1). This is followed by overnight charge screening with NaCl (step 3.2), removal of the NaCl excess and of unbound HS-DNA oligonucleotides (step 3.3), and final redispersion in 1× TAE containing 0.001 % tween 80 (step 3.4, see details below).

The functionalization described here involves several steps. This makes it more time consuming than other DNA functionalization approaches reported recently,[41, 42] which are well-suited for hybridization experiments. However, one important advantage of our approach relates

to its robustness in terms of high reproducibility and tailored DNA grafting. Furthermore, the Au NR-DNA conjugates obtained in this way offer several advantages with respect to other conjugates reported previously, especially with regard to their potential deployment in the biomedical field: they do not contain CTAB, they are very stable under stringent buffer and cell culture media conditions and, importantly, they are highly biocompatible. All these aspects will be discussed in detail throughout the manuscript.

Figure 1B depicts a TEM micrograph of the short aspect ratio CTAB-capped Au NRs, synthesized by a seed-mediated growth method described elsewhere.[17, 54, 55] Figure 1C shows a micrograph of the same Au NRs after functionalization with single-stranded HS-DNA, consisting in this case of a 5'-thiol-$C_6$-$T_{18}$-3' sequence (the sequence used as default throughout this work, unless otherwise indicated). Comparison of the TEM micrographs and photos of each colloidal dispersion (see insets) indicates that the NRs preserve their original morphology and dimensions, and that no aggregation occurs during the functionalization, as confirmed by the vis-NIR spectra shown in Figure S2 (Electronic Supplementary Information, ESI). By adjusting the concentration of [NaCl] (step 3.2), it is possible to fine-tune the number of DNA strands loaded on the Au NRs (see Figure 1D and discussion below).

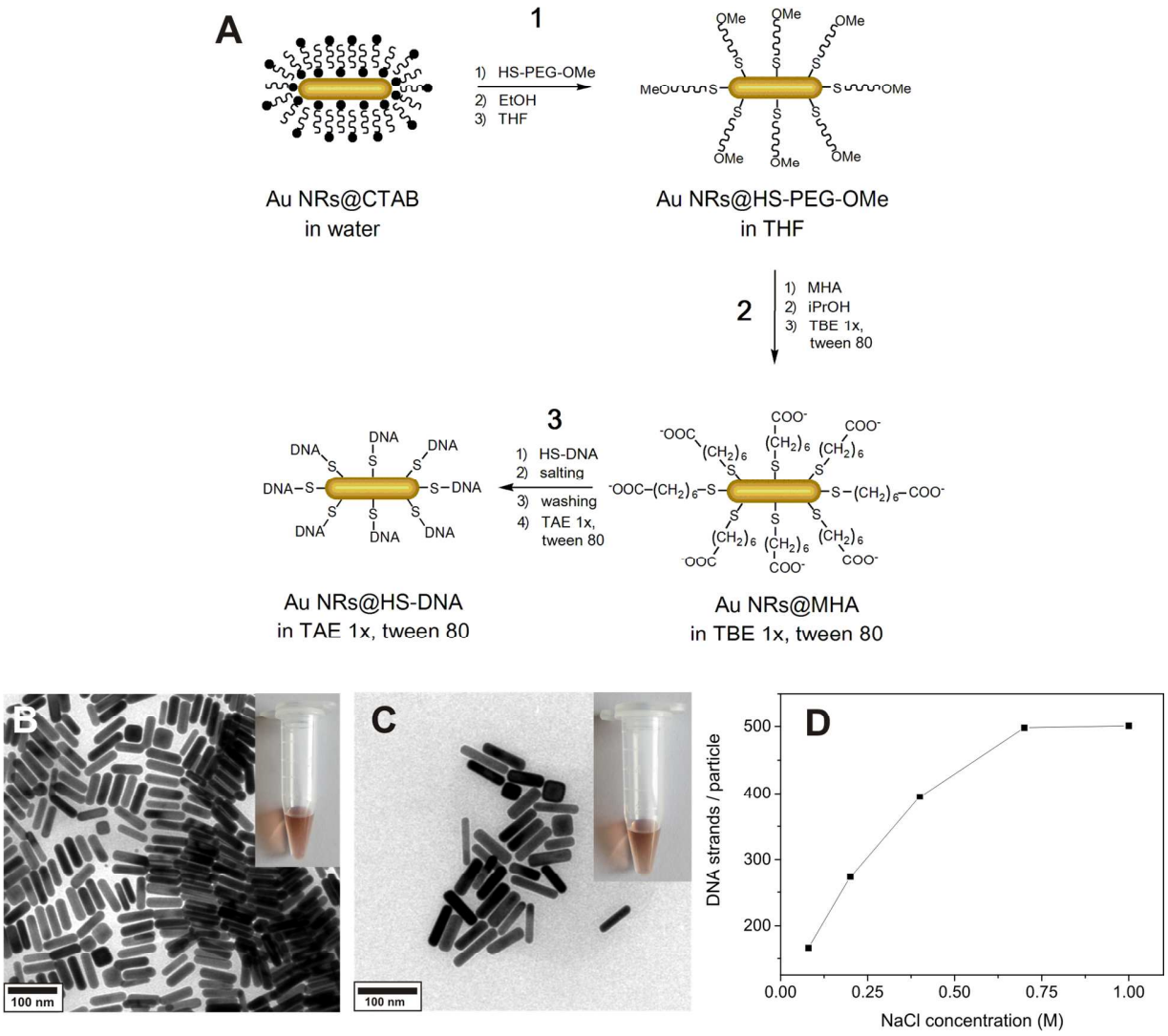


**Figure 1.** (A) Schematic representation of the stepwise surface functionalization of Au NRs with HS-DNA. Step 1: partial displacement of CTAB molecules by HS-PEG-OMe and transfer into organic medium, namely THF. Step 2: modification of the Au NR's surface with MHA, ionization of the terminal carboxylic acid group by isopropanol addition, and redispersion in buffer medium. Step 3: DNA functionalization *via* charge screening followed by 3× washing, and redispersion in buffer. (B) TEM micrograph of the CTAB-stabilized Au NRs (L×W=64×16 nm). The inset is the photograph of the corresponding dispersion. (C) TEM micrograph of the same Au NRs functionalized with HS-DNA (here 5'-thiol-$C_6$-$T_{18}$-3') and redispersed in 1× TAE

buffer containing 0.001 % tween 80. The inset is the photograph of the corresponding dispersion. (D) Influence of the final [NaCl] used during charge screening on the number of DNA strands loaded *per* Au NR. DNA functionalization was performed at room temperature in the presence of 0.001 % tween 80.

In the following, we highlight and discuss key experimental aspects to consider for the successful functionalization and stability of the Au NRs (Figure 1A).

*Step 1: Aqueous-to-organic transfer via PEGylation.* The first step consists of a partial PEGylation of the Au NRs@CTAB (step 1.1, Figure 1A). PEGylation was performed to enable a gradual aqueous-to-organic phase transfer first (step 1) and subsequent back transfer to aqueous medium (step 2, see below). In this way, a complete CTAB removal from the Au NRs' surface is possible, as previously demonstrated by Thierry *et al. via* XPS analysis.[53] We have demonstrated the efficient removal of the surfactant in the final Au NRs@HS-DNA sample by XPS (see discussion further below). HS-PEG-OMe binds to the Au surface through the thiol groups and acts as a steric barrier stabilizing the Au NRs during the gradual transfer from water to ethanol first (step 1.2, Figure 1A), and ultimately to THF (step 1.3, Figure 1A). We performed the PEGylation in order to obtain a partial coverage of the Au NR surface without surface saturation, so that further functionalization with MHA (step 2) and HS-DNA (step 3) is more likely. Thus, as a compromise between partial surface coverage and colloidal stability in a low dielectric constant solvent such as THF, we found that a dose of 20 molecules of HS-PEG-OMe *per* $nm^2$ of Au is optimal. The colloidal stability provided by lower doses was found to be low, while higher

ones tend to 'block' the Au NRs' surface, thus leading to lower HS-DNA loadings in step 3 (see Figure S3 and Table S1, ESI).

*Step 2: Organic-to-aqueous transfer via MHA functionalization.* To transfer the PEGylated Au NRs from THF into an aqueous, high ionic strength, medium (needed for HS-DNA functionalization, step 3), the Au NRs@HS-PEG-MeO in THF were incubated with MHA, soluble in THF as well. MHA is a short chain thiolated carboxylic acid that binds to the gold surface through the thiol group. Upon grafting, the MHA-modified Au NRs (Au NRs@MHA) gradually flocculate (see vis-NIR spectrum, red curve, in Figure S4A). Subsequent addition of a protic solvent such as isopropanol to the flocculated NRs facilitates their redispersion in a high ionic strength medium,[40] 1× TBE in our case. The longitudinal plasmon band of the Au NRs@MHA in 1× TBE (blue curve, Figure S4A) shows a significant inhomogeneous broadening, indicating that a non-negligible amount of Au NRs aggregate upon redispersion in buffer. We found that by increasing the number of MHA molecules added to the Au NRs@HS-PEG-MeO in THF, the Au NRs@MHA could be redispersed in 1× TBE with no significant aggregation occurring, as determined from vis-NIR spectroscopy. However, if the number of MHA molecules added was too high (> 300 molecules/Au $nm^2$), they blocked the Au surface for further functionalization with HS-DNA (step 3) in such a way that almost no HS-DNA could graft on the surface (results not shown). Consequently, it is important to carry out the MHA modification step as a compromise, (i) yielding an MHA-modified surface, whose polar properties suffice for Au NR redispersion in buffer without significant aggregation, but (ii) without inhibiting subsequent DNA grafting due to the presence of a too densely packed MHA monolayer on the Au NRs. Our experimental results revealed that functionalization with a dose

of 300 molecules MHA / Au $nm^2$ yielded the best results fulfilling both requirements. Under those experimental conditions we also found that the inhomogeneous broadening of the longitudinal plasmon band of Au NRs@MHA in 1× TBE (see Figure S4A, blue curve) can be significantly decreased when the nonionic surfactant tween 80 is present during redispersion in the buffer medium (Figure S4A, green and orange curves). This stabilizing effect of nonionic surfactants, prior to modification with DNA oligonucleotides, was also reported previously for 13 and 40 nm citrate-capped spherical Au nanoparticles.[64] Since the Au NR surface is not fully blocked by MHA ligands the surfactant can physisorb and, therefore, stabilize the Au NRs against aggregation resulting in much narrower longitudinal plasmon bands, even when present in a concentration as low as 0.001%.

*Step 3: DNA functionalization.* For DNA functionalization (step 3, Figure 1A), Au NRs@MHA in 1× TBE containing 0.001 % tween 80 were mixed with HS-DNA oligonucleotides (5'-thiol-$C_6$-$T_{18}$-3' in the example shown here) in order to render their surface with a theoretical number of 1 HS-DNA strand / Au $nm^2$ (see Table S2, which summarizes the effect of the HS-DNA/Au NR molar ratio on the final DNA loading capacity). The particles were first incubated with the oligonucleotides for 15 min (red curve, Figure S4B), and then charge screening was performed to overcome the electrostatic repulsion between the negatively charged MHA carboxylic groups and the negatively charged DNA backbone. In a typical DNA functionalization experiment, we incubated the thiolated DNA and the Au NRs@MHA for 17 h in the presence of 0.08 M NaCl (concentration reached in four salting steps). These conditions are similar to the ones reported by Hurst *et al.* for DNA functionalization of citrate-capped spherical Au nanoparticles.[36] Nevertheless, we found that performing a 15 s sonication after each

salting step is important to enhance DNA grafting (see Table S3). We observed no sign of loss in colloidal stability during the salting process (see Figure S4B and Figure S5). Following removal of the NaCl excess and of the unbound HS-DNA strands, the Au NRs@HS-DNA were finally redispersed in 1× TAE containing 0.001 % tween 80. It is worth noting that 3 centrifugation/redispersion cycles are needed in order to ensure the efficient removal of unbound oligonucleotides (see Table S4 and further details in the Materials and Methods section). Effective DNA grafting was confirmed by zeta potential (ξ) measurements in water. The positive ξ= +48.8 mV of the original CTAB-capped Au NRs changed to ξ= -7.1 mV for the Au NRs@HS-PEG-MeO, to ξ= -10.1 mV for the Au NRs@MHA, and to highly negative (ξ= -29.9 mV) for the Au NRs@HS-DNA.

In order to fine-tune the amount of DNA strands loaded on the Au NRs' surface, we evaluated the influence of temperature and [NaCl]. Performing DNA grafting at 50 °C *vs.* room temperature (23 °C) leads to a higher DNA loading (see Table S5, ESI). However, it also results in a partial reshaping of the Au NRs as indicated by a small blue-shift of their longitudinal plasmon band (see extinction spectra in Figure S6), in agreement with previous works.[65, 66] Alternatively, performing charge screening at high NaCl concentrations provides a much better control over DNA loading without affecting the morphology and stability of the NRs, as shown in Figure 1D. DNA loading increases ~ three-fold, from 167 DNA strands / Au NR (0.04 DNA strands / Au $nm^2$) to 501 DNA strands / Au NR (0.14 DNA strands / Au $nm^2$) by increasing the [NaCl] from 0.08 M to 1.0 M. Between 0.08 M and 0.7 M NaCl, we observe a gradual increase in the number of loaded DNA strands *per* Au NR due to an effective charge screening of the repulsive forces between the negatively charged DNA backbones. However, above 0.7 M NaCl

the charges are fully screened. Therefore, an additional increase in [NaCl] does not induce any further DNA loading on the Au NRs, thus achieving a plateau of maximum DNA loading, ~ 501 DNA strands / Au NR in this case. A similar saturation effect above 0.7 M NaCl was reported by Hurst *et al.*[36] for 15 nm spherical Au NPs. The gel electrophoresis results shown in Figure S7 show that, regardless of their loading, all DNA-functionalized Au NRs run towards the positive electrode. However, the narrower and better defined bands obtained for the Au NRs with higher DNA loadings, indicate that more homogeneous coatings are obtained when higher NaCl concentrations are used during the salting step. We also found that the utilization of an aged Au NRs@MHA sample can have a positive impact in terms of DNA loading (see Figure S8 and Table S6).

One of the most remarkable features of our Au NRs@HS-DNA relates to their high and long-term colloidal stability in high ionic strength media. Figure 2 illustrates this by showing the spectral changes occurring on Au NR-DNA conjugates loaded with 194 DNA strands / Au NR (*i.e.*, with 0.05 DNA strands / Au $nm^2$) after storage for 56 days in the absence (Figure 2A) or in the presence of high concentrations of a divalent (5 mM $MgCl_2$, Figure 2B) or of a monovalent (2 M NaCl, Figure 2C) salt. In all cases, the longitudinal plasmon band of the DNA-modified Au NRs remains practically unchanged, indicating that all samples remain highly stable over time despite the high ionic strength of the salt-containing media. In the absence of extra salt added, no significant spectral changes occur, just a small improvement in terms of a slight narrowing, symmetry and intensity increase of the longitudinal plasmon band with increasing storage time. This is probably due to a significant DNA desorption over time for this sample (see Figure S9, ESI). Upon DNA desorption it is likely that tween physisorbs further on the surface of the DNA-

functionalized AuNRs, thus increasing slightly the overall stability of the sample. On the other hand, when the nanorods are incubated in a buffer medium containing 5 mM $MgCl_2$, a small inhomogeneous broadening at *ca.* 1000 nm starts to become evident after 56 days (see Figure 2B). This is ascribed to a non-negligible DNA desorption, which is far less pronounced in this sample as compared to the sample with no extra salt added (see Figure S9). However, in this case tween physisorption seems to not suffice in providing a similar stabilization effect (see Figure S10). The van der Waals attraction between the nanorods is favored by the high ionic strength of the medium and, hence, it is likely that the stabilizing effect of tween cannot compensate for this effect, thus resulting in a slight broadening of the longitudinal plasmon band. The spectra shown in Figure 2C illustrate the high stability of our Au NRs@HS-DNA-6-FAM in 2 M NaCl after 56 days incubation, despite the higher ionic strength (I, $I = \frac{1}{2}\sum_{i=1}^{n} c_i z_i^2$, with $c_i$ being the concentration of the ion *i* and $z_i$, its charge) of this solution (I = 2 M) *vs.* I = 0.015 M for the 5 mM $MgCl_2$ solution. While all these results are quite promising, the deployment of AuNRs@HS-DNA in the biomedical field requires redispersing them in complex biological media. In the presence of serum proteins, particles become coated by a protein corona and can form aggregates of up to micrometer size.[67-69] Therefore, we tested the stability of our Au NRs-DNA conjugates upon redispersion in DMEM cell culture medium containing 10% FCS. The spectrum is shown in Figure 2D and further confirms the colloidal robustness of our DNA-modified Au NRs.

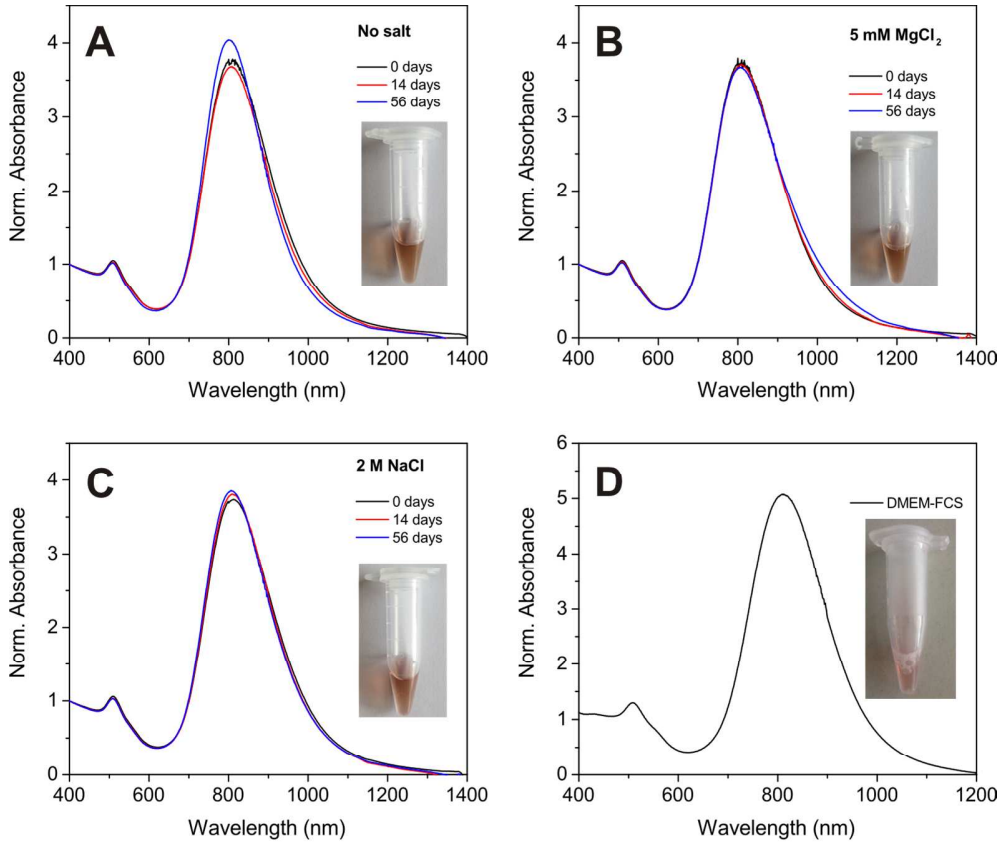


**Figure 2.** Vis-NIR spectra of Au NRs@HS-DNA-6-FAM (grafting density: 194 DNA strands / Au NR, *i.e.*, 0.05 DNA strands / Au nm$^2$) in 1× TAE containing 0.001 % tween 80. Note that 6-FAM tagged HS-DNA oligonucleotides were used in order to enable DNA quantification. In (A) no extra salt was added (reference sample), while in (B) and (C) 5 mM $MgCl_2$ and 2 M NaCl were added, respectively. Panels A-C show the spectra measured directly after DNA functionalization (0 days, black curves), after 14 days (red curves), and after 56 days (blue curves). The insets show photographs of the corresponding samples after 56 days incubation. (D) Vis-NIR spectrum of a different Au NRs@HS-DNA-6-FAM sample (Au NR length × width = 72 × 19 nm; grafting density: 221 DNA strands / Au NR, *i.e.*, 0.046 DNA strands / Au nm$^2$) after redispersion in DMEM containing 10% FCS. A photograph of this sample is shown in the inset. All spectra were normalized at 400 nm.

As mentioned earlier, the main advantage of performing an aqueous-organic-aqueous transfer of the Au NRs prior to oligonucleotide grafting lies in the efficient removal of the cationic CTAB surfactant.[53] Free CTAB molecules are known to induce cytotoxicity.[70, 71] We verified that CTAB is effectively not present in our Au NRs@HS-DNA. This was confirmed by the absence of the characteristic Br 3d peak in the XPS spectrum of Au NRs@HS-DNA (see XPS spectra in Figures S11-S12 and Table S7). Given this positive result, we decided to test the cytotoxicity of the DNA-functionalized Au NRs on adherent lung carcinoma A549 cells in a concentration series after 24 h. Viability for the cell population was assessed by the MTS assay, whose results are shown in Figure 3A. Increasing concentrations of the Au NRs@HS-DNA (expressed as Au atom concentrations) from 1 µg/mL ($5 \times 10^{-3}$ mM) up to 100 µg/mL (0.5 mM) had no effect on cell viability, which remained >95% in the whole concentration range examined. Note that, since the MTS assay measures absorption, Au NRs incorporated in the cells, as well as Au NRs adsorbed on the surface of the well plate, lower the absorbance intensity. Therefore, the viability is in fact even closer to 100%.

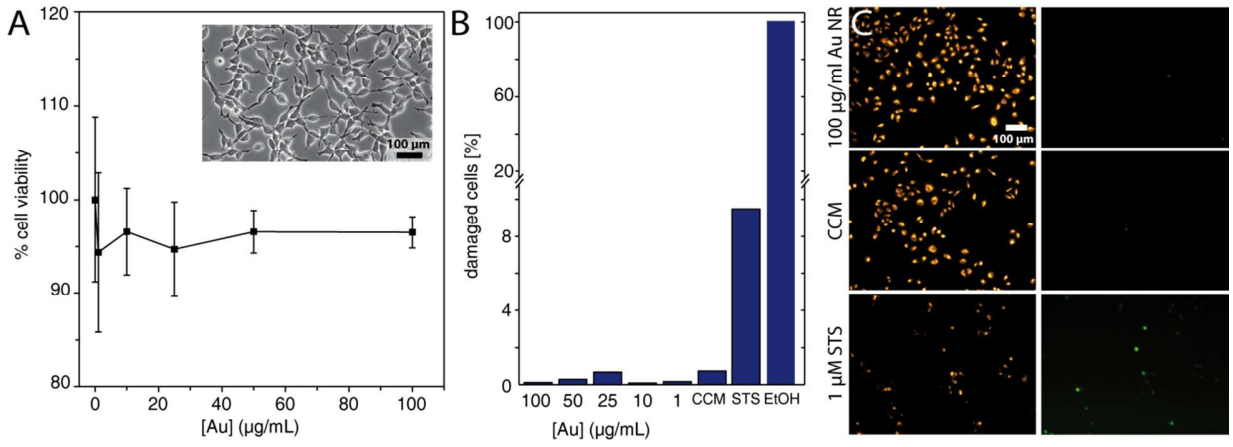

**Figure 3.** Cell viability. (A) Graph depicting the viability of lung carcinoma A549 cell population in DMEM with 10% FCS upon incubation for 24 h with the indicated doses of DNA-functionalized Au NRs (Au NRs' length × width = 64 × 12 nm, DNA grafting density = 0.063 strands / Au $nm^2$). Note that the concentration is expressed as atomic Au concentration. The HS-DNA sequence used herein was 5'-thiol-C6-T18-3'-6-FAM. The inset contains a representative phase contrast microscopy image of viable cells after incubation for 24 hours. (B) Bar graph depicting the viability and the membrane integrity of single cells using c12-resazurin and SYTOX green. (C) Exemplary microscopy fluorescence images for the highest Au NRs@HS-DNA dose employed (100 μg/mL), for the negative (CCM), and for the positive (1 μM STS) control. Healthy cells display an orange fluorescence, but no green fluorescence from the nucleus. Cells with a stained (green) nucleus indicate membrane leakage. The Au NRs@HS-DNA used for the experiments in panels (B) and (D) had a length × width = 72 × 19 nm and a DNA grafting density = 0.046 DNA strands / Au $nm^2$.

Beside the cell population-based viability assays, we assessed the viability, as well as the membrane leakage, at the single cell level using $c_{12}$-resazurin and an impermanent nucleic acid dye. Healthy cells should show only a fluorescence signal from the metabolized $c_{12}$-resazurin, but no signal from the nucleus. Cells with a compromised membrane should show additional fluorescence of the nucleus, and dead cells only the fluorescence from the nucleus. In Figure 3B the percentage of damaged cells is displayed in a bar graph. The number of cells with a compromised membrane or dead lie below 1 % for all Au NRs@HS-DNA doses tested. In contrast, for the positive control with 1 μM STS, this percentage is *ca.* 10%, while for EtOH it is 100 %. Figure 3C depicts some exemplary fluorescence microscopy images for the highest Au

NRs@HS-DNA dose and for the controls, with the fluorescence of the $c_{12}$-resorufin in the left column and the nucleus staining, in the right column. The cells exposed to Au NRs@HS-DNA show the same fluorescence behavior as the CCM control.

The viability tests only give a rough indication about the toxicity of a given nanomaterial. Therefore, more sensitive measurements are necessary. Measuring the ROS activity, for example, can provide direct information about the stress level of a cell. Thus, we checked the ROS activity for all Au NRs@HS-DNA doses after 24 h exposure. Figure 4A shows three exemplary fluorescence images of the ROS activity for the highest Au NRs@HS-DNA dose tested, for a negative, and for a positive control. Whereas hardly any fluorescence signal is detected for the Au NRs@HS-DNA and the negative control, the cells treated with menadione have an increased ROS level. The normalized frequency distribution of the single cells as a function of their measured ROS level, is displayed in Figure 4B for the different exposure conditions. Compared to the negative control (CCM), the distribution for all Au NRs@HS-DNA doses are very similar, remaining at low ROS levels. In contrast, the ROS activity for the menadione treatment is noticeably higher.

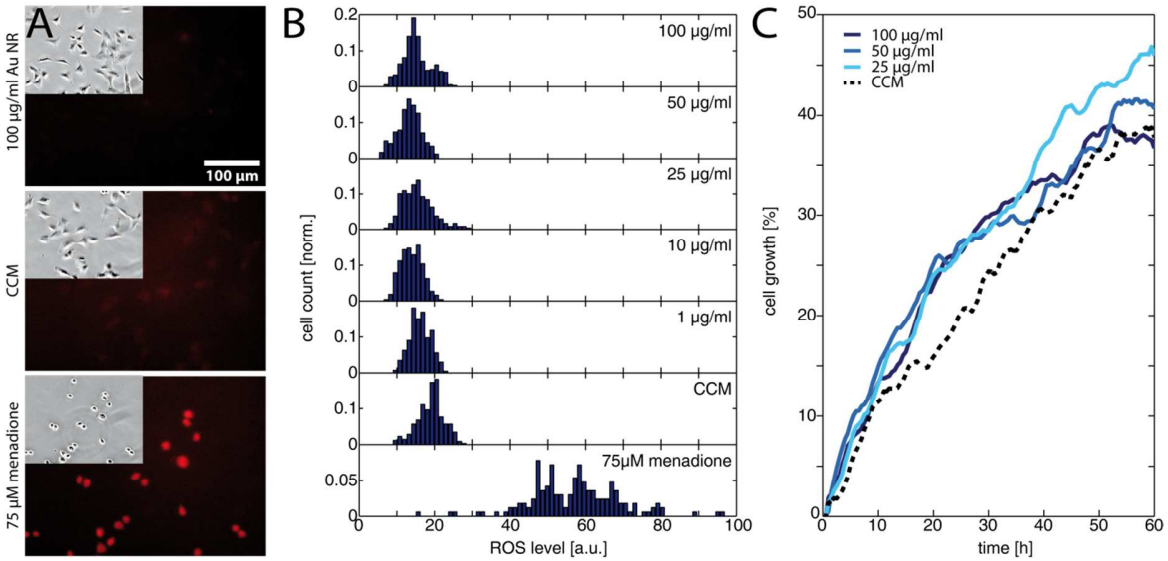


**Figure 4**. ROS level and cell growth. (A) Exemplary fluorescence images of the red fluorescent CellROX marker and bright field images (as inset) for the highest Au NRs@HS-DNA dose (top), for the negative (CCM, center), and positive control (75 µM menadione, bottom). The fluorescence of the marker correlates directly to the ROS level. (B) Frequency distribution of single cells for the ROS level. No ROS activity was detected for any of the Au NRs@HS-DNA doses tested. In contrast, the positive control menadione induced ROS activity. (C) Growth rate of A549 cells over 60 h in the presence of the as-indicated Au NRs@HS-DNA doses. The cell growth in percentage for the negative control (dotted curve) and for the different doses tested (solid curves) shows the same proliferation rate.

In summary, all these results for viability, ROS activity, and cell proliferation indicate that functionalizing Au NRs with single-stranded DNA as described above yields highly biocompatible Au NR-DNA conjugates. The negligible cytotoxicity is mainly ascribed to the efficient removal of CTAB, but also to their high colloidal stability, since colloidal aggregates are also known to promote cytotoxic effects.[52]

So far we have shown that highly stable and biocompatible DNA-functionalized Au NRs can be obtained. Up to now the focus was set on Au NRs with an aspect ratio ~ 4 and functionalized with a thiolated multi-T DNA sequence. Nevertheless, functionalization of higher aspect ratio Au NRs with other DNA sequences works equally well with the described approach. This is particularly advantageous for applications where the plasmonic potential of the NIR-tunable longitudinal plasmon band of the Au NRs is to be exploited, as will be shown below. In order to test the DNA hybridization potential of the Au NR-DNA conjugates and to assess the possibility of driving their selective DNA melting with a NIR laser, we shift our focus in the following to higher aspect ratio gold nanorods displaying a significant plasmon absorption at 1064 nm. For this we functionalized two aliquots of an Au NR batch with dimensions L × W = 93 × 14 nm (A.R. = 6.65) with two different single-stranded DNA sequences, namely with a 5'-thiol-$C_6$-$A_{20}$GGTTCA**GGCACAG**CACATCAA-3'-6-FAM sequence, and with a 5'-thiol-$C_6$-$A_{10}$**CTGTGCC**-3'-6-FAM. Note that both sequences are complementary through the sequences marked in bold and with the multi-A sequence serving as a spacer. The extinction spectra of both samples are shown in Figure S13 and Figure S14. Self-assembled clusters of Au NRs@HS-DNA show a melting temperature of 48.1°C for the specific buffer conditions used in the subsequent experiments (see Figure S15).

Au NPs are very efficient in converting light into heat if they are excited with high intensity light of a frequency near their plasmon resonance frequency.[72-74] In addition, the heat of the Au NPs quickly dissipates into the surrounding medium, but under suitable excitation conditions a small volume around the NPs can be locally heated to a temperature sufficient to denature DNA, while

the bulk solution remains essentially at the initial temperature.[75] This frequency-dependent local heating effect can be used to melt clusters of DNA-functionalized Au NPs that are interconnected through complementary DNA strands, and to selectively address Au NPs with different plasmon resonance frequencies in the same sample solution by using laser light whose frequency matches that of the different plasmon resonances. For the laser-assisted DNA melting experiments we used the setup schematically sketched in Figure 5A, which is a modification of the one reported by *Stehr et al.*[76, 77] in order to accommodate a NIR Nd:YAG cw-laser (1064 nm wavelength, CNI Lasers, Model: OEM-H-1064nm-3W) in addition to a frequency-doubled Nd:YAG cw-laser (532 nm wavelength, CNI Lasers, Model:OEM-F-532nm-2W). The light paths of the two laser beams were combined through a dichroic mirror. Both beams were expanded by a factor of approximately 3 and focused by a 100 mm lens into a sample. The sample (20 µL) was loaded into polystyrene microtiter strips cut out from common 384 well plates (Greiner Bio One Int.) and whose transparent bottom ensures laser light transmission. The laser beam could be moved in two dimensions in the focus plane across the sample *via* a galvanometer mounted on a translation stage. A transimpedance amplified photodetector (detector I) registered the laser light passing through the sample. An identical second detector (detector II) recorded the fluctuations of the laser light intensity by measuring the reflections of the laser light from a glass plate before the beam passed through the sample.

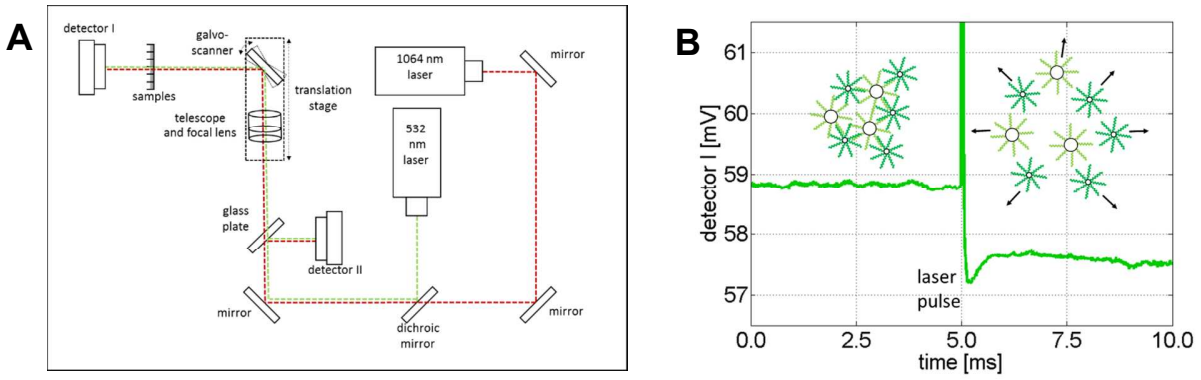

**Figure 5.** (A) Sketch of the experimental setup used for the selective laser-assisted disassembly of clusters consisting of Au NPs self-assembled with complementary DNA strands. (B) Temporal evolution of the laser light transmission at 532 nm passing through a sample containing clusters of 60 nm and 10 nm spherical Au NPs. The green curve shows the voltage output of detector I (average over 1000 transients), which is proportional to the intensity of the light passing through the sample. Upon illumination of the sample with the high intensity laser pulse (100 μs pulse after 5 ms), the NPs convert the energy of the laser light into heat and the dsDNA interconnecting the NPs inside the clusters can dehybridize. NP disassembly leads to an increased extinction at 532 nm, which is detected as a decrease in the transmitted light (for times > 5.1 ms).

The DNA melting experiments comprise three consecutive phases. The first one involves measuring the transmission of a sample by setting one of the lasers to emit a moderate amount of power (<50mW). At this power level, the transmission can be measured without causing significant warming of the nanoparticles. In the second phase, the actual laser heating step, the same laser is operated at maximum power for 100 μs. At a maximum power of 2.3 W, the green laser reaches a power density of 4.5 kW/mm² in the focal spot in the sample, while the NIR laser reaches a power density of 6.2 kW/mm² at 2.0 W maximum power. If the sample contains clusters of DNA-self-assembled Au NPs with a plasmon frequency matching the wavelength of either laser, such irradiation leads to sufficient light-to-heat conversion to melt the interconnecting DNA strands and, hence, to disassemble the clusters. In the third phase, the

transmission is measured once again with the same laser set again to moderate power (< 50 mW). If in the previous heating step, DNA melting results in cluster disassembly, it leads to a change in the extinction of the sample that can be observed as a transmission change on detector I. Figure 5B illustrates the transmission change for a sample containing clusters of spherical Au NPs (10 nm and 60 nm diameter) measured and heated at 532 nm. The detectable change in the extinction is typically on the order of 0.1-2%. This moderate change can be explained by the focal geometry of our laser focus, which is characterized by a Rayleigh length of approximately 600 µm. This length can be assumed to be roughly equivalent to the optical path length that effectively experiences sufficient intensity to melt the DNA, and thus to cause a disintegration of the clusters and a change in extinction. Furthermore, the focal volume can be estimated to be on the order of 1 nL and, therefore, each raw measurement results in DNA melting of only a minute fraction of the sample (*ca.* 1 nL / 20 µL = 0.005%). Because of this, it is not possible to experimentally measure *in situ* the spectral shifts occurring as a result of laser-induced melting of the irradiated clusters.[ii] Nevertheless, a comparison of the observed change in transmission upon melting at the two respective laser wavelengths with that of an analog melting experiment of the bulk solution (see Figure S15, ESI) is qualitatively consistent.

As each measurement from the tiny volume excited by the laser leads to a small signal change (0.1-1%), all our DNA melting experiments comprised the recording and averaging of a multitude of heating pulses and transmission changes for each sample. This opportunity to

[ii] Even if thousands of shots are accumulated in such a way that a meaningful portion of the solution gets excited by the laser for several minutes, a comparison of the spectra of the bulk solution would still not be appropriate. In this case, the nanoparticles within a sub-volume, and already hit by the laser, would rehybridize while the laser continues processing new sub-volumes.

conduct many melting experiments in one reaction vessel with several measurements *per* second is a unique advantage of this approach. For each heating pulse, the change in the transmission of the sample was recorded by detector I, while fluctuations of the laser intensity were recorded by detector II. The raw data were recorded from both detectors at a sampling rate of 120kS/s (16 Bit ADC, National Instruments USB-6011). By evaluating the median value of 6000 data points before and after the heating pulse for each detector the change in transmission could be approximately obtained by calculating

$$\Delta\mathrm{Trans} = \frac{\text{median intensity at detector I after the pulse}}{\text{median intensity at detector I before the pulse}} - \frac{\text{median intensity at detector II after the pulse}}{\text{median intensity at detector II before the pulse}} \quad .$$

Finally, the 60 individual measurements *per* sample of $\Delta\mathrm{Trans}$ were added to the median extinction change $\overline{\Delta\mathrm{Trans}}$ .

Figure 6 shows a comparison of the selective melting experiments, displaying the median transmission change $\overline{\Delta\mathrm{Trans}}$ at 532 and 1064 nm induced upon laser heating at the same wavelength. Specifically, the samples examined contained clusters of hybridized 10 and 60 nm spherical Au NPs (Figure 6, sample A), of hybridized high aspect ratio (93×15 nm) Au NRs (described above, Figure 6, sample B), and of a binary mixture containing a 1:1 mixture of samples A and B (Figure 6, sample C). The 10 nm and 60 nm spherical Au NPs were functionalized with two different single-stranded DNA sequences, namely with a 5'-thiol- $A_{35}$ - triethylene $\mathrm{glycol}_2$-TGGAGATAAGAG**TGAGGTT**TGG-3’ on the 10 nm spherical Au NPs and a 5'-thiol– $A_{25}$G**AACCTCA**-3’- dideoxycytidine sequence on the 60 nm spherical Au NPs. Both sequences are complementary through the sequences marked in bold. The Multi-A sequences and triethylene glycols serve as spacers, while dideoxycytidine serves as a 3’ chain terminator.

Self-assembled clusters of such spherical Au NPs show a melting temperature of 54.7°C for the specific buffer conditions used in subsequent experiments (see Figure S15). The DNA sequences on the spherical Au NPs and on the Au NRs (see above) only allowed pure clusters of either spherical Au NPs or of Au NRs to form under the experimental conditions used for the transmission experiments. Conventional melting experiments (not shown here) confirmed that under the given conditions mixed clusters do not form. In all three cases the NPs were allowed to hybridize for 60 minutes at room temperature in a PBS buffer containing 5 mM phosphate and 210 mM NaCl. Sample A only shows a significant transmission change when the 532 nm laser is used for the experiment, while for the 1064 nm laser the transmission change is negligible. The transmission change at 532 nm indicates that the double-stranded DNA that keeps the spherical gold nanoparticles self-assembled in sample A melts upon illumination with a 532 nm laser due to the significant light absorption of the clusters at this wavelength. In contrast, at 1064 nm their absorption is negligible, and thus, illumination with a 100 μs laser pulse at this wavelength does not induce a significant light-to-heat conversion that suffices to reach the melting temperature of the double-stranded DNA. The results are analogous for sample B, though in this case laser-assisted DNA melting (NP disassembly) is attained with a 1064 nm laser due to the strong light absorption of the clusters at this wavelength, and is almost negligible for the 532 nm one. Importantly, the results obtained for a 1:1 mixture of both cluster types (sample C) confirm that in such a binary mixture it is possible to selectively address (melt) the dsDNA of the spherical gold nanoparticle clusters or the dsDNA of the Au NR clusters by selecting a suitable laser wavelength. With the 532 nm laser, only the clusters consisting of the spherical Au nanoparticles disassemble, while with the 1064 nm laser only the clusters comprised of the Au NRs undergo disassembly. These measurements show, that different dsDNAs can be selectively addressed and

optothermally dehybridized within one solution, regardless of their respective melting temperature. Even though in our experiments the clusters solely composed of spherical Au NPs have a higher melting temperature ($T_M$=54.7°C, see Figure S15) than those composed of only Au NRs ($T_M$=48.1°C), they can be selectively melted without affecting the latter ones[iii]. In an earlier work Poon *et al.* demonstrated that the predominant photothermal release mechanism of DNA from gold nanoparticles occurs *via* denaturation of the double-stranded DNA at laser intensities in the order of 130 kW/mm$^2$ rather than *via* the thermolysis of the Au-S bonds.[78] The laser intensities that we used in our experiments are much lower than 130 kW/mm$^2$ (namely, 4.5-6.2 kW/mm$^2$) and, hence, it can be assumed that Au-S bond breaking is negligible in our case. Moreover, we also found (data not shown) that even after applying tens of thousands of laser pulses, i.e., after having irradiated each nanoparticle in the sample several times, they still maintain their ability to self-assemble. If a substantial Au-S bond breaking had occurred, such a reversible self-assembly would not be possible.

[iii] In conventional hybridization and melting experiments in bulk, it was confirmed that no mixed clusters comprising spherical and rod-like NPs form under our experimental conditions (data not shown).

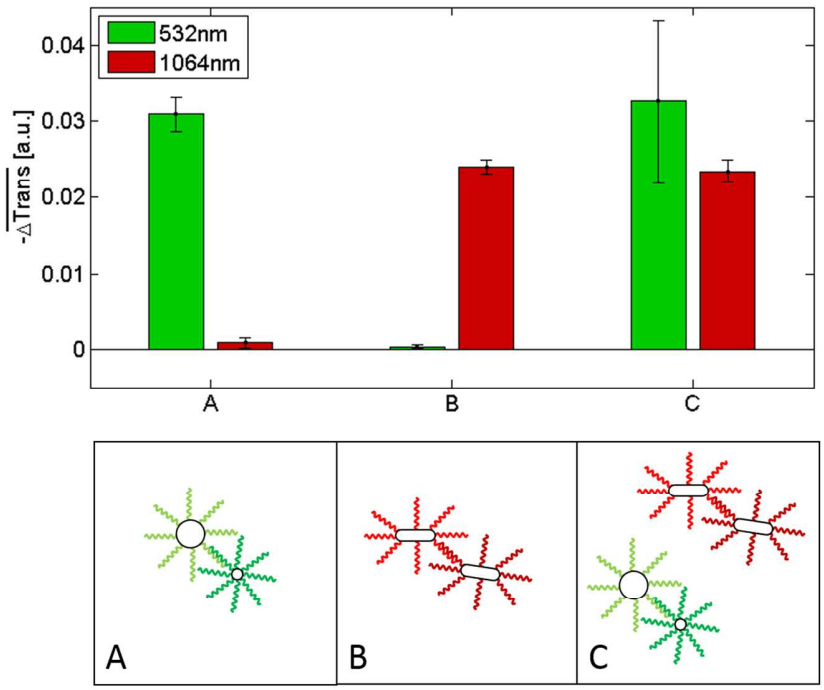


**Figure 6.** Top: $\overline{-\Delta \mathrm{Trans}}$ for samples A, B and C upon 100 µs laser heating and transmission detection at 532 nm (green bar) and 1064 nm (red bar). The data correspond to the median over 60 single measurements, while the error bars show the standard error of the median values. Bottom: schematic illustration of the NP configurations in samples A, B and C before laser heating. Note that in reality, clusters can reach sizes of hundreds or thousands of individual NPs.

Having shown that it is possible to selectively induce the ultrafast melting of the dsDNA that allows self-assembly of either all-spherical or all-rod-like gold nanoparticles, we investigated the potential of DNA-functionalized Au NRs as NIR-addressable probes for the detection of an ssDNA target in binary nanoparticle mixtures analogous to that of sample C in Figure 6. For the detection of the ssDNA target a competitive assay was designed. The role of the ssDNA target was to saturate the 'capture' oligonucleotides on one of the NP types (either the spheres or the

rods) in order to prevent cluster formation and, thus, suppress the corresponding transmission change upon laser heating. For this purpose, the NPs functionalized with DNA complementary to the target DNA were first incubated with the ssDNA target for 15 minutes at room temperature in order to inactivate them for clustering. Thereafter, the remaining NPs (spheres and rods) were added to the solution, allowing the NPs bearing complementary DNA sequences to hybridize for 45 minutes. The results of these experiments are summarized in Figure 7. In sample A we added an ssDNA target complementary to the 60 nm Au nanoparticles (dark green strand). As a result of hybridization, the target blocked the assembly of the 60 nm Au nanoparticles with the 10 nm ones. Hence, in the mixture only the Au NRs could form clusters by means of DNA hybridization. As shown in Figure 7, a significant transmission change at 1064 nm occurs after irradiation with a 1064 nm laser pulse, while for irradiation with 532 nm pulses, the transmission change at this wavelength is negligible. This result confirms that in this scenario only the Au NRs can form clusters. On the other hand, addition of an ssDNA target complementary to the capture sequences on the Au NRs (sample B in Figure 7) prevents their self-assembly with the Au NRs functionalized with the complementary strands. Therefore, no variation in extinction at 1064 nm occurs upon irradiation with 1064 nm laser pulses. However, since the DNA strands of the 60 and 10 nm Au NPs can hybridize, DNA melting can be triggered upon irradiation with a 532 nm laser (see corresponding transmission change in Figure 7). The results for sample C, where no target DNA is present, illustrate that both cluster types (all-spherical and all rod-like) can form and, thus, disassemble upon laser irradiation, since no target DNA hinders the formation of either of them. The results presented here demonstrate that both the spherical Au NPs and the Au NRs can be used as laser-addressable probes for multiplex DNA assays, or for ultrafast and selective DNA melting assays. While the detection assay works equally well for

both NP types, the NIR-addressability of the high aspect ratio Au NR-DNA conjugates used herein offers a competitive advantage. They can provide access to the biological window and, therefore, this makes them highly attractive for the interrogation of clinical samples. In this regard, and given their biocompatible character, they could also potentially be used for DNA detection in *in vivo* environments.

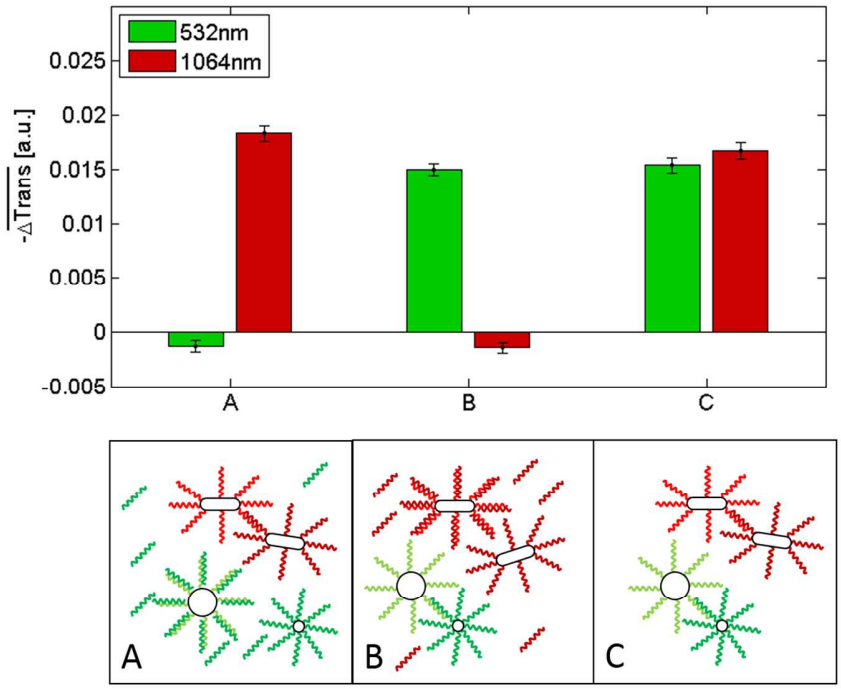


**Figure 7.** Top: $-\overline{\Delta \mathrm{Trans}}$ for samples A, B and C upon 100 µs laser heating and transmission detection at 532 nm (green bar) and 1064 nm (red bar). The data displayed are the median over 60 single measurements. The error bars show the standard error of the median values. Bottom: schematic illustration of the NP configurations and target DNA in samples A, B and C before laser heating. Note that, in reality, the clusters can reach sizes of hundreds or thousands of individual NPs. Sample C serves as a control, since no target DNA was added to this sample.

Note that the slightly smaller transmission change in this sample *vs.* that of sample C in Figure 6 may be attributed to the 15 minutes shorter hybridization time (45 *vs.* 60 min.). Longer hybridization times lead to larger clusters which, in turn, lead to larger transmission changes.

## CONCLUSION

In summary, we have shown that through a careful aqueous-to-organic phase transfer, involving partial PEGylation, subsequent back-transfer to buffer, and oligonucleotide grafting, Au NRs of different aspect ratios can be functionalized with single-stranded thiol-ending DNA. The process is highly reproducible and yields Au NR-DNA conjugates with a controlled number of DNA strands *per* particle and long-term stability in high ionic strength and cell culture media. A MTS, membrane leakage, ROS activity, and cell proliferation assay with adherent lung carcinoma A549 cells indicated a high biocompatibility of the Au NR-DNA conjugates, ascribed to the efficient CTAB removal during the functionalization process and to their high colloidal stability. The Au NR-DNA conjugates undergo self-assembly with nanoparticles functionalized with complementary oligonucleotides and, importantly, they can be selectively addressed with a NIR laser in a mixture containing clusters of hybridized DNA-functionalized spherical Au NPs and clusters of hybridized Au NRs. This is enabled by the distinctive NIR plasmonic absorption of the Au NR-DNA conjugates, which through an efficient light-to-heat conversion upon illumination with a NIR laser (1064 nm, microsecond pulses) leads to the ultrafast and selective melting of the dsDNA that keeps the Au NR-DNA clusters together. The data presented here are a first proof of concept and demonstrate that two different DNA sequences (even with similar or identical melting temperatures) can be selectively addressed and thermally melted in a single sample container. To the best of our knowledge, no other concept exists that allows to do the

same. With our approach one can optothermally address and denature different types of DNA sequences independently. This opens new opportunities for, *e.g.*, gene expression studies or, perhaps, for conducting a multiplex PCR with different protocols for each sequence. We have demonstrated that Au NR-DNA conjugates can serve as NIR-addressable probes and mediators for ultrafast DNA melting. Furthermore, given their biocompatibility and the access they grant to the biological window, they are ideally suited for *in vivo* DNA detection or for applications in *in-vitro* diagnostics.

ACKNOWLEDGMENTS

We acknowledge the Federal Ministry of Economics and Technology (Germany) for funding of the ZIM project KF2260002AJ1. We thank Dr. Madathumpady Abubaker Habeeb Muhammed for the synthesis of the high aspect ratio Au NR sample and Christoph Hohmann (NIM) for graphical support.

**Electronic supplementary information (ESI) available**. Vis-NIR spectra at the different steps of the DNA functionalization process; tables showing the effect of the number of centrifugation cycles on the amount of unbound DNA left in solution and the effect of temperature on the number of DNA strands grafted on the Au NRs' surface; effect of additional parameters/substances on the DNA loading capacity of the Au NRs; time evolution of DNA desorption in different media; XPS spectra; UV-vis-NIR spectra of high aspect ratio Au NRs

functionalized with DNA; and melting curves for clusters of Au NRs and clusters of spherical Au NPs, as well as their respective vis-NIR spectra at different temperatures.

NOTES AND REFERENCES

1. B. Pelaz, S. Jaber, D. J. de Aberasturi, V. Wulf, T. Aida, J. M. de la Fuente, J. Feldmann, H. E. Gaub, L. Josephson, C. R. Kagan, N. A. Kotov, L. M. Liz-Marzán, H. Mattoussi, P. Mulvaney, C. B. Murray, A. L. Rogach, P. S. Weiss, I. Willner and W. J. Parak, *ACS Nano*, 2012, **6**, 8468-8483.

2. E. C. Dreaden, A. M. Alkilany, X. Huang, C. J. Murphy and M. A. El-Sayed, *Chem. Soc. Rev.*, 2012, **41**, 2740-2779.

3. A. Sanchez-Iglesias, M. Grzelczak, J. Perez-Juste and L. M. Liz-Marzan, *Angew. Chem. Int. Ed.*, 2010, **49**, 9985-9989.

4. X. Gao, Y. Cui, R. M. Levenson, L. W. K. Chung and S. Nie, *Nat. Biotechnol.*, 2004, **22**, 969-976.

5. J. Rongchao, C. YunWei, C. A. Mirkin, K. L. Kelly, G. C. Schatz and J. G. Zheng, *Science*, 2001, **294**, 1901-1903.

6. I. Kriegel, C. Jiang, J. Rodríguez-Fernández, R. D. Schaller, D. V. Talapin, E. da Como and J. Feldmann, *J. Am. Chem. Soc.*, 2012, **134**, 1583-1590.

7. I. Kriegel, J. Rodriguez-Fernandez, A. Wisnet, H. Zhang, C. Waurisch, A. Eychmueller, A. Dubavik, A. O. Govorov and J. Feldmann, *ACS Nano*, 2013, **7**, 4367-4377.

8. A. J. Blanch, M. Doeblinger and J. Rodriguez-Fernandez, *Small*, 2015, **11**, 4550-4559.

9. M. A. H. Muhammed, M. Doeblinger and J. Rodriguez-Fernandez, *J. Am. Chem. Soc.*, 2015, **137**, 11666-11677.

10. W. Li, R. Zamani, P. Rivera Gil, B. Pelaz, M. Ibáñez, D. Cadavid, A. Shavel, R. A. Alvarez-Puebla, W. J. Parak, J. Arbiol and A. Cabot, *J. Am. Chem. Soc.*, 2013, **135**, 7098-7101.

11. A. Guerrero-Martínez, B. Auguié, J. L. Alonso-Gómez, Z. Džolić, S. Gómez-Graña, M. Žinić, M. M. Cid and L. M. Liz-Marzán, *Angew. Chem. Int. Ed.*, 2011, **50**, 5499-5503.

12. Q. Liu, Y. Cui, D. Gardner, X. Li, S. He and I. I. Smalyukh, *Nano Lett.*, 2010, **10**, 1347-1353.

13. H. J. Parab, H. M. Chen, T. C. Lai, J. H. Huang, P. H. Chen, R. S. Liu, M. Hsiao, C. H. Chen, D. P. Tsai and Y. K. Hwu, *J. Phys. Chem. C*, 2009, **113**, 7574-7578.

14. T. R. Kuo, V. A. Hovhannisyan, Y. C. Chao, S. L. Chao, S. J. Chiang, S. J. Lin, C. Y. Dong and C. C. Chen, *J. Am. Chem. Soc.*, 2010, **132**, 14163-14171.

15. T. Kawano, Y. Niidome, T. Mori, Y. Katayama and T. Niidome, *Bioconjugate Chem.*, 2009, **20**, 209-212.

16. T. S. Hauck, T. L. Jennings, T. Yatsenko, J. C. Kumaradas and W. C. W. Chan, *Adv. Mater.*, 2008, **20**, 3832-3838.

17. J. Rodriguez-Fernandez, M. Fedoruk, C. Hrelescu, A. A. Lutich and J. Feldmann, *Nanotechnology*, 2011, **22**, 245708.

18. X. H. Huang, I. H. El-Sayed, W. Qian and M. A. El-Sayed, *J. Am. Chem. Soc.*, 2006, **128**, 2115-2120.

19. E. B. Dickerson, E. C. Dreaden, X. H. Huang, I. H. El-Sayed, H. H. Chu, S. Pushpanketh, J. F. McDonald and M. A. El-Sayed, *Cancer Lett.*, 2008, **269**, 57-66.

20. W. I. Choi, J. Y. Kim, C. Kang, C. C. Byeon, Y. H. Kim and G. Tee, *ACS Nano*, 2011, **5**, 1995-2003.

21. L. Tong, Q. Wei, A. Wei and J.-X. Cheng, *Photochemistry and Photobiology*, 2009, **85**, 21-32.

22. H. F. Wang, T. B. Huff, D. A. Zweifel, W. He, P. S. Low, A. Wei and J. X. Cheng, *Proc. Natl. Acad. Sci. USA*, 2005, **102**, 15752-15756.

23. M. Tebbe, C. Kuttner, M. Männel, A. Fery and M. Chanana, *ACS Appl. Mater. Interfaces*, 2015, **7**, 5984-5991.

24. H. W. Liao and J. H. Hafner, *Chem. Mater.*, 2005, **17**, 4636-4641.

25. T. B. Huff, M. N. Hansen, Y. Zhao, J. X. Cheng and A. Wei, *Langmuir*, 2007, **23**, 1596-1599.

26. A. Gole and C. J. Murphy, *Langmuir*, 2005, **21**, 10756-10762.

27. V. Baumann, M. A. Habeeb Muhammed, A. J. Blanch, P. Dey and J. Rodríguez-Fernández, *Isr. J. Chem.*, 2016, **56**, 195-213.

28. C. A. Mirkin, R. L. Letsinger, R. C. Mucic and J. J. Storhoff, *Nature*, 1996, **382**, 607-609.

29. Z. D. Wang, J. Q. Zhang, J. M. Ekman, P. J. A. Kenis and Y. Lu, *Nano Lett.*, 2010, **10**, 1886-1891.

30. Z. D. Wang, L. H. Tang, L. H. Tan, J. H. Li and Y. Lu, *Angew. Chem. Int. Ed.*, 2012, **51**, 9078-9082.

31. L. Y. Zhang, C. X. Guo, Z. M. Cui, J. Guo, Z. L. Dong and C. M. Li, *Chem. Eur. J.*, 2012, **18**, 15693-15698.

32. X. Q. Liu, F. Wang, R. Aizen, O. Yehezkeli and I. Willner, *J. Am. Chem. Soc.*, 2013, **135**, 11832-11839.

33. L. H. Tan, H. Xing and Y. Lu, *Acc. Chem. Res.*, 2014, **47**, 1881-1890.

34. D. K. Lim, K. S. Jeon, J. H. Hwang, H. Kim, S. Kwon, Y. D. Suh and J. M. Nam, *Nature Nanotechnology*, 2011, **6**, 452-460.

35. J. Do, R. Schreiber, A. A. Lutich, T. Liedl, J. Rodriguez-Fernandez and J. Feldmann, *Nano Lett.*, 2012, **12**, 5008-5013.

36. S. J. Hurst, A. K. R. Lytton-Jean and C. A. Mirkin, *Anal. Chem.*, 2006, **78**, 8313-8318.

37. X. Zhang, B. Liu, M. R. Servos and J. Liu, *Langmuir*, 2013, **29**, 6091-6098.

38. B. Liu, E. Y. Kelly and J. Liu, *Langmuir*, 2014, **30**, 13228-13234.

39. W. Zhou, F. Wang, J. Ding and J. Liu, *ACS Appl. Mater. Interfaces*, 2014, **6**, 14795-14800.

40. A. Wijaya and K. Hamad-Schifferli, *Langmuir*, 2008, **24**, 9966-9969.

41. J. Li, B. Zhu, Z. Zhu, Y. Zhang, X. Yao, S. Tu, R. Liu, S. Jia and C. J. Yang, *Langmuir*, 2015, **31**, 7869-7876.

42. D. Shi, C. Song, Q. Jiang, Z.-G. Wang and B. Ding, *Chem. Commun.*, 2013, **49**, 2533-2535.

43. Z. Li, Z. Zhu, W. Liu, Y. Zhou, B. Han, Y. Gao and Z. Tang, *J. Am. Chem. Soc.*, 2012, **134**, 3322-3325.

44. W. Ma, H. Kuang, L. Xu, L. Ding, C. Xu, L. Wang and N. A. Kotov, *Nat. Commun.*, 2013, **4**.

45. S. Pal, Z. Deng, H. Wang, S. Zou, Y. Liu and H. Yan, *J. Am. Chem. Soc.*, 2011, **133**, 17606-17609.

46. C. Zhou, X. Duan and N. Liu, *Nat. Commun.*, 2015, **6**.

47. A. Kuzyk, R. Schreiber, H. Zhang, A. O. Govorov, T. Liedl and N. Liu, *Nat. Mater.*, 2014, **13**, 862-866.

48. Z. Chen, X. Lan, Y.-C. Chiu, X. Lu, W. Ni, H. Gao and Q. Wang, *ACS Photonics*, 2015, **2**, 392-397.

49. C. Shen, X. Lan, X. Lu, W. Ni and Q. Wang, *Chem. Commun.*, 2015, **51**, 13627-13629.

50. X. Lan, X. Lu, C. Shen, Y. Ke, W. Ni and Q. Wang, *J. Am. Chem. Soc.*, 2015, **137**, 457-462.

51. J. H. Joo and J.-S. Lee, *Anal. Chem.*, 2013, **85**, 6580-6586.

52. H. Takahashi, Y. Niidome, T. Niidome, K. Kaneko, H. Kawasaki and S. Yamada, *Langmuir*, 2006, **22**, 2-5.

53. B. Thierry, J. Ng, T. Krieg and H. J. Griesser, *Chem. Commun.*, 2009, 1724-1726.

54. B. Nikoobakht and M. A. El-Sayed, *Chem. Mater.*, 2003, **15**, 1957-1962.

55. M. Z. Liu and P. Guyot-Sionnest, *J. Phys. Chem. B*, 2005, **109**, 22192-22200.

56. X. Ye, C. Zheng, J. Chen, Y. Gao and C. B. Murray, *Nano Lett.*, 2013, **13**, 765-771.

57. A. Wijaya, S. B. Schaffer, I. G. Pallares and K. Hamad-Schifferli, *ACS Nano*, 2009, **3**, 80-86.

58. J. Zhang, S. P. Song, L. H. Wang, D. Pan and C. H. Fan, *Nat. Protoc.*, 2007, **2**, 2888-2895.

59. L. M. Demers, C. A. Mirkin, R. C. Mucic, R. A. Reynolds, R. L. Letsinger, R. Elghanian and G. Viswanadham, *Anal. Chem.*, 2000, **72**, 5535-5541.

60. E. Dulkeith, M. Ringler, T. A. Klar, J. Feldmann, A. M. Javier and W. J. Parak, *Nano Lett.*, 2005, **5**, 585-589.

61. D. V. Guzatov, S. V. Vaschenko, V. V. Stankevich, A. Y. Lunevich, Y. F. Glukhov and S. V. Gaponenko, *J. Phys. Chem. C*, 2012, **116**, 10723-10733.

62. N. R. Jana, L. Gearheart, S. O. Obare and C. J. Murphy, *Langmuir*, 2002, **18**, 922-927.

63. J. Rodriguez-Fernandez, J. Perez-Juste, P. Mulvaney and L. M. Liz-Marzan, *J. Phys. Chem. B*, 2005, **109**, 14257-14261.

64. S. M. Xu, H. Yuan, A. Xu, J. Wang and L. J. Wu, *Langmuir*, 2011, **27**, 13629-13634.

65. M. B. Mohamed, K. Z. Ismail, S. Link and M. A. El-Sayed, *J. Phys. Chem. B*, 1998, **102**, 9370-9374.

66. Y. Horiguchi, K. Honda, Y. Kato, N. Nakashima and Y. Niidome, *Langmuir*, 2008, **24**, 12026-12031.

67. B. Díaz, C. Sánchez-Espinel, M. Arruebo, J. Faro, E. de Miguel, S. Magadán, C. Yagüe, R. Fernández-Pacheco, M. R. Ibarra, J. Santamaría and Á. González-Fernández, *Small*, 2008, **4**, 2025-2034.

68. A. Petri-Fink, B. Steitz, A. Finka, J. Salaklang and H. Hofmann, *European Journal of Pharmaceutics and Biopharmaceutics* 2008, **68**, 129-137.

69. Z. E. Allouni, M. R. Cimpan, P. J. Høl, T. Skodvin and N. R. Gjerdet, *Colloids and Surfaces B: Biointerfaces*, 2009, **68**, 83-87.

70. T. Niidome, M. Yamagata, Y. Okamoto, Y. Akiyama, H. Takahashi, T. Kawano, Y. Katayama and Y. Niidome, *J. Control. Release*, 2006, **114**, 343-347.

71. A. M. Alkilany, P. K. Nagaria, C. R. Hexel, T. J. Shaw, C. J. Murphy and M. D. Wyatt, *Small*, 2009, **5**, 701-708.

72. A. O. Govorov, W. Zhang, T. Skeini, H. Richardson, J. Lee and N. A. Kotov, *Nanoscale Res. Lett.*, 2006, **1**, 84-90.

73. A. O. Govorov and H. H. Richardson, *Nano Today*, 2007, **2**, 30-38.

74. G. Baffou, R. Quidant and F. Javier Garcia de Abajo, *ACS Nano*, 2010, **4**, 709-716.

75. P. Keblinski, D. G. Cahill, A. Bodapati, C. R. Sullivan and T. A. Taton, *J. Appl. Phys.*, 2006, **100**, 054305.

76. J. Stehr, C. Hrelescu, R. A. Sperling, G. Raschke, M. Wunderlich, A. Nichtl, D. Heindl, K. Kürzinger, W. J. Parak, T. A. Klar and J. Feldmann, *Nano Lett.*, 2008, **8**, 619-623.

77. C. Hrelescu, J. Stehr, M. Ringler, R. A. Sperling, W. J. Parak, T. A. Klar and J. Feldmann, *J. Phys. Chem. C*, 2010, **114**, 7401-7411.

78. L. Poon, W. Zandberg, D. Hsiao, Z. Erno, D. Sen, B. D. Gates and N. R. Branda, *ACS Nano*, 2010, **4**, 6395-6403.

TOC ENTRY

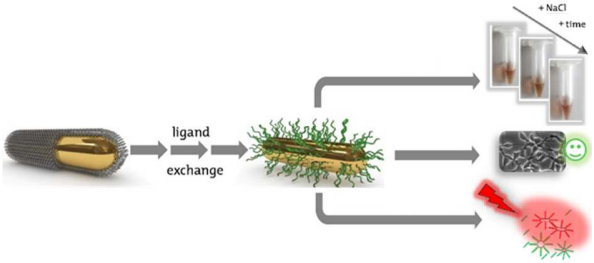


Colloidally stable and biocompatible DNA-functionalized Au nanorods are proved as NIR-addressable probes and mediators for ultrafast and sequence-selective DNA melting.

# Supporting Information for

# Highly stable and biocompatible gold nanorod-DNA conjugates as NIR probes for ultrafast sequence-selective DNA melting

*Verena Baumann,[1,3] Peter Johan Friedrich Röttgermann,[2,3] Frederik Haase,[1,3,#] Katalin Szendrei,[1,3,#] Priyanka Dey, [1,3] Katja Lyons,[1,3] Regina Wyrwich,[5] Matthias Gräßel,[1,3,4] Joachim Stehr,[4] Lars Ullerich,[4] Federico Bürsgens,[4] Jessica Rodríguez-Fernández[1,3]**

[1]Photonics and Optoelectronics Group, Department of Physics and Center for NanoScience (CeNS), Ludwig-Maximilians-Universität München, Amalienstr. 54, 80799 Munich (Germany)

[2]Soft Condensed Matter Group, Department of Physics and Center for NanoScience (CeNS), Ludwig-Maximilians-Universität München, Geschwister-Scholl-Platz 1 80539 Munich (Germany)

[3]Nanosystems Initiative Munich (NIM), Schellingstr. 4, 80799 Munich (Germany)

[4]GNA Biosolutions GmbH, Am Klopferspitz 19, 82152 Martinsried (Germany)

[5]Department of Chemistry, Ludwig-Maximilians-Universität München, Butenandtstr. 5-13 (E), 81377 Munich (Germany)

[#]Current address: Max Planck Institute for Solid State Research, Heisenbergstr. 1, 70569 Stuttgart, Germany.

*e-mail: jessica.rodriguez@lmu.de

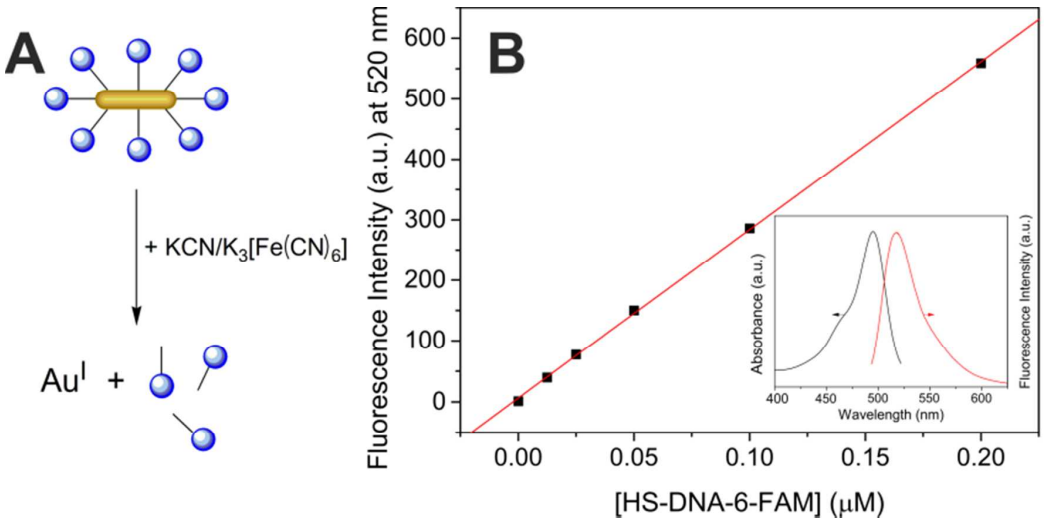


**Figure S1.** (A) Sketch showing the oxidation reaction of gold nanorods with cyanide in order to quantify the number of released HS-DNA-6-FAM strands (the blue spheres depict the fluorescent 6-FAM moiety). (B) Calibration curve for DNA quantification: linear fit of the fluorescence intensity of HS-DNA-6-FAM at 520 nm *vs.* the concentration of HS-DNA-6-FAM. Note that the experimental conditions (medium, concentration of oxidizing agents, etc.) used herein for the determination of the calibration curve were the same as the ones during the oxidation experiments. Inset: absorption (black) and emission (red) spectra of HS-DNA-6-FAM. The emission spectrum was measured upon excitation at $\lambda$ = 485 nm. The emission maximum is centered at 520 nm.

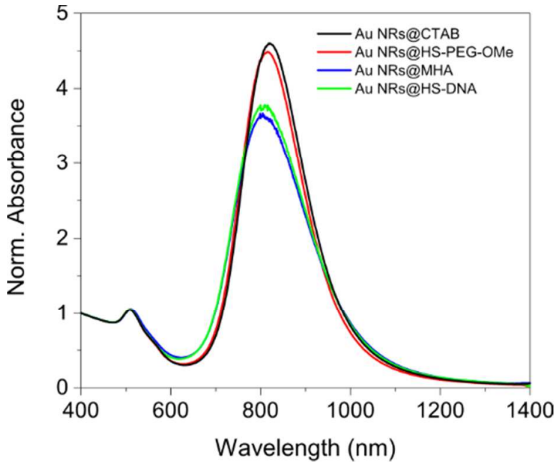


**Figure S2.** Vis-NIR spectra of Au NRs@CTAB in water (black), Au NRs@HS-PEG-OMe in water (red), Au NRs@MHA in TBE 1× containing 0.001 % tween 80 (blue), and Au NRs@HS-DNA-6-FAM in TAE 1× containing 0.001 % tween 80 (green). All spectra were normalized at 400 nm. The specific HS-DNA sequence used herein was 5'-thiol-C6-TTTTTTTTTTTTTTTTTT-3'. Colloidal stability is preserved during all functionalization steps.

**Effect of the HS-PEG-OMe dose on the DNA loading capacity**

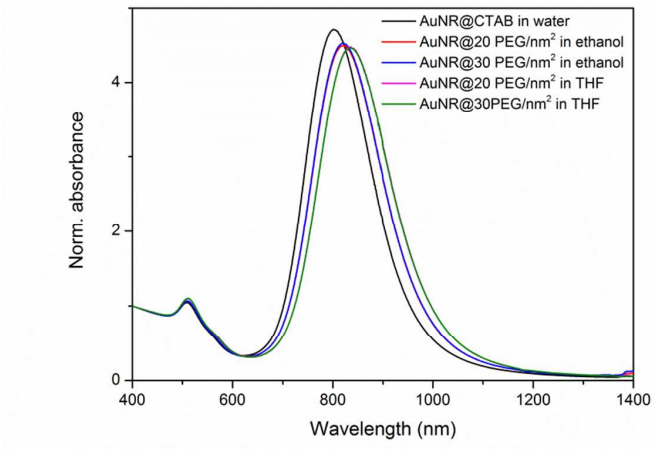


**Figure S3.** Vis-NIR spectra of Au NRs@HS-PEG-OMe after functionalization with a PEG dose of 20 and 30 PEG molecules / Au $nm^2$. The spectra are shown for both samples in

ethanol and in THF. The spectrum of the Au NRs@CTAB in water (black curve) is also provided for comparison. Note that the red spectrum is overlaid by the blue spectrum, indicating no significant differences between both samples at the ethanol redispersion step. The magenta spectrum is also overlaid by the green spectrum, which further confirms that there are no significant differences between both samples after redispersion in THF. All spectra were normalized at 400 nm for comparison.

**Table S1.** Effect of the HS-PEG-OMe dose used (20 *vs.* 30 molecules / Au $nm^2$) on the DNA loading achieved for Au NRs@HS-DNA-6-FAM (samples shown in Figure S3). The MHA dose used was 300 molecules / Au $nm^2$, while the molar ratio HS-DNA-6-FAM/Au NRs was set to 10000 in both cases. The quantification results show the detrimental effect (lower DNA loading) of PEGylating at doses larger than 20 molecules / $nm^2$. Even though the difference is not dramatic for 20 *vs.* 30 HS-PEG-OMe molecules / Au $nm^2$, larger doses lead to very low DNA loadings (results not shown).

| **HS-PEG-OMe dose** | **DNA strands/particle** | **DNA strands / Au $nm^2$** |
|---|---|---|
| 20 PEG / Au $nm^2$ | 184 | 0.050 |
| 30 PEG / Au $nm^2$ | 158 | 0.043 |

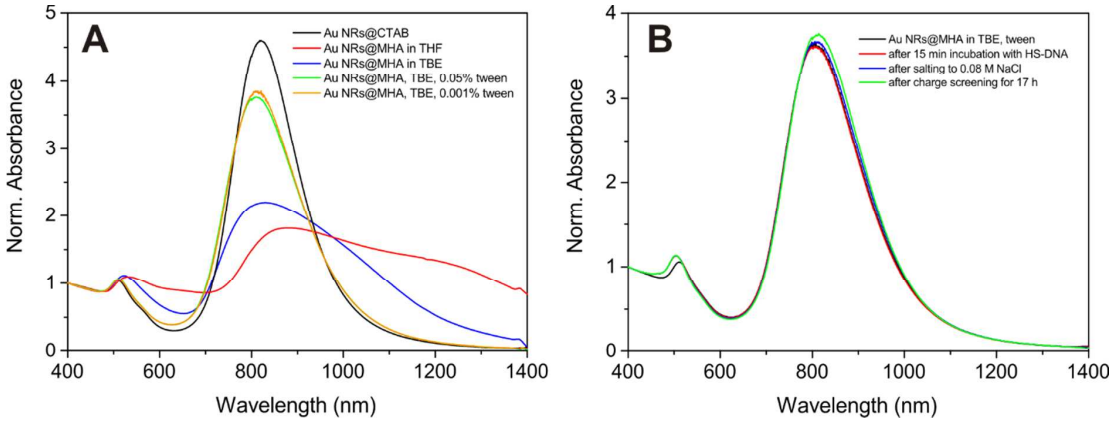


**Figure S4.** (A)Vis-NIR spectra showing the effect of the absence or presence of tween 80 in TBE 1× buffer upon redispersion of flocculated Au NRs@MHA. The graph includes the spectra of the Au NRs@CTAB in water plotted as reference (black), the flocculated Au NRs@MHA in THF (red), the Au NRs@MHA after redispersion in TBE 1× buffer (blue), in TBE 1× containing 0.05 % tween 80 (green) and in TBE 1× containing 0.001 % tween 80 (orange). All spectra were normalized at 400 nm. It can be seen that in the absence of tween 80 the Au NRs@MHA aggregate significantly. (B) Vis-NIR spectra of Au NRs@MHA in TBE 1× containing 0.001 % tween 80 (black) after incubation with the HS-DNA oligonucleotides for 15 min (red), after stepwise addition of NaCl to a final concentration of 0.08 M (blue), and after charge screening for 17 h (green). All spectra were normalized at 400 nm. The specific HS-DNA sequence used herein was 5'-thiol-C6-TTTTTTTTTTTTTTTTTT-3'. Colloidal stability was maintained throughout all steps.

**Effect of the molar ratio HS-DNA-6-FAM / Au NRs on the DNA loading capacity**

**Table S2.** Effect of the molar ratio n(HS-DNA-6-FAM) : n(Au NRs) on the DNA loading. In the experiments shown below the PEG dose used was set to 30 PEG/nm$^2$ and DNA functionalization was carried out by performing the salting step up to a final concentration of [NaCl] = 0.08 M.

| n(HS-DNA) : n(Au NR) | DNA strands/particle | DNA strands/nm$^2$ |
|---|---|---|
| 3700 | 158 | 0.043 |
| 8000 | 107 | 0.029 |
| 20000 | 105 | 0.028 |

Compared to our standard conditions, where the n(HS-DNA) : n(Au NR) = 3700, *i.e.*, the added dose is set to 1 HS-DNA strand / Au nm$^2$, a slightly lower DNA loading is obtained for n(HS-DNA) : n(Au NR) = 8000 (2.2 HS-DNA strands / Au nm$^2$), and 20000 (5.4 HS-DNA strands / Au nm$^2$). The most plausible explanation for this, *a priori*, counterintuitive effect relates to the high electrostatic repulsion of the negatively charged DNA backbones. The [NaCl] used (0.08 M) is enough to compensate for this repulsion at lower n(HS-DNA) : n(Au NR) ratios. However, it does not suffice when the relative concentration of DNA backbones is much larger (n(HS-DNA) : n(Au NR) = 8000 and 20000) and, hence, it cannot give rise to any increase in DNA loading. Therefore, unless the NaCl concentration is concomitantly increased along with the n(HS-DNA) : n(Au NR) ratio, increasing the latter ratio alone does not give rise to any DNA loading increase.

**Effect of sonication during charge screening on the DNA loading capacity**

**Table S3.** Effect of performing a 15 s sonication after each salting step on the final DNA loading. In the experiments below the final salting concentration was set to [NaCl] = 0.4 M, while the molar ratio n(HS-DNA) : n(Au NRs) was set to 10000. These results demonstrate the significant, positive, effect of sonication on the DNA loading capacity of the Au NRs. See the corresponding spectra in Figure S5.

| 15 s sonication after each salting step | DNA strands/particle | DNA strands/nm$^2$ |
|---|---|---|
| no | 352 | 0.095 |
| yes | 409 | 0.111 |

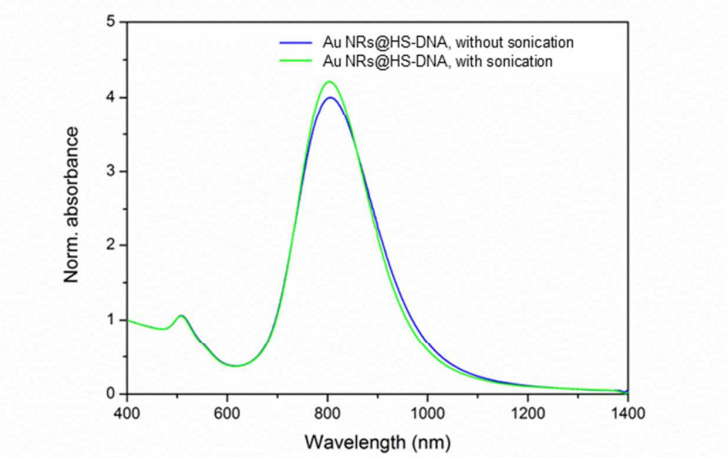


**Figure S5.** Vis-NIR spectra of Au NRs@HS-DNA in 1× TAE containing 0.001% tween 80 (washed samples). The Au NRs were functionalized with HS-DNA by performing no sonication during salting (blue curve), or by carrying out a 15 s sonication at the end of each salting step (green curve), see DNA loading data in Table S3 above. Both spectra are normalized at 400 nm.

**Table S4.** Influence of the number of centrifugation steps and the presence of tween 80 on the $[\text{HS-DNA-6-FAM}]_{free}$ / $[\text{HS-DNA-6-FAM}]_{total}$ ratio of Au NRs@HS-DNA-6-FAM after washing. Note that here "centrifugation cycle" refers to a whole centrifugation and redispersion cycle.

| Number of centrifugation cycles | $[HS\text{-}DNA\text{-}6\text{-}FAM]_{free}$ / $[HS\text{-}DNA\text{-}6\text{-}FAM]_{total}$ (%) |
|---|---|
| 2 (no tween 80) | 34.4 |
| 2 (in the presence of 0.001 % tween 80) | 8.75 |
| 3 (no tween 80) | 0.352 |
| 3 (in the presence of 0.001 % tween 80) | 0.006 |

We optimized the washing conditions of our DNA-functionalized Au NRs so that the amount of free (unbound) DNA strands present after washing is minimal ($[HS\text{-}DNA\text{-}6\text{-}FAM]_{free}/[HS\text{-}DNA\text{-}6\text{-}FAM]_{total} < 0.01$). The results in Table S4 clearly indicate that by increasing the number of centrifugation cycles from 2 to 3, the percentage ratio $[HS\text{-}DNA\text{-}6\text{-}FAM]_{free}/[HS\text{-}DNA\text{-}6\text{-}FAM]_{total}$ drops from 34.4% to 0.352 %. Furthermore, by adding 0.001 % tween 80, the ratio $[HS\text{-}DNA\text{-}6\text{-}FAM]_{free}/[HS\text{-}DNA\text{-}6\text{-}FAM]_{total}$ further decreases from 8.75 % (for 2 centrifugation cycles) down to 0.006 % (for 3 centrifugation cycles), as compared to the results in the absence of tween. In general, we observed that the surfactant decreases the affinity of the Au NRs@HS-DNA-6-FAM to the walls of the centrifugation tube. This enables the formation of a more compact pellet and thus, allows for a better removal of the supernatant, which contains unbound DNA strands. Based on these results the optimized washing conditions for DNA-functionalized Au NRs were set to 3×, in the presence of 0.001 % tween 80.

**Table S5.** Influence of the incubation temperature during the 17 h charge screening. Note that the temperature (23 °C *vs.* 50 °C) was strictly controlled for 17 hours once a final [NaCl] = 0.08 M was reached. In all cases, for quantification purposes, DNA functionalization was performed with HS-DNA-6-FAM oligonucleotides.

| Temperature during DNA functionalization | DNA strands / Au NR | DNA strands / Au $nm^2$ |
|---|---|---|
| 23 | 151 | 0.04 |
| 50 | 322 | 0.09 |

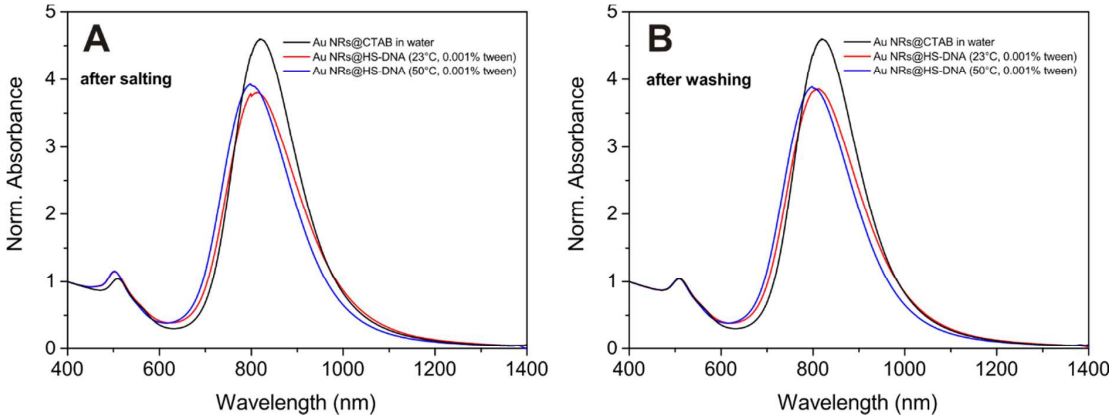


**Figure S6.** Effect of the incubation temperature on the vis-NIR spectra of Au NRs upon DNA functionalization. (A) Extinction spectra of the Au NRs@HS-DNA after salting overnight for 17 h at 23°C and 50°C in the presence of 0.001% tween 80. (B) Extinction spectra of the same batches after 3× washing with TAE 1× containing 0.001% tween 80. The spectrum of Au NRs@CTAB in water (black) is included as reference. All spectra were normalized at 400 nm. In all cases the stability of the Au NRs is preserved. Nevertheless, for the samples incubated at 50 °C a small blue-shift of the longitudinal plasmon band of the Au NRs can be observed. This is due to a slight decrease in the aspect ratio of the Au NRs resulting from partial reshaping at higher temperatures, as previously reported.[1,2]

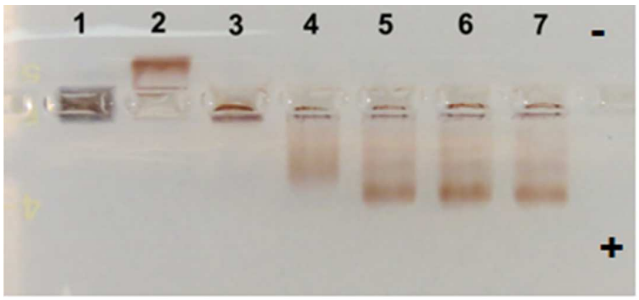


**Figure S7.** Photograph illustrating the gel electrophoresis results for a batch of Au NRs (length × width = (64±12) × (16±3) nm) bearing different functionalities on their surface. The samples correspond to: Au NRs@CTAB (1), Au NRs@HS-PEG-OMe (2), Au NRs@MHA (3), Au NRs@HS-DNA loaded with 0.050 strands / Au $nm^2$ (4), Au NRs@HS-DNA loaded with 0.115 strands / Au $nm^2$ (5), Au NRs@HS-DNA loaded with 0.123 strands / Au $nm^2$ (6), and Au NRs@HS-DNA loaded with 0.116 strands / Au $nm^2$ (7). The number of DNA strands loaded was controlled by adjusting the [NaCl] from 0.08 M to 0.7 M, from (4) to (7), respectively. In general, the larger the DNA loading, the more homogeneous the bands. Indeed, the sample with the lowest DNA loading (4) shows the strongest band smearing. These gel electrophoresis results indicate that the loading on the Au NRs' surface gets more homogeneous as larger NaCl concentrations are used during the salting step.

**Effect of Au NRs@MHA aging on the DNA loading capacity**

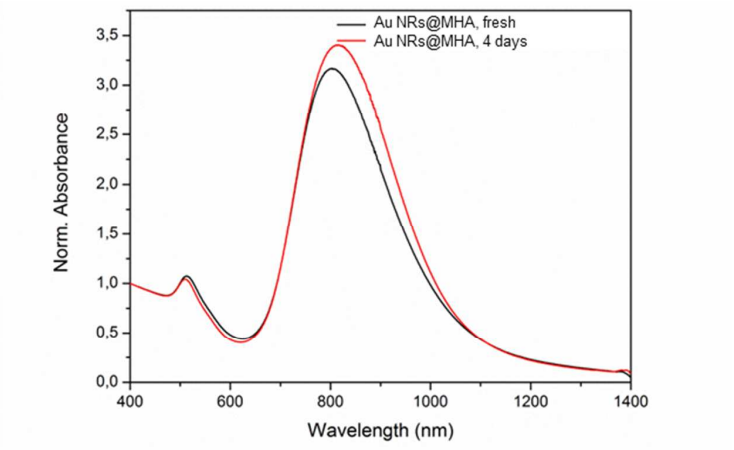


**Figure S8.** Vis-NIR spectra of MHA-functionalized Au NRs in 1× TBE containing 0.001% tween 80. Spectra measured immediately after MHA functionalization (black curve) and after 4 days storage at room temperature (red curve). The spectra are normalized at 400 nm. A slight increase of the relative longitudinal plasmon band intensity points to a slight improvement in colloidal stability upon aging for 4 days. This could be due to two reasons: (i) upon desorption of some MHA molecules from the Au NRs' surface, tween 80 may physisorb and lead to a slightly better sample stability; (ii) it can also be that a small portion of the Au NRs@MHA remain flocculated after redispersion in buffer and that these redisperse (thus, increasing the overall stability slightly) upon longer incubation in the tween-containing buffer.

**Table S6**: Results summarizing the effect of Au NR@MHA aging on the final DNA loading. The samples used herein are those whose spectra are shown in Figure S8.

| Au NRs@MHA storage | DNA strands/particle | DNA strands/nm$^2$ |
|---|---|---|
| 0 days | 627 | 0.170 |
| 4 days | 852 | 0.231 |

When DNA functionalization was performed straight after the preparation of the Au NRs@MHA, a loading of 627 DNA strands/particle (0.170 DNA strands/nm$^2$) was obtained. In contrast, when DNA functionalization was carried out with the aged sample (4 days in this case), a notable larger loading was achieved (852 DNA strands/particle, *i.e.*, 0.231 DNA strands/nm$^2$). Thus, it can be concluded that the aging time of the Au NRs@MHA sample has a strong (positive) effect on the DNA loading capacity. As indicated above, some MHA molecules may desorb from the nanorods' surface, allowing the tween 80 molecules to physisorb. The physisorbed tween 80 molecules are weakly grafted on the NRs' surface. Therefore, their replacement by HS-DNA is more favorable than the replacement of MHA molecules, whose Au-S binding is much stronger. This can explain the higher DNA loadings obtained for the aged Au NRs@MHA sample.

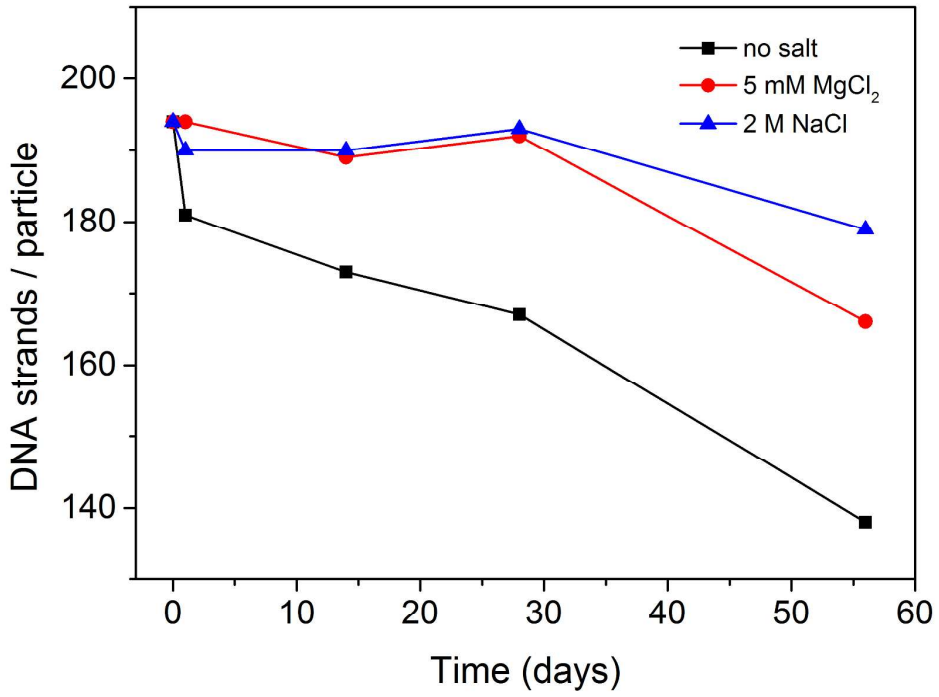


**Figure S9.** Assessment of DNA detachment from the DNA-functionalized Au NRs shown in Figure 2A, 2B, and 2C, upon incubation in salt-containing media. Evolution of the number of DNA strands *per* Au NR as a function of time for an Au NR@HS-DNA-6-FAM sample in TAE 1× (containing 0.001 % tween 80) upon storage without addition of any extra salt (black curve), and upon addition of 5 mM $MgCl_2$ (red curve), and 2 M NaCl (blue curve). The sample containing no extra salt is the one presenting the most significant and gradual DNA detachment over time (29 % after 56 days). However, when the ionic strength of the medium is increased by addition of mono- (NaCl) or divalent ($MgCl_2$) salts, *i.e.*, when the electrostatic repulsion between the negatively charged DNA backbones is conveniently screened, DNA detachment from the Au NRs' surface is significantly reduced. For the sample in 2 M NaCl, DNA detachment is reduced to ~ 8 % after 56 days. For the sample in 5 mM $MgCl_2$, the result is slightly worse (~ 14 %), which may be related to the slightly lower stability of the Au NRs@HS-DNA-6-FAM in 5 mM $MgCl_2$ *vs.* in 2 M NaCl after 56 days (see spectra in Figure S10). Nevertheless, over a time period of 56 days the salt containing

samples show a relatively stable amount of loaded DNA and, in either case (NaCl and $MgCl_2$), the stability of the DNA-modified Au NRs is maintained (see Figure 2 and Figure S10).

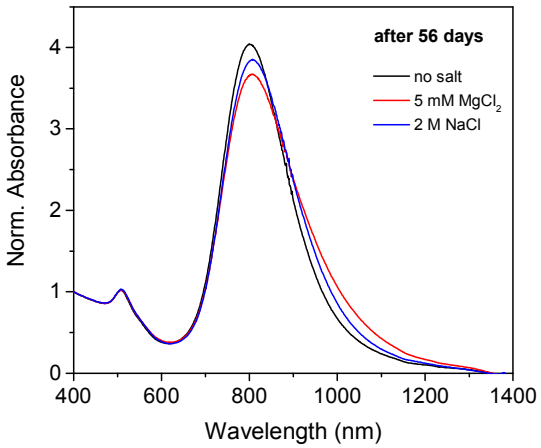


**Figure S10.** Vis-NIR spectra of the Au NRs@HS-DNA-6-FAM shown in Figure 2A, 2B, and 2C (grafting density: 194 DNA strands / Au NR, *i.e.*, 0.05 DNA strands / Au $nm^2$) in 1× TAE containing 0.001 % tween 80. The spectra were taken after 56 days storage in the above medium (no extra salt added), in 5 mM $MgCl_2$, and in 2 M NaCl. All spectra were normalized at 400 nm for comparison. The overall concentration of HS-DNA-6-FAM in those samples (after having taken into account the actual concentration of Au NRs@HS-DNA-6-FAM and their corresponding grafting density) is ~ $4.9\times10^{-8}$ M. The absorption of HS-DNA-6-FAM is low at this concentration and gets overlapped by the stronger absorption of Au. This explains why the characteristic FAM absorption is not detected in our extinction spectra.

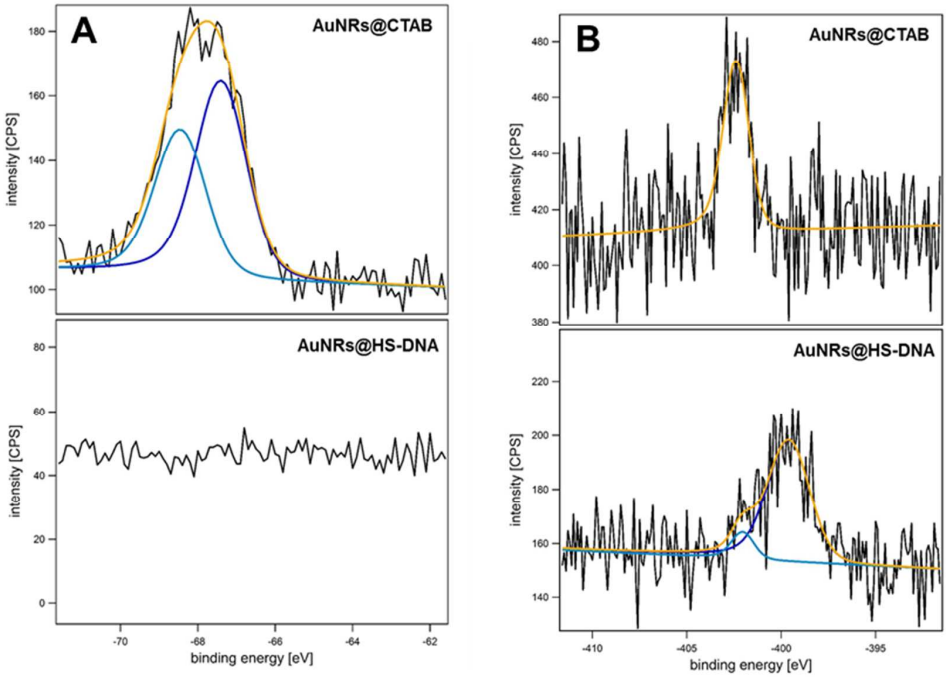


**Figure S11.** XP spectra of (A) Br3d and (B) N1s for the AuNRs@CTAB and for the Au NRs@HS-DNA. In (A) the peaks correspond to the $3d_{5/2}$ and $3d_{3/2}$ photoelectron lines of anionic Br. These peaks are present in the Au NRs@CTAB, but not in the Au NRs@HS-DNA, which indicates that the DNA functionalization worked well regarding CTAB removal. In (B), the N 1s spectrum for the Au NRs@CTAB consists of a peak at ~402 eV, which indicates the presence of N in an ammonium salt (CTAB). For the Au NRs@HS-DNA, the N 1s spectrum can be mainly fitted by a peak at ~400 eV, ascribed to the presence of N in an organic matrix. The spectrum also contains a weak shoulder at ~402 eV, ascribed to the presence of N in an ammonium salt. The almost complete vanishing of the peak at ~402 eV in the Au NRs@HS-DNA as compared to the Au NRs@CTAB is due to the CTAB removal; while the appearance of the new strong peak at ~400 eV stems from the presence of N in the organic DNA matrix. The dimensions of the analyzed Au NRs were: length × width = 72 × 19 nm. For the Au NRs@HS-DNA sample, the DNA grafting density was 221 DNA strands / Au NR, *i.e.*, 0.046 DNA strands / Au nm$^2$.

**Table S7.** Relative N/Au/Br/S/C/O and N/Au/Br atomic ratios determined from the XP spectra of the Au NRs@CTAB and of the sputter-cleaned Au NRs@HS-DNA sample shown in Figure S11. The atomic ratios are normalized to 1 with respect to Au.

| | N/Au/Br/S/C/O (normalized to Au=1) | N/Au/Br |
|---|---|---|
| Au NRs@CTAB | 1.6/1/2/40.5/4 | 1.6/1/2 |
| Au NRs@HS-DNA | 62.5/1/~0/71.6/424.8/27.3 | 62.5/1/~0 |

The peaks were fitted using a Doniach-Sunjic function[3] convoluted with a Gaussian after a linear background subtraction. Intensities of surface species were corrected by the specific cross sections.[4] For the analyzer, the apparatus specific transmission function was determined and peak areas were corrected accordingly.

For the sample Au NRs@CTAB, a clear peak is visible in the Br 3*d* spectrum, indicating the presence of $Br^-$. Also in the N 1*s* spectrum a clear peak can be seen. Based on its binding energy of ~402 eV, one would assign it to the presence of ammonium salt, or in this case, CTAB.[5] When we measured the Au NRs@HS-DNA sample as prepared, there was no gold detectable in the Au 4*f* spectrum. Probably the DNA strands around the Au NRs were too large and XPS was challenged with its limited penetration depth. Because of this, the Au NRs@HS-DNA sample was then sputter-cleaned twice (1 kV, 4 μA, 15 min) to investigate deeper layers. After the second sputter-cleaning process we could identify a clear peak in the Au 4*f* spectrum. In the Br 3*d* spectrum of the cleaned sample there is no peak detectable, which demonstrates the absence of $Br^-$ (also in the spectra of the sample as prepared and after the first cleaning step there was no Br visible). The detection limit of the instrument is in this case ~ 1 %, so this result proves that the Br content of the sample Au NRs@HS-DNA is below the detection limit. The N 1*s* peak of ammonium salt decreased compared to the Au

NRs@CTAB sample, and there is a second peak at ~400 eV that demonstrates the presence of N in an organic matrix environment (DNA).[5]

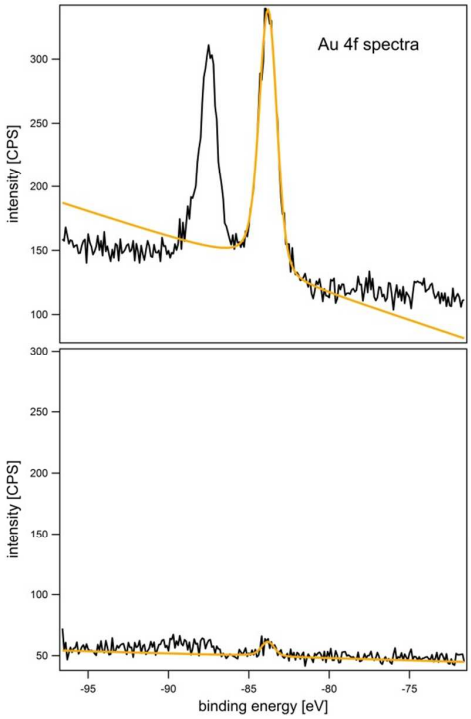


**Figure S12.** XP spectrum of Au 4*f* for the Au NRs@CTAB (top) and for the AuNRs@HS-DNA (bottom). The peak position in both cases indicates that gold is present as Au(0). The peak in the spectrum of the Au NRs@HS-DNA is significantly smaller because it gets attenuated by the large DNA strands surrounding the gold.

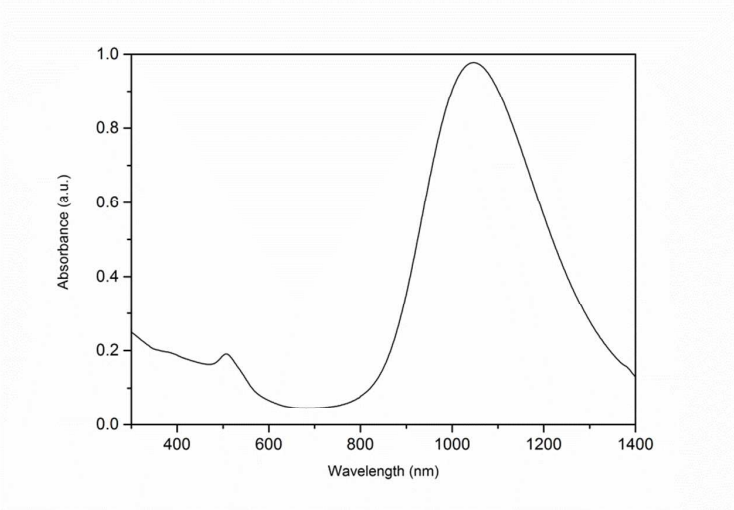


**Figure S13.** UV-vis-NIR spectra of high aspect ratio Au NRs (length × width = 93 × 14 nm, AR = 6.65) functionalized with a 5'-thiol-$C_6$-$A_{20}$GGTTCA**GGCACAG**CACATCAA-3'-6-FAM DNA sequence. The grafting density on the Au NRs' surface is 0.016 strands/Au $nm^2$.

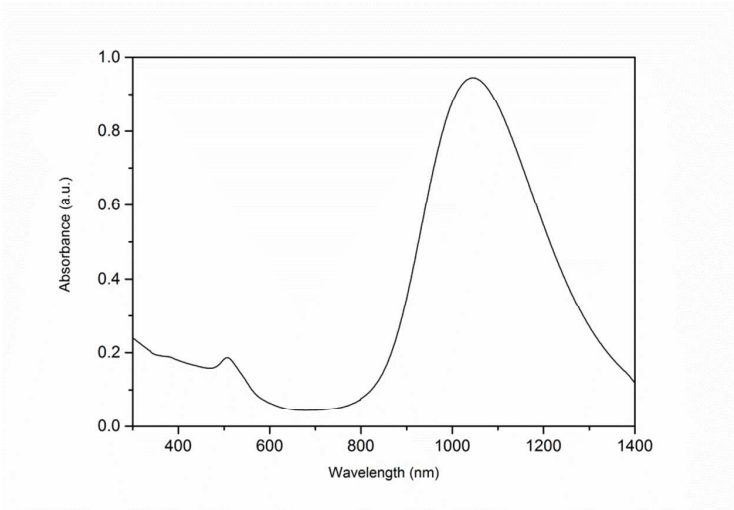


**Figure S14.** UV-vis-NIR spectra of high aspect ratio Au NRs (length × width = 93 × 14 nm, AR = 6.65) functionalized with a 5'-thiol-$C_6$-$A_{10}$**CTGTGCC**-3'-6-FAM sequence. The grafting density on the Au NRs' surface is 0.025 strands/Au $nm^2$.

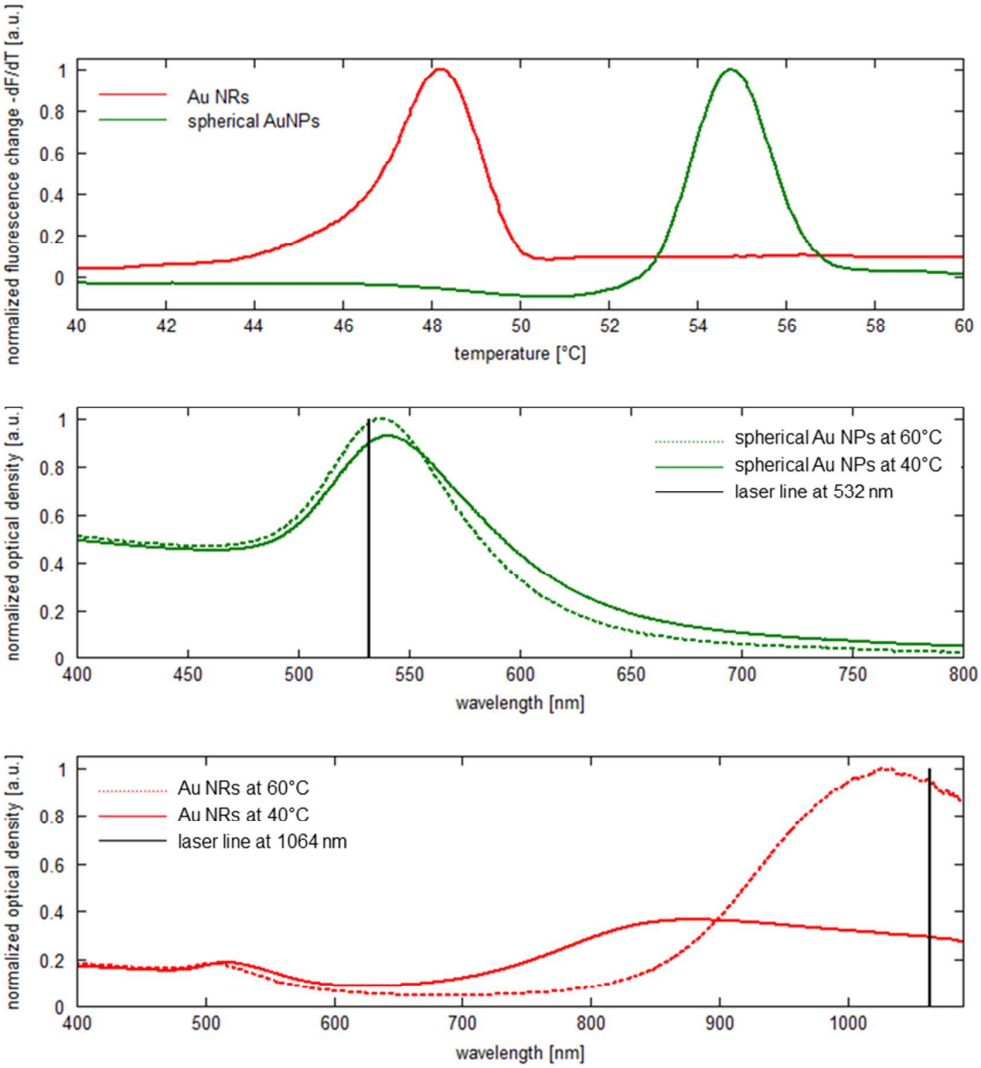


**Figure S15.** Top: melting curves of clusters of ssDNA-functionalized spherical Au NPs (green curve) and Au NRs (red curve) as prepared for the transmission experiments presented in Figure 6. The melting curves were obtained with a Roche Diagnostics LightCycler96 Real-Time PCR system. The graph shows the negative normalized change in fluorescence at 514 nm over temperature (–dF/dT) for the reporter fluorescent dye FAM (100 nM were added to the sample solution). The excitation wavelength was set to 470 nm. As the temperature rises,

the DNA strands connecting the NP clusters melt. This leads to an increased absorption of the NPs at the excitation and emission wavelength (see center and bottom panels) and, in consequence leads to a decreased fluorescence signal of the reporter molecule. The measurement shows a melting temperature of 54.7 °C for the sample containing clusters of spherical Au NPs and 48.1 °C, for the sample containing clusters of Au NRs. Center: extinction spectrum of clusters of ssDNA-functionalized spherical Au NPs at 40 °C (solid green curve) and at 60 °C (dashed green curve), as prepared for the transmission experiments shown in Figure 6. Both curves were normalized to the optical density of the plasmon resonance peak of the spherical Au NPs at a wavelength of 538 nm at 60°C. The normalized optical density shows an increase at 532 nm when the sample is heated to 60 °C (see vertical black line for reference). This can be attributed to the melting of DNA connecting the clusters at 54.7 °C, as shown in the top panel (green curve). Bottom: extinction spectrum of clusters of ssDNA-functionalized Au NRs at 40 °C (solid red curve) and at 60 °C (dashed red curve), as prepared for the transmission experiments presented in Figure 6. Both curves were normalized to the optical density of the longitudinal plasmon resonance peak of the Au NRs at a wavelength of 1027 nm at 60°C. The normalized optical density shows an increase at 1064 nm when the sample is heated to 60 °C (see vertical black line for reference). This can be attributed to the melting of DNA connecting the clusters at 48.1 °C, as shown in the top panel (red curve). The extinction spectra for the center and bottom panels were obtained with an Agilent Technologies Varian Cary 50 UV-Vis Spectrophotometer.

REFERENCES

1. R. Kofman, P. Cheyssac, A. Aouaj, Y. Lereah, G. Deutscher, T. Bendavid, J. M. Penisson and A. Bourret, *Surface Science*, 1994, **303**, 231-246.

2. H. Petrova, J. Pérez-Juste, I. Pastoriza-Santos, G. V. Hartland, L. M. Liz-Marzán and P. Mulvaney, *Phys. Chem. Chem. Phys.*, 2006, **8**, 814-821.

3. S. Doniach and M. Sunjic, *Journal of Phys. C*, 1970, **3**, 285.

4. J. J. Yeh and I. Lindau, *Atomic Data and Nuclear Data Tables*, 1985, **32**, 1.

5. J. F. Moulder, J. Chastain and R. C. King, *Handbook of X-Ray Photoelectron Spectroscopy: A Reference Book of Standard Spectra for Identification and Interpretation of XPS Data*, Physical Electronics Eden Prairie, MN, 1995.

# Publication 7:
# Stochastic Transitions and Relative Affinity of Single Cells on Double-Well Micropatterns

# Stochastic transitions and relative affinity of single cells on double-well micropatterns

*A. Fink†[1], P. J. F. Röttgermann†[1], C. Broedersz[2], J. O. Rädler,[1,*]*

[1.] Fakultät für Physik & CeNS, Ludwig-Maximilians-Universität, Geschwister-Scholl-Platz 1, 80539 München, Germany

[2.] Arnold-Sommerfeld-Center for Theoretical Physics and Center for NanoScience, Faculty of Physics, Ludwig-Maximilians-Universität München, Theresienstrasse 37, 80333 Munich, Germany

*corresponding author: raedler@lmu.de,
*† authors equally contributed*

**Keywords:** Cell Migration, Micro-Patterning, Detailed Balance, Protein Affinity

## Abstract

Cells migrating on adhesive micropattern are confined to spread on predefined areas. Micropatterns can be used to direct and probe living cells in an artificial two-state system. Cells are placed. Here, we study MDA-MB-231 cells on arrayed pairs of adhesion-sites that are pairwise connected by thin guidance cues. Single cell traces are extracted via time-lapse fluorescent microscopy. We find that cells preferentially occupy a single adhesion site. Yet, from time to time protrusions reach into the neighbouring site and the cells subsequently transition to the next site. We show that the hopping process is stochastic and exhibits exponentially distributed stay times. The hopping rates decay with increasing bridge length. In case of a symmetric pattern the average spatial cell occupancy shows two distinct and equal maxima reflecting a relative occupancy of one. When adhesion sites are different two maxima of different height reflect the occupancies indicating a preferential occupation of one of the two adhesion sites. The dumbbell-shaped setup may be used as lab-on-a-chip device for tissue engineering or drug screening applications, as they allow to measure the relative affinity of cells for different surfaces and to quantify the direct response of motility on drug treatment.

## Introduction

Micropatterns offer accurately defined micro environments allowing the study of cell organisation and migration. Such environments, consisting of tuneable adhesive areas with cell-repellent surroundings, can be created using microcontact printing. A wide range of questions can be addressed in cell studies on 2D micropatterns. Once seeded, cells readily adapt to the shape and size of the underlying pattern. Micropattern size affects cell survival (1) and confinement (2). Adjacent micropatterned stripes or areas made of different proteins have been used to explore cellular affinities for surfaces for fibroblasts (3) and nerve cells (4). The speed, persistence (6) and the direction of motion (2, 5) of migrating cells is influenced by the underlying micropatterns. The tracking of cell motion on micropatterned surfaces allows the extraction of characteristic motility parameters like adhesion energies on the micropatterns and cell elasticity (Schreiber et al., (7)).

These extracted parameters can be either used for cell phenotyping – or as calibrating input parameters for computational models allowing the reconstruction of experimental data as well as the prediction of cellular behaviour. Thus, shape and traction forces of stationary cells on any micropattern can be predicted, using a cellular Potts model. (8) Furthermore, the shape of a spreading cell can be modelled, taking into account actin

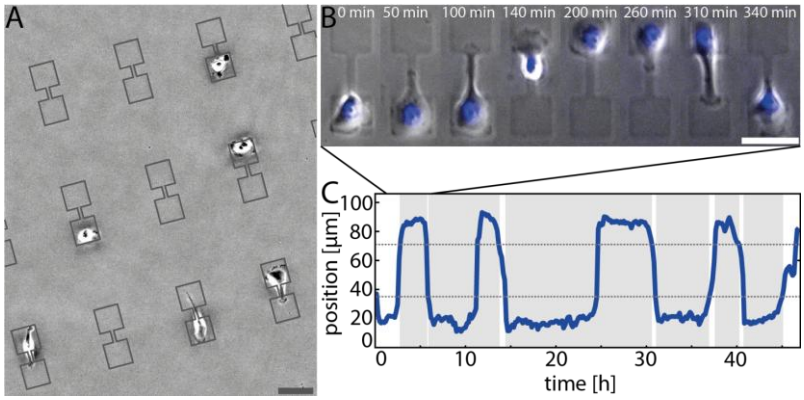


***Figure 1****: A: Overview of single cells on a microstructured surface. Dumbbell-shaped symmetric patterns consist of two square islands (35µm x 35 µm) which are connected by bridges of varying lengths (7-47 µm) and coated with fibronectin. Scale bar: 50 µm. B: Exemplary time series of a single cell transitioning from left to right, and back. Scale bar: 50 µm. C: Exemplary cell track (along the long axis of the dumbbell) of nuclear positions plotted against time. The centre-of-mass track clearly shows the observed transitions between resting states and quick transitions from one adhesion site to the other.*

and myosin concentrations, as well as adhesion site dynamics (9). Simulations, taking these constraints into account, show the spontaneous emergence of periodic cellular migration for crawling cells on stripe patterns.(10) In these models cells are simulated as active machinery with an intrinsic stochastic excitability that leads to spontaneous formation of protrusions.

Active matter difficult. Special case when detailed balance is fulfilled. Then Boltzmann distribution for probability ratio. This allows us to assign energies to each of the two states by measuring the occupancies. These energies can then be termed 'surface affinities'.

We have observed bidirectional cell motion due to the subsequent encounters of MDA-MB-231 cells with micropattern boundaries on 2D dumbbells. These dumbbells offer two distinct adhesion sites connected by a narrow bridge. Thus, we can combine single-cell resolution and the possibility for automated tracking with surface functionalisation. Here we study the stochastic transitions of single cells on patterns with a single occupied and a neighbouring empty adhesion site, quantifying hopping rates and occupancy. Firstly, we vary the length of the connecting bridge. Secondly, we introduce asymmetry through a variation of adhesion site dimensions while maintaining a constant bridge length. Thirdly, we place a second protein on one of the adhesive islands and vary the protein inset size and the type of protein, respectively. The observed quantities yield the differential surface affinity of MDA-MB-231 cells.

## Results & Discussion

### Phenomena on dumbbell-shaped symmetric micropatterns

**Figure 1A** shows an overview of the micropatterned structures occupied by single cells. Micropatterns are designed in a dumbbell-shape, with a narrow stripe terminating into square islands at each of its ends. These squares measure (35 x35) $\mu m^2$, while the bridge length is varied from d=7.5 µm to 47.5 µm for the symmetric setup. Cells preferably adhere onto the island areas, where they adapt the underlying square shape. After adhesion, 95an hour, 95% of the cells spontaneously start migrating on these two-well patterns. A time series (**Figure 1B**) illustrates the typical behaviour of the cells. After a resting time (0 min), cells start sensing their environment by lamellipodial protrusion, following the direction indicated by the bridge (50 and 100min). Once the opposite unoccupied adhesion site is "sensed", the whole cell body transmigrates to that site (140 min) and the cells spread again. To achieve high-throughput tracking of the motion of cells, centre-of-mass positions of the fluorescently labelled nuclei are recorded using fluorescence microscopy. An exemplary

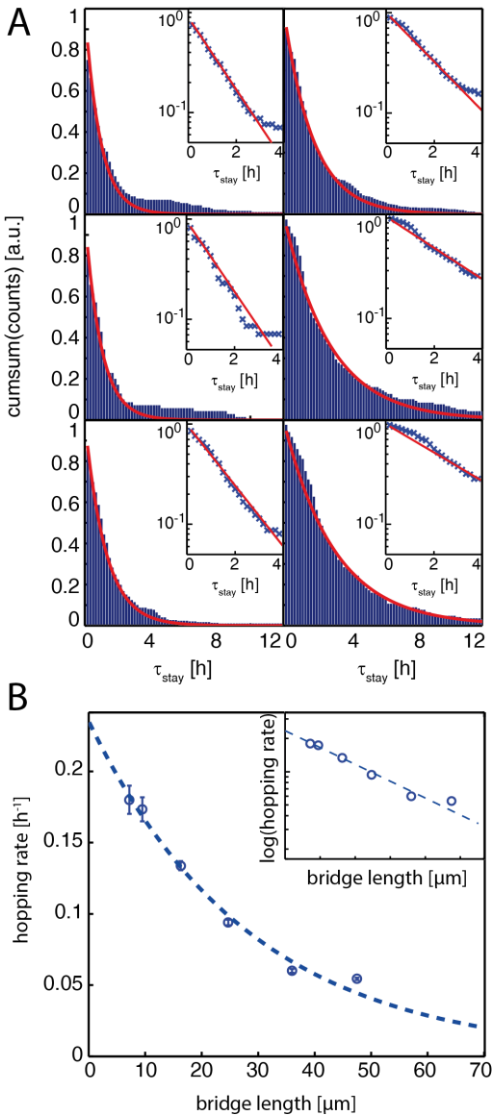


***Figure 2.*** *Stay times are extracted from position-time traces. A: Survival functions of stay times for all geometries. The distributions broaden with increasing bridge lengths. An exponential decay is plotted to the distributions. Inset: Data is shown on a semi-logarithmic scale. The fit agrees well with the data for stay times < 3h and for patterns with bridges < 26.7 µm. B: The time constant from the exponential fits was extracted and plotted against bridge lengths. An exponential decay seems a reasonable approximation to the data.*

trajectory of the nucleus, plotted against time, is displayed in **Figure 1C**. Distinct transitions between the adhesive islands, marked by the steep sections of the curve, can clearly be seen. As the transitions typically take only a fraction of the time a cell spends on each island, the transitions will be referred to as “hops”. The average number of hops per cells during a typical measurement decreases with increasing bridge length. The 2.5 h for a bridge length of xx µm. This characteristic behaviour of spreading, rounding, hopping and the reversal of the direction of motion is sustained periodically, and is only interrupted upon cell division. Resting states are characterised by distinct stay times, defined as the time interval in which the centre of mass of the cell is located within the adhesion site. The fluctuations in nuclear position in the resting state, visible as little spikes in the flat parts of the curve, may be attributed to either random nuclear motion or to the displacement of the cell body due to pseudopod formation.

## Dependence of stay times on the bridge length

All the steps between the arrival of the cell on a previously unoccupied adhesion site and the start of a successful transition to the neighbouring island happen on distinct time scales, which eventually sum up to yield a total stay time. Thus, stay times are comprised by the repolarisation time, the time for lamellipodial extension on the bridge and the time during which the lamellipodial fan spreads on the unoccupied island while the cell nucleus is still within the original adhesion site. The repolarisation time results from the redistribution of actin, previously localised in the cell front, after the migrating cell encounters the border of a pattern. As an asymmetric distribution of actin and myosin is a necessary requirement for cells to migrate and conditions for repolarisation are equal on the presented squares, the repolarisation time is assumed to be a constant quantity. As each adhesive square offers the same micro-environment, the time for the generation of the fan-like lamellipodial tip is assumed to be very similar for all cells.

In **Figure 2A** the survival functions of the stay times are plotted against the bridge length**.** The distributions become broader with increasing bridge lengths. Nuclear residence times on the connective stripes are excluded from the stay times used for further analysis. Thus, the broadening of distributions for longer bridges is not due to longer transition times between islands.

The insets in **Figure 2A** show the survival function, and an exponential fit to it, on a semi-logarithmic scale allowing better evaluation of the fit results. The same fit is also shown plotted on the normal scale. For stay times shorter than 3h plot and data are in good agreement. Deviations for short stay times arise for patterns with bridge lengths longer than 24.7 µm. However, the fit yields a good first-order approximation. In order to determine how the decay constants scale with bridge length, values are extracted from the linear fits to the survival functions and plotted (**Figure 2B**). The decrease of hopping rates with increasing bridge length in our two-state system can be well described by an exponential. The process we observe is analogous to particle diffusion in a thermal double-well potential described by Arrhenius' Law: The bridge length L is the equivalent of the thermal energy barrier E. Thus, the hopping rate Gamma is given by:

$$\Gamma = \nu \, exp(-\kappa L),$$

where ν denotes the attempt frequency, κ is some scaling factor and L the bridge length.

In the case of two equally sized squares (symmetric case), both adhesion sites are energetically equivalent for a cell. The bridge connecting both islands acts as an energy barrier because successful transitions require the growth and extension of a lamellipodium. Therefore, longer bridges correspond to higher energy barriers. Furthermore, due to the bridge being of a narrower width than the edges of the islands, a stochastic barrier for the randomly forming membrane protrusions is introduced. The extension of the lamellipodium is not a linear process, either. It is more a succession of extensions and retractions. Each such attempt is counted in ν, which is linked to the cell-line dependent cellular motility.

## The Influence of Asymmetry

Having understood the hopping behaviour of cells in a symmetric case, a different, asymmetric set of micropatterns can now be probed. In the first case, the edge lengths of the adhesive squares are varied while a constant bridge length (16.5 µm) is maintained. Cells seeded on these patterns show the same periodic succession of spreading, lamellipodial protrusion, rounding and hopping as on the symmetric patterns.

**Figure 3A** shows the stay frequencies for all cells plotted against the long axis of the pattern, for each of the five geometries. A strong spatial bias in stay probabilities is observed for any of the asymmetric patterns. The strongest difference in stay probability distributions is found for the 40 - 25 and 35 – 35 patterns, where for

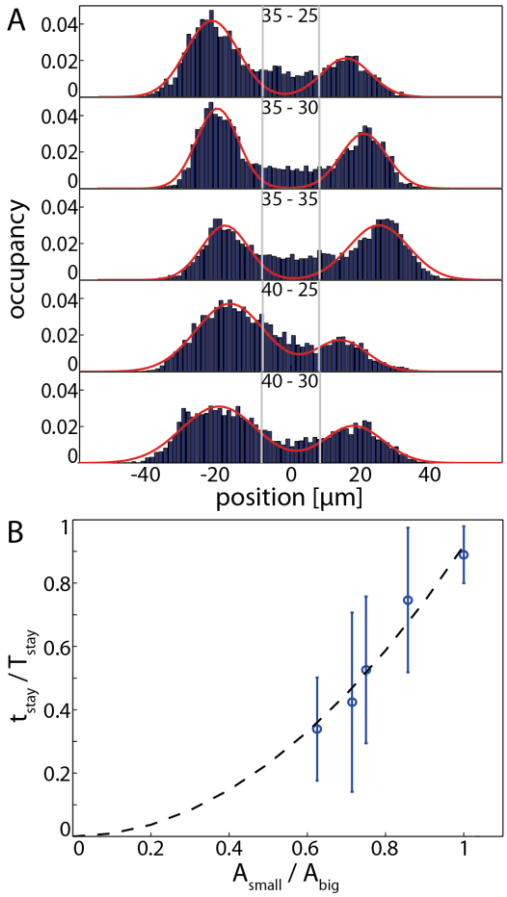


***Figure 3*** *A: Asymmetry in adhesion site areas leads to asymmetry in island occupation probabilities. Occupancies are plotted against positions for 35 – 15, 40 – 25, 40 – 30 and 35 – 35 micropatterns. A sum of two Gaussians was fitted to the curves and area under the curve taken for the calculation of occupancy ratios. B: Time ratios of the individual occupancies on each side of the asymmetric patterns are plotted against the ratio of island areas. The curve ~ $x^{-2}$ is a guide for the eye.*

the latter, two equally sized probability distributions for island occupancy can be seen. Furthermore, occupancies increase with increasing island area.

For the quantification of stay probabilities on each island, a sum of two Gaussians was fitted to the distributions. The ratios of the Gaussians' amplitudes are plotted against the ratio of the areas of both adhesive squares (**Figure 3B)**. A curve proportional to $x^{-2}$ was fitted to the data points as a guide to the eye.

In the view of active matter theory, the relation between the probabilities of occupancies would be:

$$\frac{P(A)}{P(B)} = \exp\left(-\frac{\Delta E}{kT}\right).$$

with probability *P* of *A* and *B*, energy difference $\Delta E$.

No directional bias in the number of hops is found. Our data suggest that the time a cell spends on one adhesion site is determined the relative size of the island with respect to cell size. On islands which are relatively small, cells cannot fully spread and thereby retain a rounded shape. Thus, fewer adhesions are formed (11) and a lower force is needed to initiate a hop. Moreover, for such rounded cells, narrow bridges impose smaller barriers, as the cells do not have to contract much in order to fit onto the bridge. This results in higher hopping rates. However, adhesion sites cannot be made infinitely small as very small adhesion sites may not offer sufficient adhesion area for both, the leading edge and the cell body with nucleus (data not shown). In contrast, cells are able to fully spread on large islands, forming more focal adhesions which need to

be detached for motion. Furthermore, islands which are larger than cells, offer a surface on which motile cells exhibit 2D migration, prolonging the stay times on those islands.

The observations of cellular hopping on asymmetric dumbbells are thus limited between square sizes of 15 x 15 $\mu m^2$ and 40 x 40 $\mu m^2$.

**Observations for differently patterned adhesion islands**

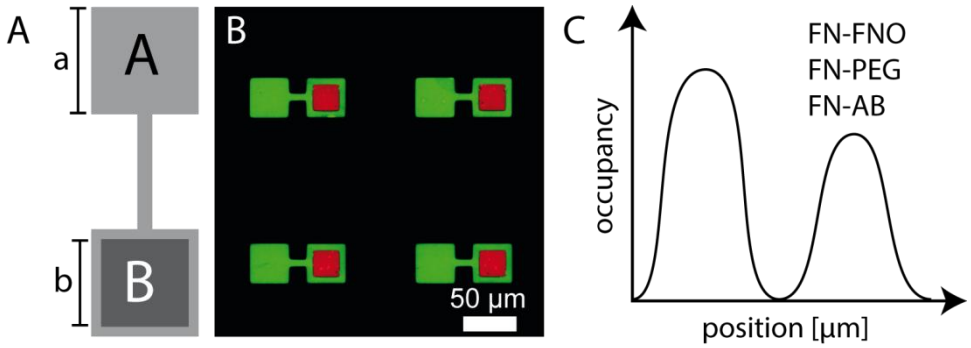


***Figure 4****: A: Schematic drawing of the geometry and principle of the double-protein dumbbells with site A with edge length a and site B with inner square of edge length b. B: Fluorescence image of double-protein patterns made with labelled fibronectin (full square) and laminin (inset). C) Schematic occupation distribution, measured for dumbbell patterns with fibronectin in square A and fibronectin, fibrinogen(FNO), PLL-PEG and an antibody(AB) used to fill square B, respectively.*

Observing the striking sensitivity of our setup to variations in surface characteristics, we decided to design a set of double-well patterns of different surface chemistry as shown in **Figure 4A**. Here, we intend to test the effect of different ECM proteins on occupancy and transition statistics.

Moreover, we have designed a similar setup of dumbbells made of one protein with variably-sized protein insets dedicated to the presentation of a second protein. Here, we want to study the sensitivity of the cells to small changes in protein composition.

## Conclusion

The aim of this study was to describe the migratory behaviour of single cells on dumbbell-shaped micropatterns. Thus, we designed micropatterns consisting of two square adhesion sites connected by a guidance cue of varying length. Starting with a symmetric two-well setup, we have subsequently varied the size of adhesion sites, their protein coating and the surface ligand spacing while keeping the distance between sites constant. Fluorescently labelled nuclei of MDA-MB-231 cells were tracked for up to 50 h.

Here, we have shown that the hopping rates of the periodic migration, exhibited by cells on the double-well patterns, are described by an exponential law of the bridge lengths. Hopping rates and stay probabilities vary, depending on the size of adhesion sites, the ligand spacing on their surface and their chemical composition, thus enabling us to directly compare cellular affinities for adhesion sites.

As each hop is preceded by the growth of a fan-like lamellipodial tip on the unoccupied adhesion site, our setup might enable us to directly compare traction force generation in the lamellipodium. However, further quantification of lamellipodial protrusion statistics and fan area is necessary to fully understand the role of the lamellipodium prior to a cellular transition. To conclude, we have seen that cell hopping on dumbbell-shaped micropatterns is mediated by the stochastic extension and retraction of a lamellipodium and the subsequent growth of its fan-like tip on the unoccupied adhesion site. Cellular transitions are sensitive to surface characteristics. Thus, hopping rates and occupancies should be robust indicators of the affinity of a

cell for a certain substrate, allowing the direct evaluation of relative affinities for substrates of different dimensions, geometries, surface chemistries, and with different ligand spacings. Due to easy fabrication and reproducibility, the dumbbell-shaped double-well patterns can be used as lab-on-a-chip devices for cell separation and cell sorting. In addition, the dumbbell-shaped micropatterns are a versatile tool with potential applications in cancer therapy, as the effects of chemotherapeutic drugs on cell motility and possible deterring effects of surface coatings on invasive cells can be directly studied.

## Material and Methods

### Cell Culture

MDA-MB-231 human breast carcinoma epithelial cells (DSMZ) were cultured in Minimum Essential Medium (c.c.pro) supplemented with 10% fetal calf serum and 2 mM L-glutamine (c.c.pro). For maintenance, cells were grown up to 70-90% confluence at 37°C and 5% $CO_2$ atmosphere, washed with PBS and trypsinized for 5 min. For experiments, cell suspensions were centrifuged at 1000 rcf for 3 min and re-suspended in Leibovitz L15 medium (Life Technologies) with 10% fetal calf serum. Cells were seeded at a concentration of about 10,000 cells per and, after 3 h incubation time, nuclei were stained with 25 nM Hoechst33342 (Life Technologies).

### Sample Preparation

Micropatterns were fabricated by microscale plasma-induced protein patterning, for detailed protocol see Segerer et al. (12) In brief, samples for the single-protein dumbbell patterns were microstructured on uncoated µ-dishes (ibidi GmbH) using FN (YOProteins) with an incubation time of 45 minutes. Surrounding areas were passivated using PLL(20kDa)-g(3.5)-PEG(2kDa) (SuSoS). The following geometries were used in the symmetric, single-protein setup: squares of 35x35 µm², connected by bridges of 7.2, 9.5, 16.3, 24.7, 36 and 47.5 µm length and 5 µm width. For the asymmetric single-protein dumbbells, the squares of the following edge lengths in µm were combined 35 – 25, 35 – 30, 40 – 25, 40 – 30 and 40 - 35. The asymmetric patterns were connected by a bridge of 16.5 µm length and 5 µm width.
Samples for the multi-protein patterns were prepared as also described in Segerer et al (12).

### Time-Lapse Microscopy

Images were taken with either an inverted iMIC digital microscope (TILL Photonics) or an Nikon Ti Eclipse microscope with a heating stage (ibidi GmbH) at 37°C. Brightfield with phase-contrast images and fluorescent images (light source: Oligochrome TILL Photonics or SOLA (Lumencor)) were recorded at 10-fold magnification and in 10 min intervals for up to 50h. Each geometry was measured at least thrice.

### Data Analysis

Raw images were pre-processed in *ImageJ*. For automated tracking of the cell nuclei, a band pass filter was applied to the fluorescent images with a subsequent binarization of the images. After plasma etching, dumbbell patterns were visible on the brightfield images which were used to determine the reference boundary of a pattern for cell movement. This value was then subtracted from centre-of-mass nuclear coordinates for absolute distances. All further analysis was carried out using *MATLAB*. The nuclear centre-of-mass position data was binned according to the corresponding islands, with 0 being attributed to all positions on non-island areas. Stay times were calculated by counting the number of consecutive equal non-zero elements. Stay times at the very beginning and end of each measurement were excluded due to unknown start and endpoints. In general, a cell was defined to be ‘on the island’ as long as the centre-of-mass of its nucleus was not registered on the bridge.

Mean stay times, and their inverse, λ, were extracted after plotting the survival function of stay times for each pattern and subsequently fitting

$$F = exp(-\lambda t).$$

Error bars correspond to the confidence intervals from fits.

To the stay distributions on the asymmetric patterns, a sum of two Gaussians was fitted:

$$F = A \exp\left(\frac{x-\mu_a}{2\sigma_a}\right)^2 + B \exp\left(\frac{x-\mu_b}{2\sigma_b}\right)^2.$$

To achieve good agreement between data and fits, all counts on positions corresponding to the bridges were defined as outliers. Maxima of the data were determined to give bounds for the Gaussians' amplitudes, as well as the positions of the mean value (with restriction to be on the islands). The standard deviation was limited to less than half of the island width. The ratio of total occupancies for each pattern was calculated as the ratio of areas under the Gaussian curves. Error bars correspond to cell-to-cell variations.

## Acknowledgements

Financial support by the Deutsche Forschungsgemeinschaft (DFG) via project B01 within the Sonderforschungbereich (SFB) 1032 is gratefully acknowledged.

## Rerferences

1. Chen CS, Mrksich M, Huang S, Whitesides GM, & Ingber DE (1997) Geometric Control of Cell Life and Death. *Science* 276(5317):1425-1428.
2. Mahmud G*, et al.* (2009) Directing cell motions on micropatterned ratchets. *Nat Phys* 5(8):606-612.
3. Ricoult SG, Thompson-Steckel G, Correia JP, Kennedy TE, & Juncker D (2014) Tuning cell–surface affinity to direct cell specific responses to patterned proteins. *Biomaterials* 35(2):727-736.
4. Vielmetter J, Stolze B, Bonhoeffer F, & Stuermer CAO (1990) In vitro assay to test differential substrate affinities of growing axons and migratory cells. *Exp Brain Res* 81(2):283-287.
5. Kumar G, Ho CC, & Co CC (2007) Guiding Cell Migration Using One-Way Micropattern Arrays. *Advanced Materials* 19(8):1084-1090.
6. Kushiro K & Asthagiri AR (2012) Modular Design of Micropattern Geometry Achieves Combinatorial Enhancements in Cell Motility. *Langmuir* 28(9):4357-4362.
7. Kandere-Grzybowska K*, et al.* (2007) Cell motility on micropatterned treadmills and tracks. *Soft Matter* 3(6):672-679.
8. Albert Philipp J & Schwarz Ulrich S (2014) Dynamics of Cell Shape and Forces on Micropatterned Substrates Predicted by a Cellular Potts Model. *Biophysical Journal* 106(11):2340-2352.
9. Shao D, Levine H, & Rappel W-J (2012) Coupling actin flow, adhesion, and morphology in a computational cell motility model. *Proceedings of the National Academy of Sciences* 109(18):6851-6856.
10. Camley BA, Zhao Y, Li B, Levine H, & Rappel W-J (2013) Periodic Migration in a Physical Model of Cells on Micropatterns. *Physical Review Letters* 111(15):158102.
11. Chen CS, Alonso JL, Ostuni E, Whitesides GM, & Ingber DE (2003) Cell shape provides global control of focal adhesion assembly. *Biochemical and Biophysical Research Communications* 307(2):355-361.
12. Segerer FJ*, et al.* (2015) A Versatile and Novel Method to Create Multi Functionalized Micro Patterns. *Biomaterials, Biointerphases, 2016*.

# Publication 8:
# Time-Correlations of Single Cell Dual Fluorescence Markers - a Kinetic Fingerprint in Nanoparticle Induced Apoptosis

# Time-correlations of single cell dual fluorescence markers -a kinetic finger print in nanoparticle induced apoptosis

*Peter. J. F. Röttgermann,[1§] Alexandra Murschhauser,[1§] David Garry,[2] Martina F. Ober,[1] Daniel Woschée,[1] Yan Yan,[2] Kenneth A. Dawson,[2*] Joachim O. Rädler[1*]*

1. Faculty of Physics and Center for NanoSciene (CeNS), Ludwig-Maximilians-Universität, Geschwister-Scholl-Platz 1, 80539 Munich, Germany
2. Centre for BioNano Interactions, School of Chemistry and Chemical Biology, University College Dublin, Belfield, Dublin, Ireland,

§ contributed equally
* corresponding authors

**Dynamics of cell fate decisions in living cells like apoptosis are highly heterogeneous at the single-cell level. Yet symptomatic order and timing of events is expected for various signaling cascades, suitable to identify apoptotic pathways induced by nanoparticles. Here, we monitor the time lines of apoptotic events in automated time-lapse microscopy in combination with single cell micro-arrays. We use multiple fluorescent apoptosis markers to indicate lysosomal break (LMP), loss of mitochondrial outer membrane permeabilization (MOMP), increase of ROS level (ROS), caspase 3 activation (CASP), exposure of phosphatidylserine to the outer membrane (PS-FLIP) and loss of plasma membrane integrity accompanied with nucleus staining (PMP). By pair wise labeling and time correlation analysis, we establish sequences of events with high temporal resolution. Our experiments show that apoptosis induced by polystyrene nanoparticles, functionalized with amide groups, is triggered by the lysosomal break of the loaded NPs. Multi-dimensional time-correlation provides a dynamic fingerprint to classify interaction of nanoparticles with cells.**

# Introduction

Nanoparticles (NPs) have shown cytotoxicity on cells in many studies. Up to now different sources have been identified to play a key role in inducing cell death but it is still little known about the sequence of death events as many different pathways of cell death can extent high complexity. However, there are common events/features in cell death which occur in many pathways e.g. increase in ROS level, lysosomal permeabilization (LMP) as well as the permeabilization of the outer mitochondria membrane (MOMP) [1]. Previous work showed evidence that PS-$NH_2$ trigger apoptosis via lysosomal pathway [2], [3]. The group of Dawson analysed $EC_{50}$ values from dose-response curves of LMP, MOMP, and PMP. These $EC_{50}$ values give first indication about the lysosomal pathway.
As most of events happen in order of minutes as well as exhibit complex behaviour, real-time imaging is needed. Feedback loops make it difficult to determine the initiator. Many examples have shown that LMP-pathway has a feedback loop for ROS and ROS is increased by the LMP /cathepsin release via mitochondria.
Additionally, cells are heterogeneous in their response[4, 5]. This can effect in different ways of dying and subpopulation can be observed. Time resolved measurement can shed light on the dynamics and enables are more detailed view on the pathways.
Time-resolved measurements of apoptotic events on single cell arrays can be used to get detailed answers about the timing of events in the pathway of cell death. [6]. [7]We established a high throughput (HT) time lapse setup for

a dynamic single cell response detection. High-Content Analysis (HCA)can further confirm findings from the time resolved measurement.

In this paper we show conceptionally the time relation of early and late apoptotic markers using time resolved measurements on single cell arrays as well as HCA analysis.
By measuring pair wise combinations of cell death markers and principal component analysis we are able to correlate the timing of apoptosis events and determine sequences in cell death pathways.
We prove pathways induced by PS-NH2 NPs. Thus, signals of LMP, MOMP, ROS level, Caspase3, membrane change (pSIVA) and plasma membrane permeabilization (PMP) are pair wise correlated.

# Results and Discussion

## Single cell arrays allow efficient assessment of individual time lines

The late apoptotic events are discussed first. The CellEvent Caspase 3/7 is a cell permeant marker with a DEVD peptide sequence (asparagine-glutamine-valine-asparagine) binding site. The peptide gets cleaved upon caspase-3 and -7 activity and hence fluoresces green by integration with nucleus DNA described by a sharp sigmoidal onset function. The exponential decay after the onset is caused by photo-bleaching. The pSIVA-IANBD fluoresces only when bound to PhS, which is transposed to the outer leaflet of the plasma membrane at the execution phase of apoptosis. The fluorescence time courses are well described by the same sigmoidal increase and decay as identically to the caspase signal.
The nuclear stain (PI/Toto3 iodide) binds specifically to DNA and unspecifically to RNA. The chromophore is non-fluorescent in the absence of nucleus acids as well as plasma membrane impermeable, and hence only fluoresces upon loss of plasma membrane integrity.
Figure 1 shows the process of data acquisition. Cells are seeded on microstructured single cell arrays. The single cell array allows easy automated tracking of cells and keeping cells at similar conditions (adhesion area, same amount of exposed NP). After six hours of incubation cells are exposed to NPs together with respectively two various fluorescent markers without any washing step. The fluorescent markers are indicators for different cell death events: LysoTracker for permeabilization and/or rupture of the lysosomes (LMP), TMRM for the mitochondrial outer membrane permabilization (MOMP), CellROX for reactive oxygen species level (ROS), Cell Event Caspase 3/7 for caspase 3 and 7 activation, pSIVA-IANBD for the externalization of phosphatidylserine to the outer leaflet of the plasma membrane (PhS-Flip) and PI/Toto3 for the loss of plasma membrane integrity (PMP). Fluorescent tracks are recorded in 8wells for the NPs as well as for negative control (cell culture medium), and positive control (STS) every 10 min for up to 30 h. Each individual cell track is then further analysed; characteristic quantities are extracted by fitting each individual cell track.
Figure 1 b) shows the hypothetical pathway for PS-$NH_2$: NP accumulate in the lysosomes and lead to a break (LMP), followed by release of cathepsin. Cathepsin is known to induce apoptosis by triggering the intrinsic pathway the permeabilization of the mitochondria (MOMP) [citate]. Release of mitochondria content initiator caspases. The loss of MOMP lead additionally to a huge flux of ROS into cytosol, which again can trigger the LMP. (→ feedback loop ) At point of no return effector caspases 3 and 7 are activated. The execution pathway is determined by the externalization of phosphatidylserine to the outer leaflet of the plasma membrane (PhS-FLIP) and late events such as loss of plasma membrane integrity (PMP).

## Marker specific phenomenological time course

The time-lapse image acquisition yields single cell fluorescence time courses with high temporal resolution. **Figure 2 a)** shows typical time series of single cell fluorescence markers after induction of apoptosis through NP 25 µg/ml (see also movies in the **Supplementary Material**). While each individual time course is distinct and the overall onset times show a great variability and each fluorescent marker has defined features in the time courses. For example, each marker shows distinct discontinuities, which allow for the definition of defined event times. In the following we describe the characteristic commons in the time lines and how to retrieve the

event times using automated routines using simple mathematical descriptors. The late apoptotic events are discussed first.

The CellEvent Caspase 3/7 is a cell permeant marker with a DEVD peptide sequence (asparagine-glutamine-valine-asparagine) binding site. The peptide gets cleaved upon caspase-3 and -7 activity and hence fluoresces green by integration with nucleus DNA described by a sharp sigmoidal onset function. The exponential decay after the onset is caused by photo-bleaching.

The pSIVA-IANBD fluoresces only when bound to PhS, which is transposed to the outer leaflet of the plasma membrane at the execution phase of apoptosis. The fluorescence time courses are well described by the same sigmoidal increase and decay as identically to the caspase signal.

The nuclear stain (PI/Toto3 iodide) binds specifically to DNA and unspecifically to RNA. The chromophore is plasma membrane impermeable and hence fluoresces only upon loss of plasma membrane integrity.

The early markers show a more complex signal behavior.

The lysosome marker (Lysotracker) is based on a pH dependent fluorophore which can enter vesicle-like particles such as lysosomes or endosomes. In the acidic environment of the lysosomes, the marker gets protonated which leads to fluorescence and hinders the marker to release the vesicle. The cell traces of LysoTracker show a small initial quadratic increase with a sigmoid breakdown at $t_{Lyso}$. The breakdown can be most likely be associated with the rupture of the lysosomes.

In active mitochondria with a membrane potential $\Delta\Psi m$ TMRM gets accumulated. More TMRM accumulates upon hyper-polarization whereas TMRM is released upon loss of the membrane potential. Firstly, the fluorescence of TMRM linearly increases and subsequently decreases (sigmoid) at $t_{MOMP}$ which can be associated with MOMP. The fluorescence is followed by a plateau period and a small increase, likely associated with the increase of caspase induced fluorescence (due to the measurement with pair wise markers).

CellROX fluoresces upon oxidation in presence of oxygen radicals. The initial increase of the fluorescence time course can be directly correlated to the amount of generated ROS. The sigmoidal break down $t_{ROS}$ could be possibly explained by either a massive ROS production (e.g. at MOMP) and subsequent destruction of the marker or by the release of the marker out of the cell.

## Distribution functions of apoptotic onset-times

The distribution of marker event times are extracted as follows ( explained in detail in the Supplement): For the early markers, the breakdown event is determined by the time at which the curve deviates more than 3% from the initial parabola in relation to the amplitude. For the late markers, the onset event is determined by the intersection point between the basal fluorescence and the tangent of the fit parameter tstep.

The distribution of marker on-set times was evaluated in an automated manner from fluorescence time series of about 500 cells per marker. Figure 3 shows the frequency distributions of onset times for the case of PS-NH2 (25µg/ml) induced apoptosis (Fig3a) compared to apoptosis induced by staurosporine (2 µM) (Fig3a).

The distributions show a broad heterogeneous response of the populations. In order to compare single cell distributions Gaussians were fitted. For the NP exposure the mean times of the distributions are all within 2 hours around 24 h. For the STS exposure more distinct differences in the timing can be recognized.As the time differences are small compared to the width of the distributions, the mean times are an insufficient way for the determination of sequence of events.

## Two-color pair-correlation of successive events

Due to the broad distribution of the onset times of each marker the time correlation of successive markers is a better way for determination of sequences, as the time difference between two events can be measured directly. In Fig. 4 the event times are plotted for each pair wise marker combination where $t_n$ and $t_{n+1}$ are denoted as the times of two successive events. Early markers (upper row) and late markers (middle row) are plotted separately. The color encodes for the following different pairs of apoptotic markers: MOMP-ROS (light blue), LMP-MOMP (medium blue), LMP-ROS (dark blue), LMP/MOMP-PhS-Flip (yellow), PhS-Flip-Casp (red), and Casp-PMP (dark red) and LMP-PMP (dark brown). The ellipses display the correlations obtained from a

principal component analysis, whereas the axes of the ellipses correspond to the first two principal components for each combination with a one sigma interval (67% of data). The data shows the statistics of about 500 cells (note statistic is lower for some marker combinations). If the ellipse is above the dotted diagonal, marker n+1 follows marker n.

The pair wise correlation of LysoTracker and MOMP for the NP exposure shows a clear sequence emerging the evidence that PS-$NH_2$ triggers the lysosomal pathway. In contrast, the time difference between MOMP and ROS breakdown is very small. This means that ROS is directly correlated with the permeabilization of the mitochondria. For consistency, the combination of LMP and ROS breakdown is also measured. The result is similar to that of LMP and MOMP although broader distributed. The time correlation of STS is different in comparison to the one of the PS-$NH_2$-NP exposure. Two populations can be identified for the combination LMP-MOMP, on the one hand a population which dies early and where MOMP follows after LMP and on the other hand a population where cells die at later time points and where vice-versa LMP follows shortly after MOMP. Furthermore, a distinct time difference between MOMP and ROS can be identified which indicates another ROS breakdown behavior than for the NPs. The consistency check of the combination LMP-ROS suffers again from low statistic.

The late marker combinations do have some inconsistencies in their sequences of events. Most prominently, the onset event of caspase3 follows after the PhS-Flip and the PMP, whereas in the cell death pathway caspase3 is responsible for the execution pathway of PhS-Flip and the PMP. This discrepancy may be related to the indirect staining which probably causes a delay in fluorescence. Nevertheless, this marker can be used for discrimination when a cell has taken the caspase-dependent pathway or died via necrosis but cannot used for the evaluation of time sequences. The ellipse with the combination LMP and PhS-Flip (orange) needs also further consideration, as this contradicts the observation of the early marker correlation. Here, additional experiments and increased statistic are necessary. Last, an early event (LMP) is compared with the latest event (PMP), shown for STS (dark brown). The control shows a higher time difference than the early distribution which is consistent with the data of the early markers.

By the principal components analysis, a sequence of events can be derived. This is displayed in the lower panel of Fig. 4, in which average delay times $\Delta t = \langle t_{n+1} - t_n \rangle$ of both markers are plotted as bars in relation to the mean event time of marker $n$. The error bars represent the width of the single cell distribution of marker $n$ and hence constitute a measure for the uncertainty of the mean event time (position of the bars). For the NPs, no clear sequence whereas for STS a sequence of LMP, MOMP, ROS, PhS-Flip and PMP can be determined. The events follow in short time intervals. Note that for simplicity's sake the bivalent LMP-MOMP behavior is not taken into account here. Another consistency check shows that the sum of $t_{LMP\text{-}MOMP}$ and $t_{MOMP\text{-}PhS\ Flip}$ is smaller than the total time difference $t_{LMP\text{-}PMP}$, whereas $t_{PhS\ Flip\text{-}PMP}$ is not evaluated yet. Furthermore, the correlation analysis can provide information on the noise of a system as it also points out the width of a correlation.

## The ROS marker indicates a continuous signal increase

ROS plays a crucial role in apoptosis, as it is involved in different compartments of the cell. Thus, dose-dependent measurements were performed with ROS in combination with PI to check whether a different NP dose changes the cell behaviour. Besides the event times, further parameters from the fit functions are extracted, in particular the amplitude and the linear increase of the ROS level. In Fig. **5a**, the ROS activity (linear increase) is plotted against time point of cell death $t_{step}$(PI) for the negative control, for the positive control STS, and different NP doses. Up to a dose of 25 µg/ml, ROS activity is low as well as the fraction of dead cells. At 100 µg/ml, two populations can be discriminated: Cells which have a high ROS level die early (between 0 and 10 h), and cells which have a low ROS level die at later time points. In comparison to STS, ROS activity is moderate, and time response in cell death is broad. This dose-response analysis shows that cells respond differently upon NP dose. In Fig. 5b, averaged data of $t_{event}$ and quadratic increase in relation to NP dose is plotted. The product of $t_{event}$ and ROS increase leads to a constant value showing the direct correlation between those parameters (see Fig. 5c).

### Intracellular Lysosomal Fate Statistics

An important aspect is the study of the lysosomal signal. As each cell contains many single lysosomes, the mean signal, which is recorded in the time-lapse measurements, could lead to false conclusion, as especially the amount of uptaken NP could differ among the lysosomes. Thus, HCA analysis could give details on the lysosomal distribution in a cell. For the HCA measurements, cells were recorded with 60x resolution in a 10 min time interval. For each frame, ROIs of cells were determined and the number, total intensity, and total area of lysosomes were extracted. In Fig. 6b distributions on the total number of lysosomes are displayed at the beginning (0h) and up to 5h. A clear shift towards lower number of lysosomes can be observed. The mean signals from the distributions are plotted against time for the total intensity, total area and the number of lysosomes. The intensity and the area of the lysosomes decrease approximately at the same time, whereas the number of lysosomes decreases later. This could be interpreted as a sign that the lysosomes shrink before they rupture or by some bleaching artifacts. A shrinkage of the lysosomes are in contradiction to previous studies.

## Conclusion

In summary, we performed time-resolved measurements with multiple fluorescent cell death markers in pair wise combinations. Each single cell was fitted with a phenomenological fit functions from which characteristic event times were extracted. The pairwise combination of the event times using principal component analysis allows precise determination of time differences. This can be used to determine the induction and signal pathway of cell death. First preliminary results could confirm that amino-modified polystyrene particle induce cell death via the lysosomal pathway.

## Methods

### Cell Culture and Staining

A549 cell line (ATCC) was cultured in modified Eagle's medium with Earle's salts (c-c-pro), 2 mM L-glutamine (c-c-pro), and 10% fetal calf serum. Cells were grown to 70-80% confluence, trypsinized and centrifuged at 1000 rcf for 3 min. Cell pellets were re-suspended in either cell medium or, for the experiments in Leibovitz's L15 medium (ginco, Life Technologies) with 10% fetal calf serum.

Lysosomes were stained with Lysotracker Deep Red (75 nM, Life Technologies), mitochondria with Tetramethylrhodaminmethylester (10 nM, Sigma Aldrich), Cell Event Caspase 3/7 (3%, ThermoFisher), ROS level with CellROX green (100 nM), PS-exposure with polarity Sensitive Indicator for Viability and Apoptosis) (2%, Novus Biologicals). For nucleus staining different impermeant dyes Toto3 iodide (2µM, Life Technologies) and propidium iodide (1%, Life Technologies) were added. All dyes were applied without any further washing step.

### Micropatterning

The micro-structured surfaces were produced by selective oxygen plasma treatment (Femto Diener, 40 W for 3 min) on a topas substrate (µ-dishes ibidi GmbH) with subsequent passivation. A detailed protocol can be looked up at Segerer, et al. Selectivity was achieved using a polydimethylsiloxane (PDMS) stamp (cast from a master produced by photolithography) as a mask. The parts exposed to plasma were passivated with PLL(20k)–g(3.5)-PEG(2k) (SuSoS AG) at 2 mg/ml in aqueous buffer (10 mM HEPES pH 7.4 and 150 mM NaCl). The remaining sectors were rendered cell adherent by exposure to 35 µg/ml fibronectin (YoProteins) for 1 h. The probes were thoroughly rinsed with PBS; before cell seeding the samples were stored in cell medium at room temperature. PLL-g-PEG surfaces without patterns were treated in the same way. 30 µm x 30 µm square adhesion sites were used, as this size turned out to be reasonable for single-cell adhesion of all three cell lines. Cells were seeded to achieve a filling of roughly one cell per adhesion site (e.g. for a lattice distance of 90 µm, 8,000 cells were seeded per well).

### Time-Resolved Fluorescence Microscopy

Images were taken with an inverted Nikon Ti eclipse microscope with phase contrast and a fluorescent lamp with multiple filter sets (DAPI, CFP, GFP, Propidium iodide, Cy5). Samples were kept at a constant temperature of 37°C with an ibidi heating system (ibidi GmbH). Pictures were recorded every 10 min over a period of 30 h.

### Image and Data Analysis

Raw images were pre-processed in ImageJ: For the image analysis on the cell grid and a background correction were used in an in house written plugin. Onset times of the different markers and the principal component analysis were analyzed in MATLAB.

## Acknowledgements

Financial support by FP7 EU grant NanoMILE and the Excellence Cluster 'Nanosystems Initiative Munich (NIM)' is gratefully acknowledged.

## References:

1. Vanden Berghe T, Vanlangenakker N, Parthoens E, Deckers W, Devos M, Festjens N, *et al.* Necroptosis, necrosis and secondary necrosis converge on similar cellular disintegration features. *Cell Death Differ* 2010, **17**(6)**:** 922-930.

2. Wang F, Bexiga MG, Anguissola S, Boya P, Simpson JC, Salvati A, *et al.* Time resolved study of cell death mechanisms induced by amine-modified polystyrene nanoparticles. *Nanoscale* 2013, **5**(22)**:** 10868-10876.

3. Anguissola S, Garry D, Salvati A, O'Brien PJ, Dawson KA. High content analysis provides mechanistic insights on the pathways of toxicity induced by amine-modified polystyrene nanoparticles. *PloS one* 2014, **9**(9)**:** e108025.

4. Xia X, Owen MS, Lee RE, Gaudet S. Cell-to-cell variability in cell death: can systems biology help us make sense of it all? *Cell death and differentiation* 2014, **5:** e1261.

5. Spencer SL, Gaudet S, Albeck JG, Burke JM, Sorger PK. Non-genetic origins of cell-to-cell variability in TRAIL-induced apoptosis. *Nature* 2009, **459**(7245)**:** 428-432.

7. Röttgermann PJF, Dawson KA, Rädler JO. Time-Resolved Study of Nanoparticle Induced Apoptosis Using Microfabricated Single Cell Arrays. *Microarrays* 2016, **accepted**.

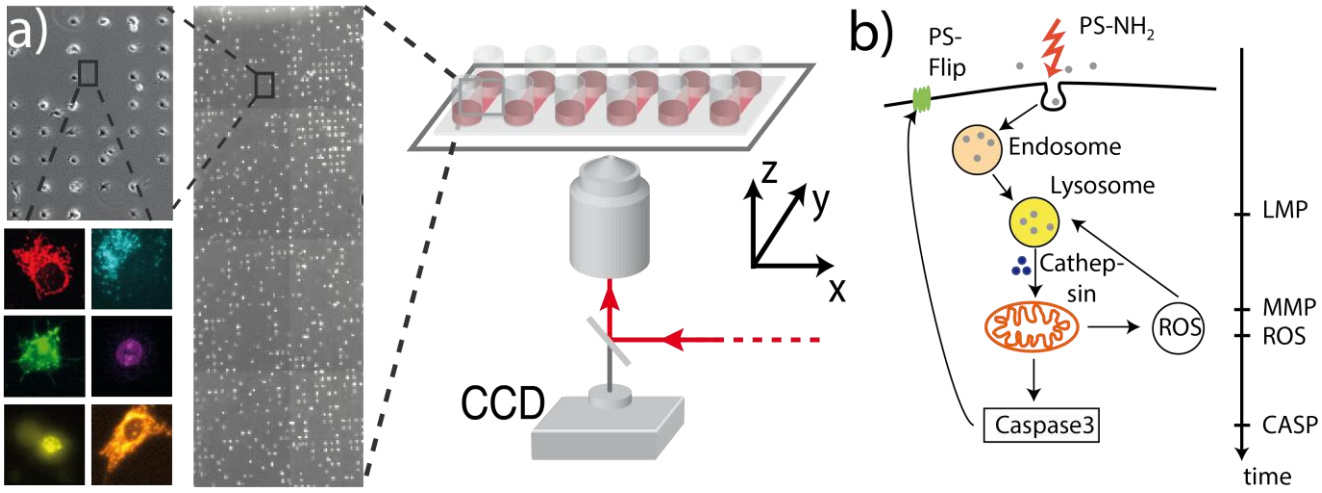


***Figure 1.*** *a) Experimental setup. Cells are seeded on micropatterns . After 6 hours of incubation cell arrange into a single cell array. Over 50% of the sites are occupied by single cells. One well contains at least 1000 single occupied cells. Different cell organelles are stained: Mitochondria (red), Lysosomes (cyan), phosphatidylserine (green), nucleus (magenta), nucleus by caspase cleaved product (yellow), ROS (orange) b) Hypothetical schematic lysosomal apoptotic signal pathway induced by PS-$NH_2$ NPs.*

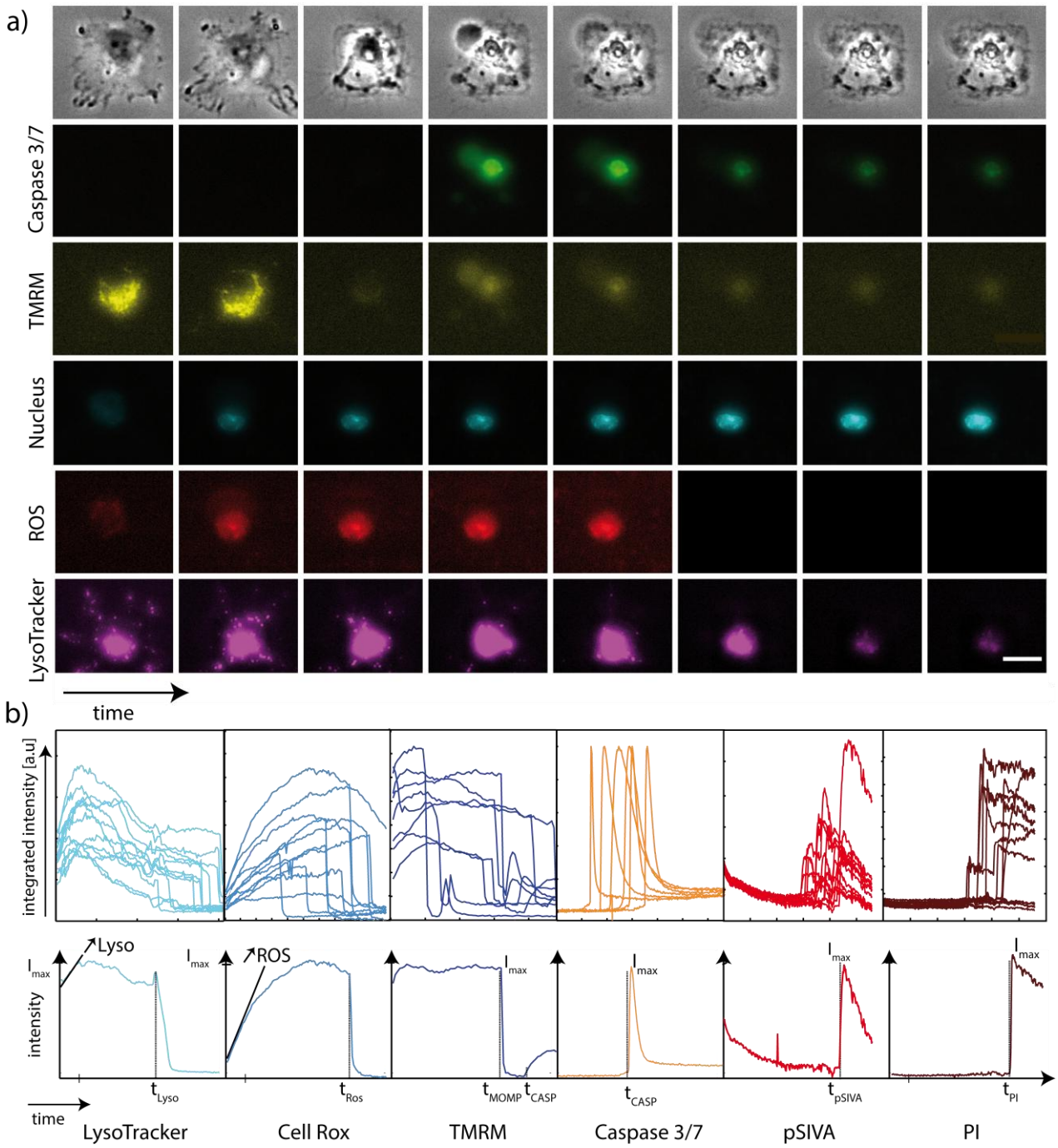


***Figure 2*** *a) Time series of cell death at selected time points (0-24 h): Caspase3/7 (green) indicates caspase3/7 activation, TMRM marker (yellow) indicates the staining of mitochondrial potential, nucleus marker (cyan) stains plasma membrane permeabilization with subsequent staining of the nucleus, CellROX fluoresces red in presence of oxidative stress and LysoTracker (purple) stains the lysosomes. Scale bar: 25 µm. b) Exemplary time traces of single cells: Lysosomes (LysoTracker), ROS-level (CellROX), MOMP (TMRM), Caspase3/7 activation (Cell Event Caspase3/7), PhS-Flip (pSIVA-IANBD), nucleus staining by PI or Toto3 (NUC). The early markers (first three graphs) and the late markers (last three graphs) show similar characteristic behavior. By fitting phenomenological functions to the single cell traces using a maximum likelihood fitting routine characteristic parameters such as event times, slope of increase and maximal intensity can be extracted.*

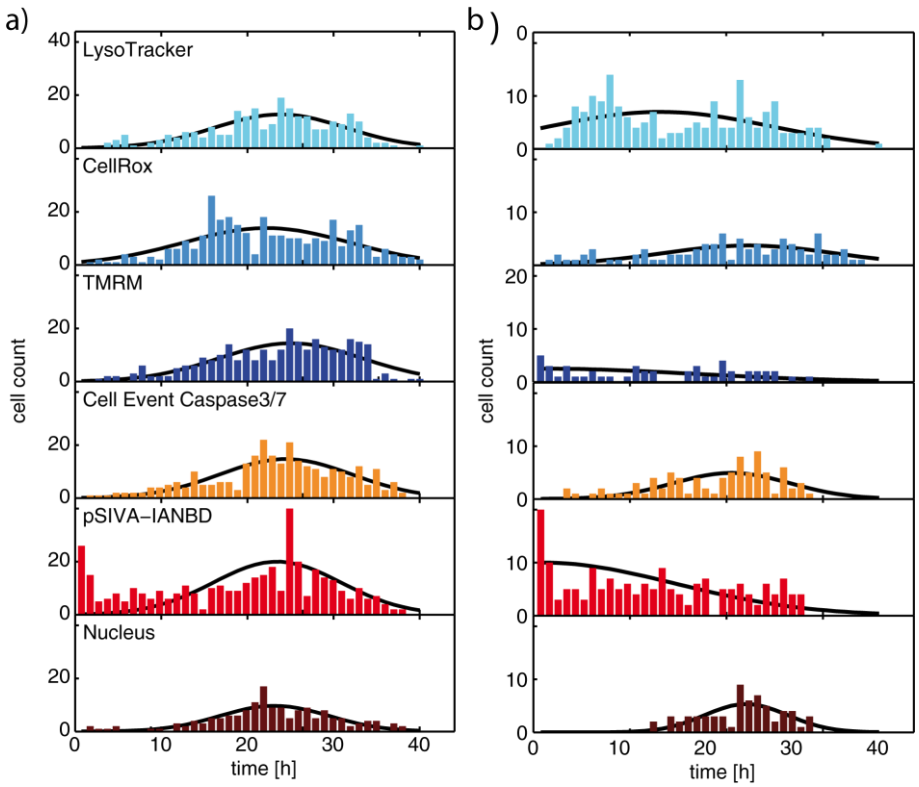


***Figure 3.*** *Frequency distributions of single cell event times for various markers: LysoTracker (light blue), CellROX (medium blue), TMRM (dark blue) Caspase3/7 (orange), pSIVA-IANBD (red), and Nucleus (dark red) for a exposure with a) 25 µg/ml PS-$NH_2$ and b) 2 µM STS. In order to evaluate mean times, Gaussians were fitted to the distributions. The mean times of the distributions show no clear sequence. However, for STS the single cell responses are more broadly distributed.*

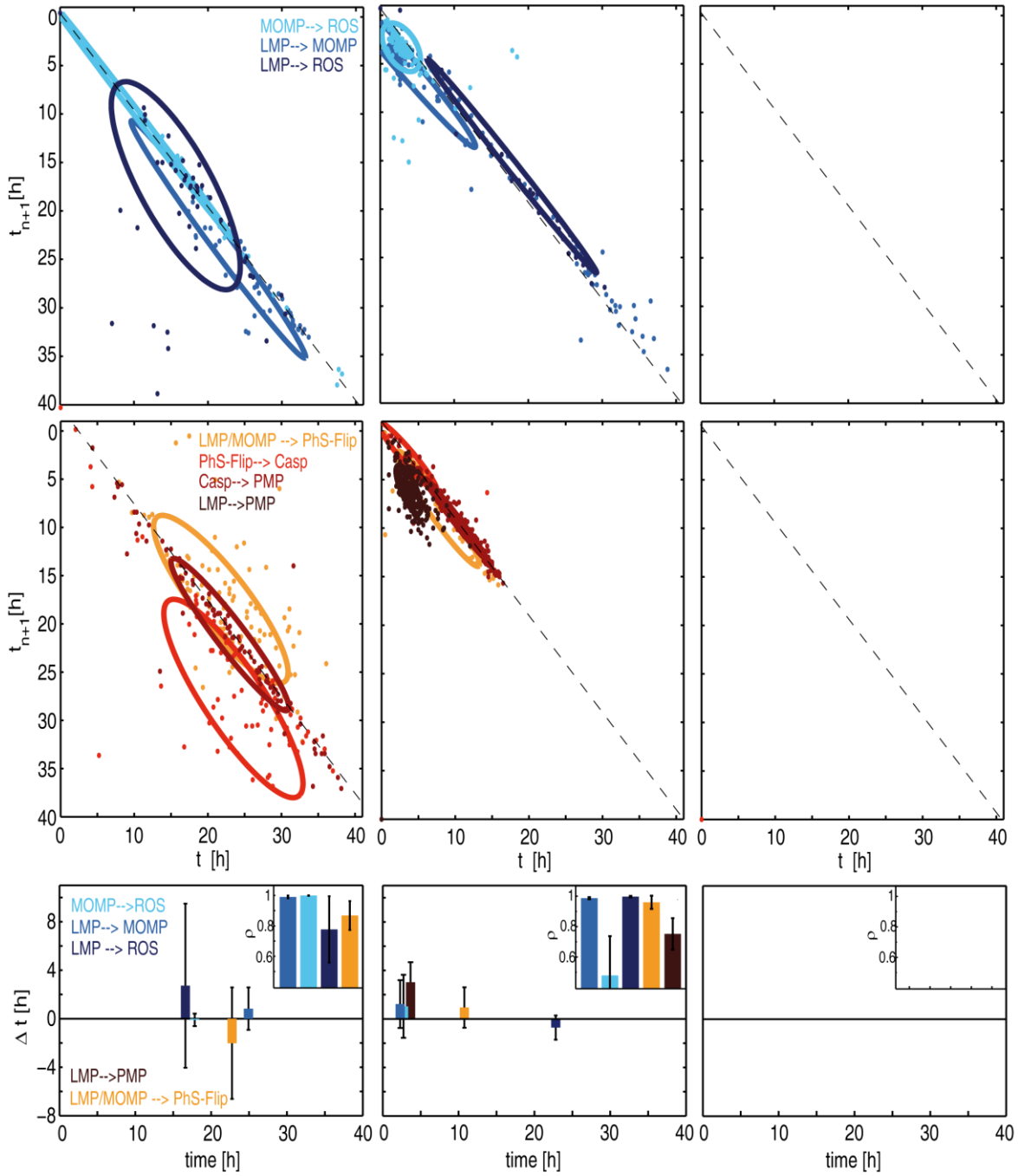


***Figure 4:*** *Two-dimensional representation of event times $t_n$ and $t_{n+1}$ of pair wise markers of NP PS-$NH_2$ treated cells(a), STS (b) and FAS (c) induced cell death. The upper row shows the marker combinations of the early death events with MOMP - ROS (light blue), LMP – MOMP (blue), LMP – ROS (dark blue), the middle row the combinations of the late markers with LMP/MOMP - PhS-Flip (orange), PhS-Flip - Casp3 (red), Casp - PMP (dark red), and LMP - PMP (dark brown). The ellipses display a one sigma interval (67% of data) of the principal component analysis. Lower row: Bar plot of $\Delta t = t_{n+1} - t_n$ of successive events, in particular the time distance between the diagonal shown in the ellipse plots, vs. the mean event time $t_n$. The error bar corresponds to the width of the single cell distribution of marker n. Caspase3 was excluded from the analysis for the event order, as the event times occur after all the other markers and hence cannot be used for the time correlation.*

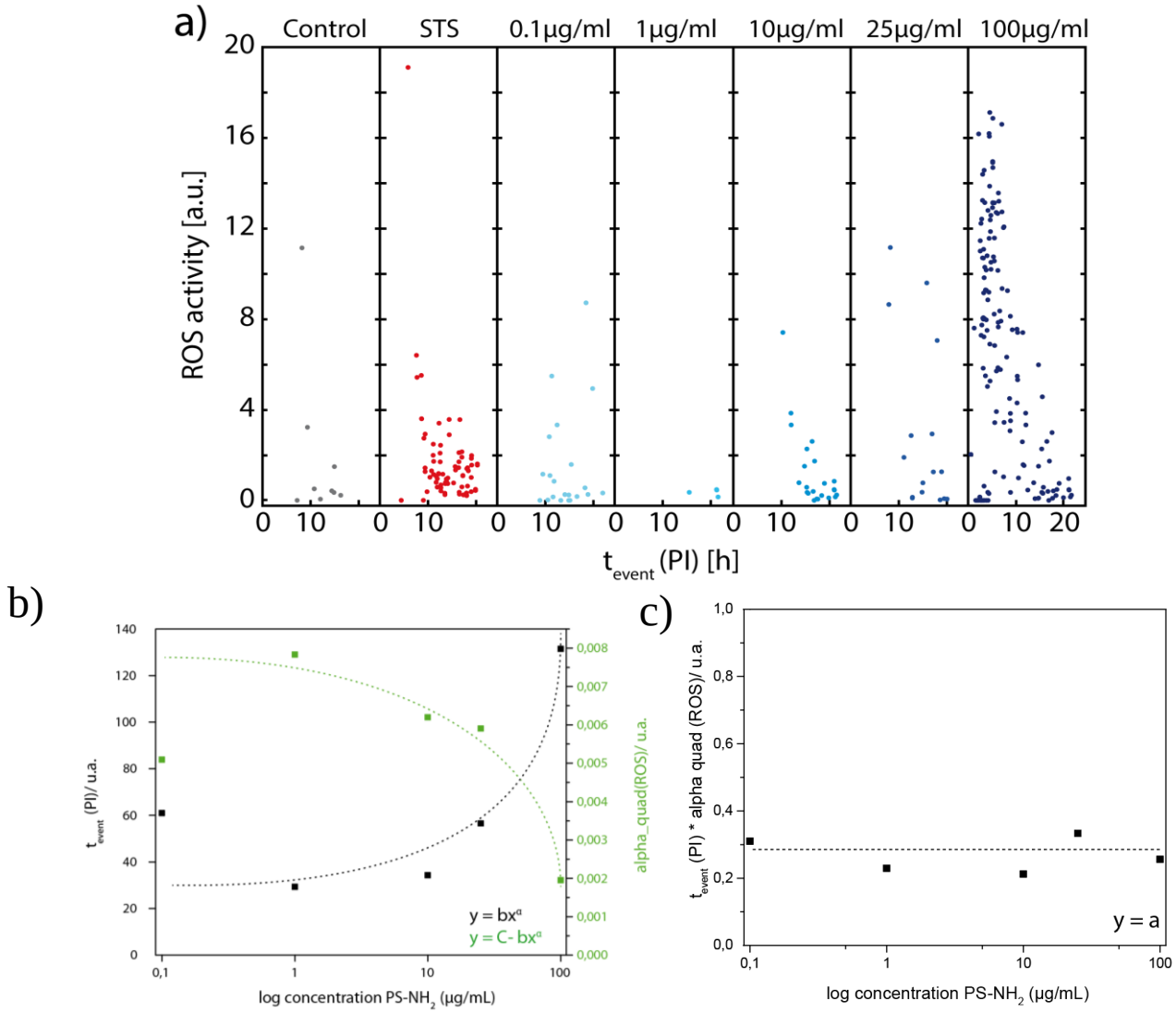


***Figure 5:*** *ROS activity was measured for different NP doses (0.1, 1, 10, 25 and 100 µg/ml), for a negative control (cell culture medium) as well as for a positive control (STS). The ROS activity (linear increase of the fluorescence) is plotted against the time of death* $t_{event}$*. High ROS activity is observed for the highest NP dose. Cells which die early have a high ROS level, whereas cells which die late, similar to that of STS, exhibit a low level. Correlation analysisof ROS for different NP doses: a) Scatter plot with dependence of ROS increase and ROS drop signal (offset time). b) Averaged data of* $t_{event}$ *and quadratic increase in relation to NP dose. As a guide for the eye, power law is plotted. c) Product of* $t_{event}$ *and ROS increase leads to a constant value showing the direct correlation between those parameters.*

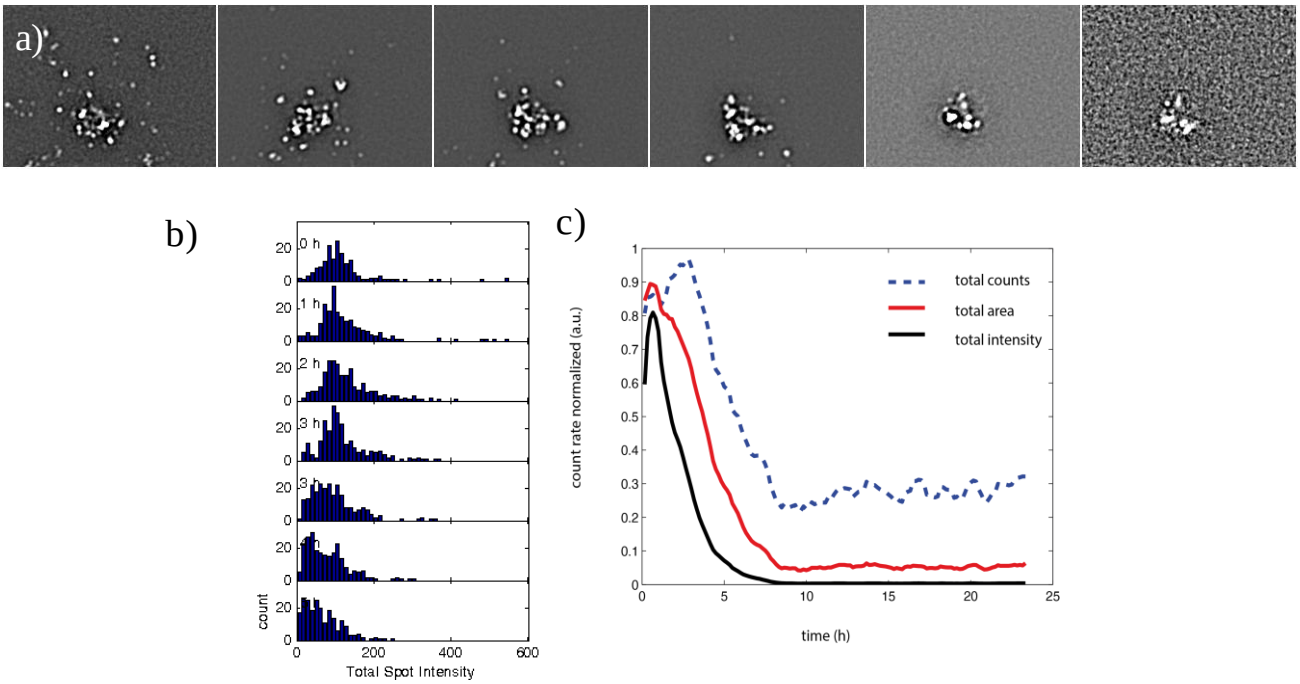


***Figure 6:*** *a) Time series of a single cell, lysosomes are highlighted as white spots. b) The number of lysosomes per cell, the total area and the total intensity were measured over a period of 24 h. The distributions of the total number of lysosomes at the beginning (0 h) in comparison to the time after 5 h show a shift towards less lysosomes per cell. c) Averaged numbers of the total counts (blue dotted), the total lysosomal area (red) and the total lysosomal intensity (black) are plotted against time. A clear shift between the number of lysosomes and the area can be observed.*

# Supplement 1: Algorithms

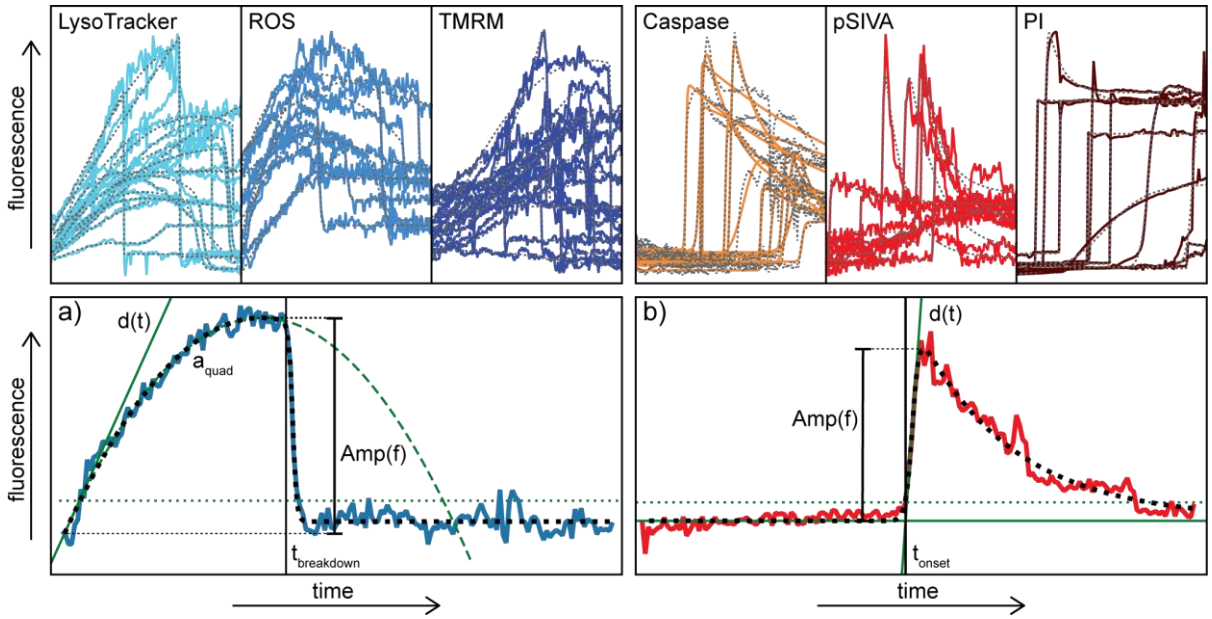


**Figure S1**: Upper row: Exemplary time traces for the various markers (LysoTracker, ROS, Caspase, TMRM, pSIVA, and PI) of the experimental data (colored lines) and the corresponding fits (dashed lines). The early markers are characterized by a parabolic ascent followed by a steep breakdown, and the late markers by a steep onset followed by a decay.
Lower row: Overview of the signatures extracted from the fits (dotted black lines) of the single cell traces (orange/blue line) with their amplitudes and the corresponding noise levels (dotted green lines). (a) shows an early marker trace with its initial slope (solid green line). The marker breakdown time (vertical black line) is the time from which on the trace deviates from the parabolic behaviour (dashed green line). (b) shows a late marker trace. The marker onset time (vertical black line) is the time when the onset tangent (diagonal solid green line) crosses the initial fluorescence level (horizontal solid green line).

In the main text we described some signatures of the single cell traces. The signatures were not extracted directly from the traces but from marker-specific phenomenological functions that had been fitted to the traces. In this section we want to describe the phenomenological functions we fitted to the traces and the rules we used to extract the signatures.

**Phenomenological functions**

The six markers are divided into two classes, based on their characteristic behaviour: the early markers (LysoTracker, ROS, and TMRM) and the late markers (Caspase, pSIVA, and PI). Exemplary time traces for the markers with the corresponding fits are shown in Fig. S1. Marker specific functions were fitted with a maximum likelihood method assuming a gaussian probability distribution .

The traces of the late markers were fitted with the phenomenological function

$$f(t) = A + B \cdot \sigma(t) \cdot \left(e^{\gamma\left(t_{\text{step}} - t\right)} + b\right), \qquad \text{(S1)}$$

with the sigmoid function

$$\sigma(t) = \frac{1}{1 + e^{\alpha(t_{\text{step}} - t)}} \tag{S2}$$

and the fit parameters $A$, $B$, $\gamma$, $t_{\text{step}}$, $b$, and $\alpha$. $A$ is the global offset of the function, and $B$ the scaling factor, specifying the peak height. $\sigma(t)$ describes the rise of the fluorescence at time $t_{\text{step}}$ with a steepness $\alpha > 0$. The signal decay caused by photobleaching is described by time $t_{\text{step}}$, a decay constant $\gamma$ and an offset $b$ between the initial level $A$ and the final level.

The traces of the early markers were fitted with the phenomenological function

$$f(t) = \sigma(t) \cdot \left(a_{\text{const}} + s\, a_{\text{quad}}(t - t_{\text{vertex}})^2\right) + \left(1 - \sigma(t)\right) \cdot b, \tag{S3}$$

with the fit parameters $a_{\text{const}}$, $s$, $a_{\text{quad}}$, $t_{\text{vertex}}$, and $b$. The sigmoid function $\sigma(t)$ describing the transition from the parabola to the final value $b$ is the same as in (S2), with the sharpness $\alpha < 0$. The first term describes a parabola with constant coefficient $a_{\text{const}}$, quadratic coefficient $a_{\text{quad}}$, and vertex at $t_{\text{vertex}}$. $s \in \{-1, +1\}$ determines the opening direction of the parabola and is fixed to $s = -1$ for LysoTracker and ROS.

For each fitted trace, the minimum value $\min(f) \coloneqq \min_{i=1,\dots,N}(f_i)$ and the maximum value $\max(f) \coloneqq \max_{i=1,\dots,N}(f_i)$ of the datapoints $f_i \coloneqq f(t_i)$ with the timepoints $t_i$ for $i = 1, \dots, N$ are calculated. This allows to define the amplitude of a trace as

$$\text{amp}(f) \coloneqq \max(f) - \min(f). \tag{S4}$$

The times corresponding to minimum and maximum are denoted as $t_{\text{min}}$ and $t_{\text{max}}$, respectively. Moreover, we define the value of half amplitude $f_{1/2}$ as

$$f_{1/2} \coloneqq \frac{\min(f) + \max(f)}{2} \tag{S5}$$

and the time $t_{1/2}^{<}$ of half amplitude before the maximum as

$$t_{1/2}^{<} \coloneqq t_i \,|\, i \in \{1, \dots, N\} \text{ such that } \left|f_i - f_{1/2}\right| \text{ minimal and } t_i < t_{\text{max}}. \tag{S6}$$

**Rules for determination of signatures**

The fluorescence onset time $t_{\text{on}}$ of the late markers is the intersection of the ascent tangent at half maximum with the initial value, and is given by

$$t_{\text{on}} \coloneqq \frac{\left(f_1 - f_{1/2}\right)}{\left.\frac{\mathrm{d}f}{\mathrm{d}t}\right|_{t = t_{1/2}^{<}}} + t_{1/2}^{<}, \tag{S7}$$

where

$$\left.\frac{\mathrm{d}f}{\mathrm{d}t}\right|_{t = t_{1/2}^{<}} \coloneqq \frac{f_{j+1} - f_{j-1}}{t_{j+1} - t_{j-1}}, \tag{S8}$$

with $j \in \{2, \dots, N-1\} \mid t_j = t_{1/2}^{<}$.

The fluorescence breakdown time $t_{\text{breakdown}}$ of the early marker signals is the time at which the deviation from the initial parabolic behaviour exceeds an empirical threshold $\Delta p_{\max}$, a good value for which showed to be 3% of the trace amplitude. Let the parabola values $\{p_i\}_{i\in\{1,\dots,N\}}$ be given by

$$p_i = a_{\text{const}} + s\, a_{\text{quad}}(t_i - t_{\text{vertex}})^2, \tag{S9}$$

with the parameter values obtained from the fit. Then, the breakdown time is

$$t_{\text{breakdown}} = \min_{i\in\{2,\dots,N-1\}}(t_i | p_i - f_i > \Delta p_{\max}). \tag{S10}$$

An overview of the signatures extracted from the fits is given in fig. S1.

In addition to the event times, also the trace amplitude and the event slopes are extracted from the fits. The amplitude is defined in .(S4). The onset slope is the slope of the tangent to the rising edge with the largest slope, the breakdown slope is the slope of the tangent to the falling edge with the smallest slope.

**Filter rules**

For discrimination between an apoptosis signal and undefined behaviour, filter rules were determined.

Any traces with amplitudes $\text{amp}(f)$ larger than 100 times the median of amplitudes are sorted out to eliminate outliers, as well as traces with amplitudes smaller than 10% of the largest amplitude of the remaining traces, which can hardly be distinguished from noise. Another criterion aims at traces with transient, narrow peaks, which are caused by fluorescent dirt particles floating through the image. Also traces that merely show a monotonously increasing or decreasing signal are filtered out since they bear too few information.

Additionally, there are specific filter rules for the two marker classes.

Late marker traces are sorted out if the maximum value is reached before the minimum value, or if the fluorescence is changing too fast at the beginning or still increasing at the end of the measurement.

Early marker traces are sorted out if the maximum value is at the first or at the very last timepoint of the measurement, if the kink steepness $\gamma$ is smaller than an empiric threshold, or if the fluorescence breakdown is too shallow.

# Danksagung

Ich möchte mich an dieser Stelle bei allen bedanken, die mich bei der Entstehung meiner Doktorarbeit unterstützt haben. Im Besonderen gilt mein Dank

**Prof. Joachim Rädler**, der mir die Möglichkeit gegeben hat das spannende Feld der Zellbiophysik zu entdecken, so selbständig arbeiten zu können und immer mit guten Ideen und Inspirationen zur Seite zu stehen,

meinen Kollaborationspartnern, durch die ich neue Einblicke in die Welt der Neutronenstreuung (**Bert Nickel**, **Samira** und **Ida**), der DNA-Goldrods (**Jessica Rodríguez-Fernández** und **Verena**) und der Toxizität von Nanopartikeln (**Kenneth Dawson** und **Daithi**) erhalten durfte,

**Gerlinde** für die großartige Stütze in der Zellkultur und für ein immer offenes Ohr in auch nicht wissenschaftlichen Themen, **Susi K.** für die Hilfsbereitschaft im Labor und die Gespräche über "mindando" bei einem Tässchen Espresso, **Claudia** für die kleinen Hilfen im Labor und den Kaffeepausen, **Charlott**, **Max** und **Susi R.** für die Herstellung der Strukturen,

**Tobias** für die unermüdliche und sofortige Hilfe in Sachen IT, **Margarete** und **Andrea** für die Unterstützung in allen organisatorischen Dingen,

der kompletten Zell-Crew, **Felix** (mit dem ich nun schon seit der BA-Arbeit einen gemeinsamen Weg gegangen bin), **Matthias**, **Christoph**, **Anita**, **Fang**, **Rafael**, **Jürgen**, **Valentin**, **Devid**, für die anregenden Diskussionen in den Zellmeetings und dass ich für euch der "Hood-Grumbler" sein durfte, sowie den Ehemaligen **Alicia**, **Carolin**, **Svenja**, **Farzad**, **Tina**,

dem in allen Belangen "best-equipped" Büro am Lehrstuhl mit **Andi**, **Judith**, **Silvia**, **Matthias R.**, **Tino**, **Ellie**, **Robert**, **Michi E.**, **Michi I.**, **Ricarda** und **Alex G.** die gekommen und gegangen sind. Zeit für mich zu gehen...,

den Studenten, die ich betreuen durfte und dabei viel gelernt habe: **Isabelle**, **Amira**, **Alexandra F.**, **Tina**, **Lisa** und **Daniel**

meiner Nachfolgerin **Alexandra M.**, der ich alles Gute für das faszinierende Projekt der Single-Cell Toxizitätsstudien wünsche,

dem **gesamten Lehrstuhl Rädler** mit seiner entspannten Atmosphäre, den unvergesslichen Antholz-Winterschulen, den zahlreichen Aktivitäten (Kickerturniere, LS-Wanderungen, Grillabende) und dem ich mit weinendem Auge die Schnapsbar überlassen werde,

meiner "zweiten Heimat" in der Uni, der **AG Braun**, insbesondere **Christof**, **Simon**, **Manu**, **Ike**, **Georg**, **Matthias**, **Lorenz** für die Kaffeepausen an der goldenen Espresso-Maschine, den Mi-Meetings, und den unvergesslichen Schokobrunnenaktionen,

den eifrigen **Korrekturlesern** für ihre Mühen mein Englisch gerade zu rücken,

und zu guter Letzt **meiner Familie**, die mir Rückhalt und Anerkennung gegeben haben und insbesondere **Susi S.**, die mich in allen Lebenslagen unterstützt und auch motiviert hat, und dafür, dass du einfach da bist!